MICROSTRUCTURE-SENSITIVE SIMULATION OF SHOCK LOADING IN METALS

A Thesis
Presented to
The Academic Faculty

by

Jeffrey T. Lloyd

In Partial Fulfillment
of the Requirements for the Degree
Doctor of Philosophy in the
Mechanical Engineering

Georgia Institute of Technology
May, 2014

Copyright © 2014 by Jeffrey T. Lloyd

MICROSTRUCTURE-SENSITIVE SIMULATION OF SHOCK LOADING IN METALS

Approved by:

Dr. David L. McDowell, Advisor
G.W.W. School of Mechanical Engineering
Georgia Institute of Technology

Dr. John D. Clayton
ARL/WMRD, Impact Physics Branch
Aberdeen Proving Ground

Dr. Min Zhou
G.W.W. School of Mechanical Engineering
Georgia Institute of Technology

Dr. Naresh N. Thadhani
School of Materials Science and Engineering
Georgia Institute of Technology

Dr. Shuman Xia
G.W.W. School of Mechanical Engineering
Georgia Institute of Technology

Dr. Julian J. Rimoli
School of Aerospace Engineering
Georgia Institute of Technology

Date Approved: March 19, 2014

ACKNOWLEDGEMENTS

I would like to thank my advisor Dr. David McDowell, for his enthusiasm, encouragement, and desire to help me understand a broad field yet making specific contributions to a narrow set of problems during my Ph.D. efforts at Georgia Tech. I would like to thank members of my reading committee for their valuable input: Dr. John Clayton, Dr. Min Zhou, Dr. Naresh Thadhani, Dr. Shuman Shia, and Dr. Julian Rimoli. I am grateful to have had the opportunity to spend one summer at Sandia National Laboratories in Livermore, CA under the guidance of Dr. Jonathan Zimmerman as well as two summers at the Army Research Laboratory in Aberdeen, MD under the guidance of Dr. John Clayton and Dr. Richard Becker. I would also like to thank Dr. Ryan Austin for continued discussions concerning development of the plane wave method and viscoplastic model.

It has been a privilege to work with such a large group of talented, social-minded friends at Georgia Tech, which arranged in a very particular order from tallest to shortest are: Dr. Ryan Austin, Dr. Jason Mayeur, Dr. Brett Ellis, Shreevant Tiwari, Michael Kirka, William Musinski, Matthew Priddy, Chris Lammi, Sam Britt, Dr. Rajesh Prasannavenkatesan, Ben Smith, Jin Song, Dr. Jagan Padbidri, Shuozhi Xu, Dr. Gustavo Castelluccio, and Dr. Anirban Patra. I would also like to thank many of the friends that I have met over my last 10 years at Georgia Tech since beginning as an undergraduate in 2004.

I am very fortunate to have a supportive and loving family from which I have received considerable guidance, support, and encouragement. I would especially like to thank my parents Mike, Cathy, and Leslee, my brothers Mike, Bill, Jeff, and their families, and my grandparents Colleen and Gammy. And finally, this thesis would not have been possible without the love and support of my wife, Melanie.

TABLE OF CONTENTS

LIST OF TABLES

LIST OF FIGURES

SUMMARY

A constitutive model has been developed to model the shock response of single crystal aluminum from peak pressures ranging from $2-110$ GPa. This model couples a description of higher-order thermoelasticity with a dislocation-based viscoplastic formulation, both of which are formulated for single crystals. The constitutive model has been implemented using two numerical methods: a plane wave method that tracks the propagating wave front; and an extended one-dimensional, finite-difference method that can be used to model spatio-temporal evolution of wave propagation in anisotropic materials. The constitutive model, as well as these numerical methods, are used to simulate shock wave propagation in single crystals, polycrystals, and pre-textured polycrystals. Model predictions are compared with extensive existing experimental data and are then used to quantify the influence of the initial material state on the subsequent shock response. A coarse-grained model is then proposed to capture orientation-dependent deformation heterogeneity, and is shown to replicate salient features predicted by direct finite-difference simulation of polycrystals in the weak shock regime. The work in this thesis establishes a general framework that can be used to quantify the influence of initial material state on subsequent shock behavior not only for aluminum single crystals, but for other face-centered cubic and lower symmetry crystalline metals as well.

CHAPTER I

INTRODUCTION

The focus of this work is to develop a framework that can be used to directly model microstructure sensitivity of the shock loading response in metals. Most engineering applications that require an optimized material system to perform at strain rates ranging from $10^4 - 10^{10}$ s^{-1} use materials that have undergone significant pre-processing to alter their initial microstructure. Unlike in lower rate applications, wherein a variety of tests can be performed to directly observe material substructure development during loading or directly after loading, high rate experiments occur extremely fast and violently, which renders in-situ material observation nearly impossible. Despite these complications, a significant amount of experimental work has been performed to measure the influence of microstructure in high strain rate and shock loading experiments performed on single crystal and polycrystalline metals [20, 21]. Experiments have shown single crystal orientation in metals influences precursor decay [22], dynamic strength [14, 13], localization behavior [23], and spall strength [24, 25, 26]. Similarly, experiments have quantified the influence of microstructure features such as grain size [24, 27] and extent of cold rolling [19] on the dynamic compression and spall response of polycrystals. A unifying feature from all of these studies is that although the initial microstructure can be quantified before and after the experiment, an understanding is lacking of how this initial microstructure influences the resultant material in the shocked state. Although experimental efforts are underway to capture time-resolved microstructure evolution during shock loading, these capabilities have not been developed at the time of this work. Therefore, to understand how initial microstructure influences the resultant substructure that develops during shock loading, computational methods and microstructure-sensitive constitutive models need to be developed that can directly model initial and evolving microstructure during shock loading.

Since experiments show that initial microstructure significantly affects many aspects

of the shock response of materials, but the influence of this initial microstructure on the shocked material state is poorly understood, the objectives of this work are the following:

- Develop a thermoelastic-viscoplastic model that can address the physics of single crystal deformation at high rates based on an arbitrary initial material state.
- Develop computational tools that can be used to rapidly assess constitutive models for single crystal deformation and directly model plate impact experiments.
- Quantify single crystal orientation dependence on the observed response and microstructure evolution at high rates.
- Understand differences between the shock response of annealed and pre-textured polycrystalline metals.

In this work, aluminum is chosen as the material of interest. Due to its relatively low density, aluminum has been used extensively in armor applications that are designed to withstand extremely high loading rates. Because of its widespread use, there is a relatively large body of existing experimental data concerning the response of aluminum at high rates. Although the work performed in this thesis focuses on this particular high stacking fault FCC metal, the constitutive framework and computational tools developed in this thesis are general and can readily be extended to modeling lower symmetry crystals as well.

Nearly all of the constitutive models used to capture high strain rate deformation in metals are macroscopic in nature, with some noteworthy past [22, 28] and recently developed models [29, 30, 31, 32, 33]. The most widely used constitutive models have been developed to fit a set of experimentally observed relations which, stated generally, show that the dynamic strength is influenced by the strain, strain rate, and temperature. Although these models are extremely useful when used in an interpolative fashion, where the material response is already well characterized experimentally, they generally give little insight into the physical processes that occur at high rates. They also generally lack proper consideration of path dependence and lack dependence on initial material state. One aspect that complicates development of micromechanics based models is that they are computationally demanding.

To capture development of material anisotropy during deformation, either a two or three-dimensional formulation must generally be employed, even if problems of interest such as plate impact experiments are inherently one-dimensional. To facilitate rapid development of advanced micromechanics based models, computationally efficient numerical methods must be developed that can incorporate material anisotropy.

To meet the goals of this work and to facilitate rapid development of general micromechanics based constitutive models for modeling high strain rate deformation, this work has the following components:

- Develop a single crystal model that incorporates single crystal thermoelasticity with a physics-based internal state variable representation of plastic deformation applicable to high rates.
- Extend the plane wave method developed to model isotropic materials so that it can be used to directly model single crystals.
- Characterize the orientation-dependent response of single crystal aluminum.
- Create a methodology and numerical implementation that can be used to simulate plate impact using an extended one-dimensional, finite-difference method for anisotropic material response.
- Directly model spatio-temporal response of single crystals, polycrystals, and pre-textured polycrystals and analyze shocked material state.
- Determine differences between plane wave and finite-difference methods, and determine whether or not information from plane wave method can be used to predict polycrystal deformation response.

In Chapter 2, a thermodynamic formulation used to describe thermoelastic-viscoplastic materials that employs internal state variables to represent the instantaneous state of the material is developed for both continuous as well as discontinuous deformation. General theories for thermoelastic deformation are then presented in the context of this general theory, where it is observed that many "equations of state" traditionally used to describe high-pressure experiments invoke thermoelastic constitutive assumptions used in the context

of a specific generalization of this general thermodynamic theory. Then, existing macroscale dynamic strength as well as dislocation-based models are presented in the context of this thermodynamic theory. Advantages, limitations, as well as the physical motivation of these theories are discussed in the context of general viscoplastic internal state variable theory.

A specific thermoelastic-viscoplastic model is developed in Chapter 3 to model single crystal aluminum. To capture thermoelastic deformation, two formulations that employ different strain measures are developed and compared, namely, the elastic total Lagrangian Green strain and an Eulerian material strain [34]. It is shown that for problems that experience large compression the Eulerian material strain converges more rapidly towards physically realistic behavior than the conventional Green strain. A single crystal viscoplastic model is developed by extending a physically-based high strain rate viscoplastic model [35, 36] to model single crystals by appealing to existing physically based crystal plasticity theories that incorporate the effect of forest and parallel dislocation densities [37].

In Chapter 4, the plane wave method is extended so that it can be used to model materials that exhibit a general thermoelastic-viscoplastic, anisotropic material response. The plane wave method is used to simulate the response of aluminum single crystals subjected to peak pressures ranging from approximately $0 - 30$ GPa. Wave profiles and viscoplastic deformation characteristics are compared with existing experimental data from longitudinal plate impact studies on single crystal aluminum samples that contain three-fold or greater symmetry ([100], [110], and [111] orientations). A parametric study is then performed on general orientations by performing simulations on thousands of randomly oriented single crystals shocked at peak pressures ranging from $0 - 30$ GPa. It is shown that a scalar "modified Taylor factor" $\langle M \rangle$ can be used to quantify some orientation-dependent shock characteristics reasonably well, especially in the weak shock regime.

A numerical algorithm is developed and implemented in Chapter 5 to simulate longitudinal plate impact and laser shock loading by use of the extended one-dimensional, finite-difference method for anisotropic materials. Although this method is one-dimensional, it can be used to model quasi-longitudinal and quasi-transverse wave formation, which is necessary to capture general, anisotropic single crystal response. Because this method can

capture spatio-temporal effects that cannot be modeled using the plane wave method, it is used to simulate plate impact as well as laser shock experiments on single crystal aluminum up to 110 GPa. The model is then used to directly simulate vapor-deposited polycrystals and characterize the effect of orientation on the observed response. A method is then developed to use results from quasi-static cold-rolling simulations as direct input into polycrystal simulations of cold-rolled specimens. Effects of pre-texturing on the viscoplastic response are quantified.

In Chapter 6, direct comparisons are made between plane wave and finite-difference simulations of plate impact. The approximation introduced by assuming uniaxial strain for impact of low-symmetry aluminum single crystals is examined. Additionally, the approximation introduced by utilizing an artificial viscosity in the finite-difference method is also analyzed. A general trend emerges: when transient spatio-temporal effects can be neglected, the plane wave method is preferable, as it is two to three orders of magnitude more computationally efficient than finite-difference simulations and does not use an artificial viscosity. A coarse-grained model that uses results from the plane wave method is then used to capture the influence of individual single crystals on the polycrystalline response. It is shown that the model can reproduce aspects of finite-difference simulations of polycrystals in a purely analytical framework, thus circumventing the need for computationally demanding finite-difference simulations.

In Chapter 7, the unique contributions of this work are summarized and compared with recent computational studies of high strain rate single crystal deformation. Limitations of the constitutive and computational frameworks presented of this work are explored, and future applications and pathways for this research are explored.

Notation in the following Chapters uses upper case Latin indices to indicate the reference configuration (A_{AB}), Greek indices to indicate the intermediate configuration ($A_{\alpha\beta}$), and lower case Latin indices to indicate the current configuration (A_{ab}). Repeated subscripts are summed over the range.

CHAPTER II

THERMODYNAMICS BACKGROUND AND EXISTING HIGH RATE CONSTITUTIVE MODELS

2.1 Introduction

In this chapter, it will be shown that many existing theories and associated constitutive models used to describe high strain rate and shock deformation can be viewed as subsets of a general thermodynamic framework that is used to model thermoelastic-viscoplastic materials undergoing arbitrary deformation histories (continuous or discontinuous), and which employ internal state variables to characterize the instantaneous response of the material. Framing the capabilities as well as limitations of existing theories within this context serves as motivation for the form of the thermoelastic-viscoplastic constitutive model developed in Chapter 3, as well as historical developments and observations that this constitutive model builds upon.

2.2 Continuum mechanics background for thermoelastic materials with evolving internal state variables

2.2.1 Continuum quantities and balance equations

Consider a local thermodynamic process acting on a material point $\mathbf{X}$ in the absence of couple stresses, external radiation, and body forces, which is defined as a process that obeys the balance laws of momentum and energy acting on some body B specified by the following quantities [38]:

- The spatial position $\mathbf{x} = \chi(\mathbf{X}, t)$ is mapped by χ
- The symmetric Cauchy stress tensor $\boldsymbol{\sigma} = \boldsymbol{\sigma}(\mathbf{X}, t)$
- The internal energy $\mathcal{E} = \mathcal{E}(\mathbf{X}, t)$ per unit mass
- The heat flux vector $\mathbf{q} = \mathbf{q}(\mathbf{X}, t)$ per unit mass
- The entropy $\eta = \eta(\mathbf{X}, t)$ per unit mass

- The absolute temperature $\theta = \theta(\mathbf{X}, t)$
- The vector of internal state variables $\boldsymbol{\alpha}_i = \boldsymbol{\alpha}_i(\mathbf{X}, t)$

Three quantities commonly used in continuum mechanics are the deformation gradient $\mathbf{F}$, the velocity gradient $\mathbf{L}$, and the Jacobian J. The deformation gradient is the mapping between spatial and material points in an infinitesimal region such that $d\mathbf{x} = \mathbf{F} \cdot d\mathbf{X}$. Mathematically, this is expressed as the gradient of $\chi(\mathbf{X}, t)$ with respect to the material coordinates, i.e.,

$$\mathbf{F} = \nabla_0 \boldsymbol{\chi}(\mathbf{X}, t) = \frac{\partial \mathbf{x}}{\partial \mathbf{X}}, \qquad F_{iA} = \frac{\partial x_i}{\partial X_A}, \tag{2.1}$$

Similarly, the velocity gradient is the mapping between the velocity ($\mathbf{v} = \dot{\mathbf{x}}$) and the spatial position in an infinitesimal region such that $d\mathbf{v} = \mathbf{L} \cdot d\mathbf{x}$. Mathematically, this implies the velocity gradient is expressed as the gradient of $\mathbf{v}$ with respect to the spatial coordinates. If $\chi(\mathbf{X}, t)$ is smoothly invertible in $\mathbf{X}$, which implies that $\mathbf{F}$ is invertible, then the velocity gradient can be expressed as

$$\mathbf{L} = \nabla \mathbf{v}(\mathbf{X}, t) = \frac{\partial \mathbf{v}}{\partial \mathbf{x}} = \dot{\mathbf{F}} \cdot \mathbf{F}^{-1}, \qquad L_{ij} = \frac{\partial v_i}{\partial X_A} \frac{\partial X_A}{\partial x_j} = \frac{d}{dt}\left(\frac{\partial x_i}{\partial X_A}\right) \frac{\partial X_A}{\partial x_j}. \tag{2.2}$$

The Jacobian is defined as the mapping between the spatial and material volume in an infinitesimal region such that $dV = J dV_0$ and $\rho_0 = J\rho$, where V_0 and ρ_0 indicate the reference material volume and density, respectively. It is straightforward to show that $J = \det \mathbf{F}$.

Consider that the body $\mathcal{B}$ is a closed domain that is enclosed by the boundary $\partial\mathcal{B}$ with outward unit normal vector n_j. If the body is approximated as a continuum, then the conservation of a quantity of interest $\mathcal{A}_i$ takes the form [39]

$$\frac{d}{dt}\int_{\mathcal{B}} \mathcal{A}_i dV + \int_{\partial\mathcal{B}} \beta_{ij} n_j dS = \int_{\mathcal{B}} C_i dV, \tag{2.3}$$

where β_{ij} is the flux of $\mathcal{A}_i$ and C_i is the rate of supply of $\mathcal{A}_i$ due to an external system. If it is assumed that a local neighborhood of points has a velocity v_i and that $\mathcal{A}_i$ and its associated quantities are continuously differentiable, then the strong form of the above conservation equation becomes

$$\frac{\partial \mathcal{A}_i}{\partial t} + \frac{\partial}{\partial x_j}\left(\mathcal{A}_i v_j + \beta_{ij}\right) - C_i = 0. \tag{2.4}$$

The above two equations can be applied to scalar quantities by removing the subscript i from each of the above quantities.

For the conservation of mass, let $\mathcal{A}_i = \rho$. It is assumed there is no mass flux ($\beta_{ij} = \mathbf{0}$) or external mass production ($C = 0$), which results in the equation for the conservation of mass such that

$$\frac{\partial \rho}{\partial t} = -\frac{\partial}{\partial x_j}(\rho v_j) = -\left(\frac{\partial \rho}{\partial x_j} v_j + \rho \frac{\partial v_j}{\partial x_j}\right) \tag{2.5}$$

Using the definition for the material derivative of ρ in Equation (A.2), the above equation can be shown to be equivalent to $\dot{\rho}/\rho = L_{kk}$. For conservation of momentum, let $\mathcal{A}_i = \rho v_i$. The flux acting on the momentum is the Cauchy stress ($\beta_{ij} = -\sigma_{ij}$); assuming no external body forces ($C_i = \mathbf{0}$), Equation 2.4 gives

$$\begin{gathered}
\frac{\partial \rho}{\partial t} v_i + \rho \frac{\partial v_i}{\partial t} + \frac{\partial \rho}{\partial x_j} v_i v_j + \rho \frac{\partial v_i}{\partial x_j} v_j + \rho v_i \frac{\partial v_j}{\partial x_j} - \frac{\partial \sigma_{ij}}{\partial x_j} = 0 \\
-\left(\frac{\partial \rho}{\partial x_j} v_i v_j + \rho v_i \frac{\partial v_j}{\partial x_j}\right) + \rho \frac{\partial v_i}{\partial t} + \frac{\partial \rho}{\partial x_j} v_i v_j + \rho \frac{\partial v_i}{\partial x_j} v_j + \rho v_i \frac{\partial v_j}{\partial x_j} - \frac{\partial \sigma_{ij}}{\partial x_j} = 0 \\
\rho \frac{\partial v_i}{\partial t} + \rho \frac{\partial v_i}{\partial x_j} v_j = \frac{\partial \sigma_{ij}}{\partial x_j} \\
\rho \frac{dv_i}{dt} = \frac{\partial \sigma_{ij}}{\partial x_j}, \qquad \text{or} \qquad \rho \dot{\mathbf{v}} = \nabla \cdot \boldsymbol{\sigma}.
\end{gathered} \tag{2.6}$$

For the balance of energy, let $\mathcal{A} = \rho\left(\mathcal{E} + \frac{1}{2} v_k v_k\right)$. The flux acting on the energy is due to the work of stress as well as conduction ($\beta_j = -\sigma_{ji} v_i + q_j$) and assuming no energy is radiated from external sources gives

$$\begin{gathered}
\frac{\partial \rho}{\partial t}\left(\mathcal{E} + \frac{1}{2} v_k v_k\right) + \rho\left(\frac{\partial \mathcal{E}}{\partial t} + \frac{1}{2} v_k v_k\right) + \rho \frac{\partial v_j}{\partial x_j}\left(\mathcal{E} + \frac{1}{2} v_k v_k\right) + \rho \frac{\partial}{\partial x_j}\left(\mathcal{E} + \frac{1}{2} v_k v_k\right) v_j \\
-\frac{\partial \sigma_{ji}}{\partial x_j} v_i - \sigma_{ji} \frac{\partial v_i}{\partial x_j} + \frac{\partial q_j}{\partial x_j} = 0
\end{gathered} \tag{2.7}$$

$$\begin{gathered}
\rho \frac{\partial \mathcal{E}}{\partial t} = \sigma_{ji} \frac{\partial v_j}{\partial x_i} - \rho \frac{\partial \mathcal{E}}{\partial x_j} v_j - \frac{\partial q_j}{\partial x_j} \\
\rho \frac{d\mathcal{E}}{dt} \sigma_{ij} \frac{\partial v_i}{\partial x_j} - \frac{\partial q_j}{\partial x_j}, \qquad \text{or} \qquad \rho \dot{\mathcal{E}} = \boldsymbol{\sigma} : \mathbf{L} - \nabla \cdot \mathbf{q}.
\end{gathered} \tag{2.8}$$

In many cases, it is advantageous to frame the balance laws in terms of material coordinates. To do so, the stress is expressed in terms of the first Piola-Kirchhoff tensor $\mathbf{P}$, which expresses the current force acting on the original material surface area. In terms of

the Cauchy stress, it will be shown to take the form

$$\mathbf{P} = J\boldsymbol{\sigma}\mathbf{F}^{-T}, \qquad P_{iA} = J\sigma_{ij}F^{-1}_{Aj}, \tag{2.9}$$

where $\mathbf{F}^{-T}$ indicates the inverse of the transpose. Although this form of $\mathbf{P}$ can be found in literature [40], it is not necessary to impose this form yet. The balance laws for linear momentum and energy in material coordinates are found using the same process to find the form of Equations (2.6) and (2.8). The resultant forms of the material balance of momentum and energy are

$$\dot{\mathbf{v}} = \frac{1}{\rho_0}\nabla_0 \cdot \mathbf{P}, \qquad \frac{dv_i}{dt} = \frac{1}{\rho_0}\frac{\partial P_{iA}}{\partial X_A}, \tag{2.10}$$

$$\dot{\mathcal{E}} = \frac{1}{\rho_0}\left(\mathbf{P} : \dot{\mathbf{F}} - \nabla_0 \cdot \mathbf{Q}\right), \qquad \frac{d\mathcal{E}}{dt} = \frac{1}{\rho_0}\left(P_{iA}\dot{F}_{iA} - \frac{\partial Q_A}{\partial X_A}\right), \tag{2.11}$$

where $\mathbf{Q}$ is the material heat flux vector in the reference frame.

2.2.2 Thermoelastic-viscoplastic formulation

The rate of entropy production γ per unit mass, which using the Clausius-Duhem inequality is assumed to be non-negative, is defined as [38]

$$\gamma = \dot{\eta} + \frac{1}{\rho\theta}\left(\nabla \cdot \mathbf{q} - \frac{\mathbf{q} \cdot (\nabla\theta)}{\theta}\right) \geq 0, \qquad \gamma = \dot{\eta} + \frac{1}{\rho_0\theta}\left(\frac{\partial q_i}{\partial x_i} - \frac{q_i}{\theta}\frac{\partial \theta}{\partial x_i}\right) \geq 0. \tag{2.12}$$

Substituting the above inequality into the balance of energy equation gives

$$\gamma = \dot{\eta} + \frac{1}{\rho\theta}\left(\boldsymbol{\sigma} : \mathbf{L} - \rho\dot{\mathcal{E}} - \frac{\mathbf{q} \cdot (\nabla\theta)}{\theta}\right) \geq 0, \tag{2.13}$$

If the Helmholtz free energy per unit reference mass is introduced such that $\Psi = \mathcal{E} - \theta\eta$, with the material time derivative $\dot{\Psi} = \dot{\mathcal{E}} - \theta\dot{\eta} - \dot{\theta}\eta$, then the above balance equation may be written as

$$\theta\gamma = -\dot{\Psi} - \dot{\theta}\eta + \frac{1}{\rho}\left(\boldsymbol{\sigma} : \mathbf{L} - \frac{\mathbf{q} \cdot (\nabla\theta)}{\theta}\right) \geq 0. \tag{2.14}$$

The form of the material representation of Clausius-Duhem inequality is [41]

$$\gamma = \dot{\eta} + \frac{1}{\rho_0\theta}\left(\nabla_0 \cdot \mathbf{Q} - \frac{\mathbf{Q} \cdot (\nabla_0\theta)}{\theta}\right) \geq 0, \qquad \gamma = \dot{\eta} + \frac{1}{\rho\theta}\left(\frac{\partial Q_A}{\partial X_A} - \frac{Q_A}{\theta}\frac{\partial \theta}{\partial X_A}\right) \geq 0. \tag{2.15}$$

Substituting the above inequality into the balance of energy equation gives the inequalities in terms of in terms of $\mathcal{E}$ or Ψ as

$$\gamma = \dot{\eta} + \frac{1}{\rho_0 \theta}\left(\mathbf{P} : \dot{\mathbf{F}} - \rho\dot{\mathcal{E}} - \frac{\mathbf{Q}\cdot(\nabla_0\theta)}{\theta}\right) \geq 0, \tag{2.16}$$

$$\theta\gamma = -\dot{\Psi} - \dot{\theta}\eta + \frac{1}{\rho_0}\left(\mathbf{P} : \dot{\mathbf{F}} - \frac{\mathbf{Q}\cdot(\nabla_0\theta)}{\theta}\right) \geq 0. \tag{2.17}$$

To proceed and derive relations between thermodynamic quantities generally used in constitutive relations, an assumption must be made concerning the partition of elastic and plastic deformation. It is assumed that the deformation can be decomposed into elastic and plastic parts [42, 43], i.e.,

$$\mathbf{F} = \mathbf{F}^E\mathbf{F}^P, \qquad F_{iA} = F^E_{i\alpha}F^P_{\alpha A}, \tag{2.18}$$

where $\mathbf{F}^E$ and $\mathbf{F}^P$ are the elastic and plastic components of the deformation gradient, respectively.

For a thermoelastic-viscoplastic material with evolving internal variables denoted by $\boldsymbol{\alpha}_i$ (internal variables may be represented by scalars or tensors), an appropriate choice for the constitutive law is either $\Psi = \widehat{\Psi}\left(\mathbf{F}^E, \theta, \nabla\theta, \boldsymbol{\alpha}_i\right)$ or $\Psi = \widehat{\Psi}\left(\mathbf{F}^E, \theta, \nabla_0\theta, \boldsymbol{\alpha}_i\right)$. Substituting $\dot{\Psi}$ into the balance of energy inequality (Equations (2.14) and (2.17)) and factoring common terms for spatial coordinates gives

$$\begin{aligned} &-\left(\frac{\partial\Psi}{\partial\theta} + \eta\right)\dot{\theta} + \left(\frac{1}{\rho}\boldsymbol{\sigma}\cdot\mathbf{F}^{E-T} - \frac{\partial\Psi}{\partial\mathbf{F}^E}\right) : \dot{\mathbf{F}}^E - \frac{\partial\Psi}{\partial(\nabla\theta)}\cdot\frac{d(\nabla\theta)}{dt} - \sum_i \frac{\partial\Psi}{\partial\boldsymbol{\alpha}_i} * \dot{\boldsymbol{\alpha}}_i \\ &\quad - \frac{\mathbf{q}\cdot(\nabla\theta)}{\rho\theta} + \frac{1}{\rho}\boldsymbol{\sigma} : \mathbf{L}^P \geq 0, \end{aligned} \tag{2.19}$$

where the plastic velocity gradient in spatial coordinates is defined as $\mathbf{L}^P = \mathbf{L} - \mathbf{L}^E = \mathbf{F}^E\cdot\dot{\mathbf{F}}^P\cdot\mathbf{F}^{P-1}\cdot\mathbf{F}^{E-1} = \mathbf{F}^E\cdot\mathbf{L}^P_0\cdot\mathbf{F}^{E-1}$. Here, $\mathbf{L}^P_0 = \dot{\mathbf{F}}^P\cdot\mathbf{F}^{P-1}$ denotes the velocity gradient in the intermediate configuration. In Equation 2.19, $*$ denotes the appropriate vector or scalar operation associated with the internal state variable, $\boldsymbol{\alpha}_i$, and summation is implied on repeated indices for succinctness in the remainder of this work. A similar derivation is made for material coordinates, i.e.,

$$\begin{aligned} &-\left(\frac{\partial\Psi}{\partial\theta} + \eta\right)\dot{\theta} + \left(\frac{1}{\rho_0}\mathbf{P}\cdot\left(\mathbf{F}^P\right)^T - \frac{\partial\Psi}{\partial\mathbf{F}^E}\right) : \dot{\mathbf{F}}^E - \frac{\partial\Psi}{\partial(\nabla_0\theta)}\cdot\frac{\partial(\nabla_0\theta)}{\partial t} - \frac{\partial\Psi}{\partial\boldsymbol{\alpha}_i} * \dot{\boldsymbol{\alpha}}_i \\ &\quad - \frac{\mathbf{Q}\cdot(\nabla_0\theta)}{\rho_0\theta} + \frac{1}{\rho_0}\mathbf{P} : \left(\mathbf{F}^E\cdot\dot{\mathbf{F}}^P\right) \geq 0. \end{aligned} \tag{2.20}$$

It is assumed that both the plastic strain rate and rate of internal variables are zero for an instantaneous reversible deformation, i.e., $\dot{\mathbf{F}}^P = \mathbf{0}$ and $\dot{\boldsymbol{\alpha}}_i = \mathbf{0}$ [44]. If the material deforms under an admissible thermodynamic process [38], then the following equalities must hold for spatial coordinates:

$$\eta = -\frac{\partial \Psi}{\partial \theta}, \qquad \boldsymbol{\sigma} = \rho \frac{\partial \Psi}{\partial \mathbf{F}^E} \cdot \left(\mathbf{F}^E\right)^T, \qquad \frac{\partial \Psi}{\partial \left(\nabla \theta\right)} = 0. \tag{2.21}$$

For material coordinates, these are written as

$$\eta = -\frac{\partial \Psi}{\partial \theta}, \qquad \mathbf{P} = \rho_0 \frac{\partial \Psi}{\partial \mathbf{F}^E} \cdot \mathbf{F}^{P-T}, \qquad \frac{\partial \Psi}{\partial \left(\nabla_0 \theta\right)} = 0. \tag{2.22}$$

As a check, it is seen that using the above two equations that contain the term $\partial \Psi / \partial \mathbf{F}^E$ give $\mathbf{P} = J \boldsymbol{\sigma} \mathbf{F}^{-T}$, which matches the known form of $\mathbf{P}$ in terms of $\boldsymbol{\sigma}$ given in Equation (2.9). The last relation in the above two equations also implies that Ψ and therefore η, $\boldsymbol{\sigma}$, and $\mathbf{P}$ are all independent of the temperature gradient (rate of heat conduction).

Substituting in the above terms, the remaining terms in the energy inequality become

$$\frac{1}{\rho} \boldsymbol{\sigma} : \mathbf{L}^P - \frac{\partial \Psi}{\partial \boldsymbol{\alpha}_i} * \dot{\boldsymbol{\alpha}}_i - \frac{\mathbf{q} \cdot \left(\nabla \theta\right)}{\rho \theta} \geq 0, \tag{2.23}$$

for spatial coordinates and

$$\frac{1}{\rho_0} \mathbf{P} : \left(\mathbf{F}^E \cdot \dot{\mathbf{F}}^P\right) - \frac{\partial \Psi}{\partial \boldsymbol{\alpha}_i} * \dot{\boldsymbol{\alpha}}_i - \frac{\mathbf{Q} \cdot \left(\nabla_0 \theta\right)}{\rho_0 \theta} \geq 0, \tag{2.24}$$

for material coordinates. The first term in each of the above equations is referred to as the rate of plastic work, i.e., $\dot{W}^P = \frac{1}{\rho} \boldsymbol{\sigma} : \mathbf{L}^P = \frac{1}{\rho_0} \mathbf{P} : \left(\mathbf{F}^E \cdot \dot{\mathbf{F}}^P\right)$. Note that $\dot{W}^P - \left(\partial \Psi / \partial \boldsymbol{\alpha}_i\right) * \dot{\boldsymbol{\alpha}}_i \geq 0$ if $\dot{\mathbf{F}}^P$ and $\dot{\boldsymbol{\alpha}}_i$ are assumed to be independent of the temperature gradient.

Equation (2.8) for the energy balance may now be combined with functional forms and dependencies derived above to give a form for the temperature evolution rate in terms of the rates of elastic deformation, plastic deformation, and internal state variable evolution

[45], i.e.,

$$\dot{\Psi} + \dot{\eta}\theta + \eta\dot{\theta} = \frac{1}{\rho}\left(\boldsymbol{\sigma} : \mathbf{L} - \nabla \cdot \mathbf{q}\right)$$

$$\frac{\partial \Psi}{\partial \mathbf{F}^E} : \dot{\mathbf{F}}^E + \frac{\partial \Psi}{\partial \boldsymbol{\alpha}_i} * \dot{\boldsymbol{\alpha}}_i + \dot{\eta}\theta = \frac{1}{\rho}\left(\boldsymbol{\sigma} : \mathbf{L} - \nabla \cdot \mathbf{q}\right)$$

$$\frac{1}{\rho}\left(\boldsymbol{\sigma} \cdot \mathbf{F}^{E-T}\right) : \dot{\mathbf{F}}^E + \frac{\partial \Psi}{\partial \boldsymbol{\alpha}_i} * \dot{\boldsymbol{\alpha}}_i + \dot{\eta}\theta = \frac{1}{\rho}\left(\boldsymbol{\sigma} : \left(\dot{\mathbf{F}}^E \cdot \mathbf{F}^{E-1} + \mathbf{L}^P\right) - \nabla \cdot \mathbf{q}\right)$$

$$\dot{\eta}\theta = \dot{W}^P - \frac{1}{\rho}\left(\nabla \cdot \mathbf{q}\right) - \frac{\partial \Psi}{\partial \boldsymbol{\alpha}_i} * \dot{\boldsymbol{\alpha}}_i$$

$$-\theta\left(\frac{\partial^2 \Psi}{\partial \theta \partial \mathbf{F}^E} : \dot{\mathbf{F}}^E + \frac{\partial^2 \Psi}{\partial \theta^2}\dot{\theta} + \sum_\beta \frac{\partial^2 \Psi}{\partial \theta \partial \boldsymbol{\alpha}_i} * \dot{\boldsymbol{\alpha}}_i\right) = \dot{W}^P - \frac{1}{\rho}\left(\nabla \cdot \mathbf{q}\right) - \frac{\partial \Psi}{\partial \boldsymbol{\alpha}_i} * \dot{\boldsymbol{\alpha}}_i$$

$$\bar{c}\dot{\theta} = \dot{Q}^E + \dot{Q}^P - \frac{1}{\rho}\left(\nabla \cdot \mathbf{q}\right). \tag{2.25}$$

A similar derivation is made for the temperature evolution rate using using Equation (2.11) for material coordinates, i.e.,

$$\dot{\Psi} + \dot{\eta}\theta + \eta\dot{\theta} = \frac{1}{\rho_0}\left(\mathbf{P} : \dot{\mathbf{F}} - \nabla_0 \cdot \mathbf{Q}\right)$$

$$\frac{\partial \Psi}{\partial \mathbf{F}^E} : \dot{\mathbf{F}}^E + \frac{\partial \Psi}{\partial \boldsymbol{\alpha}_i} * \dot{\boldsymbol{\alpha}}_i + \dot{\eta}\theta = \frac{1}{\rho_0}\left(\mathbf{P} : \dot{\mathbf{F}} - \nabla_0 \cdot \mathbf{Q}\right)$$

$$\frac{1}{\rho_0}\left(\mathbf{P} \cdot \left(\mathbf{F}^P\right)^T\right) : \dot{\mathbf{F}}^E + \frac{\partial \Psi}{\partial \boldsymbol{\alpha}_i} * \dot{\boldsymbol{\alpha}}_i + \dot{\eta}\theta = \frac{1}{\rho_0}\left(\mathbf{P} : \left(\dot{\mathbf{F}}^E \cdot \mathbf{F}^P + \mathbf{F}^E \cdot \dot{\mathbf{F}}^P\right) - \nabla_0 \cdot \mathbf{Q}\right)$$

$$\dot{\eta}\theta = \dot{W}^P - \frac{1}{\rho_0}\left(\nabla_0 \cdot \mathbf{Q}\right) - \frac{\partial \Psi}{\partial \boldsymbol{\alpha}_i} * \dot{\boldsymbol{\alpha}}_i$$

$$-\theta\left(\frac{\partial^2 \Psi}{\partial \theta \partial \mathbf{F}^E} : \dot{\mathbf{F}}^E + \frac{\partial^2 \Psi}{\partial \theta^2}\dot{\theta} + \sum_\beta \frac{\partial^2 \Psi}{\partial \theta \partial \boldsymbol{\alpha}_i} * \dot{\boldsymbol{\alpha}}_i\right) = \dot{W}^P - \frac{1}{\rho_0}\left(\nabla_0 \cdot \mathbf{Q}\right) - \frac{\partial \Psi}{\partial \boldsymbol{\alpha}_i} * \dot{\boldsymbol{\alpha}}_i$$

$$\bar{c}\dot{\theta} = \dot{Q}^E + \dot{Q}^P - \frac{1}{\rho_0}\left(\nabla_0 \cdot \mathbf{Q}\right). \tag{2.26}$$

In Equations (2.25) and (2.26), which are equivalent, the following definitions are used:

$$\bar{c} = -\theta\frac{\partial^2 \Psi}{\partial \theta^2}, \qquad \dot{Q}^E = \theta\frac{\partial^2 \Psi}{\partial \theta \partial \mathbf{F}^E} : \dot{\mathbf{F}}^E, \qquad \dot{Q}^P = \dot{W}^P - \left(\frac{\partial \Psi}{\partial \boldsymbol{\alpha}_i} - \theta\frac{\partial^2 \Psi}{\partial \theta \partial \boldsymbol{\alpha}_i}\right) * \dot{\boldsymbol{\alpha}}_i. \tag{2.27}$$

Here, $\bar{c}$ is the specific heat at constant strain and internal variable, $\dot{Q}^E$ is the thermoelastic heating rate, and $\dot{Q}^P$ it the plastic heating rate. Both of the above derivations imply $\bar{c} = \hat{c}\left(\mathbf{F}^E, \theta, \boldsymbol{\alpha}_i\right)$; however, this assumption is generally relaxed so that specific heat is solely a function of temperature, i.e., $\bar{c} = \hat{c}\left(\theta\right)$ [46, 45]. The fraction of plastic work that is converted to heat is defined as the Taylor-Quinney factor, β [47]. Although the Taylor-Quinney factor is commonly set to a constant between $0.9 - 1.0$, in this framework it is a

function of internal state variable evolution equations [48], i.e.,

$$\beta = 1 - \frac{1}{\dot{W}^P}\left(\frac{\partial \Psi}{\partial \boldsymbol{\alpha}_i} - \theta \frac{\partial^2 \Psi}{\partial \theta \partial \boldsymbol{\alpha}_i}\right) * \dot{\boldsymbol{\alpha}}_i = \frac{\dot{Q}^P}{\dot{W}^P}. \tag{2.28}$$

From this general theory, it is straightforward to make simplifications that greatly reduce the complexity of this framework. It is also useful to classify existing constitutive theories as subsets of this general framework.

The parallel development of a finite-deformation, thermodynamically consistent formulation in terms of both spatial as well as material coordinates shows that it is straightforward to extend this framework for other stress and deformation measures. The simplest way to complete the theory for other strain measures, for example, will be shown for the elastic Green strain, defined as $\mathbf{E}^E = \frac{1}{2}\left(\left(\mathbf{F}^E\right)^T \cdot \mathbf{F}^E - \mathbf{I}\right)$. The Helmholtz free energy then takes the form $\Psi\left(\mathbf{E}^E\left(\mathbf{F}^E\right), \theta, \boldsymbol{\alpha}_i\right)$. To find the equivalent stress measure, we insert this form of the free energy into the second part of Equation (2.21) to get

$$\begin{aligned}
\sigma_{ij} &= \rho \frac{\partial \Psi}{\partial F^E_{i\alpha}} \left(F^E_{\alpha j}\right)^T = \rho \frac{\partial \Psi}{\partial E^E_{\beta\gamma}} \frac{\partial E^E_{\beta\gamma}}{\partial F^E_{i\alpha}} F^E_{j\alpha} \\
&= \rho \frac{\partial \Psi}{\partial E^E_{\beta\gamma}} \frac{\partial}{\partial F^E_{i\alpha}} \left[\frac{1}{2}\left(F^E_{\beta k} F^E_{k\gamma} - \delta_{\beta\gamma}\right)\right] F^E_{\alpha j} \\
&= \frac{1}{2}\rho \frac{\partial \Psi}{\partial E^E_{\beta\gamma}} \left[F^E_{i\gamma}\delta_{\alpha\beta} + F^E_{i\beta}\delta_{\gamma\alpha}\right] F^E_{\alpha j}. \\
&= \frac{\rho}{\rho_{\text{int}}} F^E_{i\beta} \Sigma_{\beta\alpha} F^E_{\alpha j}.
\end{aligned}$$

Defining $\boldsymbol{\Sigma} = \rho_{\text{int}} \partial \Psi / \partial \mathbf{E}^E$, where $\rho_{\text{int}} = \rho J^E = \rho_0 J^{P-1}$ is the density in the intermediate configuration following $\mathbf{F}^P$, gives

$$\sigma_{ij} = J^{E-1} F^E_{i\alpha} \Sigma_{\alpha\gamma} F^E_{\gamma j}, \qquad \boldsymbol{\sigma} = J^{E-1} \mathbf{F}^E \cdot \boldsymbol{\Sigma} \cdot \left(\mathbf{F}^E\right)^T, \tag{2.29}$$

which is the commonly used form of the second Piola-Kirchhoff (PK2) stress in terms of the Cauchy stress [40]. Equations relating $\mathbf{E}^E$ and $\boldsymbol{\Sigma}$ to $\mathbf{F}^E$ and $\boldsymbol{\sigma}$ are then used to determine quantities such as $\dot{Q}^E$ and $\dot{W}^P$ in order to complete the thermodynamic formulation in terms of the elastic Green strain and the PK2 stress.

2.2.3 Thermodynamics of discontinuous systems

The previous section was developed for a continuum where it was assumed that quantities of interest were smoothly differentiable. In high rate deformation experiments such as plate

impact, laser ablation, and explosive loading, changes in the material state can occur at very high rates and during small time scales, and are often approximated as discontinuous changes in material state. When the state of the material changes discontinuously, the material state is no longer continuously differentiable and Equation (2.4) does not hold. The balance equations need to be recast in terms of jump conditions, which are used to define the change in material state across the discontinuity. The discontinuous change in a quantity of interest $\mathcal{A}_i$ from state $(+)$ to $(-)$ is denoted

$$[\mathcal{A}_i] = \mathcal{A}_i^- - \mathcal{A}_i^+. \tag{2.30}$$

The identity $[\mathcal{A}_i\mathcal{C}_i] = \bar{\mathcal{A}}_i\,[\mathcal{C}_i] + \bar{\mathcal{C}}_i\,[\mathcal{A}_i]$ will also be used subsequently, where an overbar denotes the average such that $\bar{\mathcal{A}}_i = \frac{1}{2}\left(\mathcal{A}_i^- + \mathcal{A}_i^+\right)$

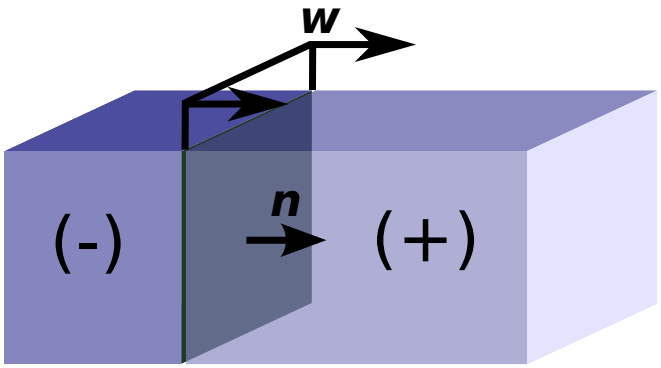

Figure 2.1: Material with states $(+)$ and $(-)$ separated by a propagating surface with unit normal $\mathbf{n}$ traveling with velocity $\mathbf{w}$.

Consider a material with states $(+)$ and $(-)$ separated by a surface S with unit normal $\mathbf{n}$ propagating with a velocity $\mathbf{w}$, shown schematically in Figure 2.1. If the material in either state is assumed to have velocity $\mathbf{u}$, then the velocity of the material relative to the propagating shock is $\mathbf{v} = \mathbf{u} - \mathbf{w}$. For this problem, the jump form of the balance law given in Equation (2.3) is [39]

$$[(\mathcal{A}_i v_j + \beta_{ij})\, n_j] = 0. \tag{2.31}$$

To apply the above equation to scalar quantities remove the index i. The balance of mass,

momentum, and energy use the same parameters that were used to derive Equations (2.5)-(2.8). The balance of mass ($\mathcal{A} = \rho, \beta_j = \mathbf{0}$) results in

$$\begin{gathered}
[\rho v_j]\, n_j = 0 \\
\rho^- v_j^- n_j = \rho^+ v_j^+ n_j = m = \rho v_j n_j,
\end{gathered} \tag{2.32}$$

where ρv_i does not have a superscript because it holds for both material states. The balance of momentum ($\mathcal{A}_i = \rho u_i, \beta_{ij} = -\sigma_{ij}$) results in

$$\begin{gathered}
[(\rho u_i v_j - \sigma_{ij})\, n_j] = \mathbf{0} \\
[\rho u_i v_j]\, n_j = [\sigma_{ij}]\, n_j \\
u_i^- \rho^- v_j^- n_j - u_i^+ \rho^+ v_j^+ n_j = [\sigma_{ij}]\, n_j \\
\rho v_j n_j\, [u_i] = [\sigma_{ij}]\, n_j.
\end{gathered} \tag{2.33}$$

The balance of energy $\left(\mathcal{A} = \rho\left(\mathcal{E} + \frac{1}{2}u_k u_k\right), \beta_i = -\sigma_{ij}u_j + q_i\right)$ results in

$$\begin{gathered}
\left[\left(\rho\left(\mathcal{E} + \frac{1}{2}u_k u_k\right) v_i - \sigma_{ij}u_j\right) n_i\right] = 0 \\
\left[\rho\left(\mathcal{E} + \frac{1}{2}u_k u_k\right) v_i - \sigma_{ij}u_j\right] n_i = 0 \\
\rho^-\left(\mathcal{E}^- + \frac{1}{2}u_k^- u_k^-\right) v_i^- n_i - \sigma_{ij}^- u_j^- n_i - \rho^+\left(\mathcal{E}^+ + \frac{1}{2}u_k^+ u_k^+\right) v_i^+ n_i + \sigma_{ij}^+ u_j^+ n_i = 0 \\
m\left[\mathcal{E} + \frac{1}{2}u_k u_k\right] = \rho v_j n_j \left[\mathcal{E} + \frac{1}{2}u_k u_k\right] = [\sigma_{ij}u_j]\, n_i
\end{gathered} \tag{2.34}$$

assuming that $[q_i] \to 0$, i.e., conduction is negligible. The traditional Hugoniot energy relation is recovered when Equation (2.33) and (2.34) are combined, i.e.,

$$\begin{gathered}
m\,[\mathcal{E}] + m\bar{u}_i\,[u_i] = \bar{\sigma}_{ij}\,[u_j]\, n_i + [\sigma_{ij}]\,\bar{u}_j n_i \\
m\,[\mathcal{E}] + m\bar{u}_i\,[u_i] = \bar{\sigma}_{ij}\,[u_j]\, n_i + m\,[u_i]\,\bar{u}_i \\
m\,[\mathcal{E}] = \rho v_j n_j\,[\mathcal{E}] = \bar{\sigma}_{ij}\,[u_j]\, n_i.
\end{gathered} \tag{2.35}$$

Because conduction is ignored across the discontinuous propagating surface, the Clausius-Duhem inequality given in Equation (2.12) becomes

$$[\eta] \geq 0. \tag{2.36}$$

2.3 Fluid simplification

2.3.1 Thermodynamics of continuum response

Many definitions exist for a fluid, one of which is that a fluid can be defined as a material that has no long range order, which implies it cannot support a shear stress when at rest ($\sigma_{ij} + p\delta_{ij} = 0$). The thermodynamic state of a fluid depends only on its current volume or density, or other equivalent thermodynamic descriptions. The free energy function of a simple fluid where volumetric viscosity effects are neglected can be written as

$$\Psi = \widehat{\Psi}\left(V\left(\mathbf{F}\right), \theta\right), \tag{2.37}$$

where it is noted that this is a specialized form of the free energy for a thermoelastic material with evolving internal state variables with the following restrictions: $\boldsymbol{\alpha}_i = \dot{\boldsymbol{\alpha}}_i = \mathbf{0}$, $\mathbf{F}^P = \mathbf{1}$, and $V = V_0 \det\mathbf{F} = V_0 J = J/\rho_0$. Using Equation (2.21), the stress response of the material is given by

$$\begin{aligned} \boldsymbol{\sigma} = \rho\frac{\partial\Psi}{\partial\mathbf{F}^E}\left(\mathbf{F}^E\right)^T = \rho\frac{\partial\Psi}{\partial\mathbf{F}}\mathbf{F}^T = \rho\frac{\partial\Psi}{\partial V}\frac{\partial V}{\partial\mathbf{F}}\mathbf{F}^T = \rho\frac{\partial\Psi}{\partial V}\frac{\partial\left(V_0 J\right)}{\partial\mathbf{F}}\mathbf{F}^T, \\ \boldsymbol{\sigma} = \frac{\rho}{\rho_0}\frac{\partial\Psi}{\partial V}J\mathbf{F}^{-T}\mathbf{F}^T = \frac{\partial\Psi}{\partial V}\mathbf{F}^{-T}\mathbf{F}^T = \frac{\partial\Psi}{\partial V}\mathbf{I}, \end{aligned} \tag{2.38}$$

where the identity given in Equation (A.4) was used [49]. The pressure p is defined as the negative of the derivative of the Helmholtz free energy with respect to volume at constant temperature, i.e.,

$$p = -\frac{\partial\Psi}{\partial V}, \tag{2.39}$$

such that p is positive in compression, which is a standard convention in fluid mechanics. Combining Equations (2.38) and (2.39) determines the Cauchy stress in terms of the pressure. In this case the stress response of the material is purely hydrostatic, where the Cauchy stress can be written as

$$[\boldsymbol{\sigma}] = \begin{bmatrix} -p & 0 & 0 \\ 0 & -p & 0 \\ 0 & 0 & -p \end{bmatrix}, \qquad \sigma_{ij} = -p\delta_{ij}, \tag{2.40}$$

where it is seen that $\boldsymbol{\sigma}$ is determined uniquely by p. Although this conclusion is expected, it helps reinforce that definitions in the continuum mechanics framework are consistent with well-accepted relations in fluid dynamics.

The balance of momentum from Equation (2.6) for the fluid response is

$$\frac{\partial v_i}{\partial t} = \frac{1}{\rho}\frac{\partial}{\partial x_j}\left(-p\delta_{ij}\right) = -\frac{1}{\rho}\frac{\partial p}{\partial x_i} = -\frac{J}{\rho_0}\frac{\partial p}{\partial x_i}. \tag{2.41}$$

The balance of energy from Equation (2.8) for fluids becomes

$$\frac{\partial \mathcal{E}}{\partial t} = \frac{1}{\rho}\left(-pL_{kk} - \frac{\partial q_i}{\partial x_i}\right) = \frac{J}{\rho_0}\left(\frac{-p\dot{J}}{J} - \frac{\partial q_i}{\partial x_i}\right) = -\frac{1}{\rho_0}\left(p\dot{J} - J\frac{\partial q_i}{\partial x_i}\right). \tag{2.42}$$

Following the derivation for the rate of temperature change in Equation (2.25), the modified version of this relation for fluids becomes

$$c_v\dot{\theta} = \dot{Q} - \frac{1}{\rho}\left(\nabla\cdot\mathbf{q}\right). \tag{2.43}$$

The specific heat at constant volume, c_v, now assumes the general form $c_v = -\theta\partial^2\Psi/\partial\theta^2 = \hat{c}\left(V\left(\mathbf{F}\right),\theta\right)$. The total heat generation rate is

$$\dot{Q} = \theta\frac{\partial^2\Psi}{\partial\theta\partial\mathbf{F}} : \dot{\mathbf{F}} = \theta\frac{\partial^2\Psi}{\partial\theta\partial V}\frac{\partial V}{\partial\mathbf{F}} : \dot{\mathbf{F}} = -\theta\frac{\partial p}{\partial\theta}\frac{\partial V}{\partial\mathbf{F}} : \dot{\mathbf{F}} = -\theta\frac{\partial p}{\partial\theta}\dot{V}. \tag{2.44}$$

Rewriting the temperature change balance equation gives

$$\frac{\dot{\theta}}{\theta} = -\frac{1}{c_v}\frac{\partial p}{\partial\theta}\dot{V} - \frac{1}{\rho}\left(\nabla\cdot\mathbf{q}\right) = -\left(\rho\Gamma\dot{V} + \frac{1}{\rho}\left(\nabla\cdot\mathbf{q}\right)\right) = -\left(\frac{\Gamma\dot{J}}{J} + \frac{1}{\rho}\left(\nabla\cdot\mathbf{q}\right)\right) \tag{2.45}$$

where $\Gamma = \left(1/\rho c_v\right)\left(\partial p/\partial\theta\right)$ is the Grüneisen parameter, which measures the variation of internal energy at constant volume.

2.3.2 Thermodynamics of shock response

Understanding the shock response of fluids is not only important for studying the response of fluids but also for solids. Peak pressures achieved in shock loading experiments can range from a few GPa to several hundred GPa. In contrast, the shear strength of many solids is less than 1 GPa, with most pure metals having strengths closer to the range of $10 - 100$ MPa. Therefore, in the case of modeling the shock response of pure metals, the strength contribution is small relative to the peak pressure. Because the strength is a small

fraction of the total response, many approaches ignore this contribution and model the high rate response of metals using a hydrodynamical fluid treatment.

For uniaxial plate impact experiments for which the material response is approximated as a fluid, the jump conditions in Equations (2.32)-(2.35) become

$$[\rho v_1] = 0 \tag{2.46}$$

$$\rho v_1 [u_1] = -[p] \tag{2.47}$$

$$m\left[\mathcal{E} + \frac{1}{2}u_1 u_1\right] = \rho v_1 \left[\mathcal{E} + \frac{1}{2}u_1 u_1\right] = -[p u_1] \tag{2.48}$$

$$m[\mathcal{E}] = \rho v_1 [\mathcal{E}] = -\bar{p}[u_1]. \tag{2.49}$$

Although these relations express the conventional balance of momentum, energy, and Hugoniot energy relations commonly used in modeling shock wave experiments, they differ significantly in notation due to their generality. To compare these relations with conventional notation generally used to describe normal plate impact results [50] and assure they describe equivalent processes, consider the schematic shown in Figure 2.2, which depicts the compression of a gas initially at rest by a piston. The balance of mass, momentum, energy, and Hugoniot energy relations that correspond to the notation in Figure 2.2 are

$$\rho_0 U_s = \rho (U_s - U_p) \tag{2.50}$$

$$\rho_0 U_s U_p = P - P_0 \tag{2.51}$$

$$\rho_0 U_s \left(E - E_0 + \frac{1}{2}U_p^2\right) = P U_p \tag{2.52}$$

$$E - E_0 = \left(\frac{P + P_0}{2}\right)\left(\frac{1}{\rho_0} - \frac{1}{\rho}\right) = \frac{(P + P_0)(V - V_0)}{2}, \tag{2.53}$$

where E is the energy, U_s is the shock wave speed, U_p is the particle velocity, $V = 1/\rho$ denotes the specific volume, and U_0 is the particle velocity in front of the shock wave, which is assumed to be zero.

The balance equations corresponding to Figures 2.1 and 2.2 are compared. The balance

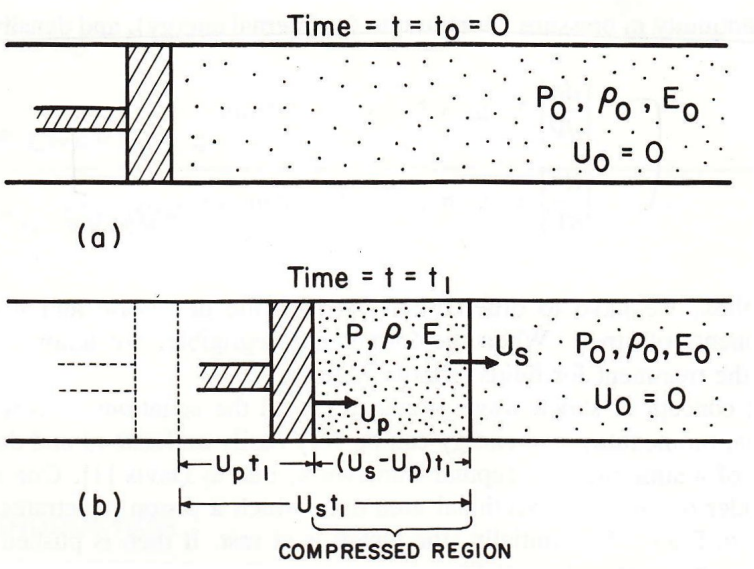

Figure 2.2: Hydrodynamic state of an idealized 1-D system (a) before compression and (b) after some finite compression. Reprinted with permission from [1]. Copyright 1994, John Wiley and Sons.

of mass in both systems is

$$
\begin{aligned}
[\rho v_1] &= 0 \\
\rho^+ v_1^+ &= \rho^- v_1^- \\
\rho^+ \left(u_1^+ - w_1\right) &= \rho^- \left(u_1^- - w_1\right) \\
\rho^+ w_1 &= \rho^- \left(w_1 - u_1^-\right) \\
\rho_0 U_s &= \rho \left(U_s - U_p\right)
\end{aligned}
\tag{2.54}
$$

where $w_1 = U_s$, $u_1^- = U_p$, $\rho^- = \rho$, $u_1^+ = U_0 = 0$, and $\rho^+ = \rho_0$. The balance of momentum in both systems is

$$
\begin{aligned}
\rho v_1 \left[u_1\right] &= -\left[p\right] \\
\rho^+ v_1^+ \left(u_1^- - u_1^+\right) &= -\left(p^- - p^+\right) \\
\rho^+ \left(u_1^+ - w_1\right)\left(u_1^- - u_1^+\right) &= -\left(p^- - p^+\right) \\
\rho^+ \left(u_1^+ - w_1\right)\left(u_1^- - u_1^+\right) &= -\left(p^- - p^+\right) \\
\rho_0 U_s U_p &= P - P_0
\end{aligned}
\tag{2.55}
$$

where $p^- = P$ and $p^+ = P_0$. The balance of energy in both systems is

$$\begin{aligned}
\rho v_1 \left[\mathcal{E} + \frac{1}{2}u_1 u_1\right] &= -\left[p u_1\right] \\
\rho^+ \left(u_1^+ - w_1\right)\left(\mathcal{E}^- + \frac{1}{2}u_1^- u_1^- - \mathcal{E}^+ - \frac{1}{2}u_1^+ u_1^+\right) &= -\left(p^- u_1^- - p^+ u_1^+\right) \\
-\rho^+ w_1 \left(\mathcal{E}^- - \mathcal{E}^+ + \frac{1}{2}u_1^- u_1^-\right) &= -p^- u_1^- \\
\rho_0 U_s \left(E - E_0 + \frac{1}{2}U_p^2\right) &= P U_p,
\end{aligned} \tag{2.56}$$

where $\mathcal{E}^- = E$ and $\mathcal{E}^+ = E_0$. The Hugoniot energy relation in both systems is

$$\begin{aligned}
\rho v_1 \left[\mathcal{E}\right] &= -\bar{p}\left[u_1\right] \\
\rho^+ \left(u_1^+ - w_1\right)\left(\mathcal{E}^- - \mathcal{E}^+\right) &= -\frac{p^+ + p^-}{2}\left(u_1^- - u_1^+\right) \\
-\rho^+ w_1 \left(\mathcal{E}^- - \mathcal{E}^+\right) &= -u_1^- \frac{p^+ + p^-}{2} \\
\frac{\rho^+ w_1}{u_1^-}\left(\mathcal{E}^- - \mathcal{E}^+\right) &= \frac{p^+ + p^-}{2} \\
E - E_0 &= \left(\frac{P + P_0}{2}\right)\left(\frac{1}{\rho_0} - \frac{1}{\rho}\right),
\end{aligned} \tag{2.57}$$

where $\rho^+ w_1 / u_1^- = \rho_0 U_s / U_p = (1/\rho_0 - 1/\rho)^{-1}$ is found using mass conservation. The above equations confirm that the jump conditions generally applied to plate impact experiments are a subset of the jump conditions for fluids derived from a general thermodynamic consideration given in Equations (2.32)-(2.35).

If the initial state of the material is known, Equations (2.46)-(2.49) comprise three unique equations in terms of five unknowns $\left(\text{e.g., } \mathcal{E}^-, \rho^-, p^-, v_1^-, w\right)$. An additional equation that is often introduced is a relationship between the shock speed and particle velocity, i.e.,

$$w = c_0 + s_1 v_1^- + s_2 \left(v_1^-\right)^2 + \ldots \tag{2.58}$$

where c_0, s_1, s_2, etc. are constants. For most metals, only c_0 and s_1 are required to fit a majority of data for peak shock pressures up to hundreds of GPa. Values of these proportionality constants have been determined for most pure metals as well as many alloys by performing normal plate impact experiments [50, 51, 52, 10]. With the relationship given in Equation (2.58), all of the quantities in the jump conditions for mass, momentum, and energy conservation can be uniquely determined in terms of a single parameter. Note that

the downstream $(-)$ quantities only hold for the material in the shocked state and provide no information concerning the deformation processes that occur in the shock.

2.4 Equations of state

An equation of state is a constitutive relation that can be used to uniquely characterize the equilibrium state of the material for arbitrary thermo-mechanical loading conditions. Often, an equation of state given in literature is based on a particular relation between quantities of interest, which by itself does not fully characterize the material. Cast in a particular framework, however, certain constitutive relations can be used to entirely specify the material behavior under arbitrary loading conditions.

2.4.1 Mie-Grüneisen

Often, constitutive theories in continuum mechanics are related to macroscopic observations and quantities that parameterize observed thermodynamic behavior. In the case of the Mie-Grüneisen equation of state, statistical mechanics is used to relate macroscopic thermodynamic quantities with the Hamiltonian of an idealized many-particle assembly. By making certain assumptions about the average behavior of the many-particle system, the macroscopic and microscopic theories can be related by a single parameter Γ. The following derivation closely follows that found in [53] and [1].

Consider a simple harmonic oscillator vibrating at frequency ν. The oscillator vibrates at different quantized energy levels whose energy is $nh\nu$ where n is a positive integer, and h is Planck's constant. The probability distribution of oscillators is assumed to follow a Boltzmann distribution where each energy level is represented by a unique state, i.e.,

$$P^{\alpha} = \frac{e^{-n^{\alpha}h\nu^{\alpha}/k\theta}}{\sum_{\beta} e^{-n^{\beta}h\nu^{\beta}/k\theta}}, \tag{2.59}$$

where k is Boltzmann's constant. Noting that $\sum_{\beta} e^{-n^{\beta}h\nu^{\beta}/k\theta} = \frac{1}{1-e^{-h\nu/k\theta}}$, the mean energy $\bar{\epsilon}$ an oscillator is given by

$$\bar{\epsilon} = \sum_{\alpha} P^{\alpha} n^{\alpha} h\nu^{\alpha} = \frac{h\nu}{e^{h\nu/\theta} - 1}. \tag{2.60}$$

Now consider the total energy of $3N$ oscillators vibrating at different frequencies. Combining the kinetic energy of a single oscillator given in Equation (2.60) with an assumed

potential energy $\phi(\nu)$ and ground state energy $h\nu/2$ to give the total internal energy of the system, i.e.,

$$\mathcal{E} = \phi(\nu) + \sum_{\beta=1}^{3N} \left[\frac{1}{2} h\nu^{\beta} + \frac{h\nu^{\beta}}{e^{h\nu^{\beta}/k\theta} - 1} \right]. \tag{2.61}$$

From statistical mechanics, the Helmholtz free energy is related to the internal energy and temperature through

$$\Psi = -k\theta \ln \sum_{\beta=1}^{3N} \exp\left(E^{\beta}/k\theta\right) = \phi(\nu) + \sum_{\beta=1}^{3N} \frac{1}{2} h\nu^{\beta} + k\theta \sum_{\beta=1}^{3N} \ln\left(1 - e^{-h\nu^{\beta}/k\theta}\right). \tag{2.62}$$

By definition, the equilibrium thermodynamic pressure is

$$p = -\left.\frac{\partial \Psi}{\partial V}\right|_{\theta} = -\frac{d\phi}{dV} + \frac{1}{V} \sum_{\beta=1}^{3N} \Gamma^{\beta} \left[\frac{1}{2} h\nu^{\beta} + \frac{h\nu^{\beta}}{e^{h\nu^{\beta}/k\theta} - 1} \right], \tag{2.63}$$

where Γ^{β} is defined as

$$\Gamma^{\beta} = -\left.\frac{V}{\nu^{\beta}} \frac{\partial \nu^{\beta}}{\partial V}\right|_{\theta} = -\left.\frac{\partial \ln \nu^{\beta}}{\partial \ln V}\right|_{\theta}. \tag{2.64}$$

Although the form of Ψ given in Equation (2.62) constitutes a the complete thermodynamic description of the system, it cannot be readily implemented in the continuum thermodynamic description developed in Sections 2.2 or 2.3 because the continuum frameworks do not take into account the discrete oscillators and their respective frequencies. Grüneisen assumed all of the oscillators have the same value of Γ such that $\Gamma^{\beta} \approx \Gamma$ [54], which gives

$$\Gamma = -\left.\frac{\partial \ln \nu}{\partial \ln V}\right|_{\theta}. \tag{2.65}$$

Substituting in the above assumption of constant Γ into the pressure relation gives

$$p = -\frac{d\phi}{dV} + \frac{\Gamma}{V} \sum_{\beta=1}^{3N} \left[\frac{1}{2} h\nu^{\beta} + \frac{h\nu^{\beta}}{e^{h\nu^{\beta}/kT} - 1} \right] = -\frac{d\phi}{dV} + \frac{\Gamma}{V} \mathcal{E}_{vib}, \tag{2.66}$$

where $\mathcal{E}_{vib}$ represents the vibrational contribution of oscillators to the total energy. The above relation between energy and pressure can be used to uniquely determine the state of a fluid with respect to any point on the Hugoniot if $\Gamma(V)$ is defined such that

$$p - p_H = \frac{\Gamma(V)}{V} (\mathcal{E} - \mathcal{E}_H), \tag{2.67}$$

where the subscript H denotes a point on the Hugoniot. Because detailed measurements that uniquely relate thermodynamically measurable quantities are often lacking for shock

experiments, a commonly employed assumption is that the ratio of Γ/V is constant throughout deformation, i.e.,

$$\frac{\Gamma}{V} \approx \frac{\Gamma_0}{V_0}, \qquad \therefore \qquad \Gamma = \frac{\Gamma_0 V}{V_0} = \Gamma_0 J. \tag{2.68}$$

The assumption that $\Gamma = \Gamma(V)$ is a restrictive form of the generalized Grüneisen parameter presented in Equation (2.45) for a general fluid response. This assumption also implies that c_v is solely a function of entropy [53].

2.4.2 Murnaghan

Murnaghan may have been one of the first to note that the elastic coefficients in Hooke's Law for isotropic elasticity may not remain constant during deformation [55]. He noted that the isotropic medium also may not remain isotropic as stress is applied. To address hydrostatic compression experiments performed by Bridgman, Murnaghan postulated that the elastic coefficients may be expressed as a linear function of pressure. In hydrostatic compression of an isotropic elastic solid, the volume and pressure derivatives can be expressed in terms of the specific volume and its derivative, i.e.,

$$\frac{1}{V}\frac{\partial V}{\partial p} = -\frac{1}{\lambda + 2\mu/3}, \tag{2.69}$$

where λ and μ the Lamé coefficients. These coefficients are expressed as a linear function of the pressure [56], i.e.,

$$\lambda + \frac{2}{3}\mu = B_\theta = V\frac{\partial^2 \Psi}{\partial V^2} = -V\frac{\partial p}{\partial V} = c\,(1 + kp)\,, \tag{2.70}$$

where B_θ is the isothermal bulk modulus, c is a constant with dimensions of stress, and k is a constant with units of inverse stress. Note that the Murnaghan equation allows specification of a non-zero tangent isothermal bulk modulus, i.e.,

$$\frac{\partial B_\theta}{\partial p} = B'_\theta = ck, \tag{2.71}$$

where increased volumetric resistance with increasing pressure requires $ck > 0$. Using this notation, the Murnaghan equation can be rewritten in a more conventional form as

$$B_\theta = B_0 + B'_\theta p, \tag{2.72}$$

where $B_0 = c$ is the reference bulk modulus [46].

For the specialized case of the uncoupled thermoelastic response of a fluid the free energy can be decomposed additively such that $\Psi = \hat{\Psi}(V, \theta) = \Psi_1(V) + \Psi_2(\theta)$ [45]. In this case, the general form of the free energy following the Murnaghan relation for the bulk modulus is

$$\Psi_1(V) = \Psi_0 + \frac{V}{k} + \frac{c_1 V^{1-ck}}{1-ck}, \tag{2.73}$$

where c_1 is a constant and Ψ_0 is the reference free energy. The material is assumed to have zero pressure at some reference volume, which gives the initial condition $-\partial\Psi_1/\partial V|_{V=V_0} = 0$. Because the free energy can be chosen arbitrarily, it is also assumed to be zero at the reference volume, giving the initial condition condition $\Psi_1|_{V=V_0} = 0$. Combining these two initial conditions with the above form of $\Psi_1(V)$ gives the specific form of the Murnaghan equation of state used to describe uncoupled thermoelasticity of a fluid, i.e.,

$$\Psi = \frac{1}{1-ck}\left[c(V_0 - V) + \frac{V}{k}\left(1 - \left(\frac{V_0}{V}\right)^{ck}\right)\right] + \Psi_2(\theta). \tag{2.74}$$

The Murnaghan free energy is equivalently written in terms of the reference and tangent isothermal bulk moduli, i.e.,

$$\Psi = \frac{B_0}{1-B'_\theta}\left[V_0 - V + \frac{V}{B'_\theta}\left(1 - \left(\frac{V_0}{V}\right)^{B'_\theta}\right)\right] + \Psi_2(\theta). \tag{2.75}$$

2.4.3 Thermoelasticity

Thermoelasticity addresses the recoverable response of solids to arbitrary deformation and temperature histories. In thermoelasticity, it is assumed that plastic deformation does not occur, i.e., $\mathbf{F}^P = \mathbf{I}$ and $\boldsymbol{\alpha}_i = \mathbf{0}$. Using these assumptions, the free energy can be written as $\Psi = \hat{\Psi}\left(\mathbf{F}^E, \theta\right) = \hat{\Psi}(\mathbf{F}, \theta)$. Unlike the equations of state given in Sections 2.4.1 and 2.4.2, which are used to capture the pressure-dependent fluid response, thermoelasticity must be able to capture arbitrary stress states. For Ψ to be a proper energy measure, it must obey objectivity. Under an orthogonal tensor transformation $\mathbf{Q}$, the free energy becomes

$$\hat{\Psi}(\mathbf{F}, \theta) \rightarrow \hat{\Psi}(\mathbf{Q} \cdot \mathbf{F}, \theta). \tag{2.76}$$

At this point a strain measure must be introduced which is invariant under arbitrary rotation. Many admissible forms of the strain tensors exist that obey objectivity, e.g., the right

stretch $\mathbf{U}$ where $\mathbf{F} = \mathbf{R} \cdot \mathbf{U}$, the logarithmic material strain $\ln(\mathbf{U})$, the Green strain, etc. In this section, with an eye towards plasticity theory, the Green strain will be used, i.e.,

$$\Psi\left(\mathbf{E}\left(\mathbf{Q} \cdot \mathbf{F}\right), \theta\right) = \Psi\left(\mathbf{E}\left(\mathbf{F}\right), \theta\right), \tag{2.77}$$

where $\mathbf{E} = \frac{1}{2}\left(\mathbf{F}^T \cdot \mathbf{F} - \mathbf{I}\right)$ denotes the Green strain, which is clearly objective from $\mathbf{F}^T \cdot \mathbf{Q}^T \cdot \mathbf{Q} \cdot \mathbf{F} = \mathbf{F}^T \cdot \mathbf{F}$.

In the case of thermoelasticity for an isotropic solid, the energy must be solely a function of the three scalar invariants of $\mathbf{E}$. Since $\mathbf{E}$ is symmetric, the three strain invariants are

$$I_1 = \mathrm{tr}\mathbf{E}, \qquad I_2 = \frac{1}{2}\left(\mathbf{E} : \mathbf{E} - (\mathrm{tr}\mathbf{E})^2\right), \qquad I_3 = \det\mathbf{E}, \tag{2.78}$$

where I_1, I_2, and I_3 are first, second, and third order in strain, respectively. Therefore, for isotropic thermoelasticity, the Helmholtz free energy is expressed in terms of an expansion about the scalar invariants to arbitrary order [55, 57], i.e.,

$$\Psi = \hat{\Psi}\left(I_1, I_2, I_3, \theta\right). \tag{2.79}$$

To include the effect of higher order strain and temperature terms, the free energy is expanded about a reference state in terms of strain and temperature components up to third order [6], i.e.,

$$\begin{aligned} \Psi \quad &= \quad a_1 I_1^2 + a_2 I_2 + a_3 I_1^3 + a_4 I_1 I_2 + a_5 I_3 \\ &+ \quad b_1 I_1 \Delta\theta + b_2 I_1^2 \Delta\theta + b_3 I_2 \Delta\theta + b_4 I_1 \left(\Delta\theta\right)^2 \\ &+ \quad d_1 \Delta\theta + d_2 \left(\Delta\theta\right)^2 + d_3 \left(\Delta\theta\right)^3, \end{aligned} \tag{2.80}$$

where for $a_1 - a_5$ are isothermal elastic constants, $b_1 - b_4$ are thermo-mechanical coupling constants, and $d_1 - d_3$ are thermal constants. The constants are defined as the derivative with respect to the respective invariants about a reference state, e.g., $a_1 = \partial^2\Psi/\partial I_1^2$, $b_1 = \partial^2\Psi/\partial I_1 \partial\theta$, etc. Using Equation (2.21) the state of stress can be expressed in terms of the strain invariants and the elastic and thermo-mechanical coupling constants. For waves propagating in isotropic materials, Truesdell presented a formulation of the elastic constants directly in terms of pure wave propagation velocities [58]. Generally for polycrystalline materials, however, effective isotropic constants are calculated by applying an

averaging scheme to higher order single crystal constants due to difficulties with creating polycrystalline samples with low grain boundary density, a randomly oriented texture, and that contain no voids [59, 60].

Birch noted that the higher order strain theory first correctly developed by Murnaghan [55] did not need to be specialized only for the case of isotropic solids [61]. He developed a theory for the finite elastic strain of cubic solids, which is readily generalized to materials that possess no symmetry. For the thermoelastic description of a material without any assumption about the symmetry the material possesses, the free energy must be expanded about the entire strain tensor instead of a scalar measure. Expanding about terms up to third order in temperature and strain gives

$$\begin{aligned} \Psi \quad &= \quad \frac{1}{2}C_{ABCD}E_{AB}E_{CD} + \frac{1}{6}C_{ABCDEF}E_{AB}E_{CD}E_{EF} \\ &- \quad \beta_{AB}E_{AB}\Delta\theta - \beta_{ABCD}E_{AB}E_{CD}\Delta\theta - \beta'_{AB}E_{AB}\left(\Delta\theta\right)^2 \\ &+ \quad d_1\Delta\theta + d_2\left(\Delta\theta\right)^2 + d_3\left(\Delta\theta\right)^3, \end{aligned} \tag{2.81}$$

where C_{ABCD} and C_{ABCDEF} denote isothermal elastic constant tensors whereas β_{AB}, β'_{AB}, and β_{ABCD} denote thermo-mechanical coupling constant tensors. The coupling constant tensors are again defined as derivatives about the reference state, e.g., $C_{ABCD} = \partial^2\Psi/\partial E_{AB}\partial E_{CD}$. Although the form of the constant tensors for a material that possesses no inherent symmetry only implies that the tensors are symmetric, most materials belong to higher symmetry groups, which greatly simplifies the form of the elastic and thermoelastic constants. The form of the second and third order elastic constants for all eleven Laue groups are given in [49]. If fourth order elastic constants are used, the form of fourth order elastic constants for cubic materials is given in [62] and relations between these constants for higher symmetry point groups are derived in [63].

Although ceramics, geological materials, and some select other materials may undergo general finite thermoelastic deformation due to their large yield strengths, thermoelasticity is often used to describe large volumetric compression that occurs in materials. Murnaghan and Birch used their theory of finite deformation and the pressure-dependence of elastic moduli to describe results from experiments performed by Bridgman that quantified the

pressure-volume dependence of both liquids and solids under large hydrostatic pressures. Although describing the macroscopic hydrostatic response is extremely important for quantifying the dependence of the bulk and shear modulus on the applied pressure, it is difficult to extract the full set of higher order constants from this method.

Ultrasonic pulse measurements have been used to determine higher order elastic constants by measuring pure mode elastic wave velocities along different directions of single crystals [64]. This method cannot be used to directly specify all third order and higher constants, but gives a plausible range of values they may assume. This ultrasonic pulse method was generalized to include measurements of hydrostatically pre-stressed specimens by initially loading the specimen with a diamond anvil cell and then applying the ultrasonic elastic wave method [65]. This method can be used to directly express isentropic third order elastic constants in terms of wave velocities [66, 67]. These isentropic constants can be converted to isothermal constants by use of Maxwell equations [49, 68]. For materials with large yield strengths or materials that exhibit nearly elastic perfectly-plastic behavior, longitudinal plate impact experiments may also provide a useful tool to characterize elastic constants [69]. Specifically, in the case of materials with large strengths, minimal elastic heating occurs before the onset of yield, thus simplifying interpretation of constants even further. Determination of fourth and higher order elastic constants is often based on empirical fits of isotropic elastic constants (using Cauchy relations [46]) to existing pressure-volume equations of state used to describe experimental plate impact results.

2.5 Viscoplasticity

2.5.1 General theory

Although the thermoelastic-viscoplastic formulation presented in Section 2.2.2 accounted for the thermodynamics and kinematics associated with viscoplastic materials, it did not expand upon specific plastic deformation or internal state variable evolution laws. The form of equations given in this section will be left as general so that specific models can be framed within the context of simplifications to the general theory. In the context of thermoelastic-viscoplastic deformation theory presented in Section 2.2.2, these components

of mathematical plasticity theory must be defined:

1. A constitutive equation for the plastic velocity gradient, which may take the form $\mathbf{L}^P\left(\mathbf{F}^E, \theta, \boldsymbol{\alpha}_i\right)$
2. A constitutive equation for internal state variable evolution, which may take the form $\dot{\boldsymbol{\alpha}}_i\left(\mathbf{F}^E, \theta, \boldsymbol{\alpha}_i\right)$

It is assumed $\dot{\boldsymbol{\alpha}}_i$ is independent of conduction; this is a typical simplifying assumption but is not necessary. The potential forms for $\mathbf{L}^P$ and $\dot{\boldsymbol{\alpha}}$ are subject to the constraint of the Clausius-Duhem inequality given in Equation (2.23). In Equation (2.23), because $\boldsymbol{\sigma} : \mathbf{L}^P$ contains the symmetric Cauchy stress, it is equivalent to $\boldsymbol{\sigma} : \mathbf{D}^P$, which implies $\mathbf{W}^P = \frac{1}{2}\left(\mathbf{L}^P - (\mathbf{L}^P)^T\right)$ does not enter into the Clausius-Duhem inequality. Up to this point no part of the theory has addressed potential forms for the plastic flow and internal state variable evolution equations nor has the theory been related to more classical rate-independent plasticity theory [70]. Generally, specification of forms for $\mathbf{L}^P$ and $\dot{\boldsymbol{\alpha}}$ are based either on a physics-based description of known dissipative processes, notions of maximum dissipation, or some combination thereof [71].

One method to construct internal state variable equations and evolution laws is based on the notion that internal state variables are used to describe a non-equilibrium processes; however, by including these internal state variables into the thermodynamic framework the material is assumed to pass through a sequence of constrained equilibrium states. By assuming the material passes through these constrained states, it is implied that if $\boldsymbol{\alpha}_i$ is held constant that by special choice of prescribed $\mathbf{F}^E$ and θ, the material can attain an equilibrium state [72]. For the material to pass through these constrained thermodynamic states, the rate of rearrangement of the given process must be fully determined by the thermodynamic force ($\mathbf{f}_i$) associated with this process [72]. Mathematically, this is stated as

$$\dot{\boldsymbol{\alpha}}_i\left(\mathbf{F}^E, \theta, \mathbf{f}_i\right), \qquad \text{where} \qquad \mathbf{f}_i = \frac{1}{\rho}\frac{\partial \Psi}{\partial \boldsymbol{\alpha}_i}. \tag{2.82}$$

The flow rule associated with this thermodynamic driving force is then constructed as

$$\mathbf{D}^P = \frac{\partial \mathbf{f}_i}{\partial \boldsymbol{\sigma}} * \dot{\boldsymbol{\alpha}}_i. \tag{2.83}$$

Using a framework such as the one given by Equations (2.82) and (2.83) ensures a viscoplastic flow potential exists and that generalized normality is ensured in the space of dissipative variables. Recall that the above framework is a constitutive assumption that assumes non-equilibrium processes can be described as a sequence of constrained equilibrium states and whose rate equations can be written in terms of a viscoplastic potential. These assumptions may be appropriate for processes where the response of $\dot{\boldsymbol{\alpha}}_i$ to $\mathbf{f}_i$ is rapid for small changes in $\mathbf{f}_i$, or where a large change in $\mathbf{f}_i$ results in a small change in $\dot{\boldsymbol{\alpha}}_i$; however, when these to processes change on the same time scale the process may be far from constrained equilibrium [71]. For these cases, a more general construction that does not enforce generalized normality may be more appropriate [73, 74].

For viscoplastic processes wherein rate-dependent effects are included, the viscoplastic formulation can be constructed with the following components [73, 75]:

1. Static yield surfaces, which may take the form $F_i\left(\mathbf{F}^E, \theta, \boldsymbol{\alpha}_i\right)$
2. A constitutive equation for the plastic deformation rate, which may be expressed as $\mathbf{D}^P = ||\mathbf{D}^P||\mathbf{n}^P = g_i\left(\langle F_i \rangle\right)\mathbf{n}^P$ where $\mathbf{n}^P = \mathbf{D}^P/||\mathbf{D}^P|| = \sum_i \frac{\partial Q_i/\partial \boldsymbol{\sigma}}{\sum_j ||\partial Q_j/\partial \boldsymbol{\sigma}||}$ defines the direction of plastic flow, Q_i are the set of viscoplastic potential functions, and g_i are the set of viscosity functions
3. A constitutive equation for internal state variable evolution, which may take the form $\dot{\boldsymbol{\alpha}}_i\left(\mathbf{F}^E, \theta, \boldsymbol{\alpha}_i\right)$

Viscoplastic deformation and internal state variable evolution occur when any component of $F_i \geq 0$. The relations connecting the distance from the static yield surfaces to the magnitudes of plastic flow are defined by the viscosity functions, where if the rate-independent limit is approached $g_i\left(\langle F_i \rangle\right)$ can be replaced by $\dot{\lambda}_i$ such that [73]:

$$\dot{\lambda}_i \begin{cases} = 0 & F_i < 0 \\ = 0 & F_i = 0 \qquad \text{and} \qquad \dot{F}_i < 0 \\ \geq 0 & F_i = 0 \qquad \text{and} \qquad \dot{F}_i = 0. \end{cases} \tag{2.84}$$

In the rate-independent limit, $F_i = 0$ defines the static yield surfaces. Two types of processes are distinguished in the following framework: *associative* and *non-associative* flow.

Associative flow occurs when the direction of expansion of the yield functions is coincident with the direction of plastic flow. Mathematically, this implies the static yield surfaces are equivalent to the viscoplastic potential functions, i.e., $F_i = Q_i$. Ensuring associated flow is equivalent to ensuring generalized normality, where in both cases the plastic flow can be constructed as a function of plastic potentials [44]. On the other hand, non-associative flow is defined as a process wherein the direction of expansion of the yield functions does not coincide with the direction of plastic flow. During non-associated flow, a few instances may appear that are reminiscent of non-equilibrium processes: a small increment in the yield function may correspond to large changes in plastic flow; large changes in the yield function may correspond to relatively small changes in plastic flow. Often, these instances are encountered in the treatment of porous solids or materials wherein plasticity couples strongly with damage effects [75].

2.5.2 Simplified frameworks

Although the previous section outlined the general theory of viscoplasticity for materials that may be represented by a large number of internal variables, in most applications a relatively small number of important physical processes are distinguished and are represented using an internal state variable description. The following section was also developed for a general material response; however, in many applications in plasticity theory the material is well described by treating it as as initially isotropic. In this section, some commonly employed simplified models are highlighted, as they form the basis for dynamic strength models presented in Section 2.6.

For isotropic materials, as was the case in thermoelasticity theory, the response must depend only on stress invariants given as

$$I_1' = \mathrm{tr}\boldsymbol{\sigma}', \qquad I_2' = \frac{1}{2}\left(\boldsymbol{\sigma}' : \boldsymbol{\sigma}' - \left(\mathrm{tr}\boldsymbol{\sigma}'\right)^2\right), \qquad I_3 = \det\boldsymbol{\sigma}', \tag{2.85}$$

where $\boldsymbol{\sigma}' = \boldsymbol{\sigma} + p\mathbf{I}$ is the deviatoric portion of the Cauchy stress and I_1', I_2', and I_3' are the first, second, and third invariants of the Cauchy stress deviator. Noting that $I_1' = 0$, the components from plasticity theory can be further simplified, i.e.,

1. $\mathbf{L}^P\left(\mathbf{F}^E, \theta, \boldsymbol{\alpha}_i\right) \rightarrow \mathbf{L}^P\left(I_2', I_3', \theta, \boldsymbol{\alpha}_i\right)$

2. $\dot{\boldsymbol{\alpha}}_i \left(\mathbf{F}^E, \theta, \boldsymbol{\alpha}_i\right) \rightarrow \dot{\boldsymbol{\alpha}}_i \left(I_2', I_3', \theta, \boldsymbol{\alpha}_i\right)$.

Now consider the following simplifications: the material state may be characterized by a back stress α and a drag stress κ wherein α is responsible for translation of the yield surface, which is used to represent the internal stress fields due to lattice defects, and κ is responsible for the expansion of the yield surface, which is used to represent the total long range stress field contribution of lattice defects throughout the material; the thermodynamic driving force for plastic deformation is I_2'; there is a single static yield surface F which is equivalent to the plastic potential Q, i.e., associated flow (generalized normality) is assumed; and, the viscosity function is negligible. Following these simplifications, this simplified viscoplastic theory may be expressed as:

1. The yield surface $F\left(I_2', \theta, \alpha, \kappa\right) = 0$, which in this case is equivalent to the viscoplastic potential
2. The plastic deformation rate $\mathbf{D}^P = \dot{\lambda} \partial F / \partial \boldsymbol{\sigma}$
3. The evolution rate for the back stress $\dot{\alpha}\left(I_2', \theta, \alpha, \kappa\right)$ and the drag stress $\dot{\kappa}\left(I_2', \theta, \alpha, \kappa\right)$.

In this framework the skew symmetric component of the plastic velocity gradient ($\mathbf{W}^P = \mathbf{L}^P_{skew}$) must be defined by imposing additional constraints such as objectivity. Often, the yield surface is expressed as a function of a yield function and the associated internal state variables. In the case of a back stress and drag stress, the yield surface is expressed in terms of the yield function as

$$F\left(I_2', \theta, \alpha, \kappa\right) = f\left(I_2' - \alpha, \theta\right) - \kappa = 0. \tag{2.86}$$

The most widely implemented isotropic flow function is the von Mises criterion. Neglecting back stress and assuming isothermal conditions, it assumes that plastic deformation is solely a function of I_2' and that the flow function takes the form $f\left(I_2'\right) = I_2'$. For uniaxial tension tests, the onset of yielding begins when $I_2' - \kappa^2 = 0$, which occurs when $\kappa = \sigma_Y / \sqrt{3}$, where σ_Y is the yield stress in uniaxial tension. Similarly, for uniaxial shear tests, yielding occurs when $\kappa = \tau_Y$, where τ_Y is the shear stress at yield. Another stress measure that is often used to describe von Mises plasticity is an effective

stress $\sigma_{\mathit{eff}} = \sqrt{\frac{2}{3}\sigma'_{ij}\sigma'_{ij}} = \frac{2}{\sqrt{3}}\sqrt{I'_2}$. For rate-independent, isotropic, uniaxial tension the yield surface would then be $F = \sigma_{\mathit{eff}} - \frac{2}{3}\sigma_Y = 0$.

For most of the phenomenological dynamic strength models presented in the following section, a coarse description of material strength is used. Generally, these models are derived to fit known macroscopic behavior and are not concerned with partitioning numerous plastic deformation and yielding mechanics. As such, all of the models presented in Section 2.6 are implemented in the context of isotropic plasticity, employ a von Mises yield function, and neglect the back stress contribution to hardening.

2.6 Strength models

2.6.1 Steinberg-Guinan

Because the Steinberg-Guinan (SG) model was developed to model the one-dimensional response of experienced by isotropic materials subjected to longitudinal plate impact experiments, it is inherently one-dimensional. For one-dimensional compression of isotropic materials, the longitudinal stress, strain rate, and their deviators are connected through

$$\sigma'_{11} = \sigma_{11} - \frac{1}{3}\sigma_{kk} = \sigma_{11} + p, \qquad \dot{\epsilon}'_{11} = \dot{\epsilon}_{11} - \frac{1}{3}\dot{\epsilon}_{kk} = \dot{\epsilon}_{11} + \frac{1}{3\rho}\frac{\partial \rho}{\partial t}, \qquad \dot{\sigma}'_{11} = 2\mu\dot{\epsilon}'_{11}. \quad (2.87)$$

For this special loading case, it can be shown that $I'_2 = \frac{3}{4}\sigma'^2_{11}$ [76]. In terms of the viscoplastic theory of internal state variables, it will be shown that the SG model can be written in the context of isotropic hardening von Mises plasticity, i.e., $F = f\left(I'_2\right) - \kappa = 0$ such that $f\left(I'_2\right) = \sqrt{I'_2}$ and $\kappa = \sigma_Y\left(p, V, \theta\right)/\sqrt{3}$. In the context of ISV theory of plasticity, the flow surface cannot be expressed in terms of the thermoelastic state and internal state variables that characterize the material's current state. Therefore, this model cannot be used to characterize the instantaneous state of the material nor capture its evolving history.

Steinberg and Guinan proposed a constitutive relation for the dependence of μ and σ_Y on temperature and compression for use in one-dimensional wave propagation codes [2], i.e.,

$$\mu\left(p, V, \theta\right) = \mu_0 + \frac{\partial \mu}{\partial p}\frac{p}{\eta^{1/3}} + \frac{\partial \mu}{\partial \theta}\left(\theta - \theta_0\right) \quad (2.88)$$

$$\sigma_Y\left(p, V, \theta\right) = \sigma_0\left(\frac{\mu}{\mu_0}\right)\left[1 + \beta\left(\epsilon + \epsilon_{p0}\right)\right]^n, \quad (2.89)$$

where $\eta = \rho/\rho_0 = V_0/V$ is the compression, β and n are work hardening parameters, ϵ_{p0} is the initial plastic strain, which is usually set to zero, and items with subscript 0 refer to the reference state ($p_0 = 0$ and $\theta_0 = 300$ K). Pressure and temperature derivatives of the shear moduli have been tabulated for 65 elements based on experiments performed on single crystals and polycrystals [60]. The strain hardening is bounded by σ_{max} through the simple relation $\sigma_0 \left[1 + \beta \left(\epsilon + \epsilon_{p0}\right)\right]^n \leq \sigma_{max}$, which corresponds to the strength at $\dot{\epsilon} \approx 10^5\ s^{-1}$. Often, σ_{max} is taken as the largest value of flow strength found in quasi-static experiments (an implied assumption is that it is possible to achieve the highest measured strength of the material during quasistatic deformation, which may be questionable).

The simple form of the Steinberg-Guinan constitutive relation is predicated on experimental observations that σ_Y and μ both depend on p; however, they determined there was not sufficient evidence to suggest that the relations used to describe their pressure dependence should differ. Therefore, they were able to eliminate an extra term in the strength dependence of p by equating the normalized pressure dependencies, i.e.,

$$\frac{1}{\sigma_Y}\frac{\partial \sigma_Y}{\partial p}\bigg|_0 \approx \frac{1}{\mu_0}\frac{\partial \mu}{\partial p}\bigg|_0. \tag{2.90}$$

The form of μ in Equation (2.88) corresponds to experimental observations that at low p, μ varies linearly with p, whereas at high pressures Thomas-Fermi theory predicts $p \propto \eta^{5/3}$ and $\mu \propto \eta^{4/3}$. As $p \to 0$ and $\eta \to 1$, the linear form of $\mu = \mu_0 + \frac{\partial \mu}{\partial p} p$ is recovered whereas for $p \to \infty$ when $\eta \gg 1$, then $\mu \propto \eta^{4/3}$.

As shown in Figure 2.3, this model is useful for modeling many aspects of plate impact experiments at high rates including melting, strain hardening, and elastic-plastic wave interactions. However, because the deviatoric response of the material is characterized in terms of a strength and shear modulus dependence only, the model clearly has its advantages and disadvantages. The material state is characterized purely in terms of pressure, volume (or density), and temperature (or energy), which are values readily available in most hydrodynamic codes. Therefore, the deviatoric response can be readily integrated implicitly with existing volumetric equations of state without adding significant computational cost or including additional state variables. Despite these advantages, the model has its

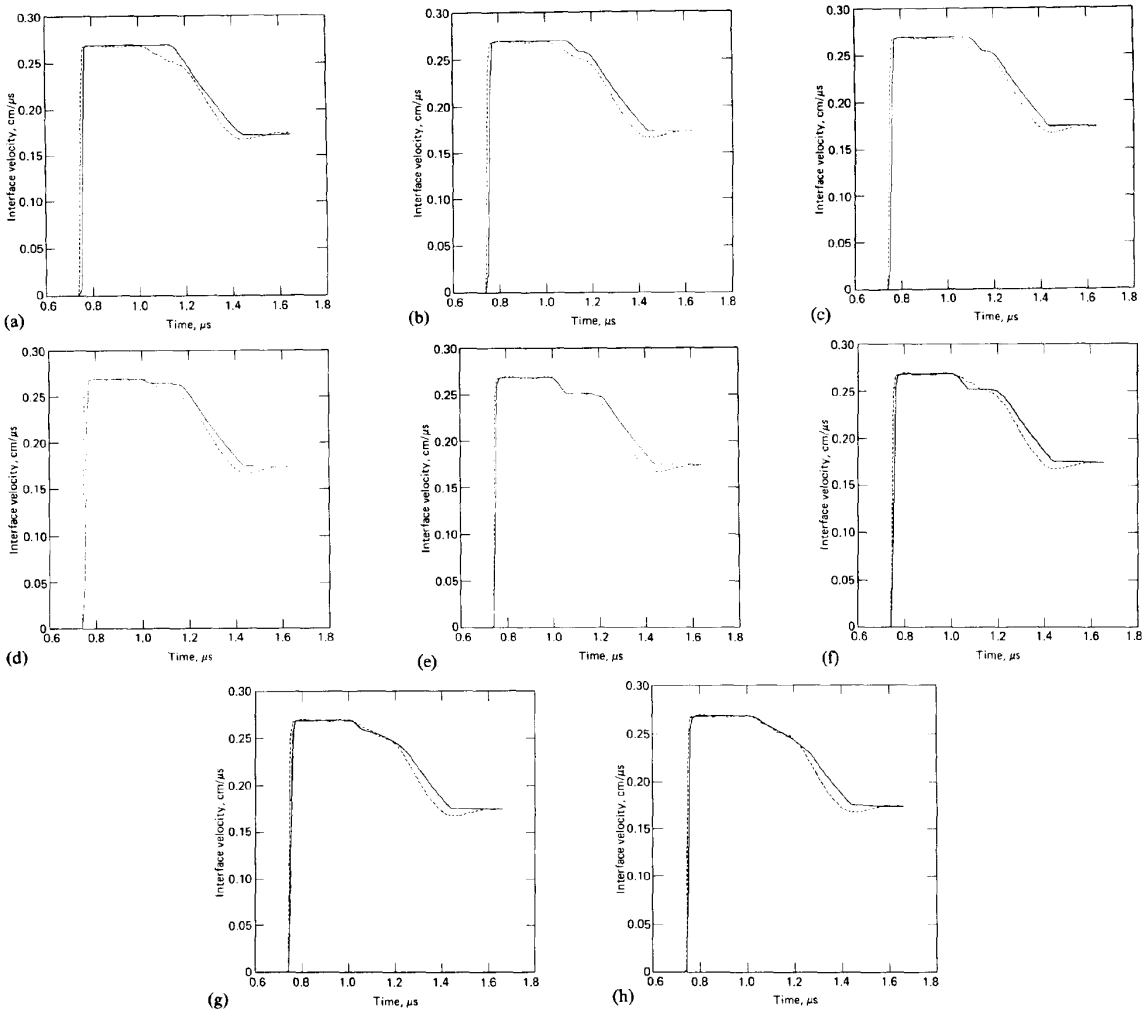

Figure 2.3: Comparison of Steinberg Guinan constitutive relation for shock loading compared to an experimental profile for aluminum. Each profile is generated by sequentially adding components of the model: (a) purely hydrodynamic response ($\sigma_Y = 0, \mu = 0$); (b) adding strength ($\sigma_Y = \sigma_0, \mu = \mu_0$); (c) adding strain hardening ($\beta > 0$); (d) adding pressure dependence of shear modulus ($\partial\mu/\partial p > 0$) for μ only; (e) adding pressure dependence of shear modulus ($\partial\mu/\partial p > 0$) for σ_Y as well; (f) adding temperature dependence ($\partial\mu/\partial t < 0$); (g) making the flow surface expansion kinematic instead of isotropic; and (h) making the flow surface expansion between kinematic and isotropic hardening. Reprinted with permission from [2]. Copyright 1980, AIP Publishing LLC.

limitations as well. The model gives no information concerning the shock structure as their is no explicit rate-dependence in the model. Furthermore, there is no notion of dependence of material strength on the state of the material. Rather, the strength is incorporated phenomenologically through the pressure, volume, and temperature. Therefore, history effects must be included in an ad-hoc manner through parameters that do not characterize the instantaneous state of the material. Other deficiencies are discussed in the introduction of [4] as motivation for the Steinberg-Lund model.

In practice, the model is often used to fit velocity profile histories for plate impact experiments in a purely interpolative manner due to its computational efficiency as well as its limited number of aphysical parameters. Yet, because it is easy to understand the effect of these parameters on the resultant wave profile and these parameters have been derived for many materials, this model has been widely implemented and is often used to describe shock wave experiments, despite its limitations.

2.6.2 Johnson-Cook

The Johnson-Cook (JC) dynamic strength model is one of the simplest constitutive models that gives an empirical description of the flow stress dependence on effective plastic strain, strain rate, and temperature, i.e., $\sigma_Y\left(\epsilon^p_{\mathit{eff}}, \dot{\epsilon}^p_{\mathit{eff}}, \theta\right)$, where the von Mises effective value of a rank two tensor $\mathbf{A}$ is given by $A_{\mathit{eff}} = \sqrt{\frac{2}{3}A_{ij}A_{ij}}$ [77]. The JC model is incorporated through an isotropic hardening von Mises flow surface $F = f(\boldsymbol{\sigma}, \theta) - \kappa = 0$, where the flow function is $f(\boldsymbol{\sigma}, \theta) = \sqrt{I_2'}$ for isotropic materials and where $\kappa = \sigma_Y\left(\epsilon^p_{\mathit{eff}}, \dot{\epsilon}^p_{\mathit{eff}}, \theta\right)/\sqrt{3}$. Assigning $\boldsymbol{\alpha}_i = \epsilon^p_{\mathit{eff}}$ as the structural ISV shows that the flow stress is related to the ISV and its instantaneous rate, i.e., $\kappa(\alpha, \dot{\alpha}, \theta)$. Consequently, the JC theory will not be able to properly capture history dependence of the structure of the material.

The constitutive model proposed by Johnson and Cook is the product of empirical relations used to describe strain hardening, strain rate hardening, and thermal softening.

i.e.,

$$\sigma_Y = \left[\sigma_0 + B\left(\epsilon^p_{eff}\right)^n\right]\left[1 + C\ln\frac{\dot{\epsilon}^p_{eff}}{\dot{\epsilon}_0}\right]\left[1 - (\theta^*)^m\right] \tag{2.91}$$

$$\text{such that} \quad \theta^* = \frac{\theta - \theta_0}{\theta_m - \theta_0},$$

where σ_0, $\dot{\epsilon}_0$, and θ_0 are the flow strength, strain rate, and temperature of some reference state and θ_m is the melting temperature. The parameters B, C, n, and m are experimentally determined model parameters that have been fit for a large number of metals using Split-Hopkinson bar data for strain rates up to approximately 10^4 s^{-1} [77]. The traditional JC model was modified to incorporate stress reduction by a factor of $\sigma_{def}/\sigma_{rec}$ due to dynamic recrystallization above a temperature θ_c by multiplying Equation (2.91) by $H(\theta)$, giving

$$\sigma_Y = \left[\sigma_0 + B\left(\epsilon^p_{eff}\right)^n\right]\left[1 + C\ln\frac{\dot{\epsilon}^p_{eff}}{\dot{\epsilon}_0}\right]\left[1 - (\theta^*)^m\right]H(\theta) \tag{2.92}$$

$$\text{where} \quad H(\theta) = u(\theta)\left[1 - \left(1 - \frac{\sigma_{rec}}{\sigma_{def}}\right)\right]^{-1}.$$

The step function $u(\theta)$ is defined as $u(\theta) = 0$ for $\theta < \theta_c$ and $u(\theta) = 1$ for $\theta > \theta_c$ [78].

This model has gained wide acceptance due to its relatively simple implementation, easily understood parameters, and ability to fit a wide range of high strain rate data. It also does not significantly add to the computational cost compared to elastic perfectly-plastic models with finite strength, and uses parameters that are readily available in most commercial finite-element and finite-difference codes. Although the model has gained wide acceptance, it is often insufficient for modeling shock behavior. Therefore, it is most often used when studying problems with strain rates up to 10^4 s^{-1}. Also, as mentioned in the context of viscoplastic internal state variable theory, it cannot properly model history dependence of structure evolution. Regardless of these deficiencies, it is one of the most widely utilized models and will most likely continue for some time as the most popular constitutive model for studying many high strain rate problems.

2.6.3 Steinberg-Lund

To address limitations of the SG model, such as the inability to capture strain-rate dependent material behavior, which in turn leads to an inability to model the increase in stress

from the precursor to the main shock (the "foot"), Steinberg and Lund (SL) proposed a model that directly incorporates a rate-dependent strength and can be used to model strain rates as low as $10^{-4}\ s^{-1}$ [4]. The SL model also extends the SG formulation to two and three-dimensional loading. The SL model is incorporated through an isotropic hardening von Mises flow surface, i.e., $F = f(\boldsymbol{\sigma}, \theta) - \kappa = 0$ where $f(\boldsymbol{\sigma}, \theta) = \sqrt{I_2'}$ for isotropic materials and $\kappa = \sigma_Y\left(p, \epsilon^p_{eff}, \dot{\epsilon}^p_{eff}, \theta\right)/\sqrt{3}$. As was the case for the JC model, the SL model will not be able to properly capture history dependence of the structure of the material because of the instantaneous dependence of the flow stress on the effective plastic strain rate.

Like the JC model, the SL model uses a dynamic flow strength, which in this case is partitioned into thermal and athermal flow stress components, i.e.,

$$\sigma_Y = \left[\sigma_\theta\left(\dot{\epsilon}^p_{eff}, \theta\right) + \sigma_a\left(\epsilon^p_{eff}\right)\right]\frac{\mu(p,\theta)}{\mu_0}, \tag{2.93}$$

where σ_θ is the thermally activated stress component and σ_a is the athermal stress component. The strain hardening relation is equivalent to the strain hardening portion of the SG model. The thermally activated flow stress is given by solving for an equation of the form $\sigma_\theta\left(\dot{\epsilon}^p_{eff}, \theta\right)$ from the equation below for $\dot{\epsilon}^p_{eff}(\sigma_\theta, \theta)$, i.e.,

$$\dot{\epsilon}^p_{eff} = \left\{\frac{1}{C_1}\exp\left[\frac{2U_k}{k\theta}\left(1 - \frac{\sigma_\theta}{\sigma_p}\right)^2 + \left(\frac{C_2}{\sigma_\theta}\right)^m\right]\right\}^{-1}, \tag{2.94}$$

where $2U_k$ is the energy to form a pair of kinks in a dislocation of length L, k is Boltzmann's constant, and σ_p is the Peierls stress. The thermally activated stress is limited such that $\sigma_\theta \leq \sigma_p$. Note that when $\sigma_\theta = \sigma_p$ then $\sigma_\theta = C_2\dot{\epsilon}^p_{eff}$, which implies C_2 is the viscous drag that acts on the effective plastic strain rate. The constants in the equation can be expressed such that they have the same form as the thermally activated strain rate proposed by Hoge and Mukherjee to describe dislocations limited by the Peierls mechanism and dislocation drag [3], i.e.,

$$\begin{aligned} C_1 &= \frac{N_m L a b^2 \nu}{2w^2} = \dot{\epsilon}_0 \\ C_2 &= \frac{D}{N_m b^2}, \end{aligned}$$

where L is the dislocation line length, w is width of the critical pair of kinks, ν is the Debye frequency, a is the separation between Peierls valleys (mean velocity of a dislocation

is assumed to be the activation frequency times the distance between Peierls valleys), $2U_k$ is the energy required to form a pair of kinks in the dislocation segment, and N_m is the mobile dislocation density. In their work, Hoge and Mukherjee account for the thermally activated flow stress in terms of the Peierls stress as shown in Figure 2.4.

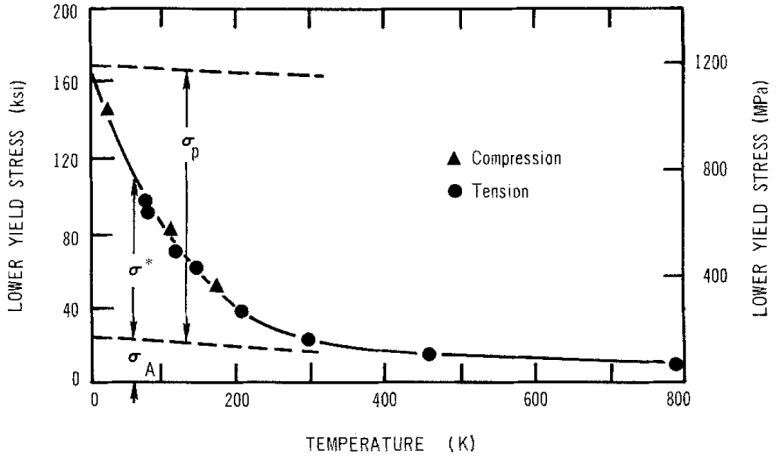

Figure 2.4: Determination of thermally activated flow stress σ_θ (represented in this figure by σ^*) in terms of temperature, the temperature-dependent Peierls stress σ_p, and the athermal flow stress σ_a. Reprinted with permission from [3]. Copyright 1977, Springer.

The SL model is able to address many shortcomings of the SG model. Because the SL model has explicit rate dependence, it is capable of modeling elastic precursor attenuation as well as shock wave structure. In Figure 2.5, a comparison is shown between the rate-independent SG model and the SL model, as well as how the drag coefficient D affects the resultant shock structure. The SL model has enough flexibility to fit most strength data as well as shock wave profiles for strain rates ranging from $10^{-4} - 10^{6}$ s^{-1}. Because it is not computationally intensive and uses parameters already in most finite element and finite difference codes as internal variables, it has been widely implemented for a variety of problems. Despite its successes, the SL model also has significant drawbacks. Like the JC model, the SL model cannot properly account for history dependence. Although model parameters can be related to the model proposed by Hoge and Mukherjee used to describe rate-dependent plastic deformation in BCC metals, in practice model parameters are often used as fitting parameters to fit to shock velocity data and wave profiles with little regard for their physical significance. This makes it difficult to correlate model behavior with

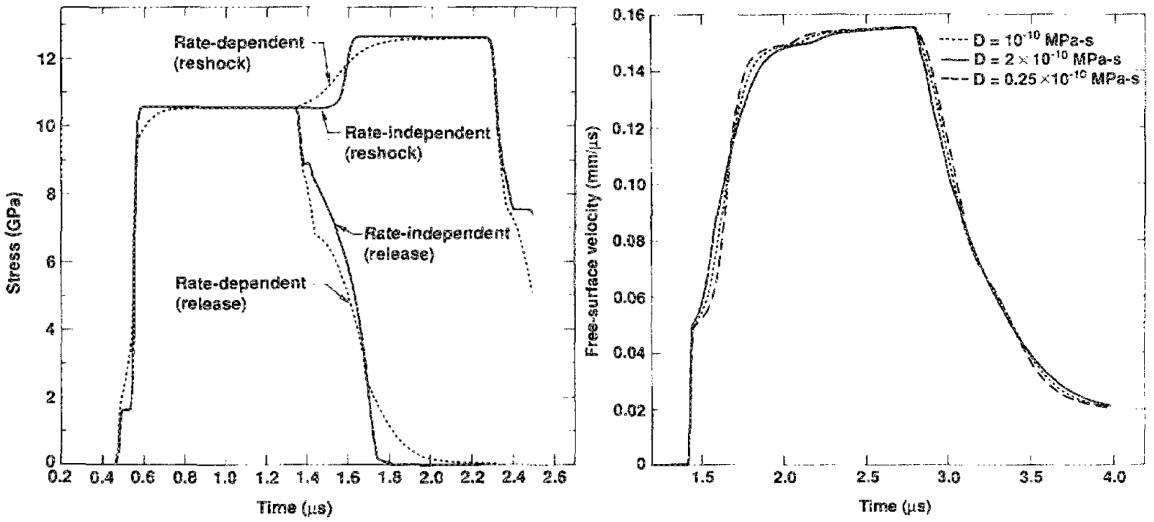

(a) (b)

Figure 2.5: Model behavior for (a) reshock and release experiments showing a comparison of SG model with Bauschinger effect parameters (denoted rate-independent) and SL model (denoted rate-dependent) and (b) effect of viscosity parameter D on SL behavior for a 5 GPa shock with release. Reprinted with permission from [4]. Copyright 1989, AIP Publishing LLC.

specific mechanisms. Therefore, the model should be used as an interpolative tool to fit experimental shock velocity profiles and strength data over a range of strain rates.

2.6.4 Zerilli-Armstrong

Zerilli and Armstrong (ZA) proposed a constitutive model similar to the JC model, except that their model was derived from the dynamics of dislocation motion and is rooted in the physics of microstructural hardening mechanisms [79, 80, 81]. Despite that the model contains a more physical basis than the JC model, it does not use these microstructural parameters as internal state variables. Therefore, writing the form of the ZA model in viscoplasticity theory with an isotropic von Mises flow surface gives $F = f(\boldsymbol{\sigma}, \theta) - \kappa = 0$ where $f(\boldsymbol{\sigma}, \theta) = \sqrt{I_2'}$ for isotropic materials and $\kappa = \sigma_Y(\epsilon_{eff}, \dot{\epsilon}_{eff}, \theta)/\sqrt{3}$. The ZA model, by construction, cannot incorporate history effects because it relates macroscopic loading parameters to describe its flow surface.

The model is based on a partitioning the total strength into contributions from an athermal strength σ_a, a thermal strength σ_θ, and a grain size dependent strength σ_G. The

ZA model uses different forms for the dynamic strength for FCC and BCC metals. These forms are motivated on experimental observations that in BCC metals, strain rate hardening is not significantly affected by prior straining because the Peierls stress is the primary factor governing strain rate hardening, whereas in FCC metals strain rate hardening is significantly affected by strain hardening because the primary short range barrier to thermal activation is entanglement by other dislocations. The two forms of dynamic strength in the ZA model that correspond to FCC and BCC metals are:

$$\text{FCC} \quad : \quad \sigma_Y = \sigma_a + B_0\sqrt{\epsilon_{\mathit{eff}}}\exp\left(\theta\left(\beta_1 \ln \dot{\epsilon}_{\mathit{eff}} - \beta_0\right)\right) + \frac{k}{\sqrt{d}} \tag{2.95}$$

$$\text{BCC} \quad : \quad \sigma_Y = \sigma_a + B\exp\left(\theta\left(\beta_1 \ln \dot{\epsilon}_{\mathit{eff}} - \beta_0\right)\right) + \frac{k}{\sqrt{d}} + K\epsilon_{\mathit{eff}}^n, \tag{2.96}$$

where for both models σ_a is based on initial flow strength contribution due to solutes and dislocations, k is the microstructural stress intensity, d is the grain size, β_0 captures thermal softening, and β_1 captures strain rate hardening. For FCC metals, B_0 captures the coupling between strain and strain rate hardening. For BCC metals B completely captures strain rate hardening, which is separate from K, which captures strain hardening.

Use of the ZA model was first justified by noting that the ZA model did a better job of predicting the deformed shape of Taylor Impact specimens than the JC model [79]. Also, because the JC model did not have differing forms for BCC and FCC metals, it could not naturally incorporate the strain rate sensitivity of BCC metals. The ZA model may also do a better job than the JC model at higher rates $\geq 10^4$ s^{-1} because it includes effects from the drag-limited dislocation velocity regime, which the JC model does not. Despite these advantages, the ZA model has a larger number of parameters and uses total strain and strain rate instead of plastic strain, which are disadvantageous. Furthermore, although the model is constructed by considering micromechanics-based viscoplasticity relations, it does not properly incorporate these through the use of internal state variables. Generally, the ZA model, due to its increased complexity yet few advantages over the JC model, has been less widely implemented and used than the JC model.

2.6.5 Mechanical Threshold Stress

Unlike the other models described previously, the Mechanical Threshold Stress (MTS) model is based on using a single ISV to describe the evolving structure of the material [82]. This ISV, termed the mechanical threshold stress ($\hat{\sigma}$), is equivalent to the flow stress at 0K. It will be shown that using $\alpha = \hat{\sigma}$, in the context of an isotropic hardening von Mises flow surface the MTS model can be expressed as $F = f(\boldsymbol{\sigma}, \theta) - \kappa = 0$ where $f(\boldsymbol{\sigma}, \theta) = \sqrt{I_2'}$ for isotropic materials and $\kappa = \sigma_Y(\dot{\epsilon}_{\mathit{eff}}, \theta, \alpha)/\sqrt{3}$. Also, the evolution of the mechanical threshold stress can be expressed as $\dot{\alpha}(\dot{\epsilon}_{\mathit{eff}}, \theta, \alpha)$. In this model the effective strain rate is uniquely determined by the flow stress and mechanical threshold stress, i.e., $\dot{\epsilon}_{\mathit{eff}}(\sigma_Y, \alpha, T)$; hence, this model fits within the context of internal state variable theory of viscoplastic deformation presented in Section 2.5. This is the first high strain rate model presented in this section that uses an internal variable to represent the evolving structure of the material and its associated rate-dependent response.

The mechanical threshold stress is partitioned into two components, an athermal component and a thermal component, i.e., $\hat{\sigma} = \hat{\sigma}_a + \hat{\sigma}_\theta$ where a hat denotes values at 0K. At finite temperature, it is assumed that only σ_θ is affected by strain rate and temperature, i.e.,

$$\sigma_Y = \hat{\sigma}_a + \sigma_\theta = \hat{\sigma}_a + s(\dot{\epsilon}_{\mathit{eff}}, \theta)\,\hat{\sigma}_\theta, \tag{2.97}$$

such that $s(\dot{\epsilon}_{\mathit{eff}}, \theta)$ is a function that describes the strain rate and temperature dependence of the thermal stress. When an Arrhenius equation for strain rate ($\dot{\epsilon}_{\mathit{eff}} = \dot{\epsilon}_0 \exp(\Delta G/k\theta)$) is combined with a phenomenological description of the effect of activation enthalpy on the thermal flow stress ($\Delta G = \mu g_0 b^3 (1 - (\sigma_\theta/\hat{\sigma}_\theta)^p)^q$), an explicit expression for the flow strength in terms of $\hat{\sigma}$, strain rate, and temperature can be derived, i.e.,

$$\sigma_Y = \hat{\sigma}_a + (\hat{\sigma} - \hat{\sigma}_a)\left[1 - \left(\frac{k\theta}{g_0 \mu b^3} \ln \frac{\dot{\epsilon}}{\dot{\epsilon}_0}\right)^{1/q}\right]^{1/p} \tag{2.98}$$

where g_0 is the normalized activation energy, and $0 \leq p \leq 1$ and $1 \leq q \leq 2$ are constants used to describe a statistically averaged obstacle profile [83]. Evolution of the material state is captured by specifying the effect of strain hardening and strain rate hardening on the

mechanical threshold stress. This is captured using Voce behavior, i.e.,

$$\frac{d\hat{\sigma}}{d\epsilon_{\mathit{eff}}} = h_0 \left(1 - h\left(\frac{\hat{\sigma} - \hat{\sigma}_a}{\sigma_s\left(\theta, \dot{\epsilon}_{\mathit{eff}}\right) - \hat{\sigma}}\right)\right) \tag{2.99}$$

where h_0 is a reference hardening rate, h is a function that is fit to the observed hardening behavior, and $\hat{\sigma}_s$ is the saturation stress for strain hardening. A phenomenological relation is used to describe the strain rate and temperature dependence of the saturation stress, i.e.,

$$\sigma_s = \hat{\sigma}_s \frac{\dot{\epsilon}_{\mathit{eff}}}{\dot{\epsilon}_{s0}} \exp\left(-\frac{\mu b^3 A}{k\theta}\right) \tag{2.100}$$

where A, $\dot{\epsilon}_{s0}$, and $\hat{\sigma}_s$ are constants. A function h that has been used to fit mechanical threshold stress data is $h(X) = \tanh\left(2X\right)/\tanh\left(2\right)$, although other functions may be used if they can better reproduce experimental trends.

To determine $\hat{\sigma}_a$, specimens are loaded to different strains, strain rates, temperatures, and deformation histories. Then, the quasistatic yield strength that exists regardless of strain, strain rate and temperature ($\hat{\sigma}_a$) is found. In the MTS formulation, the increased mechanical threshold at higher strain rates is responsible for the uptick in stresses at strain rates exceeding $10^3\ s^{-1}$. Follansbee and Kocks showed that phonon dispersion is not responsible for this uptick until approximately $10^4\ s^{-1}$ as postulated by [84], but can still be modeled using their formulation.

Unlike most other high strain rate models, the MTS model is able to capture strain and strain rate history dependence of the material response. This makes the MTS model much more valuable for simulating history-dependent responses such as would occur in reshock and release tests. Furthermore, because the MTS model uses an internal state variable to model the evolving material state, there is a notion of the final state of the material after deformation, which can be used to compare the resultant material state for tests performed to different strains, and at different strain rates and temperatures. Because the MTS model uses an internal variable to represent the evolving material state, it is more complicated to implement in finite-element and finite-difference codes compared to the SG, SL, JC, and ZA models. Also, because the MTS model is more complicated to understand, it is less widely implemented and used than other models.

The MTS model has been used extensively to model FCC and BCC metals at strain rates up to approximately 10^4 s^{-1}. Also, although more complicated flow strength or dislocation-based models have emerged (models that use two or more internal state variables), they often share certain aspects with the MTS model.

2.6.6 Preston-Tonks-Wallace

Unlike most dynamic strength models, the Preston-Tonks-Wallace (PTW) model can be used to simulate plastic deformation at rates extending from 10^{-3} s^{-1} to 10^{12} s^{-1} [85]. The model uses a non-dimensionalized stress, temperature, and plastic strain rate to capture behavior ranging from the thermally activated dislocation motion regime to the overdriven shock regime. Writing the PTW model in viscoplasticity theory with an isotropic von Mises flow surface gives $F = f(\boldsymbol{\sigma}, \theta) - \kappa = 0$, where $f(\boldsymbol{\sigma}, \theta) = \sqrt{I_2'}$ for isotropic materials and $\kappa = \sigma_Y \left(\epsilon_{eff}^p, \dot{\epsilon}_{eff}^p, \theta \right) / \sqrt{3}$. Like the ZA model, the PTW model cannot incorporate history effects because it uses effective plastic strain and strain rate as independent variables to describe the evolving structure of the material.

Because of the large number of parameters used in the PTW model (14), the notation used in [85] will be adopted where a hat indicates a non-dimensional parameter and stress and strain are referred to in terms of deviatoric components. The shear flow stress is naturally non-dimensionalized by the shear modulus through $\widehat{\tau} = \tau / \mu(\rho, \theta)$, where $\tau = \sqrt{I_2'/3}$. The temperature, which for shock loading is more naturally governed by the melting temperature instead of the Debye temperature, is normalized by $\widehat{\theta} = \theta / \theta_m(\rho)$. The authors showed through the Burakovsky-Preston relation between the Debye and melting temperature that these are not independent quantities, so normalization by one quantity instead of the other is inconsequential. Finally, the plastic strain rate $\dot{\psi}$ is normalized by the frequency of a shear wave crossing an atom, given by $\dot{\xi} \approx \omega_D / 3\sqrt{\pi}$, where ω_D is the Debye frequency. Using these non-dimensionalized quantities, the evolution equations for the stress can be found across 15 orders of magnitude in strain rate.

The thermally activated regime follows a Voce behavior where work hardening decreases as the applied stress approaches the saturation stress. Equations for the saturation and yield

stress, $\widehat{\tau}_s$ and $\widehat{\tau}_y$ respectively, in the thermally activated regime are given by

$$\widehat{\tau}_s = s_0 - (s_0 - s_\infty) \operatorname{erf}\left[\kappa\widehat{\theta} \ln\left(\gamma\dot{\xi}/\dot{\psi}\right)\right] \tag{2.101}$$

$$\widehat{\tau}_y = y_0 - (y_0 - y_\infty) \operatorname{erf}\left[\kappa\widehat{\theta} \ln\left(\gamma\dot{\xi}/\dot{\psi}\right)\right] \tag{2.102}$$

where κ and γ are constants. The constants s_0 and s_∞ are values that $\widehat{\tau}_s$ assumes at zero temperature and a limiting high temperature, respectively. The same convention applies for y_0 and y_∞. A modified Voce relation is employed for hardening, which when combined with the equations for $\widehat{\tau}_s$ and $\widehat{\tau}_y$ and integrated along a line of constant plastic strain rate yields

$$\widehat{\tau} = \widehat{\tau}_s + \frac{1}{a}\left(s_0 - \widehat{\tau}_y\right) \cdot \ln\left[1 - \left[1 - \exp\left(-a\frac{\widehat{\tau}_s - \widehat{\tau}_y}{s_0 - \widehat{\tau}_y}\right)\right] \exp\left(-\frac{ab\psi}{\left(s_0 - \widehat{\tau}_y\right)\left[\exp\left(a\frac{\widehat{\tau}_s - \widehat{\tau}_y}{s_0 - \widehat{\tau}_y}\right) - 1\right]}\right)\right], \tag{2.103}$$

where a is a dimensionless constant and b is the work hardening rate. In the overdriven shock regime, the plastic wave can overtake the elastic precursor. An interpretation by Wallace is that the plastic front overcomes the elastic precursor because heat is transported from plastic flow in the shock to the leading edge of the shock front, which causes the shock front to steepen [86, 87]. Using strong shock theory, the EOS can be coupled with irreversible thermodynamics to estimate the plastic strain rate found during the shock. The conclusion of this analysis for a variety of metals is that in the strong shock regime, the yield strength has fully saturated to a value that can be modeled by a power law such that

$$\widehat{\tau}_s = \widehat{\tau}_y = \text{const}\left(\frac{\dot{\psi}}{\dot{\xi}}\right)^\beta. \tag{2.104}$$

The temperature-dependent shear modulus is modeled using a simple linear interpolation of the form

$$\mu\left(\rho, \theta\right) = \mu_0\left(\rho\right)\left(1 - \alpha\widehat{\theta}\right), \tag{2.105}$$

which ignores the low-temperature nonlinearity.

With definitions in place for the evolution of the stress in the thermally activated and overdriven shock regimes, the only part missing from the constitutive model is connecting

the two regimes. The authors do so by simply requiring that the strength between these two regimes is continuous. For the saturation stress, the constant in the overdriven shock regime is set to $s_0\gamma^\beta$ so that the stress becomes continuous, therefore

$$\widehat{\tau}_s = \max\left\{ s_0 - (s_0 - s_\infty)\,\mathrm{erf}\left[\kappa\widehat{\theta}\ln\left(\gamma\dot{\xi}/\dot{\psi}\right)\right], s_0\left(\dot{\psi}/\gamma\dot{\xi}\right)^\beta \right\}. \tag{2.106}$$

The yield stress is slightly more complicated because of the fact that strain rate sensitivity changes rapidly around 10^3 s^{-1}. Therefore, a correction is added using the parameters y_1 and y_2 so that this drastic jump can be modeled, i.e.,

$$\widehat{\tau}_y = \max\left\{ y_0 - (y_0 - y_\infty)\,\mathrm{erf}\left[\kappa\widehat{\theta}\ln\left(\gamma\dot{\xi}/\dot{\psi}\right)\right], \min\left[y_1\left(\dot{\psi}/\gamma\dot{\xi}\right)^{y_2}, s_0\left(\dot{\psi}/\gamma\dot{\xi}\right)^\beta \right] \right\}. \tag{2.107}$$

The primary advantage of using the PTW model is that it can be used to model processes with strain rates up to 10^{12} s^{-1}, which is often near the limit or exceeds the limit of experimental spatio-temporal measurements. Like the JC, SL, and other models that use effective plastic strain and strain rate as independent variables to represent the material state, the PTW model cannot properly model history effects; however, for such large strain rate applications, the unloading or reloading history response is secondary to understanding the initial, proportional shock loading response.

2.6.7 Discussion

All of the strength models mentioned in this section have specific advantages and limitations; however, it is helpful to group them in terms of common features and differences they possess. The SG model is the only model that cannot directly incorporate strain-rate sensitivity of the flow surface. Despite their varying physical motivations and strain rates over which they are valid, the JC, SL, and PTW models all use some measure of effective plastic strain and strain rate as independent variables, and therefore cannot incorporate strain and strain rate history dependence properly. Also, it is difficult to experimentally measure effective plastic strain rate, so there is little physical motivation to use this as a parameter. The ZA model uses total strain and strain rate instead, which are even less appropriate choices of independent variable as these are imposed loading rates rather than descriptors of material state. The only model that conceptually uses an internal

state variable to capture the evolving material state is the MTS model. Furthermore, the MTS model provides an experimental basis on which to measure this structural parameter. Therefore, it can model history effects and via an internal state variable that is based on a physical description that characterizes the evolving state of the material.

In many applications at moderate strain rates $\leq 10^4$ s^{-1}, the JC model is most commonly used due to its simplicity and computational efficiency. As stated by Johnson and Cook [77]:

> It is recognized that more complicated models may indeed give more accurate descriptions of material behavior [...] however, the computational user cannot readily incorporate complicated and diverse models. The result is that a constant "dynamic flow stress" is often used.

In this context, the limited number of easy to interpret parameters makes the JC model a simple, effective way to incorporate dynamic strength. For the high strain rates encountered in shock loading $\geq 10^5$ s^{-1}, the SG and SL model are the simplest models to implement and interpret, despite that the models give little physical notion of the material state. The SG model is used predominately over the SL model because material parameters have been determined for a significantly larger number of materials for the SG model than have been determined for the SL model. The SL model is advantageous when the shock structure itself is of interest, however, because the SG only incorporates viscous non-equilibrium strain rate dependence weakly through the pressure dependence. The SL model is also advantageous over the JC model at these high rates, as the JC model is generally limited in application for strain rates up to 10^4 s^{-1}.

2.7 Dislocation-mediated plasticity

Unlike dynamic strength models, which characterize the strength of the material based on some instantaneous measure of "state" (with the exception of the MTS model), dislocation-based models explicitly track the nucleation and glide of populations of dislocations, which is related to the rate of plastic straining. The primary equation used in dislocation-based

models is the generalized Orowan equation. The Orowan equation relates the plastic shearing rate to the statistical motion of dislocations, i.e.,

$$\dot{\gamma}^{\alpha} = N_m^{\alpha} b^{\alpha} \bar{v}^{\alpha} + \dot{N}_{gen}^{\alpha} \bar{x}_{gen}^{\alpha} b^{\alpha}, \tag{2.108}$$

where α denotes an individual slip system, N_m^{α} is the density of mobile dislocations gliding with mean velocity $\bar{v}^{\alpha}$, b^{α} denotes the Burgers vector, and $\dot{N}_{gen}^{\alpha}$ denotes the rate of generation of dislocations that are assumed to glide a distance of $\bar{x}_{gen}^{\alpha}$ during the generation process. In local crystal plasticity, the plastic velocity gradient in the intermediate configuration is generally assumed to be related to the slip rates through

$$\mathbf{L}_0^P = \dot{\mathbf{F}}^P \cdot \mathbf{F}^{P-1} = \sum_{\alpha} \dot{\gamma}^{\alpha} \left(\mathbf{s}_0^{\alpha} \otimes \mathbf{m}_0^{\alpha} \right), \tag{2.109}$$

where $\mathbf{s}_0^{\alpha}$ and $\mathbf{m}_0^{\alpha}$ both denote unit vectors in the intermediate configuration, referring to the slip direction and normal to the slip plane, respectively.

The primary focus of dislocation-based models is determining forms and values of $\bar{v}^{\alpha}$ as well as evolution equations and their associated parameters used to describe the evolving dislocation density. The primary advantage of these dislocation-based models over dynamic strength models is that because the material state is characterized by a physical quantity, dislocation density. In the case of dislocation velocity, careful measurements have been performed to determine the mean velocity of dislocations in response to an applied shear stress. The dislocation density can also be measured directly before and after impact in shock-loaded specimens. Specific mechanisms that govern the evolution of dislocations have been identified by observing the response of individual as well as populations of dislocations with respect to an applied stress in carefully prepared samples. In all cases, direct observation of the initial and evolving structural state of the material allows for careful validation of the constitutive model. In each of the constitutive relations presented in this section, macroscopic models of dislocation activity are motivated either from direct experimental observation or by quantifying disagreement between macroscopically observed behavior and constitutive model predictions based on existing models of observed behavior.

In the following section, it is assumed that the internal variables used to model dislocation-mediated plasticity theory are the mobile and immobile dislocation density on each slip

system, denoted N_m^α and N_{im}^α, respectively (note that other choices of internal variable for dislocation-mediated plasticity are possible, such as partitioning edge and screw components and their associated velocities [88] or relating dislocation density with substructural features [89]). In the context of internal state variable theory, generalized normality follows if the shearing rate and evolution rate of internal variables take the following form [72, 44]:

$$\dot{\gamma}^\alpha \left(\tau^\alpha, N_m^\alpha, N_{im}^\alpha, \theta\right) \tag{2.110}$$

$$\dot{N}_m^\alpha \left(\tau^\alpha, N_m^\alpha, N_{im}^\alpha, \theta\right) \tag{2.111}$$

$$\dot{N}_{im}^\alpha \left(\tau^\alpha, N_m^\alpha, N_{im}^\alpha, \theta\right). \tag{2.112}$$

By including the second term in the generalized Orowan expression given in Equation (2.108), this theory violates generalized normality by construction, but only to the extent to which the second term contributes.

Historically, constitutive equations developed to capture dislocation density evolution and dislocation velocity contributions have been implemented for one-dimensional deformation of a material that obeys associated flow for isotropic plasticity with a von Mises flow function. For one-dimensional deformation, if it is assumed that dislocation glide and generation occurs only on planes of maximum shear ($\tau = \sqrt{I_2'/3}$), then the Orowan equation can be rewritten as

$$\dot{\gamma} = N_m b \bar{v} + \dot{N}_{gen} \bar{x}_{gen} b, \tag{2.113}$$

where the plastic deformation rate is related to the shearing rate by $\mathbf{D}^P = \boldsymbol{\sigma}'(\dot{\gamma}/2\tau)$. The flow surface takes the form $F = \sqrt{3}\tau - \kappa\left(\tau, N_m, N_{im}, \theta\right)$. For a macroscale, dislocation-based model to obey generalized normality, the evolution equations must assume the following forms:

$$\dot{\gamma}\left(\tau, N_m, N_{im}, \theta\right) \tag{2.114}$$

$$\dot{N}_m\left(\tau, N_m, N_{im}, \theta\right) \tag{2.115}$$

$$\dot{N}_{im}\left(\tau, N_m, N_{im}, \theta\right). \tag{2.116}$$

Although it may seem that dislocation-mediated plasticity is inherently different from the dynamic strength models presented in Section 2.6, the above derivations reinforce that

dislocation-based models can be viewed as strength-based models implemented into viscoplasticity theory with physically measurable quantities (in this case, dislocation density) used as internal state variables.

2.7.1 Dislocation velocity

One method that has been used to experimentally measure dislocation velocity is the process of repeated etching. In this method, an individual dislocation is moved some mean distance by applying a finite-duration stress pulse. By quantifying the duration of the stress pulse and the associated distance the dislocation traveled, the velocity of the dislocation can be quantified as a function of the applied shear stress. Johnston and Gilman used this method to measure the mean velocity of individual screw and edge dislocations in LiF single crystals with different purity, pre-processing histories, and at varying temperatures [88]. Results of these studies are shown in Figure 2.6[1]. The plot of dislocation velocity shown in Figure 2.6b and associated plots given in [88] reveal the following trends: edge dislocations travel faster than screw dislocations at the same resolved shear stress but this trend disappears as the dislocation velocities approach the shear wave speed; dislocations are not observed to travel faster than the shear wave speed; dislocations travel faster in annealed crystals than in hardened (by neutron radiation) crystals; there is a stress below which dislocations are observed not to move; and near room temperature, the velocity is related to the inverse exponential of temperature. Dislocation velocity observations have been performed for a variety of other materials and generally these trends hold, despite the orders of magnitude difference of dislocation velocity at similar shear stresses between differing materials. Because these dislocation velocities are observed experimentally, they are generally taken to be correct. Therefore, all that remains concerning dislocation velocity is to create a constitutive model that describes the aggregate mean velocity of dislocation populations based on an empirical description of experimental results, a physically-motivated model, or some combination thereof.

Based on the dislocation velocity behavior given shown in Figure 2.6b, Gilman suggested

[1]These figures can be accessed from `http://www.publish.csiro.au/nid/79/issue/6450.htm`

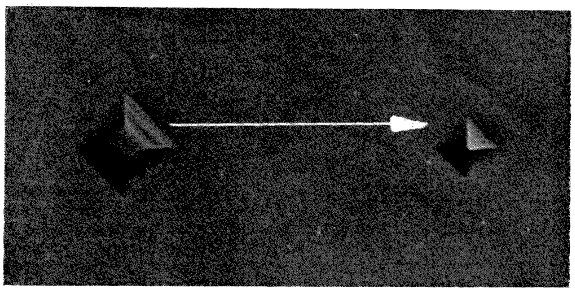

(a) Inferred distance traveled by dislocation during finite duration stress pulse (arrow) revealed by repeated etch pitting.

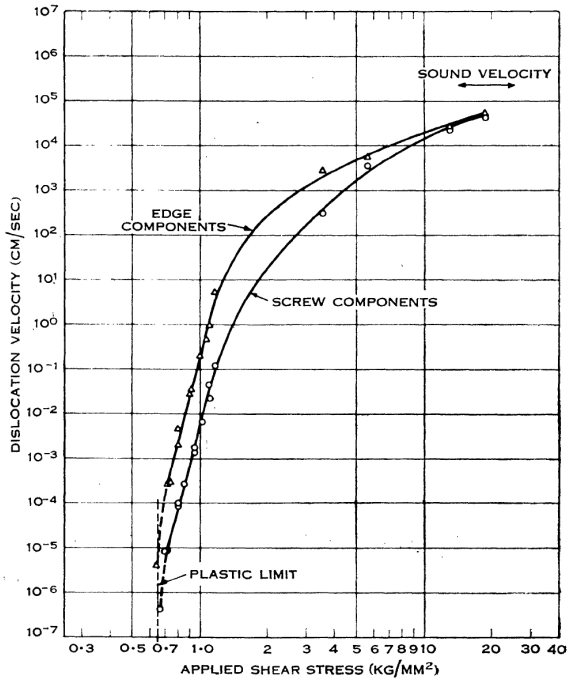

(b) Mean dislocation velocity plotted as a function of applied resolved shear stress based on repeated etch pitting method.

Figure 2.6: Mean velocity of edge and screw dislocations in LiF (a) determined from repeated etch pitting and (b) resultant behavior. Reprinted with permission from [5]. Copyright 1960, CSIRO.

that the mean velocity could be expressed as [5]

$$\bar{v} = v^* \exp\left(-D/\tau\right), \tag{2.117}$$

where D is the characteristic drag stress and v^* is the limiting dislocation velocity, generally taken to be $v^* \to c_s$ where c_s denotes the shear wave speed of gliding dislocations. Gilman noted that the form of this velocity relation satisfies appropriate limits on the shear stress, i.e., $\bar{v} \to 0$ when $\tau \to 0$ and $\bar{v} \to v^*$ when $\tau \to \infty$. This simple model does a reasonable job at capturing the moderate (linear drag) and high (shear wave limited) velocity behavior. At low velocities, however, the model does not capture sharp yielding at the yield point and lacks enough control to vary the velocity transition from the drag-limited to shear wave limited behavior. Also, because the model contains no explicit thermal dependence, D must be altered to capture different behavior at various temperatures. Gilman later modified this model so that it could better capture varying behaviors across different regimes [20], i.e.,

$$\bar{v} = v_S^* \left[1 - \exp\left(-\tau/S\right)\right] + v_D^* \exp\left(-D/\tau\right), \tag{2.118}$$

where v_S^* represents the velocity at low stress levels, S is the coupling stress that acts across the glide plane, and v_D is the mean dislocation velocity at larger stress levels. This modified equation can be used to better capture transitions between regimes that have significantly different behavior.

Johnson and Barker (JB) proposed a modified version of power law dependence to describe the mean velocity of dislocations [7], i.e.,

$$\bar{v} = \bar{v}^* \frac{\delta^n}{1+\delta^n} \qquad \text{such that} \qquad \delta = \frac{\langle \tau - \tau_0 \rangle}{T}, \tag{2.119}$$

where T is a constant with units stress, τ_0 is the back stress, n is a dimensionless constant, and $\langle\rangle$ denote Macauley brackets that have been added to the original formulation. Like the Gilman model, the JB model satisfies the relations that $\bar{v} \to 0$ when $\tau \to 0$ and $\bar{v} \to v^*$ when $\tau \to \infty$. The mean velocity is similar to that predicted by the modified Gilman model, except that the JB model can give an effect of a finite yield point. Like the Gilman model, the JB model has no effect of finite temperature, and therefore must be modified to model behavior at temperatures other than where the model was fit.

Unlike the more empirical models mentioned above, Gillis, Gilman, and Taylor proposed a more physical model where the mean velocity was based on the waiting (t_w) and running (t_r) times between obstacles [90], i.e.,

$$\bar{v} = \frac{\bar{L}}{t_w + t_r}, \tag{2.120}$$

where $\bar{L}$ denotes some mean spacing between obstacles that are overcome. Clifton has used a modified form of this equation [6] to derive waiting and running times in the thermally activated, linear drag, and shear wave velocity limited regimes. Specific forms of equations for t_w, t_r, and $\bar{L}$ are combined to give a single expression for velocity in terms of stress, temperature, and if desired, an internal state variable that characterizes mean free path of obstacles. This model is capable of capturing behavior similar to the JB model, except that it offers more control over the velocity behavior due to its increased number of parameters, especially in the thermally activated regime. Thermal coupling is included naturally in each regime. Because this model has a more physical basis, experiments, simulations, or a combination thereof can be performed to measure or calculate dislocation obstacle interaction times; however, as Clifton has noted, in practice there are often too many unknowns to justify such a complicated formulation. Clifton also noted that the JB model was sufficient to capture most observed behavior.

To compare behavior of the three models, the model by Clifton was fit to typical behavior for FCC metals where all variables besides shear stress are held fixed. Then, parameters for the JB model given by Equation (2.119) and the simple Gilman model given by Equation (2.117) were best fit to the velocity dependence captured by the Clifton model. These resultant normalized velocity versus normalized shear stress profiles are shown in Figure 2.7. Figure 2.7 shows that Gilman model is deficient at modeling distinct changes from the thermally activated to linear drag regimes, although it can effectively reproduce behavior predicted by the Clifton model after $\bar{v}/c_s > 0.4$. Figure 2.7 shows that the form of the JB model allows it to closely reproduce behavior of the Clifton model, except that it possesses sharp transitions at the yield strength. In conclusion, the JB model should be satisfactory to model most experimentally observed dislocation velocity behavior; however,

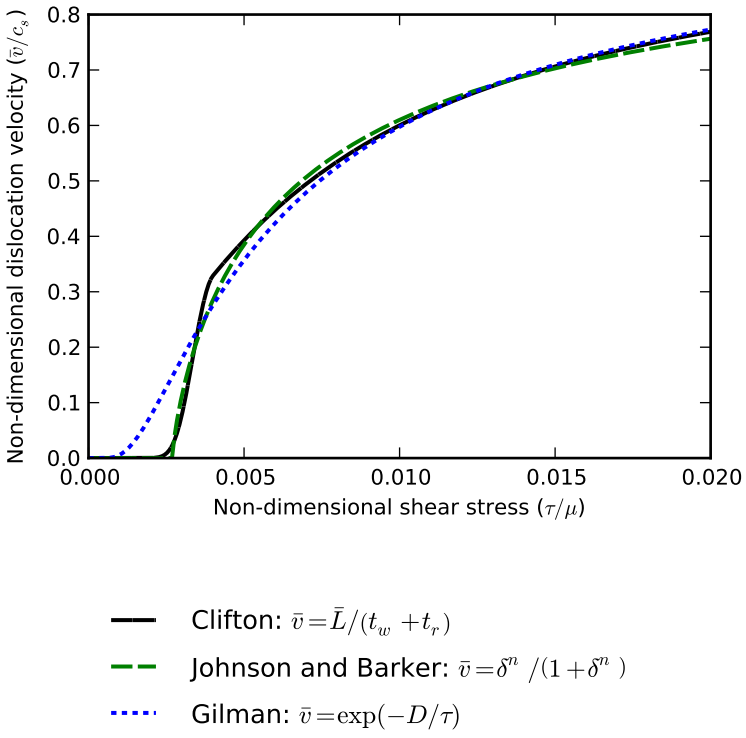

Figure 2.7: Typical shear stress dependence of mean dislocation velocity for FCC metals predicted by Clifton model [6] compared with best fit of Gilman [5] and Johnson and Barker [7] models to this behavior.

if a more physically based model is desired, the Clifton model should be employed.

With respect to macroplasticity, all three velocity equations can ensure generalized normality, such that $\bar{v}^{\alpha}\left(\tau^{\alpha}, N_{m}^{\alpha}, N_{im}^{\alpha}, \theta\right)$.

2.7.2 Dislocation density evolution

As was the case for dislocation velocity calculations, dislocation density evolution was first observed using repeated etch pitting techniques. Johnston and Gilman applied stress pulses to isolated individual dislocations and observed an increase in the dislocation density [8], as shown in Figure 2.8. One particular aspect of the dislocation density evolution shown in Figure 2.8 to note is that the dislocation density increased not only on the specific glide plane on which the original dislocations resided, but also grew on other planes that shared a parallel but offset glide plane. This is evidenced by the widening of the glide band after the applied stress pulse. Because the shear band width increased, Johnston and Gilman attributed multiplication to the double-cross glide mechanism. The double cross-glide multiplication mechanism is illustrated schematically in Figure 2.9. As seen in Figure 2.9, the expanding dislocation encounters an obstacle, cross-slips onto another plane, then expands again on the new plane from the newly created Frank-Read source. The Frank-Read source in this instance is the sessile dislocation segment that is pinned where the cross-slip plane intersects the glide plane. These multiplication sources are represented by red lines in Figure 2.9. This mechanism can be used not only to explain the increased number of dislocations during multiplication, but also the observed glide band widening seen in Figure 2.8. Although the double cross glide mechanism is not operative in all metals deformed at high rates (e.g. low SFE FCC metals or lower symmetry crystals), the form of the evolution equations used to describe double-cross glide can be used to notionally capture other multiplication mechanisms such as multiplication from distributed Frank-Read sources, single-armed Frank-Read sources, regenerative climb, or other mechanisms that may be operative [9].

Johnston and Gilman essentially proposed two different relations to model the evolving dislocation density [88]. In both of these relations, all dislocations are assumed to be mobile.

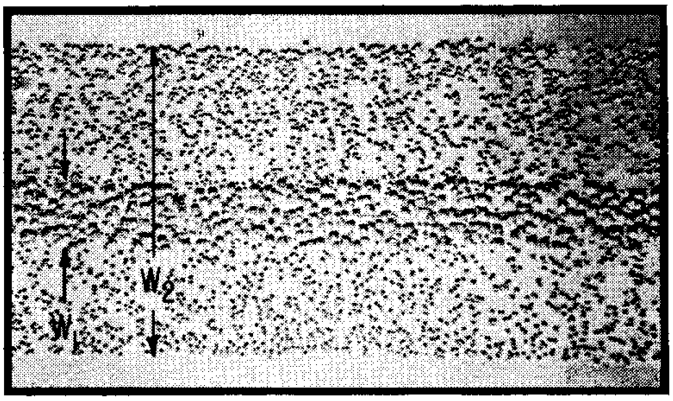

(a) Glide band with a width of W_1 before an applied stress pulse and a width of W_2 after an applied stress pulse.

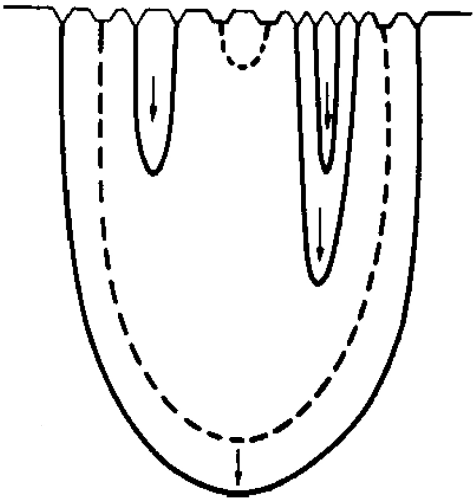

(b) Cross section schematic of dislocation expansion due to applied shear stress.

Figure 2.8: Dislocation multiplication (a) revealed by repeated etching and (b) schematic of dislocation expansion due to stress pulse. Reprinted with permission from [8]. Copyright 1960, AIP Publishing LLC.

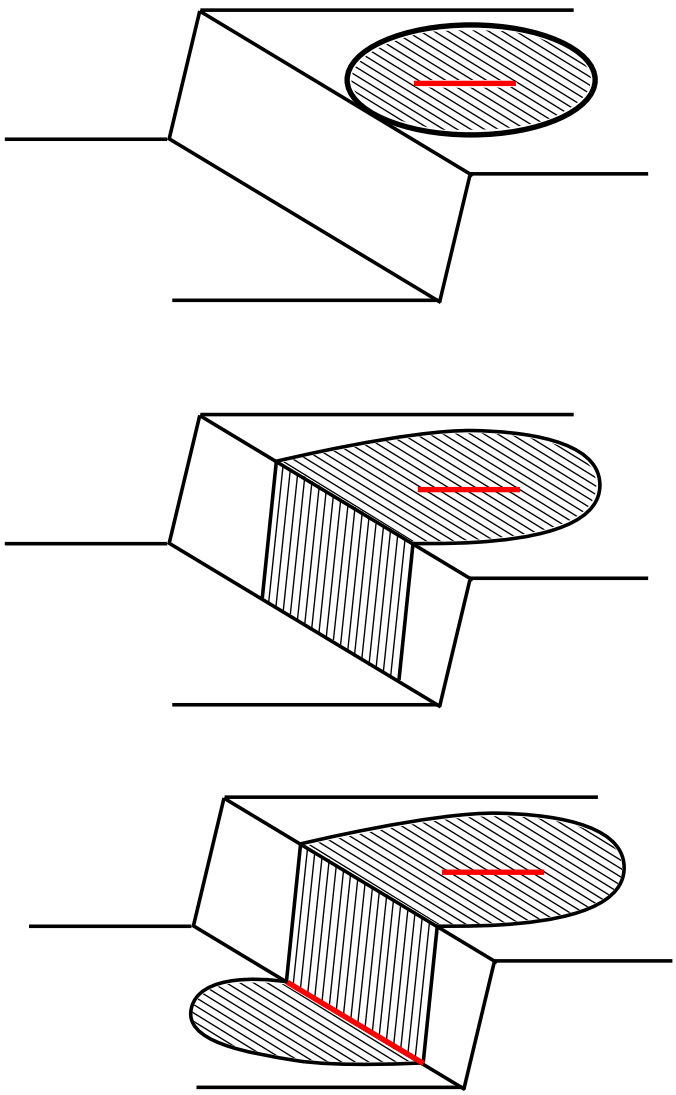

Figure 2.9: Schematic of double cross-glide multiplication mechanism for expanding dislocation loop. Figure based on image in [9].

First, they showed that the dislocation multiplication rate should be proportional to the dislocation density and velocity, i.e.,

$$\dot{N}_m = \dot{N}_{mult} = m\bar{v}N_m, \tag{2.121}$$

where m is termed the breeding rate. Using this formulation, the total dislocation density can be integrated with some simplifying assumptions to get a linear dependence of dislocation density on effective plastic strain, i.e., $N_m = N_{m0} + m\epsilon^p_{eff}/b$ [20]. Although this simple model is useful, it clearly allows the dislocation density to grow without bound, which is not what is observed experimentally. Johnston and Gilman modified the simple model so that the dislocation density saturates after some value, i.e.,

$$\dot{N}_m = \alpha N_m - \beta N_m^2, \tag{2.122}$$

where α is a multiplication coefficient and β is an attrition coefficient that accounts for dislocation annihilation. This relation can be recast in more conventional notation as $\dot{N}_m = \dot{N}_{mult} - \dot{N}_{ann}$. Both of these relations fit the form required by Equation (2.111) to ensure generalized normality. Although the above equations can be used to describe steady state dislocation motion, they do not sufficiently model increased strain hardening with increased dislocation accumulation. Specifically, the second models predicts that strain hardening saturates as the saturation dislocation density is approached, which is not observed experimentally.

Gilman later modified the model given by Equation (2.122) by introducing a notion of the fraction of dislocations that are mobile, i.e., $N_m = fN_{tot}$ [91]. Equations governing the evolution of dislocation density were created to admit the following experimentally observed trends: the total dislocation density increases linearly with accumulated plastic strain ($N_{tot} = N_{tot,0} + M\gamma$); the fraction of dislocations that are mobile decreases as the number of dislocations in the material increases because there are more dislocations that can immobilize them ($\dot{f} \propto -\dot{N}_{tot}$); and the change in the number of mobile dislocations must be proportional to the number of mobile dislocations because dislocations must be mobile to interact with other dislocations and become immobilized ($\dot{f} \propto f$). The incremental form

of f that satisfies these equations is

$$\dot{f} = -\phi f \dot{\gamma}, \tag{2.123}$$

where ϕ is a constant. This equation can be integrated by assuming proportional loading to give $f = \exp(-\phi\gamma)$. Therefore, the expression for strain rate can be written purely in terms of accumulated strain, i.e.,

$$\dot{\gamma} = (N_{tot,0} + M\gamma) \exp(-\phi\gamma)\, b\bar{v}. \tag{2.124}$$

Although the above expression cannot be expressed in terms of ISV theory, it is a desirable function to describe plastic strain rate effects because without explicitly tracking the dislocation density, the density of mobile and immobile dislocations can be expressed solely in terms of the accumulated plastic strain. Typical behavior for N_m, f, and N_{tot} given by Equation (2.124) is plotted as a function of plastic strain in [20]. Specifying a form of f and N_{tot} in terms of γ is equivalent to specifying constitutive relations for N_{mult}, N_{trap} and N_{ann} used to describe the mobile and immobile dislocation density evolution in terms of plastic strain.

In a series of papers Johnson, Jones, and other coworkers calculated plastic wave profiles and elastic precursor decay based on Equations (2.124) and (2.119) (or some close variation) and compared these results with experimental plastic wave profiles and precursor decay data found for a range of materials [7, 92, 22]. In all of their calculations, wave profiles and precursor decay data could be matched only if the initial dislocation density was set to $10^{13} - 10^{14}$ m^{-2}, which is approximately 3 orders of magnitude higher than what is experimentally observed in annealed specimens. Because dislocation velocity profiles are assumed to be reasonably correct, as they are explicitly observed, Gupta, Duvall and Fowles suggested an alternative mechanism must be responsible for additional dislocation generation. In their work, they added a stress-based heterogeneous nucleation component to Equation (2.121) such that [93]

$$\dot{N}_m = \dot{N}_{mult} + \dot{N}_{het} = n\bar{v}N_m + \bar{L}n(\tau)\,\dot{\tau}, \tag{2.125}$$

where $\bar{L}$ is the mean length of a dislocation loop created at each site and $n(\tau)$ is a distribution that describes the number of nucleation sites per unit volume that are activated by

the shear stress. In their work, $\dot{N}_{het}$ was found to be the dominant factor governing precursor attenuation and should be largely sensitive to initial material purity. By including $\dot{N}_{het}$, the initial dislocation density was able to be reduced to values more consistent with what is observed experimentally. Although their analysis specifically used $\dot{N}_{het}$ to model stress concentrations caused by defects, it can be used to model any experimentally observed heterogeneous dislocation nucleation source. Through extremely detailed analysis that minimized surface preparation and loading effects, Meir and Clifton [94] showed that even when surface and impurity effects were removed in LiF single crystals ($N_{m0} \approx 10^8$ m^{-2}), precursor attenuation observed experimentally could only be captured if heterogeneous nucleation at subgrain boundaries was included. Therefore, due to differences in computed and observed wave profiles as well as the associated elastic precursor attenuation, it is assumed that $\dot{N}_{het}$ is operative even in high purity single crystals.

For the case of multiplication, annihilation, immobilization (described up to this point by specifying $\dot{f}$), and heterogeneous nucleation, the shearing rate given in Equation (2.108) is primarily affected by the evolution of N_m and the stress dependence of $\bar{v}$. At stresses that approach a significant fraction of the theoretical strength of the material, however, the shearing rate may be dominated by glide associated with the creation of dislocation loops instead of their subsequent glide. Molecular dynamics simulations of homogeneous dislocation nucleation suggest that homogeneous nucleation occurs at shear stresses that approach the theoretical strength of the material and the homogeneous nucleation rate depends on the resolved shear stress, strain rate, temperature, and may also depend on other out of plane stresses [95, 96, 97]. In shock experiments at strain rates greater than approximately 10^6 s^{-1}, a rapid increase in strength with respect to strain rate has been attributed to homogeneous dislocation nucleation [98]. For the simplified case of a material undergoing shear only due to the slip that occurs during homogeneous dislocation generation (e.g. where glide due to mobile dislocations is negligible) the shearing rate may be expressed as

$$\dot{\gamma} = \dot{N}_{gen}\left(N_{gen}, \boldsymbol{\sigma}, \theta\right) \bar{x}_{gen}\left(N_{gen}, \boldsymbol{\sigma}, \theta\right) b. \tag{2.126}$$

Because homogeneous nucleation occurs rapidly, it has not been directly observed in high

strain rate experiments. Therefore, functional forms of Equation (2.126) are derived either from empirical fits to direct numerical simulation of homogeneous nucleation at high rates or physics-based models of nucleation from small activation volumes.

The forms of both heterogeneous and homogeneous nucleation equations given by Equations (2.125) and (2.126), respectively, are not consistent with generalized normality as they violate the potential form of the shearing rate given by Equation (2.114) by including terms that contain the rate of the shear stress and dislocation density. Physically, however, the nucleation of dislocations may be better approximated as a critical type of process rather than an associative process. In particular, once dislocations are generated, their eventual glide under such large shear stresses may not depend directly on the shear stress responsible for dislocation nucleation, but rather on the fact that the dislocations were nucleated in the first place. In the case of homogeneous nucleation, for example, once the large shear stresses required to activate homogeneous nucleation are reached, the material state may change rapidly or create instabilities with respect to relatively small increments in applied shear stress, which suggests that this nucleation is a critical type of process.

2.7.3 Discussion

Unlike dynamic strength models, dislocation-based models can be more rigorously verified experimentally because elements of dislocation activity that contribute to the viscoplastic shearing rate can be observed. Specifically, it is possible to infer the mean velocity of isolated dislocations as a function of shear stress for varying temperatures, purity, or preprocessing effects based on repeated etch-pit measurements. Because dislocations density is a physical, measurable internal state variable, comparisons can be made between model predictions and experimental results.

Although dislocation densities can be measured experimentally before and after deformation, their evolution as well as the parameters that govern them are generally determined empirically based on experimentally observed wave profiles. In practice, portions of the model are taken as known (e.g. functional form of dislocation velocity and physically-based constants) and other parameters are determined by performing a best fit to experimental

data. Because dislocation-based models are significantly more complicated to implement and understand than conventional dynamic strength based models, they are often less widely used than these models. However, dislocation-based models can be used more naturally to describe the evolution of the material state at high rates and can readily incorporate effects of pre-processing and material purity. In particular, as time resolved, high-resolution TEM and multiscale modeling techniques rapidly evolve in the coming decade, this class of model is expected to become much more widely considered and applied. Although it is more complicated, it contains the details and flexibility to incorporate experimental and computational observations of dislocation activity as more detailed observations become available.

2.8 Discussion

In this chapter, many existing theories that addressed high strain rate deformation were framed in terms of a single theory of thermoelastic-viscoplastic deformation of materials based on developments in the following sections:

- In Section 2.2 the theory for thermoelastic-viscoplastic materials undergoing arbitrary deformation histories is developed.
- In Section 2.3 it is shown that the fluid theory often used to describe high strain rate and plate impact experiments is equivalent to thermoelastic-viscoplastic theory under a set of simplifying assumptions.
- In Section 2.4 it is shown that equations of state generally used to describe fluid response fit within the context of thermoelasticity by applying simplifying assumptions to the functional form of the free energy (e.g. dependence only on volume, separation of thermal and mechanical effects).
- In Section 2.5 the general theory for viscoplastic materials is developed and presented as an extension to the classical theory of plasticity. Simplifying functional forms and consequences of forms of evolution equations are discussed.

- In Sections 2.6 and 2.7 existing constitutive models often used to describe the viscoplastic response of materials subjected to high strain rates are framed within viscoplasticity theory presented in Section 2.5. Distinct advantages and limitations of each theory are addressed.

In Sections 2.3 and 2.4, it was shown that existing theories used to address the equation of state (in this work represented by $\Psi\left(\mathbf{F}^E, \theta\right)$) generally do so under simplifying assumptions of an assumed material symmetry. The isotropic theory of thermoelasticity has been used in previous works to describe the isotropic response of annealed polycrystalline materials; however, to describe anisotropic material response the full anisotropic thermoelastic formulation given by Equation (2.81) is required. Although existing equations of state such as the Mie-Grüneisen and Murghahan do not address anisotropic deformation, these equations are based on fundamental physical or empirical descriptions of known behavior, and should be viewed as limiting cases for anisotropic theories as anisotropic effects become negligible.

Existing theories used to address viscoplastic deformation and their associated strengths and weaknesses were expanded upon in Sections 2.6 and 2.7. Of the dynamic strength models presented, all but the MTS model characterized the evolving structure of the material using a path-independent "equation of state" instead of internal state variables, which may constitute a tenuous assumption in many applications. A conclusion that can be made between strength-based and dislocation-based models is that although both formulations are capable of giving nearly equivalent responses, dislocation-based theories are advantageous because they use more physical state variables; therefore, aspects of dislocation glide, generation, and evolution can be measured experimentally. Strength-based models, on the other hand, can only be compared with experiments based on whether macroscopic behavior matches what is experimentally observed. Therefore, to make a microstructurally-sensitive crystal plasticity model, it is concluded that dislocation-based models are preferred, despite that crystal plasticity strength-based models may be able to produce nearly identical macroscopically observed behavior.

In the following Chapter, a thermoelastic-viscoplastic model is developed to address single crystal deformation based on a recent model proposed by Austin and McDowell [35, 36], which utilized isotropic thermoelasticity with a macroscopic, dislocation-based viscoplasticity model. The proposed model is constructed in the context of thermoelasticity without simplifying symmetry assumptions and dislocation-based viscoplasticity resolved for single crystal deformation.

CHAPTER III

SINGLE CRYSTAL THERMOELASTIC-VISCOPLASTIC FORMULATION

3.1 Introduction

In this chapter, a thermoelastic-viscoplastic formulation is developed to model high rate deformation in single crystals. To model single crystal deformation, both the thermoelastic and viscoplastic formulation must only make assumptions concerning symmetry based on crystal symmetry, and not some assumed isotropic response as was done for macroscale models presented in Chapter 2.

The volumetric compression achieved in plate impact and laser-shock experiments can comprise a significant portion of the total deformation. In metals and many other materials, material stiffness has been shown to increase with increasing compression [10]. Accurately capturing this increased stiffness is essential for modeling loading conditions that induce large elastic volumetric compression. To describe thermoelastic deformation in crystals, either the Helmholtz free energy or internal energy can be expanded in terms of strain about the plastically deformed intermediate configuration. In Section 3.2, finite-deformation thermoelastic formulations will be developed for two different strain measures, and their advantages and limitations will be discussed.

The dynamic strength and dislocation-based models used to describe viscoplastic deformation presented in Sections 2.6 and 2.7 were based on macroscopic observations, and were therefore developed in a simplifying isotropic framework. In Section 3.3, a high strain rate viscoplastic model is developed by combining elements of the dislocation-based models with conventional single crystal plasticity models through geometric interpretation of slip system interaction. By doing so, a minimal number of additional unknown parameters are introduced in this formulation.

To properly model the total temperature rise during shock loading, models used to

describe the internal energy contribution of lattice defects are included in Section 3.4. Although these models are viewed with relative uncertainty due to the complicated task of experimentally determining temperature rise at high rates, they are nonetheless helpful in establishing the range of behaviors that can occur based on assumed dislocation interactions.

3.2 Single crystal thermoelasticity

For the material models used to describe thermoelastic-viscoplastic deformation in this section, the material is assumed to obey the decomposition of the deformation gradient given by Equation (2.18). As a simplifying assumption, it is assumed that the free energy (or internal energy) contribution of thermoelasticity can be separated from the free energy contribution of defects captured by internal state variables $\boldsymbol{\alpha}_i$, i.e.,

$$\Psi = \Psi_1\left(\mathbf{F}^E, \theta\right) + \Psi_2\left(\boldsymbol{\alpha}_i\right) \qquad \text{or} \qquad \mathcal{E} = \mathcal{E}_1\left(\mathbf{F}^E, \eta\right) + \mathcal{E}_2\left(\boldsymbol{\alpha}_i\right), \tag{3.1}$$

noting that for this case $\Psi_2\left(\boldsymbol{\alpha}_i\right) = \mathcal{E}_2\left(\boldsymbol{\alpha}_i\right)$. In some cases, it may be desirable to include a temperature-dependent shear modulus to describe the energy contribution of dislocations; however, there are few data to support a specific formulation to model the internal energy of substructure formation [99]. The uncertainty associated with constructing a functional form for the internal energy contribution due to internal state variable evolution is significantly larger than the effect of including a temperature-dependent shear modulus dependence, unless deformation causes the temperature to approach the melting temperature of the material.

Before considering a specific thermoelastic formulation, it is recalled that the free energy (or internal energy) must be objective. Therefore, as was shown in Equation (2.76), an objective strain measure that is a function of $\mathbf{F}^E$ must be adopted. In the following section, two strain measures will be used; the Lagrangian Green strain, which was given previously as

$$\mathbf{E}^E = \frac{1}{2}\left(\left(\mathbf{F}^E\right)^T \cdot \mathbf{F}^E - \mathbf{I}\right), \qquad E^E_{\alpha\beta} = \frac{1}{2}\left(F^E_{i\alpha}F^E_{i\beta} - \delta_{\alpha\beta}\right), \tag{3.2}$$

and the Eulerian material strain, originally proposed in [100], which is given as

$$\mathbf{D}^E = \frac{1}{2}\left(\mathbf{I} - \left(\mathbf{F}^E\right)^{-1} \cdot \left(\mathbf{F}^E\right)^{-T}\right), \qquad D^E_{\alpha\beta} = \frac{1}{2}\left(\delta_{\alpha\beta} - F^{E-1}_{\alpha i}F^{E-1}_{\beta i}\right). \tag{3.3}$$

Because each strain measure introduces geometrically nonlinear terms, they each give significantly different results at large deformation, despite that they are both defined relative to the plastically deformed intermediate configuration. In the following sections, the thermoelastic portion of the free energy (or internal energy) will be used to derive stress and temperature (or entropy) at finite strain using higher order thermoelastic constants. Comparisons are then made between stress predictions at finite strain for the two formulations.

In the derivations that follow, the free energy expansion will be derived in terms of the Green strain, whereas the internal energy expansion will be derived in terms of the Eulerian material strain, i.e.,

$$\Psi = \Psi_1\left(\mathbf{E}^E, \theta\right) + \Psi_2\left(\boldsymbol{\alpha}_i\right), \qquad \mathcal{E} = \mathcal{E}_1\left(\mathbf{D}^E, \eta\right) + \mathcal{E}_2\left(\boldsymbol{\alpha}_i\right). \tag{3.4}$$

3.2.1 Lagrangian thermoelasticity from free energy

As was done in Equation (2.81) for the thermoelastic equation of state, to construct a thermodynamically consistent model, begin by considering an expansion of the thermoelastic portion of the reference free energy *per unit initial volume* due to an elastic Green strain ($\mathbf{E}^E$) and a change in temperature ($\Delta\theta = \theta - \theta_0 = \Delta\theta^E + \Delta\theta^P$) such that

$$\begin{aligned}\Psi_1\left(\mathbf{E}^E, \Delta\theta\right) = {} & \frac{1}{2!}\overline{C}_{\alpha\beta\gamma\delta}E^E_{\alpha\beta}E^E_{\gamma\delta} + \frac{1}{3!}\overline{C}_{\alpha\beta\gamma\delta\kappa\lambda}E^E_{\alpha\beta}E^E_{\gamma\delta}E^E_{\kappa\lambda} \\ & + \frac{1}{4!}\overline{C}_{\alpha\beta\gamma\delta\kappa\lambda\mu\nu}E^E_{\alpha\beta}E^E_{\gamma\delta}E^E_{\kappa\lambda}E^E_{\mu\nu} + f_1\left(\theta\right) \\ & - \overline{\beta}_{\alpha\beta}E^E_{\alpha\beta}\Delta\theta - \frac{1}{2!}\overline{\beta}_{\alpha\beta\gamma\delta}E^E_{\alpha\beta}E^E_{\gamma\delta}\Delta\theta.\end{aligned} \tag{3.5}$$

By definition, the second and higher order isothermal elastic constants for the Lagrangian Green strain are

$$\overline{C}_{\alpha\beta\gamma\delta} = \left.\frac{\partial^2\Psi}{\partial E^E_{\alpha\beta}\partial E^E_{\gamma\delta}}\right|_{\theta=\theta_0,\mathbf{E}^E=\mathbf{0}}, \quad \overline{C}_{\alpha\beta\gamma\delta\kappa\lambda} = \left.\frac{\partial^3\Psi}{\partial E^E_{\alpha\beta}\partial E^E_{\gamma\delta}\partial E^E_{\kappa\lambda}}\right|_{\theta=\theta_0,\mathbf{E}^E=\mathbf{0}}, \ldots \tag{3.6}$$

the thermo-mechanical coupling constants are

$$\overline{\beta}_{\alpha\beta} = -\left.\frac{\partial^2\Psi}{\partial\theta\partial E^E_{\alpha\beta}}\right|_{\theta=\theta_0,\mathbf{E}^E=\mathbf{0}}, \quad \overline{\beta}_{\alpha\beta\gamma\delta} = -\left.\frac{\partial^3\Psi}{\partial\theta\partial E^E_{\alpha\beta}\partial E^E_{\gamma\delta}}\right|_{\theta=\theta_0,\mathbf{E}^E=\mathbf{0}} = -\left.\frac{\partial C_{\alpha\beta\gamma\delta}}{\partial\theta}\right|_{\theta=\theta_0,\mathbf{E}^E=\mathbf{0}}, \tag{3.7}$$

and the form of the ground state thermal free energy is expressed as

$$f_1\left(\theta\right) = -c_\epsilon\theta\ln\left(\frac{\theta}{\theta_0}\right) \quad \text{such that} \quad c_\epsilon = -\left.\left(\theta\frac{\partial^2\psi}{\partial\theta^2}\right)\right|_{\theta=\theta_0,\mathbf{E}^E=\mathbf{0}}. \tag{3.8}$$

In the above definitions an overbar indicates isothermal constants. Special choice of the thermal free energy $f_1(\theta)$ in Equation (3.8) renders the specific heat capacity per unit mass at constant strain (c_ϵ) constant. Therefore, the internal energy varies linearly with respect to change in temperature [45].

The second Piola-Kirchhoff stress $\mathbf{\Sigma}$ is the derivative of the free energy with respect to the elastic Green strain in the intermediate configuration, i.e.,

$$\begin{aligned}\Sigma_{\alpha\beta} = \frac{\partial \Psi}{\partial E^E_{\alpha\beta}} &= \overline{C}_{\alpha\beta\gamma\delta} E^E_{\gamma\delta} + \frac{1}{2!}\overline{C}_{\alpha\beta\gamma\delta\kappa\lambda} E^E_{\gamma\delta} E^E_{\kappa\lambda} + \frac{1}{3!}\overline{C}_{\alpha\beta\gamma\delta\kappa\lambda\mu\nu} E^E_{\gamma\delta} E^E_{\kappa\lambda} E^E_{\mu\nu} \\ &- \overline{\beta}_{\alpha\beta}\Delta\theta - \overline{\beta}_{\alpha\beta\gamma\delta} E^E_{\gamma\delta}\Delta\theta.\end{aligned} \tag{3.9}$$

Similarly, the entropy production per unit reference volume η is the negative derivative of the free energy with respect to temperature, i.e.,

$$\eta = -\frac{\partial \Psi}{\partial \theta} = \overline{\beta}_{\alpha\beta} E^E_{\alpha\beta} + \frac{1}{2}\overline{\beta}_{\alpha\beta\gamma\delta} E^E_{\alpha\beta} E^E_{\gamma\delta} - c_\epsilon \left[\ln\left(\frac{\theta}{\theta_0}\right) + 1\right]. \tag{3.10}$$

Recall that the Cauchy stress can be found in terms of $\mathbf{\Sigma}$, using $\boldsymbol{\sigma} = J^{-1}\mathbf{P}\cdot\mathbf{F}^T = J^{E-1}\cdot \mathbf{F}^E\cdot\mathbf{\Sigma}\cdot(\mathbf{F}^E)^T$, where $J = \det\mathbf{F}$ and $\mathbf{P}$ denotes the first Piola Kirchhoff stress [40].

3.2.2 Eulerian material thermoelasticity from internal energy

Consider the thermoelastic portion of the internal energy *per unit reference volume* where η is the entropy per unit volume. Expanding the thermoelastic portion of the internal energy about a reference state up to fourth order in elastic Eulerian material strain and second order in entropy change ($\Delta\eta = \eta - \eta_0$) gives

$$\begin{aligned}\mathcal{E}_1\left(\mathbf{D}^E, \eta\right) &= \frac{1}{2!}\widehat{C}_{\alpha\beta\gamma\delta} D^E_{\alpha\beta} D^E_{\gamma\delta} + \frac{1}{3!}\widehat{C}_{\alpha\beta\gamma\delta\kappa\lambda} D^E_{\alpha\beta} D^E_{\gamma\delta} D^E_{\kappa\lambda} \\ &+ \frac{1}{4!}\widehat{C}_{\alpha\beta\gamma\delta\kappa\lambda\mu\nu} D^E_{\alpha\beta} D^E_{\gamma\delta} D^E_{\kappa\lambda} D^E_{\mu\nu} \\ &- \theta_0\left[\widehat{\Gamma}_{\alpha\beta} D^E_{\alpha\beta}\Delta\eta + \frac{1}{2!}\widehat{\Gamma}_{\alpha\beta\gamma\delta} D^E_{\alpha\beta} D^E_{\gamma\delta}\Delta\eta + \frac{1}{2!}\frac{\partial \widehat{\Gamma}_{\alpha\beta}}{\partial\eta} D^E_{\alpha\beta}(\Delta\eta)^2 - f_1(\Delta\eta)\right].\end{aligned} \tag{3.11}$$

By definition, the second and higher order isentropic elastic constants for the Eulerian material strain are

$$\widehat{C}_{\alpha\beta\gamma\delta} = \left.\frac{\partial^2 \mathcal{E}}{\partial D^E_{\alpha\beta}\partial D^E_{\gamma\delta}}\right|_{\eta=\eta_0, \mathbf{D}^E=\mathbf{0}}, \quad \widehat{C}_{\alpha\beta\gamma\delta\kappa\lambda} = \left.\frac{\partial^3 \mathcal{E}}{\partial D^E_{\alpha\beta}\partial D^E_{\gamma\delta}\partial D^E_{\kappa\lambda}}\right|_{\eta=\eta_0, \mathbf{D}^E=\mathbf{0}}, \ldots \tag{3.12}$$

the thermo-mechanical coupling constants are

$$\widehat{\Gamma}_{\alpha\beta} = -\frac{1}{\theta_0}\left(\left.\frac{\partial^2 \mathcal{E}}{\partial\eta\partial D^E_{\alpha\beta}}\right|_{\eta=\eta_0,\mathbf{D}^E=\mathbf{0}}\right),$$
$$\widehat{\Gamma}_{\alpha\beta\gamma\delta} = -\frac{1}{\theta_0}\left(\left.\frac{\partial^3 \mathcal{E}}{\partial\eta\partial D^E_{\alpha\beta}\partial D^E_{\gamma\delta}}\right|_{\eta=\eta_0,\mathbf{D}^E=\mathbf{0}}\right) = -\frac{1}{\theta_0}\left(\left.\frac{\partial C_{\alpha\beta\gamma\delta}}{\partial\eta}\right|_{\eta=\eta_0,\mathbf{D}^E=\mathbf{0}}\right), \tag{3.13}$$

and the function $f_1(\Delta\eta)$ can be approximated by Taylor expansion to arbitrary order

$$f_1(\Delta\eta) = \exp\left(\frac{\Delta\eta}{\rho_0 c_\epsilon}\right) - 1 \approx \Delta\eta + \frac{1}{2!}\frac{(\Delta\eta)^2}{\rho_0 c_\epsilon} + \frac{1}{3!}\frac{(\Delta\eta)^3}{(\rho_0 c_\epsilon)^2} + \frac{1}{4!}\frac{(\Delta\eta)^4}{(\rho_0 c_\epsilon)^3} + \dots, \tag{3.14}$$

where c_ϵ is the specific heat capacity per unit mass at constant strain. For simplicity, $f_1(\Delta\eta)$ is expanded only to second order in $\Delta\eta$.

Substituting Equation (3.14) into Equation (3.11), assuming thermoelastic coupling constants do not vary significantly with respect to entropy ($\partial\widehat{\Gamma}_{\alpha\beta}/\partial\eta \approx 0$), and assuming that energy contributions due to fourth order elastic constants are negligible, gives a further simplified form of the thermoelastic internal energy per unit volume, i.e.,

$$\begin{aligned}\mathcal{E}_1\left(\mathbf{D}^E,\eta\right) &= \frac{1}{2}\widehat{C}_{\alpha\beta\gamma\delta}D^E_{\alpha\beta}D^E_{\gamma\delta} + \frac{1}{3!}\widehat{C}_{\alpha\beta\gamma\delta\kappa\lambda}D^E_{\alpha\beta}D^E_{\gamma\delta}D^E_{\kappa\lambda} \\ &+ \frac{1}{4!}\widehat{C}_{\alpha\beta\gamma\delta\kappa\lambda\mu\nu}D^E_{\alpha\beta}D^E_{\gamma\delta}D^E_{\kappa\lambda}D^E_{\mu\nu} \\ &- \theta_0\Delta\eta\left[\widehat{\Gamma}_{\alpha\beta}D^E_{\alpha\beta} + \frac{1}{2}\widehat{\Gamma}_{\alpha\beta\gamma\delta}D^E_{\alpha\beta}D^E_{\gamma\delta} - 1 - \frac{1}{2}\frac{\Delta\eta}{\rho_0 c_\epsilon}\right].\end{aligned} \tag{3.15}$$

For this simplified internal energy, the work conjugate stress $\mathbf{\Pi}$ to the Eulerian material strain is, by definition,

$$\Pi_{\alpha\beta} = \frac{\partial\mathcal{E}}{\partial D^E_{\alpha\beta}} = \widehat{C}_{\alpha\beta\gamma\delta}D^E_{\gamma\delta} + \frac{1}{2}\widehat{C}_{\alpha\beta\gamma\delta\kappa\lambda}D^E_{\gamma\delta}D^E_{\kappa\lambda} - \theta_0\Delta\eta\left[\widehat{\Gamma}_{\alpha\beta} + \widehat{\Gamma}_{\alpha\beta\gamma\delta}D^E_{\gamma\delta}\right] \tag{3.16}$$

and the temperature is

$$\theta = \frac{\partial\mathcal{E}}{\partial\eta} = \theta_0\left[1 + \frac{\Delta\eta}{\rho_0 c_\epsilon} - \widehat{\Gamma}_{\alpha\beta}D^E_{\alpha\beta} - \frac{1}{2}\widehat{\Gamma}_{\alpha\beta\gamma\delta}D^E_{\alpha\beta}D^E_{\gamma\delta}\right]. \tag{3.17}$$

The work conjugate stress for Eulerian material strain is related to the Cauchy stress by $\sigma_{ij} = J^{E-1}F^{E-1}_{\alpha i}F^{E-1}_{\beta j}\Pi_{\alpha\beta}$ where $J^E = \det\mathbf{F}^E$ [34]. Similarly, the first Piola-Kirchhoff stress $\mathbf{P}$ consistent with Truesdell's definition [101] is related to $\mathbf{\Pi}$ by $P_{iJ} = F^{-1}_{Jk}F^{E-1}_{\alpha i}F^{E-1}_{\beta k}\Pi_{\alpha\beta}$ when $J^P = 1$.

3.2.3 Determination of thermoelastic constants for aluminum

Often, thermoelastic constants given in the literature are isentropic constants that correspond to the total Lagrangian Green strain measure. Single crystal thermoelastic and material constants for aluminum are taken from literature and are given in Table 3.1 as well as the references they were obtained from. Although isentropic elastic constants are

Table 3.1: Single crystal thermoelastic and material constants in Voigt notation for aluminum. All elastic constants are total Lagrangian Green strain isentropic constants.

Parameter(s)	Value(s) in Ref	Units	Reference
C_{11}, C_{12}, C_{44}	106.7, 60.4, 28.3	GPa	[102]
C_{111}, C_{112}, C_{123}, C_{144}, C_{166}, C_{456}	-1076, -315, 36, -23, -340, 30	GPa	[102]
C_{1111}, C_{1112}, C_{1122}, C_{1123}	25000, 3000, 3000, 500	GPa	[103]
c_ϵ	866.11	J / (kg $\cdot$ K)	[104]
c_p	902.11	J / (kg $\cdot$ K)	[104]
α	$23.2 \cdot 10^{-6}$	1/K	[105]
ρ_0	2710	kg / m^3	[104]
b	$2.86 \cdot 10^{-4}$	µm	[106]

normally provided in literature, they can be converted to isothermal constants by use of the Maxwell equations [49, 68]. Elastic isentropic constants that correspond to the Lagrangian Green strain given in Table 3.1 have been converted to isothermal constants and are presented alongside thermoelastic constants in Table 3.2. Note that third and fourth order elastic constants were not converted from isentropic to isothermal constants because the change in their relative value due to the formulation type (isentropic versus isothermal) is less than the tolerance associated with the experimental measurement of the higher order constants.

Table 3.2: Single crystal thermoelastic constants in Voigt notation for aluminum, converted to isothermal Lagrangian Green strain formulation.

Parameter(s)	Value(s)	Units
$\overline{C}_{11}$, $\overline{C}_{12}$, $\overline{C}_{44}$	103.5, 57.38, 28.3	GPa
$\overline{\beta}_1$	5.07	MPa / K
$\overline{\beta}_{11}$, $\overline{\beta}_{12}$ $\overline{\beta}_{44}$	35.1, 6.7, 14.5	MPa / K

Elastic isentropic Lagrangian constants given in the literature are converted to Eulerian material constants by expanding the free energy with respect to the deformation gradient

and equating terms of the same order, as in [34]. The isentropic Eulerian material constants are given in Table 3.3. Note that the second order elastic constants and first order Grüneisen constant were unchanged by choice of strain measure. Fourth order elastic constants were not used here as they were not derived from direct experimental observation, but rather from fitting to results of molecular dynamics simulations to ensure stiffness increased with increasing compression, which occurs naturally in the Eulerian material strain formulation [103]. Higher order Grüneisen components are found by assuming $\Gamma_0\rho_0 \approx \Gamma\rho$ and are converted for Eulerian material strain using a similar procedure, where Γ_0 and Γ denote the Grüneisen parameter in the reference and current frames, respectively.

Table 3.3: Single crystal thermoelastic constants in Voigt notation for aluminum converted, to Eulerian material strain constants from Table 3.1.

Parameter(s)	Value(s)	Units
$\widehat{C}_{11}$, $\widehat{C}_{12}$, $\widehat{C}_{44}$	106.7, 60.4, 28.3	GPa
$\widehat{C}_{111}$, $\widehat{C}_{112}$, $\widehat{C}_{123}$, $\widehat{C}_{144}$, $\widehat{C}_{166}$, $\widehat{C}_{456}$	205, -73, 36, 98, -59, 55	GPa
$\widehat{\Gamma}_1$	2.3	none
$\widehat{\Gamma}_{11}$, $\widehat{\Gamma}_{12}$ $\widehat{\Gamma}_{44}$	11.5, 2.3, 0	none

3.2.4 Comparison

During shock compression, a significant fraction of the total deformation is elastic prior to relaxation via plastic deformation. Many experimental and analytical treatments of shock compression either ignore the deviatoric response or idealize it as elastic perfectly-plastic [107]. Therefore, it is useful to understand the capabilities and limitations of the finite deformation, thermoelastic Lagrangian formulation presented in Section 3.2.1 compared with the thermoelastic Eulerian material formulation presented in Section 3.2.2.

In Figure 3.1, the elastic pressure response and bulk modulus of a [100] oriented aluminum single crystal compressed adiabatically is compared to shock Hugoniot data for polycrystalline aluminum. The elastic, adiabatic compression does not include viscoplastic heating effects, and should therefore predict a lower pressure for a given level of deformation compared to the shock Hugoniot data. Accordingly, the bulk modulus based on elastic, adiabatic compression is the isentropic bulk modulus $B_\eta = -V\partial p/\partial V|_\eta$, whereas

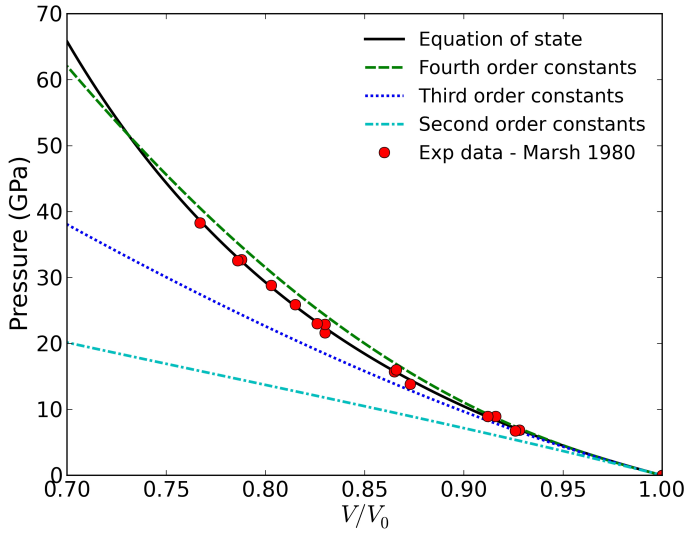

(a)

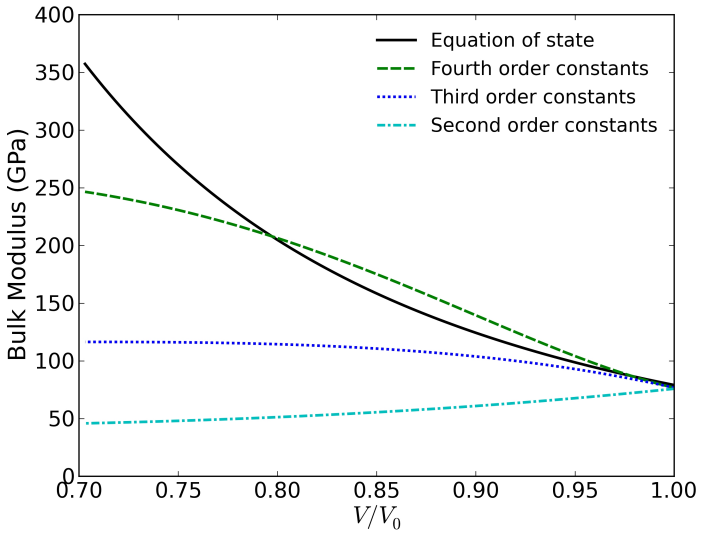

(b)

Figure 3.1: Calculated (a) pressure ($p = -\frac{1}{3}\sigma_{kk}$) and (b) bulk modulus ($B = -V\partial p/\partial V$) for adiabatic compression of a [100] oriented aluminum single crystal using Lagrangian thermoelastic formulation containing elastic constants up to second, third, and fourth order plotted as a function of uniaxial deformation ($\lambda = V/V_0 = J$). These results are compared with experimental shock Hugoniot data and the associated the equation of state relation from Ref [10].

the bulk modulus from the shock data is neither isentropic nor isothermal. Therefore, bulk modulus predictions from shock Hugoniot data should be greater than values from elastic, adiabatic compression at finite volumetric compression. Second-order elasticity predicts the correct initial bulk modulus, but does not contain terms that give a pressure-dependent bulk modulus. Because second-order elasticity does not include a pressure-dependent bulk modulus, the bulk modulus decreases with increased compression due to finite-strain effects and begins to deviate from accurate prediction of the shock response near 3 GPa. The six third-order elastic constants given in [102] were determined by measuring sound velocity derivatives when single crystals are placed in a state of hydrostatic or uniaxial stress [66]. Because these constants are measured close to the reference state, they accurately predict the pressure dependence of the bulk modulus about the reference state and reasonably capture the shock response up to 10 GPa. At higher pressures, however, results deviate substantially from the predicted response due to softening from the total Lagrangian finite strain formulation. Because no data exist for all 11 independent fourth-order constants, the four isotropic fourth-order elastic constants given in [103], which were determined by empirically fitting to single-crystal shock loading data, are used. The fourth-order elastic constants fit the predicted shock response reasonably well up to 50 GPa, as seen in Figure 3.1; however, at these large pressures plastic heating effects may also increase predicted pressures significantly. Because no other experimental data exist for the fourth-order elastic constants of aluminum, these isotropic constants should be regarded as approximate until experimental methods are developed to directly measure these fourth-order elastic constants.

Similar to Figure 3.1, Figure 3.2 shows the pressure response from single crystal adiabatic compression for the thermoelastic Eulerian material strain formulation given by Equation (3.16). A distinct advantage of the Eulerian material strain formulation that can be seen in Figure 3.2 is that even using only second order elastic constants, the formulation has a bulk modulus that increases with compression, which is consistent with experiments. Unlike the total Lagrangian formulation, introducing higher order constants reduces the pressure at similar levels of large compression. The pressure response for third order elastic

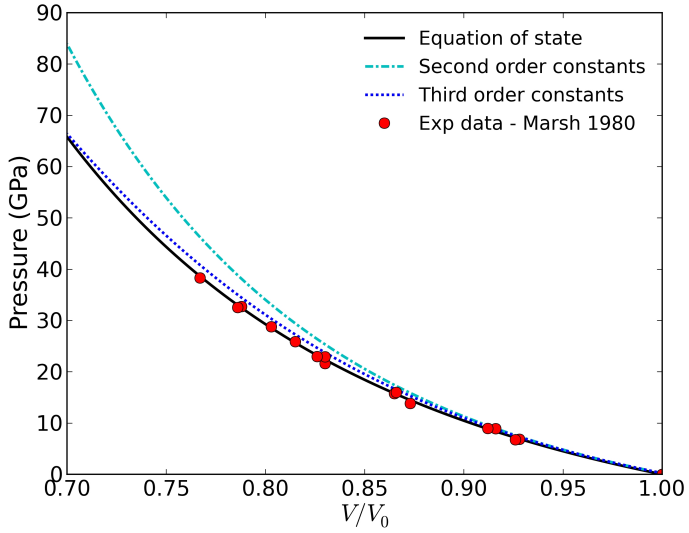

(a)

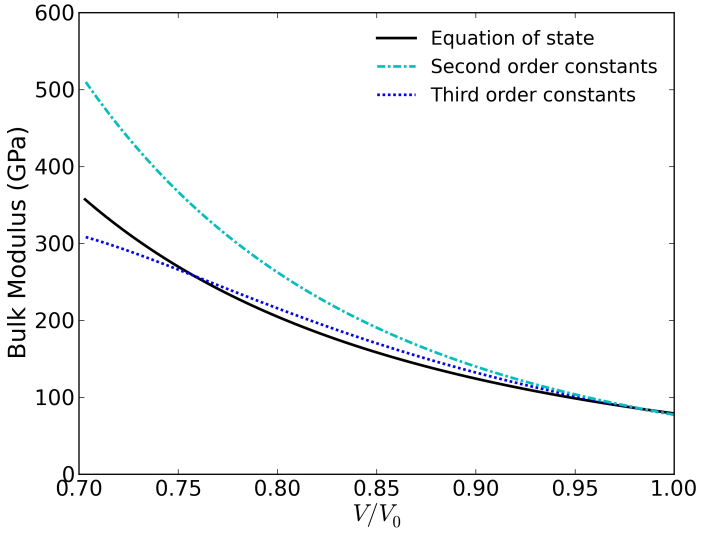

(b)

Figure 3.2: Calculated (a) pressure ($p = -\frac{1}{3}\sigma_{kk}$) and (b) bulk modulus ($B = -V\partial p/\partial V$) for adiabatic compression of a [100] oriented aluminum single crystal using an isentropic Eulerian material formulation containing elastic constants up to second and third order plotted as a function of uniaxial deformation ($\lambda = V/V_0 = J$). These results are compared with experimental shock Hugoniot data and the associated the equation of state relation from Ref [10].

constants shown in Figure 3.1 is similar to the pressure response containing up to fourth order elastic constants shown in Figure 3.2, except that it has a curvature that is more consistent with predictions from the equation of state. Because it requires less higher order terms, these results suggest that the Eulerian material strain formulation converges more rapidly towards physically observed behavior than the total Lagrangian formulation [34]. Note, however, that results from the equation of state include entropy production from the shock front, and should exhibit slightly higher shock pressures than the adiabatic, uniaxial strain solution. Therefore, the Eulerian material strain measure using up to third order elastic constants may be slightly too stiff, but does appears to do a significantly better job than the total Lagrangian formulation.

For over 60 years, it has been known that representation of the large strain elastic response by a series expansion in strain converges towards more physically realistic behavior with fewer terms using an Eulerian strain measure than a Lagrangian strain measure [61]. This can be understood by recognizing that without the use of higher order elastic constants, Lagrangian strains predict decreasing stiffness with increased compression, whereas Eulerian strains predict increasing stiffness with increased compression. However, many plasticity formulations utilize either an infinitesimal strain approximation or a total Lagrangian strain measure. Predictions shown in Figure 3.1 show that for aluminum at pressures up to approximately 15 GPa, a total Lagrangian approach containing third order elastic constants may be a good approximation whereas at pressures up to 40 GPa fourth order elastic constants may be required. However, if modeling higher peak shock pressures, it is suggested that an Eulerian material strain measure be utilized.

3.3 Dislocation-based viscoplastic model

In Sections 2.6 and 2.7, it was shown that although similar, dislocation-based models possess distinct advantages over dynamic strength models. In this section, a viscoplastic model for strength, dislocation velocity, and dislocation evolution rates is developed by extending the isotropic viscoplasticity model developed by Austin and McDowell [35, 36]. In this model, the total dislocation density is partitioned between mobile and immobile populations on

each individual slip system, i.e.,

$$N_{tot}^{\alpha} = N_{m}^{\alpha} + N_{im}^{\alpha}, \tag{3.18}$$

where N_{m}^{α} and N_{im}^{α} are the internal variables used in this model to characterize the evolving state of the microstructure. Because experimental data that quantify dislocation interactions at high rates and pressures are sparse, development of the dislocation-based viscoplastic model in the following sections appeals largely to geometric arguments for quantifying the influence of mobile and immobile dislocations on individual slip systems with parallel and forest dislocation segments on other systems where possible. Therefore, few additional parameters are needed to extend existing macroscopic theories that address dislocation motion and evolution presented in Section 2.7 to include single-crystal effects.

The total velocity gradient $\mathbf{L}$ corresponding to the decomposition of the deformation gradient given in Equation (2.18) is

$$\mathbf{L} = \dot{\mathbf{F}}^{E} \cdot \mathbf{F}^{E-1} + \mathbf{F}^{E} \cdot \dot{\mathbf{F}}^{P} \cdot \mathbf{F}^{P-1} \cdot \mathbf{F}^{E-1} = \mathbf{L}^{E} + \mathbf{F}^{E} \cdot \mathbf{L}_{0}^{P} \cdot \mathbf{F}^{E-1}, \tag{3.19}$$

where $\mathbf{L}_{0}^{P}$ denotes the plastic velocity gradient in the intermediate configuration and $\mathbf{L}^{E}$ denotes the elastic velocity gradient. The plastic velocity gradient in the intermediate configuration is found by combining the crystal-level generalized Orowan equation from Equation (2.108) with the expression for the plastic velocity gradient in terms of the slip rate from Equation (2.109) to give

$$L_{\beta\delta}^{P} = \dot{F}_{\beta J}^{P} F_{J\delta}^{P-1} = \sum_{\alpha=1}^{N} \left(N_{m}^{\alpha} b \bar{v}^{\alpha} s_{\beta}^{\alpha} m_{\delta}^{\alpha} + \dot{N}_{gen}^{\alpha} \bar{x}_{gen}^{\alpha} b s_{\beta}^{\alpha} m_{\delta}^{\alpha} \right). \tag{3.20}$$

For FCC metals, slip is assumed to occur on the twelve slip systems represented by the $\{111\}$ family of slip planes in the $\langle 110 \rangle$ direction.

3.3.1 General overview

The mean velocity of mobile dislocation used in this model is based on the crystal-level version of the macroscopic model for mean dislocation velocity proposed by Gillis, Gilman, and Taylor given in Equation (2.120), i.e.,

$$\bar{v}^{\alpha} = \frac{\bar{L}^{\alpha}}{t_{w}^{\alpha} + t_{r}^{\alpha}}. \tag{3.21}$$

The mobile and immobile dislocation density evolution rates are partitioned according to the specific mechanisms responsible for their evolution, i.e.,

$$\dot{N}_m^\alpha = \chi_{hom}\dot{N}_{hom}^\alpha + \dot{N}_{het}^\alpha + \dot{N}_{mult}^\alpha - \dot{N}_{ann}^\alpha - \dot{N}_{trap}^\alpha \tag{3.22}$$

$$\dot{N}_{im}^\alpha = (1 - \chi_{hom})\,\dot{N}_{hom}^\alpha + \dot{N}_{trap}^\alpha, \tag{3.23}$$

where $\dot{N}_{hom}^\alpha$, $\dot{N}_{het}^\alpha$, $\dot{N}_{mult}^\alpha$, $\dot{N}_{ann}^\alpha$, and $\dot{N}_{trap}^\alpha$ refer to the rates of homogeneous nucleation, heterogeneous nucleation, multiplication, annihilation, and trapping for each slip system α, and χ_{hom} quantifies the fraction of homogeneously nucleated dislocations that remain mobile after they are generated. Partitioning the evolution rates according to these individual mechanisms was first proposed in the model developed by Austin and McDowell [35, 36]. Potential forms of these evolution equations have been discussed in the context of macroscale plasticity in Section 2.7.2.

To include the interaction of dislocations on individual slip systems, dislocations are classified by fraction of the dislocation line that pierces the glide plane. Consider dislocations with a unit slip direction vector and unit slip plane normal vector given by $\mathbf{s}^\alpha$ and $\mathbf{m}^\alpha$, respectively. Ma and Roters [37] derived the density of dislocations whose dislocation line is parallel to slip system α as

$$N_p^\alpha = \sum_{\beta=1}^{N} N_{tot}^\beta \left| \mathbf{m}^\alpha \times \left(\mathbf{m}^\beta \times \mathbf{s}^\beta \right) \right|, \tag{3.24}$$

where N_{tot}^β is total dislocation density on slip system β and $(\times)$ denotes the vector cross product. Similarly, the density of forest dislocations, or dislocations whose dislocation line pierces the glide plane of slip system α is given by

$$N_f^\alpha = \sum_{\beta=1}^{N} N_{tot}^\beta \left| \mathbf{m}^\alpha \cdot \left(\mathbf{m}^\beta \times \mathbf{s}^\beta \right) \right|, \tag{3.25}$$

where $(\cdot)$ denotes the dot product. The interaction of a gliding dislocation passing parallel dislocation segments and cutting forest dislocation segments is shown schematically in Figure 3.3.

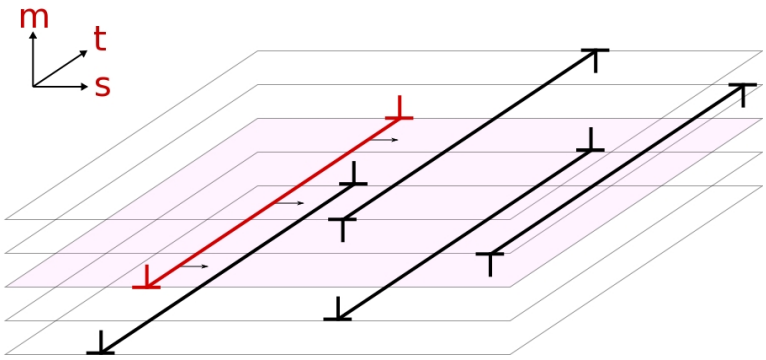

(a) Gliding dislocation (red) passing parallel dislocations.

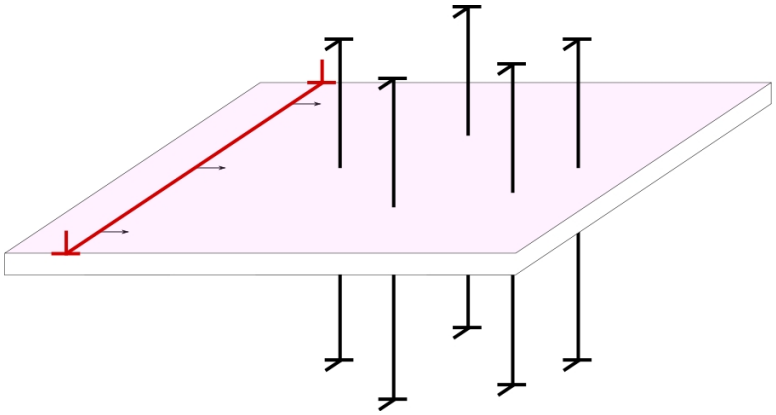

(b) Gliding dislocation (red) cutting piercing forest dislocations.

Figure 3.3: Schematic of gliding mobile dislocation with (a) parallel and (b) forest dislocations, based on Figure 2 in [11]. The triad corresponds to the slip direction vector **s**, slip normal vector **m**, and slip line vector **t** of the gliding mobile dislocation in both images.

3.3.2 Material strength

The resistance to dislocation glide on an individual slip system is governed by the obstacles that impede the motion of gliding dislocations on that system. Although experiments that infer the Stage I and Stage II hardening contribution of dislocations on particular slip systems in single-crystals undergoing quasistatic deformation and the relations based on these experiments are well established [108, 109, 110, 111], it is not clear if the same mechanisms that govern quasistatic dislocation interactions are operative during high strain rate deformation. Therefore, this work uses two simple strength descriptors based on the geometric dislocation resistance provided by dislocations on latent systems: the long range resistance provided by passing parallel dislocations (τ_{pass}) and the short-range resistance required to "cut" a forest dislocation ($\tau_{cut,0}$) [11].

Both of these strength measures can be captured by Taylor hardening relations, e.g.,

$$\tau^{\alpha}_{pass} = \alpha_{pass}\mu^{\alpha}b\sqrt{N^{\alpha}_{p}} \tag{3.26}$$

$$\tau^{\alpha}_{cut,0} = \alpha_{cut}\mu^{\alpha}_{0}b\sqrt{N^{\alpha}_{f}} \tag{3.27}$$

where α_{pass} and α_{cut} are parameters used to characterize the strength contribution of each obstacle, μ^{α} is the shear modulus associated with each slip system [112] based on the updated elastic constants [113], and b is the magnitude of the Burgers vector. The stress required for gliding dislocations to cut forest dislocations is significantly higher than the stress required to bypass dislocations whose dislocation line is parallel to the slip direction, therefore $\alpha_{cut} > \alpha_{pass}$. Note that the slip system shear modulus μ^{α} depends on both temperature and elastic strain based on the elastic constants in the current frame.

The activation enthalpy for dislocation glide can be written in phenomenological form [11] as

$$\Delta G^{\alpha} = g_0\mu^{\alpha}b^3\left\{1-\left(\frac{|\tau^{\alpha}|-\tau^{\alpha}_{pass}}{\tau^{\alpha}_{cut,0}}\right)^{p}\right\}^{q}, \tag{3.28}$$

where g_0 is a dimensionless material constant and the exponents q and p are chosen to represent a statistical distribution of obstacles [83, 114].

It is noted that the strength model developed in this Section bears a close resemblance to the Mechanical Threshold Stress model presented in Section 2.6.5, where in this case the

τ_{pass} corresponds to σ_θ and τ_{cut} correspond to $\hat{\sigma}_a$.

3.3.3 Mean dislocation velocity

As discussed in Section 3.3.1 and given by Equation (3.21), the mean velocity of dislocations is based on the sum of waiting and running times between a statistical mean distance of obstacles [6]. For dislocation motion to initiate, the resolved shear stress on an individual slip system must exceed the long-range stress barrier provided by parallel dislocation segments. When the driving force exceeds this long-range resistance, dislocation motion is further controlled by thermal activation past short-range obstacles such as forest dislocations. After the resolved stress exceeds the combined long-range stress provided by parallel dislocation segments and short-range resistance provided by forest dislocations, dislocations are free to glide between obstacles. The dislocation velocity is then limited by viscous drag and relativistic damping [35, 84].

Once the thermally-activated regime is reached ($\tau^\alpha_{pass} \leq |\tau^\alpha| < \tau^\alpha_{pass}+\tau^\alpha_{cut,0}$), dislocations wait to be thermally activated past obstacles according to some attempt frequency, v_G. The time spent waiting t^α_w at obstacles is then

$$t^\alpha_w = \frac{1}{v_G}\left[\exp\left\{\frac{\Delta G^\alpha}{k\theta}\right\} - 1\right], \tag{3.29}$$

where ΔG^α is the activation enthalpy given in Equation (3.28) and k is the Boltzmann constant. The form of the above equation ensures that $t^\alpha_w \to 0$ when dislocation motion enters the viscous drag and relativistic damping regime ($|\tau^\alpha| > \tau^\alpha_{pass} + \tau^\alpha_{cut,0}$).

The velocity of running dislocations is modeled using a viscous damping equation [6], i.e.,

$$\bar{v}^\alpha_r = \frac{\tau^\alpha_{eff} b}{B^\alpha}, \tag{3.30}$$

where B^α is a damping coefficient and τ^α_{eff} is an effective driving force determined by the glide resistance profile. In this work, the effective driving force is assumed to equal to the resolved shear stress τ^α, as the effect of long-range glide resistance is negligible compared to the drag contribution in the viscous drag regime [6]. Relativistic damping is included through modification of B^α in Equation (3.30) to ensure that $\bar{v}^\alpha_r$ does not exceed the shear

wave speed, c_s^α, i.e.,

$$B^\alpha = \frac{B_0^\alpha}{1 - (\bar{v}_r^\alpha / c_s^\alpha)^2}, \tag{3.31}$$

where $B_0^\alpha = 3k\theta z / 20 c_s^\alpha b^2$ is the temperature-dependent drag coefficient and z is the number of atoms per unit cell [115, 35]. In both the thermally-activated and drag-dominated regimes, it is assumed that the mean free spacing of obstacles is the inverse square root of the piercing forest dislocation density [11], i.e.,

$$\bar{L}^\alpha = 1/\sqrt{N_f^\alpha}. \tag{3.32}$$

Combining Equations (3.21), (3.29), (3.30), and (3.32) yields an expression for the mean dislocation velocity on each slip system, i.e.,

$$\bar{v}^\alpha = \frac{c_s^\alpha h^\alpha}{\left(\exp\left\{\Delta G^\alpha / k\theta\right\} - 1\right)\left(c_s^\alpha h^\alpha \sqrt{N_f^\alpha}/v_G\right) + 1} \operatorname{sgn}(\tau^\alpha) \quad \text{for} \quad |\tau^\alpha| > \tau_{pass}^\alpha, \tag{3.33}$$

where $h^\alpha = \sqrt{(\xi^\alpha)^2 + 1} - \xi^\alpha$ and $\xi^\alpha = B_0^\alpha c_s^\alpha / (2\tau_{eff}^\alpha b)$. The shear wave speed and Burgers vector can be slip-system dependent; however, if slip is assumed to occur on only the $\{111\}$ family of slip planes in the $\langle 110 \rangle$ directions, as in FCC metals, $b = a_0\sqrt{2}/2$ and $c_s^\alpha = c_s = \sqrt{\mu^\alpha / \rho_0}$ for all 12 slip systems [112].

3.3.4 Dislocation evolution rates

While the dislocation velocity describes the rate of plastic deformation provided by existing mobile dislocations, the dislocation evolution rates change the number of mobile dislocations that contribute to plastic deformation, provide plastic deformation directly by sweeping out a dislocated area during the generation, and contribute to glide resistance provided by immobilized dislocations.

Dislocation nucleation is modeled following the treatment in [36]. The total dislocation nucleation rate is the sum of the homogeneous and heterogeneous nucleation rates, where homogeneous nucleation depends on the thermal activation of sub-critical dislocation loops when approaching the theoretical shear strength of the crystal and heterogeneous nucleation accounts for the production of dislocations from a statistical distribution of sources.

Homogeneous nucleation is described using an Arrhenius law, i.e.,

$$\dot{N}^{\alpha}_{hom} = \dot{N}_0 \exp\left\{\frac{-g_{0,hom}\mu^{\alpha}b^3}{k\theta}\left(1 - \frac{|\tau^{\alpha}|}{\tau_{hom,0}}\right)\right\}, \tag{3.34}$$

where $\dot{N}_0$ is the reference homogeneous dislocation nucleation rate, $g_{0,hom}$ is a material constant, and $\tau_{hom,0}$ is the ideal strength of the crystal at 0K. After dislocations are homogeneously nucleated, many are quickly arrested due to interactions with other dislocations; therefore, relatively few remain mobile. This notion is accounted for by specifying χ_{hom} in Equations (3.22) and (3.23). It is assumed that the form of the homogeneous nucleation equation is identical on all slip systems, however, there is evidence that non-Schmid effects can enhance or retard homogeneous nucleation rates [96]. This model for homogeneous nucleation greatly simplifies the form of the general model for homogeneous nucleation given in Equation (2.126) by assuming $\bar{x}_{gen}$ is constant.

The model for heterogeneous nucleation is based on the model developed Gupta given in Equation (2.125) to account for dislocations that are emitted from stress concentrations. The specific model used herein is the single-crystal form of the model used by Austin and McDowell [35] to describe the statistical nucleation from sources that can be described using a more general function than that given in Equation (2.125). As such, the heterogeneous nucleation rate may be written as

$$\dot{N}^{\alpha}_{het} = \alpha_{het} f\left(\tau^{\alpha}\right) |\dot{\tau}^{\alpha}|, \tag{3.35}$$

where $f\left(\tau^{\alpha}\right)$ is a function that describes the spectrum of critical stresses required to activate the sources, α_{het} is material parameter, and $|\dot{\tau}^{\alpha}|$ is the positive stress rate on each slip system given in Equation (4.18). The form of the heterogeneous nucleation relation given in [35, 36] was used to model nucleation from stress concentrators such as grain boundaries and precipitates; however, as discussed in Section 2.7.2 heterogeneous nucleation has been observed [20] and inferred to occur in pure single-crystals [94] from subgrain boundaries, and has been shown computationally to even occur from individual dislocation sources [116]. The probability distribution function (PDF) used to describe heterogeneous dislocation

nucleation sources is given by

$$f\left(\tau^{\alpha}\right)=\frac{m+1}{\left(\tau_{max}-\tau_{min}\right)^{m+1}}\left(\left|\tau^{\alpha}\right|-\tau_{min}\right)^{m}\quad\text{if}\quad\tau_{min}\leq\left|\tau^{\alpha}\right|\leq\tau_{max},\quad 0\quad\text{otherwise,} \tag{3.36}$$

where τ_{min} and τ_{max} define the bounds of the critical stress distribution of heterogeneous nucleation from a statistical defect population and m dictates the shape of the probability distribution function used to describe those sources.

Dislocation multiplication can occur by a variety of mechanisms, for example, double cross glide, internal crossing over, and super-jog formation. Internal crossing over occurs at high dislocation velocities when the two branches of a dislocation bypassing an obstacle intersect due to their large inertia and form a second loop [20]. Super-jog formation occurs when dislocations cut through intersecting forest dislocations, which when cut enough times, forms two single-armed Frank-Read sources [9]. Although the model for dislocation multiplication proposed Gilman given by Equation (2.121) based on double cross-glide appears to be a satisfactory description for modeling macroscale multiplication, to consider the multiplication rates on individual slip systems obstacles to slip on these systems must be considered. Regardless of the specific mechanism, dislocation multiplication can be modeled by considering the probability p_{mult} that a gliding dislocation will successfully interact with a forest dislocation that pierces its glide plane and multiply to form a new dislocation. Because a mobile dislocation on slip system α encounters a linear density of $\sqrt{N_f^{\alpha}}$ forest dislocations during glide, the total dislocation multiplication rate is given by

$$\dot{N}_{mult}^{\alpha}=p_{mult}\sqrt{N_f^{\alpha}}N_m^{\alpha}\left|\bar{v}^{\alpha}\right|. \tag{3.37}$$

Dislocation annihilation occurs when dislocations on the same slip system with opposite sign pass within some critical annihilation distance [117], i.e.,

$$\dot{N}_{ann}^{\alpha}=2\alpha_{ann}b\left(N_m^{\alpha}\right)^2\left|\bar{v}^{\alpha}\right|, \tag{3.38}$$

where α_{ann} is a parameter that quantifies the annihilation rate and the factor of two accounts for the fact that two dislocations are annihilated per annihilation event. The above equation should be viewed as the single-crystal extension of the form used by Johnston and Gilman in Equation (2.122) to describe the saturation of mobile dislocations.

Like dislocation multiplication, dislocation trapping is described in a statistical sense [83] where dislocations are immobilized by obstacles in their glide plane after sweeping out some prescribed area [35]. The mean free path of statistical trapping is Λ^α, which is the harmonic mean of the individual mean free paths of obstacles impeding dislocation motion. For general polycrystalline metals this may include such obstacles as precipitates, grain boundaries, and forest dislocations. However, for pure crystals forest dislocations are the primary effective short range obstacles that immobilize mobile dislocation segments. Therefore, the trapping rate is

$$\dot{N}^\alpha_{trap} = \alpha_{dis} N^\alpha_m \left|\bar{v}^\alpha\right| \sqrt{N^\alpha_f}, \tag{3.39}$$

where α_{dis} is an adjustable parameter that serves as the proportionality constant between the trapping rate and the mean spacing of forest dislocations. Specifying a dislocation trapping equation is similar to specifying an evolution equation for the fraction of dislocations that are mobile, such as that proposed by Gilman given in Equation (2.123).

Although all dislocation generation mechanisms contribute to the shearing rate given by the second term on the right hand side of Equation (3.20), the relative contribution to the shearing rate during generation compared to the contribution to the shearing rate by glide only becomes appreciable when homogeneous nucleation occurs [36]. Therefore it is assumed that only homogeneous nucleation rate $\dot{N}_{hom}$ contributes to plastic deformation rate due to the generation of dislocations, i.e.,

$$\dot{N}^\alpha_{gen}\bar{x}^\alpha_{gen} = \dot{N}^\alpha_{hom}\bar{x}^\alpha_{hom} + \underbrace{\dot{N}^\alpha_{het}\bar{x}^\alpha_{het} + \dot{N}^\alpha_{mult}\bar{x}^\alpha_{mult}}_{\approx 0}. \tag{3.40}$$

Although the generation of dislocations during heterogeneous nucleation and multiplication does not directly contribute to the second term of Equation (3.20), they still contribute to the mobile dislocation evolution rate given by Equation (3.22) and therefore contribute to the plastic velocity gradient by altering N^α_m in Equation (3.20).

Note that from plugging Equations (3.33) and (4.10) into Equation (3.20), the immobile dislocation density contributes to the strength and to microstructure evolution, which in turn affect the dislocation evolution rates and mean velocity, but does not directly enter the equation for the plastic velocity gradient.

3.3.5 Discussion

The proposed dislocation-based single crystal viscoplastic model builds upon high rate dislocation-based models that have been used to model macroscopic high strain rate behavior over the last 60 years. In particular, it is able to span many orders of magnitude in strain rate by considering the aggregate contribution of each individual dislocation mechanism and how it contributes to the shearing rate on each individual slip system. A novel aspect of this formulation is that it merges a geometric description of dislocation interactions on individual slip systems based on quasistatic simulations and experiments with directly observed or physically motivated behavior of dislocation motion and evolution at high rates without introducing a large number of terms that are devoid of some physical description.

3.4 Internal energy of substructure

Applying the form of the free energy for the thermoelastic-viscoplastic constitutive model developed in this chapter by Equation (3.1) to the general formulation for the Taylor-Quinney factor given by Equation (2.28) gives a simplified expression for the Taylor-Quinney factor in terms of the plastic work and internal state variable evolution, i.e.,

$$\beta = 1 - \frac{1}{\dot{W}^P} \frac{\partial \Psi_2}{\partial \boldsymbol{\alpha}_i} * \dot{\boldsymbol{\alpha}}_i. \tag{3.41}$$

The simplest functional form for $\Psi_2(\boldsymbol{\alpha}_i)$, which is often employed in viscoplastic formulations, is to assume that the energy contribution due to state variables is negligible $\Psi_2(\boldsymbol{\alpha}_i) = 0$, which gives $\beta = 1$. Setting $\beta = 1$ is equivalent to assuming all plastic deformation is dissipated as heat. As pointed out in Section 2.2.2, a more realistic yet simple formulation is to assume β is a constant, which circumvents specification of $\Psi_2(\boldsymbol{\alpha}_i)$ altogether. Although in many cases setting β equal to a constant between 0.9 and 1 is a reasonable approach for describing the thermodynamic contribution of defects, Split Hopkinson bar experiments performed at strain rates of $\dot{\epsilon} \approx 10^3$ s^{-1} suggest that for metals β is a complex nonlinear function [118, 119]. Because plastic temperature rise itself is not a measurable quantity, but rather a quantity that must be inferred in the context of a framework that employs certain simplifying assumptions concerning temperature rise, it is difficult to

construct functions for $\Psi_2(\boldsymbol{\alpha}_i)$ based on direct experimental observations. Therefore, some forms of $\Psi_2(\boldsymbol{\alpha}_i)$ are considered within the context of their theoretical construction and their associated implications on macroscopic behavior.

Schreyer and Maudlin proposed both an uncoupled as well as a coupled thermoelastic-viscoplastic model to account for the internal energy contribution of defects [120]. Because their model expresses the dislocation density as a unique linear function of effective plastic strain, their model is equivalent to proposing a relation between the internal energy of defects and effective plastic strain, i.e.,

$$\Psi_2(\boldsymbol{\alpha}_i) = \Psi_2\left(\epsilon^p_{\mathit{eff}}\right) = \alpha_1 \tanh(c\epsilon^p_{\mathit{eff}}) + \alpha_2 \tanh^3(c\epsilon^p_{\mathit{eff}}), \tag{3.42}$$

where α_1, α_2, and c are constants. The above expression has been shown to have the flexibility to describe measurements of β based on Kolsky bar experiments [118]; however, this formulation cannot include path-dependence and is devoid of a micromechanics-based description of lattice defect energy. To make a connection with more physical aspects of energy storage, explicit consideration of lattice defect energy is necessary.

Consider an isolated edge or screw dislocation in an isotropic, linear elastic medium. Assume the total energy per unit dislocation length may be partitioned between a linear elastic and core energy, i.e., $E_{tot} = E_{elast} + E_{core}$. Let E_{core} represent all of the components of the energy that are not considered in E_{elast}, such as the dislocation core and dislocation line energy. Then, then E_{elast} may be written as

$$E_{elast} = \frac{\mu_0 b^2}{4\pi K} \ln\left(\frac{R}{r_0}\right), \tag{3.43}$$

where $K = 1$ for screw dislocations and $K = 1 - \nu$ for edge dislocations, R is a cutoff radius from the dislocation core in which long range stress fields contribute to the energy, and r_0 is the radius of the dislocation core (generally taken to be approximately b) [9]. Equation (3.43) can be used describe a large range of behaviors by noting that R can be a complex function of the substructure configuration, where it is noted that substructure development may have a significant effect on the the resultant stress screening behavior between dislocations.

A simple form of Equation (3.43) is constructed by assuming that for a given material, dislocations have an intrinsic internal energy that does not differ based on the substructure evolution nor the dislocation type. In this very simplified case, Equation (3.43) is re-written as

$$E_{elast} = \alpha_1 \mu_0 b^2, \tag{3.44}$$

where α_1 is a constant that is generally assumed to vary between 0.5 and 1.0 [9]. Physically, this simple form for the defect energy does not imply that the long range stress field of dislocations is not screened; rather, it implies that the screening distance does not change with respect to the evolving dislocation density. In the limiting case that the long range stress field is not screened by other dislocations, R is equivalent to the sample size, denoted L_s, and $\alpha_1 = \ln(L_s/b_0)/5\pi$ (assuming $r_0 \approx b_0$ and $K \approx 1.25$). Nabarro [121] proposed that if dislocations approximately screen long range stresses in a uniform manner, the cutoff radius R may be expressed as inversely proportional to the square root of dislocation density, i.e., $R \propto 1/\sqrt{N_{tot}}$. If no distinction is made between edge and screw dislocations, this relation may be expressed as

$$E_{elast} = \alpha_1 \mu_0 b^2 \ln\left(\frac{\alpha_2}{\sqrt{N_{tot}}}\right), \tag{3.45}$$

where $N_{tot} = \sum_\alpha N_{tot}^\alpha$ and α_1 as well as α_2 are constants. The constant α_2 is used as a kind of saturation dislocation density, where the internal energy will begin to decrease with an increasing number of dislocations when $N_{tot} > \alpha_2^2$. One complication with the above equation is that it assumes dislocations are evenly distributed throughout the specimen. This assumption may be appropriate at large strains or high strain rates; however, TEM of single crystals and polycrystals reveals that dislocation substructure forms with relatively dislocation-free zones separated from dislocation-dense zones. A comparison of the internal energy due to defects ($\Psi_2 = N_{tot} E_{elast}$) based on the two relations given by Equations (3.43)-(3.45) are compared in Figure 3.4, where constants were chosen so that at $N_{tot} = 1\mu\text{m}^{-2}$ the normalized energy density $\hat{\Psi}_2 = \Psi_2/(\mu_0 b^2) = 1$. Figure 3.4 shows that the model proposed by Nabarro can be used to incorporate decreasing energy per unit dislocation length dislocation with increasing dislocation density, although an implicit assumption is that self-similar substructure refinement and long range stress screening occurs throughout

the entire deformation process, which may be not constitute an appropriate assumption for many processes. Figure 3.4 also shows that Equation (3.44) can be used in practice to fit the mean behavior of the material throughout the deformation history, e.g. it may underestimate the internal energy contribution for relatively low dislocation densities and may overestimate the internal energy contribution at relatively high dislocation levels.

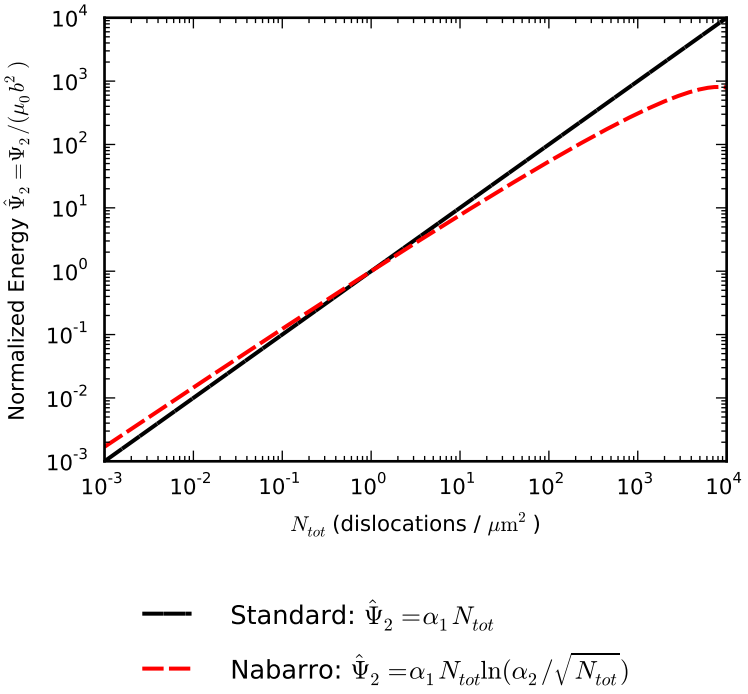

Figure 3.4: Comparison of normalized internal energy of dislocation relations plotted as a function of total dislocation density. For the standard model $\alpha_1 = 1$ whereas for the Nabarro model $\alpha_1 = 0.2$ and $\alpha_2 = e^5$ μm^{-1}.

Other potential forms of the internal energy of defects may partition the internal energy based on the type of dislocation. Generally, it is observed that dislocations are trapped into low energy dislocations structures (LEDS) consisting of dislocation dipoles, tripoles, or more complicated low energy structures [122]. On the other hand, mobile dislocations glide freely and may not have their long range stress fields shielded. Therefore, it seems reasonable to assume that the total energy could be partitioned into mobile and immobile components, taking a form similar to Equation (3.44) such that

$$\Psi_2(\boldsymbol{\alpha}_i) = N_{m,tot} E_{elast,m} + N_{im,tot} E_{elast,im} = \alpha_m \mu_0 b^2 N_{m,tot} + \alpha_{im} \mu_0 b^2 N_{im,tot}, \qquad (3.46)$$

where it is assumed that $\alpha_m > \alpha_{im}$. Arsenlis and Parks proposed a crystal plasticity formulation in which edge and screw components of the dislocation density were considered the primary state variables [123]. Using elasticity theory, the internal energy of not only isolated edge and screw dislocations can be calculated, but approximate energies can be estimated for more complicated structures such as dislocation loops and different types of disclinations [124].

It is clear that even in the relatively restricted framework where dislocation energy is uncoupled from thermoelasticity, rather complex formulations can be constructed to consider the internal energy contribution of dislocations; however, in the context of studying plate impact problems this contribution comprises a relatively small modification to the behavior of the viscoplastic model given in Section 3.3. In the present formulation, the internal energy of defects is only weakly coupled to the viscoplastic model by reducing the portion of plastic work that is converted into heat. More complex formulations that consider the direct coupling between internal energy of defects and the resultant defect structure may significantly depend on the form of $\Psi_2(\boldsymbol{\alpha}_i)$. There is sparse experimental data to justify the use of complex forms of $\Psi_2(\boldsymbol{\alpha}_i)$, although in the future lower length scale simulations may be used to inform potential forms of this relation. Also, although strain localization behavior is not examined in this text, internal energy of substructure may have a significant influence on resultant localization behavior during severe plastic deformation even for the weakly coupled viscoplastic formulation considered in this work.

3.5 Discussion

In this Chapter, a complete thermoelastic-viscoplastic formulation was developed to model high strain rate single crystal deformation at finite compression. It was shown in Section 3.2 that both Lagrangian Green strain and Eulerian material strain measures can be used to model the thermoelastic response if a sufficient number of higher order elastic constants are used; however, at large compression the Eulerian material strain may better describe the thermoelastic response. A dislocation-based viscoplastic model was developed in Section 3.3 by combining existing macroscopic equations for dislocation motion and evolution presented

in Section 2.7 (and utilized in the HSRVP model by Austin and McDowell [35, 36]) with geometric descriptions of dislocation interactions on individual slip systems. Potential forms of $\Psi_2(\boldsymbol{\alpha}_i)$ were proposed in Section 3.4 to include the contribution of dislocations to the internal energy; however, these forms should generally be used qualitatively to understand the influence of internal energy on the plastic temperature rise, as there is sparse temporally resolved temperature rise data that can be compared to. In Chapters 4 and 5, the thermoelastic-viscoplastic single crystal formulation developed in this Chapter will be used to study and understand the shock response of single crystals and polycrystals.

CHAPTER IV

PLANE WAVE SIMULATIONS

Despite the large amount of research that has been performed to quantify the high strain rate response of aluminum, few studies have addressed effects of crystal orientation and subsequent crystal-level microstructure evolution on the high strain rate response. To study orientation effects in single crystal aluminum a novel plane wave formulation is developed so that materials undergoing anisotropic, thermoelastic-viscoplastic deformation can be modeled in a thermodynamically consistent framework. Steady propagating shock waves are simulated for [100], [110], and [111] oriented single crystals and are compared with existing experimental wave profile and strength measurements as well as observed scaling laws. Influences of initial orientation and peak pressure ranging from $0 - 30$ GPa are quantified. Results indicate that orientation plays a significant role in dictating the high rate response of both the wave profile and the resultant microstructure evolution of aluminum. It is shown that the plane wave formulation can be used to evaluate microstructure-sensitive constitutive relations in a computationally efficient framework.

4.1 Introduction

Prediction of the response of metals subjected to extremely high strain rates has received significant attention from theoretical, experimental, and computational points of view. Currently, the bulk response of most metals subjected to pressures up to 100 GPa is reasonably well characterized [52, 10] and macroscopic viscoplastic constitutive equations [77, 79, 4] have been implemented in numerous finite element and finite difference codes [1]. Most widely implemented models are macroscopic in nature and can only capture microstructural effects phenomenologically by adjusting fitting parameters to desired behavior. Because these models do not readily incorporate microstructural features, effects of pre-processing and subsequent microstructure evolution during high rate deformation cannot readily be

studied using existing frameworks. Therefore, to make a connection with the extensive experimental work that has focused on microstructural effects at high rates, it is desirable to create a computational framework to address microstructure evolution at the crystal scale.

Many authors have used steady plane wave calculations to investigate shock structure and evolution instead of traditional finite element and finite difference methods. Although the plane wave method was originally established to study elastic, perfectly-plastic metals [125, 126], it has been extended to include effects of finite strain, rate-dependence, and higher order elastic constants for isotropically-deforming materials [6, 127]. The advantages of using a steady plane wave formulation are that it is computationally inexpensive and does not rely on artificial viscosity solution regularization techniques employed in finite-element and finite-difference methods [128]. While the plane wave formulation is a valuable method for high strain rate modeling and constitutive model development, until now it has only been formulated to model the isotropic response of materials. Therefore, it could not be used to explicitly model materials that exhibit anisotropic elastoplastic responses such as single-crystals, rolled materials, and composites. Also, it could not be used to model materials that develop anisotropy during deformation. The macroscopic plane wave formulation was used recently to develop and characterize the dislocation-based, isotropic viscoplastic model by Austin and McDowell [35, 36] that is capable of describing the macroscopic response of metals subjected to strain rates in the range of $10^4 - 10^{10}$ s^{-1}.

With the exception of some historical [88, 22, 28] and more recent developments [129, 29, 30, 33, 32], most computational works have focused on modeling the macroscopic response of materials subjected to high strain rates. Relatively little is known concerning the influence of crystal orientation on the shock response and microstructure evolution of materials subjected to extremely high stresses and strain rates. Therefore, new developments to model high rate single-crystal deformation should address both of these areas. To do so, first, the plane wave method is generalized to allow for anisotropic elastic and plastic responses. Then, the viscoplastic crystal model developed in Chapter 3. Finally, the plane wave formulation is used to explore the orientation-dependence of single crystal aluminum subjected to shock stresses ranging from $0 - 30$ GPa and strain rates ranging

from $10^4 - 10^{10}$ s^{-1}. It is found that crystal orientation and pressure play a key role in dictating both the wave profile and active viscoplastic dissipation mechanisms.

4.2 Plane wave method

4.2.1 Formulation

The steady plane wave formulation transforms equations of motion (momentum) and mass continuity (compatibility) from a partial differential equation (PDE) in space and time into an ordinary differential equation (ODE) by using a coordinate transformation. The following derivation closely follows [127].

Plate impact experiments performed on materials that possess less than a three-fold symmetry axis will induce quasi-longitudinal and quasi transverse waves; however, the majority of deformation is often due to the propagating quasi-longitudinal wave. For high stacking fault FCC metals, shear wave components may be negligible compared to the longitudinal wave due to crystal symmetry and a large number of available slip systems. In this case deformation may be approximated as finite uniaxial strain. For a material undergoing finite uniaxial strain, the deformation gradient $\mathbf{F}$, is written as

$$[\mathbf{F}] = \begin{bmatrix} \lambda & 0 & 0 \\ 0 & 1 & 0 \\ 0 & 0 & 1 \end{bmatrix}. \tag{4.1}$$

The one-dimensional Lagrangian equations of motion and mass continuity are

$$\frac{\partial P_{11}}{\partial X_1} = \rho_0 \frac{\partial v_1\left(X_1, t\right)}{\partial t} \quad \text{and} \quad \frac{\partial v_1\left(X_1, t\right)}{\partial X_1} = \frac{\partial \lambda}{\partial t}, \tag{4.2}$$

respectively, where P_{11} is a component of the first Piola-Kirchhoff stress (PK1), X_1 is the Lagrangian coordinate in the direction of wave propagation, and v_1 is the particle velocity in the direction of wave propagation. Define a new coordinate system Y moving with a steady propagating wave of constant speed D such that $Y = X_1 - Dt$. Transforming the equations of motion and mass continuity with respect to the new steady wave coordinate system Y gives

$$\frac{dP_{11}}{dY} = -\rho_0 D \frac{dv_1}{dY} \quad \text{and} \quad \frac{dv_1}{dY} = -D\frac{d\lambda}{dY}. \tag{4.3}$$

Integrating the first part of Equation (4.3) from $Y = +\infty$ to $Y = -\infty$ gives

$$P_{11}^{-} - P_{11}^{+} = -\rho_0 D \left(v_1^{-} - v_1^{+} \right), \tag{4.4}$$

where P_{11}^{+} and v_1^{+} correspond to the state at the beginning of the steady plastic wave ($Y \to +\infty$), whereas P_{11}^{-} and v_1^{-} correspond to the shocked state ($Y \to -\infty$). Note that the above relation is similar to the general balance of momentum jump condition across a surface of discontinuity given by Equation (2.33) with $\mathbf{v}$ and $\mathbf{n}$ in the direction X_1 and $|\mathbf{v}| = D$, except that this equation is resolved with current forces acting on the reference configuration. The steady wave transformation is shown schematically in Figure 4.1 for an attenuating wave that reaches a steady state.

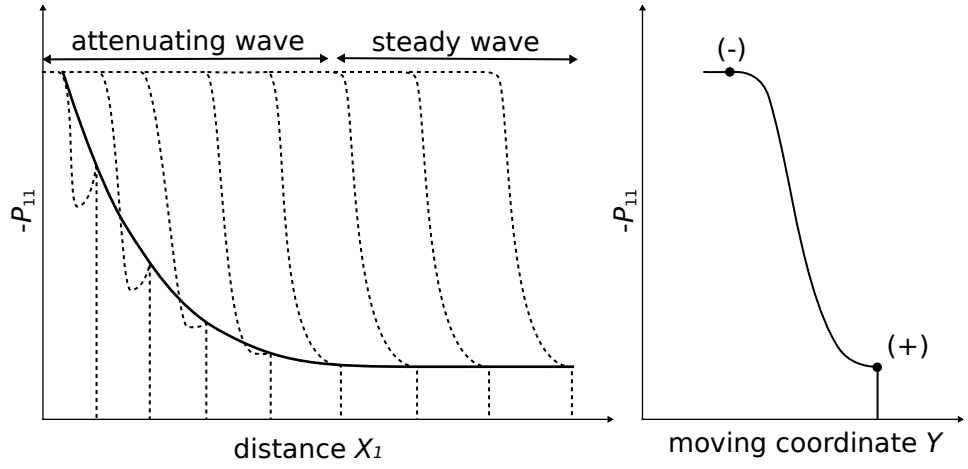

Figure 4.1: (a) Evolution of the elastic-plastic wave after impact to a steady plastic wave and a distinct elastic precursor that compresses the material to the Hugoniot Elastic Limit (HEL). (b) Representation of a steady propagating wave with moving coordinate system $Y = X_1 - Dt$ where $(+)$ corresponds to the beginning of the steady wave profile and $(-)$ corresponds to the shocked state.

For typical metals, the steady wave speed D can be fit to a linear shock velocity vs. particle velocity relation, i.e., $D = C_0 + S_1 v_1^{-}$ [10]. Also, for most metals undergoing weak shocks, there is a distinct elastic precursor wave given by the Hugoniot Elastic Limit (HEL), whereas for strong shocks there is a single wave structure. The HEL is given for most materials in literature, and is used to determine T_{11}^{+} and λ^{+} for weak shocks, whereas for strong shocks $P_{11}^{+} = 0$ and $\lambda^{+} = 1$ is assumed. Considering the peak shock stress (P_{11}^{-}) as a known input, Equation (4.4) can be used to solve for the particle velocity at the

shocked state v_1^-. The shocked particle velocity is then substituted back into the EOS to find the wave speed D. Integrating both parts of Equation (4.3) from $Y = +\infty$ to Y and substituting like terms gives the general form for the Rayleigh line

$$P_{11} - P_{11}^{+} = \rho_0 D^2 \left(\lambda - \lambda^{+}\right), \tag{4.5}$$

which must be satisfied at every point Y along the shock front.

4.2.2 Numerical implementation of plane wave formulation

In this Section, the plane wave formulation from Section 4.2.1 is combined with the total Lagrangian, finite-deformation, thermo-mechanical formulation presented in Chapter 3 to complete a model that admits a fully anisotropic, viscoplastic material response subjected to a deformation gradient $\mathbf{F}$ corresponding to uniaxial strain. For this particular model, the free energy is written as $\Psi = \Psi_1\left(\mathbf{E}^E, \theta\right) + \Psi_2\left(N_m^\alpha, N_{im}^\alpha\right)$. The associated equations for dislocation motion, evolution, and energy will be left in a general form in this section so that it can be used to model other potential forms of the constitutive model. The plane wave numerical method is based on constructing a system of ordinary differential equations (ODEs) in terms of the following independent variables: the total plastic deformation gradient ($F_{\alpha J}^P$); the mobile and immobile dislocation densities on each slip system (N_m^α and N_{im}^α, respectively); and the change in temperature due to plastic deformation ($\Delta\theta^P$).

To solve a system of ODEs, initial conditions and evolution equations must be specified in terms of the dependent variables. In the case of a weak shock, it is assumed that these initial conditions are based on the material's state at the HEL (+). The total dislocation density at the (+) state can be derived according to the HEL reported in literature and the selected strength relation. Some small fraction f^+ of the total dislocation density is assumed to be mobile, thus determining $N_m^{\alpha+}$ and $N_{im}^{\alpha+}$. It is assumed that no plastic deformation occurs up to the HEL, therefore, the temperature rise due plastic deformation at the HEL is zero ($\Delta\theta^{P+} = \int_0^+ \dot{\theta}^P = 0$) and the plastic deformation gradient is the identity tensor ($F_{\alpha J}^{P+} = \delta_{\alpha J}$). For strong shocks, the same assumptions hold.

Because the plastic deformation gradient and temperature change due to plastic deformation are independent variables that are updated incrementally, the longitudinal component of the PK1 stress can be found using the following equations along with Equation (3.9):

$$E^E_{\alpha\beta} = \frac{1}{2}\left[F^{P^{-1}}_{K\alpha}F^{P^{-1}}_{K\beta} + 2F^{P^{-1}}_{1\alpha}F^{P^{-1}}_{1\beta}\xi + F^{P^{-1}}_{1\alpha}F^{P^{-1}}_{1\beta}\xi^2 - \delta_{\alpha\beta}\right] \tag{4.6}$$

$$\Delta\theta^E = \theta_0\left[\exp\left\{-\frac{1}{c_\epsilon\rho_0}\left(\overline{\beta}_{\alpha\beta}E^E_{\alpha\beta} + \frac{1}{2}\overline{\beta}_{\alpha\beta\gamma\delta}E^E_{\alpha\beta}E^E_{\gamma\delta}\right)\right\} - 1\right] \tag{4.7}$$

$$P_{11} = J^P F^{P^{-1}}_{1\alpha}\Sigma_{\alpha\beta}F^{P^{-1}}_{1\beta}\left(1+\xi\right), \tag{4.8}$$

where $\xi = \lambda - 1$ is the compression. Equation (4.8) for P_{11} is substituted as P^*_{11} in Equation (4.5), yielding an equation that is fifth order in ξ, which can be solved numerically. With ξ now known, the resolved shear stress on each slip system can be found using

$$\tau^\alpha = \sigma_{ij}s^\alpha_i m^\alpha_j = \sigma_{ij}F^E_{i\beta}s^\alpha_\beta m^\alpha_\delta F^{E^{-1}}_{\delta j}, \tag{4.9}$$

where σ_{ij} denotes the Cauchy stress, which can easily be found in terms of the Second Piola Kirchhoff Stress $\mathbf{\Sigma}$ using Equation (2.29) where it is assumed $J = J^E = \xi + 1 = \lambda$.

Given the resolved shear stress on each slip system τ^α, constitutive equations for the total dislocation generation rate $\dot{N}^\alpha_{gen}$ and mean mobile dislocation velocity $\bar{v}^\alpha$ must be specified. Therefore, using a general form for the potential generation rate gives

$$\dot{N}^\alpha_{gen}\bar{x}^\alpha_{gen} \approx \dot{N}^\alpha_{hom}\bar{x}^\alpha_{hom} = f^\alpha_1\left(\tau^\alpha, \mu^\alpha, N^\beta_m, N^\beta_{im}, \theta\right); \tag{4.10}$$

however, the specific form used in this work for $f^\alpha_1\left(\tau^\alpha, \mu^\alpha, N^\beta_m, N^\beta_{im}, \theta\right)$ is given by Equation (3.34). As discussed in Section 2.7.1 the mean velocity of mobile dislocations overcoming obstacles can be described using various relations [20, 7, 6], where a general form is given as

$$\bar{v}^\alpha = f^\alpha_2\left(\tau^\alpha, \mu^\alpha, \theta, N^\beta_m, N^\beta_{im}\right); \tag{4.11}$$

however, the specific form used in this work for $f^\alpha_2\left(\tau^\alpha, \mu^\alpha, \theta, N^\beta_m, N^\beta_{im}\right)$ is given by Equation (3.33).

Knowing $\dot{N}^\alpha_{gen}\bar{x}^\alpha_{gen}$ and $\bar{v}^\alpha$ allows computation of the plastic velocity gradient in Equation (3.20), which is used to calculate the rate of compression as

$$\dot{\lambda} = \dot{F}^P_{\alpha J}\frac{\partial\lambda}{\partial F^P_{\alpha J}} + \frac{\partial\lambda}{\partial\left(\Delta\theta^P\right)}\dot{\theta}^P = L^P_{\alpha\beta}F^P_{\beta J}\frac{\partial\lambda}{\partial F^P_{\alpha J}} + \frac{\partial\lambda}{\partial\left(\Delta\theta^P\right)}\dot{\theta}^P, \tag{4.12}$$

where it is noted that λ can be expressed as a function of $\mathbf{F}^P$, $\Delta\theta^P$, and known quantities by use of Equations (4.8), (4.7), (4.6), and (4.5). General forms for the internal energy contribution of dislocations discussed in Section 3.4 are given by

$$\Psi_2\left(\boldsymbol{\alpha}_i\right) = f_3\left(N_m^\alpha, N_{im}^\alpha\right); \tag{4.13}$$

however, in this work this contribution will be neglected, i.e., $f_3\left(N_m^\alpha, N_{im}^\alpha\right) = 0$, which is equivalent to assuming the Taylor-Quinney factor $\beta = 1$. The first law of thermodynamics for an adiabatic process ($\dot{e} = \dot{\psi} + \dot{\theta}\eta + \theta\dot{\eta} = J\boldsymbol{\sigma} : \mathbf{L}$, where e is the internal energy per unit volume and $\mathbf{L}$ is the total velocity gradient) [38, 99] is used to derive an expression for the rate of temperature rise due to plastic deformation, i.e.,

$$\dot{\theta}^P = \frac{J^E}{c_\epsilon \rho_0} \sum_{\alpha=1}^{N} \left\{ \tau^\alpha b \left(N_m^\alpha \left|\bar{v}^\alpha\right| + \dot{N}_{gen}^\alpha \left|\bar{x}_{gen}^\alpha\right| \right) \right\} - \frac{1}{c_\epsilon \rho_0} \left(\frac{\partial f_3}{\partial N_m^\alpha} \dot{N}_m^\alpha + \frac{\partial f_3}{\partial N_{im}^\alpha} \dot{N}_{im}^\alpha \right). \tag{4.14}$$

The first term in Equation (4.14) accounts for the rate of temperature rise due to plastic deformation whereas the second term accounts for the rate of change in stored energy of cold work due to lattice defects, i.e., lattice defect energy which is not dissipated as heat. If $f_3\left(N_m^\alpha, N_{im}^\alpha\right) \neq 0$, Equation (4.14) cannot be calculated at this point because the dislocation evolution rates have not yet been evaluated; however, the second term in the equation for $\dot{\theta}^P$ varies slowly compared to nearly all other plastic variables. Therefore, a negligible error is introduced by using values of $\dot{N}_m^\alpha$ and $\dot{N}_{im}^\alpha$ found from the previous time step to calculate $\dot{\theta}^P$.

Elastic kinematic rate quantities $\dot{F}_{i\beta}^E$, L_{ij}^E, and $\dot{E}_{\alpha\beta}^E$ can be calculated explicitly in terms of $\dot{\lambda}$ and other known quantities with straightforward manipulation of Equation (2.18). The stress rate on each slip system $\dot{\tau}^\alpha$ is then calculated in terms of known quantities using the

following equations:

$$\dot{\theta}^E = \frac{-\theta \dot{E}^E_{\alpha\beta}}{2c_\epsilon \rho_0} \left(2\overline{\beta}_{\alpha\beta} + \overline{\beta}_{\alpha\beta\gamma\delta} E^E_{\gamma\delta}\right) \tag{4.15}$$

$$\dot{\Sigma}_{\alpha\beta} = \dot{E}^E_{\gamma\delta} \left(\overline{C}_{\alpha\beta\gamma\delta} + \overline{C}_{\alpha\beta\gamma\delta\kappa\lambda} E^E_{\kappa\lambda} + \frac{1}{2}\overline{C}_{\alpha\beta\gamma\delta\kappa\lambda\mu\nu} E^E_{\kappa\lambda} E^E_{\mu\nu} - \overline{\beta}_{\alpha\beta\gamma\delta}\Delta\theta\right) \tag{4.16}$$

$$-\dot{\theta}\left(\overline{\beta}_{\alpha\beta} + \overline{\beta}_{\alpha\beta\gamma\delta} E^E_{\gamma\delta}\right)$$

$$\dot{\sigma}_{ij} = \frac{1}{J^E}\left(-L^E_{kk} F^E_{i\alpha}\Sigma_{\alpha\beta} F^E_{j\beta} + \dot{F}^E_{i\alpha}\Sigma_{\alpha\beta} F^E_{j\beta} + F^E_{i\alpha}\dot{\Sigma}_{\alpha\beta} F^E_{j\beta} + F^E_{i\alpha}\Sigma_{\alpha\beta}\dot{F}^E_{j\beta}\right) \tag{4.17}$$

$$\dot{\tau}^\alpha = \dot{\sigma}_{ij} F^E_{i\beta} s^\alpha_\beta m^\alpha_\delta F^{E-1}_{\delta j} + \sigma_{ij}\dot{F}^E_{i\beta} s^\alpha_\beta m^\alpha_\delta F^{E-1}_{\delta j} + \sigma_{ij} F^E_{i\beta} s^\alpha_\beta m^\alpha_\delta \dot{F}^{E-1}_{\delta j}. \tag{4.18}$$

At this point, a constitutive equation is needed to specify the rates of change of the mobile and immobile dislocation densities, $\dot{N}^\alpha_m$ and $\dot{N}^\alpha_{im}$, respectively. General equations are given by

$$\dot{N}^\alpha_m = f^\alpha_3\left(\tau^\alpha, \mu^\alpha, \theta, \bar{v}^\alpha, \dot{\tau}^\alpha, N^\beta_m, N^\beta_{im}\right), \quad \dot{N}^\alpha_{im} = f^\alpha_4\left(\tau^\alpha, \mu^\alpha, \theta, \bar{v}^\alpha, \dot{\tau}^\alpha, N^\beta_m, N^\beta_{im}\right). \tag{4.19}$$

Specific forms of Equation (4.19) are given in Section 3.3.4.

To complete the ODE integration scheme, the derivatives of each of the independent variables must be evaluated with respect to the moving wave coordinate system $Y = X_1 - Dt$. These derivatives are evaluated in terms of known quantities

$$\frac{dF^P_{\beta J}}{dY} = -\frac{1}{D} L^P_{\beta\delta} F^P_{\delta J}, \quad \frac{d\left(\Delta\theta^P\right)}{dY} = -\frac{\dot{\theta}^P}{D}, \quad \frac{dN^\alpha_m}{dY} = -\frac{\dot{N}^\alpha_m}{D}, \quad \frac{dN^\alpha_{im}}{dY} = -\frac{\dot{N}^\alpha_{im}}{D} \tag{4.20}$$

where $L^P_{\beta\delta}$ is known by substituting Equations (4.10) and (4.11) into Equation (3.20), $\dot{\theta}^P$ is known from Equation (4.14), and $\dot{N}^\alpha_m$ and $\dot{N}^\alpha_{im}$ are given in Equation (4.19). The equations that comprise the plane wave scheme are succinctly summarized in Figure 4.2. The plane wave scheme presented in this section has made no assumptions concerning specific materials or crystal symmetries.

4.2.3 Discussion of numerical evaluations and computational efficiency

Although the plane wave numerical method for anisotropic materials presented in the previous section and summarized in Figure 4.2 seems to constitutive a fully explicit expression for determining the incremental change in plastic deformation parameters along the Rayleigh

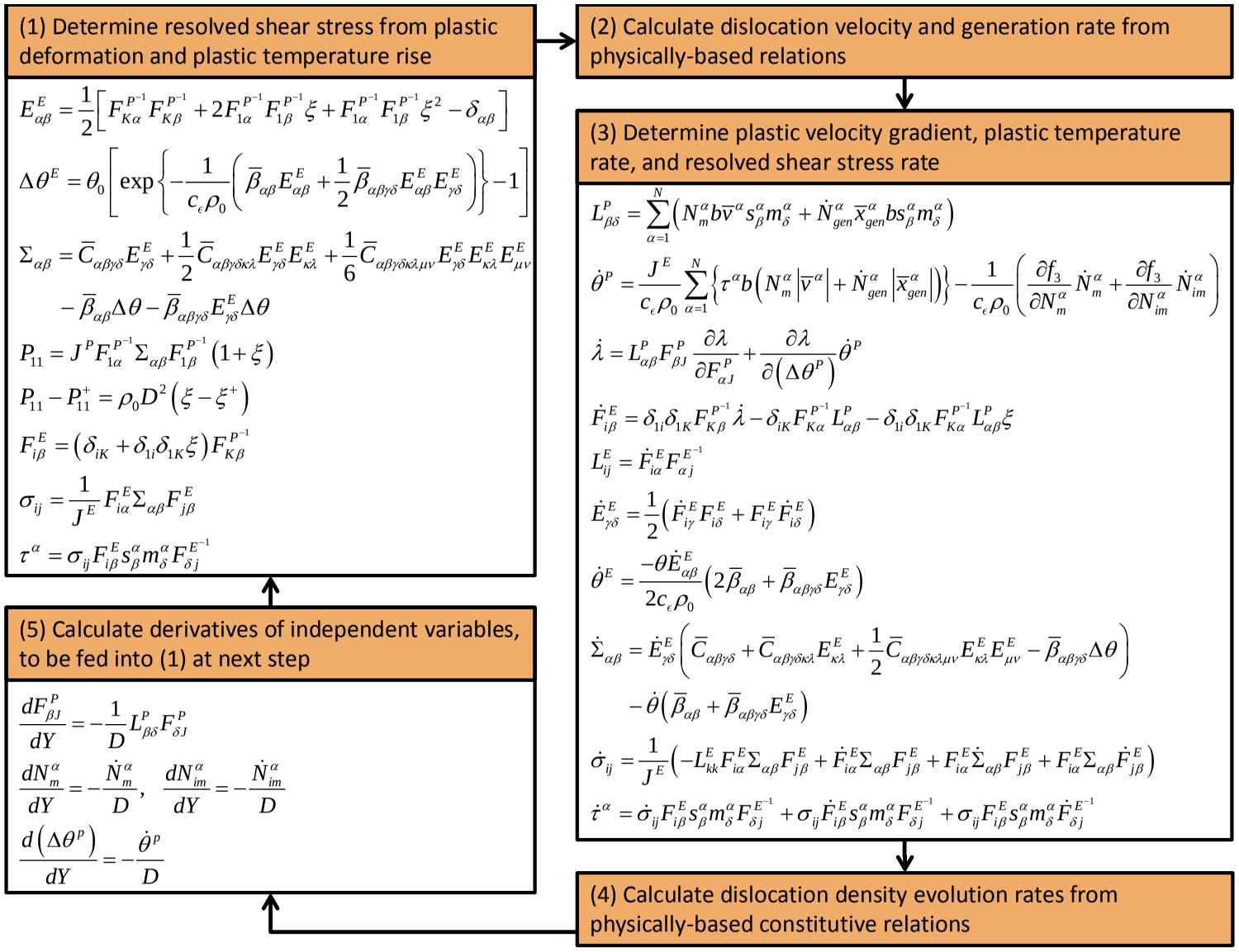

Figure 4.2: Incremental numerical algorithm for plane wave propagation in anisotropic materials whose plastic deformation is controlled by dislocation glide and generation.

line, there are two expressions that are not evaluated explicitly. Their numerical evaluation is examined further in this section.

The first expression that needs to employ numerical evaluation is the expression that is used to constrain deformation to the Rayleigh line, i.e.,

$$J^P F_{1\alpha}^{P^{-1}} \Sigma_{\alpha\beta} F_{1\beta}^{P^{-1}} (1+\xi) = P_{11}^{+} + \rho_0 D^2 \left(\xi - \xi^{+}\right). \tag{4.21}$$

If elastic constants up to third order are used then $\Sigma_{\alpha\beta}$ contains terms up to fourth order in ξ whereas if elastic constants up to fourth order are used then $\Sigma_{\alpha\beta}$ contains terms up to sixth order in ξ. Because the Rayleigh line equation involves terms either up to fifth or seventh order in ξ, it is readily solved using the Newton Raphson method.

The second expression that requires numerical evaluation is the calculation of the deformation rate along the Rayleigh line given by Equation (4.12). Not only does λ depend nonlinearly on $\mathbf{F}^P$ and $\Delta\theta^P$ through the Rayleigh line equation, but $\partial\lambda/\partial\mathbf{F}^P$ contains nine components. The numerical derivative is based on an expansion about the reference state, such that the derivative of the first term is given by

$$\frac{\partial\lambda}{\partial F_{11}^P} = \frac{\lambda\left(F_{\alpha J}^P + \delta_{1\alpha}\delta_{1J}\Delta\epsilon\right) - \lambda\left(F_{\alpha J}^P - \delta_{1\alpha}\delta_{1J}\Delta\epsilon\right)}{2\Delta\epsilon}, \tag{4.22}$$

where $\mathbf{F}^P$ was given at the beginning of the step. In this case, the function $\lambda(\mathbf{F}^P)$ is given as the solution to Equation (4.21), recalling that substitution of $\lambda = \xi + 1$ is necessary. By numerically evaluating this derivative, 18 Newton Raphson iterations must be performed in order to calculate $\partial\lambda/\partial\mathbf{F}^P$. Consequently, it was found that over 90% of the computational time used to perform the plane wave method was spent calculating $\partial\lambda/\partial\mathbf{F}^P$. In the case where the plane wave method was applied to model isotropic elastic-plastic materials, Molinari and Ravichandran showed that if $J^P = 1$, Equation (4.21) can be expressed as second order in elastic longitudinal strain, and can readily be solved using the quadratic formula [127]. Consequently, evaluation of the isotropic version of Equation (4.12) yields an explicit expression for the derivative.

4.3 Single crystal results

4.3.1 Simulation of symmetric single-crystal orientations

Simulations and experiments that characterize the single-crystal shock response along directions of three-fold symmetry are useful because only longitudinal waves form under these loading conditions. For FCC crystals shocked along the x direction, the [100], [110] and [111] orientations are the three ideal orientations that contain at least three-fold symmetry. The [100] orientation contains 8 slip systems that have an equal but non-zero resolved shear stress and 4 that are unstressed. The [110] orientation has 4 slip systems have equal resolved shear stress, 4 slip systems that experience an equal but lesser resolved shear stress, and 4 that are unstressed. The [111] orientation has 6 slip systems that experience an equal resolved shear stress and 6 that remain unstressed. Knowing the number of active systems and the shear stress on each slip system is helpful for analyzing elastic perfectly-plastic crystal deformation [130], however, in rate-dependent and path-dependent plasticity, the evolution equations must be solved incrementally.

Total Lagrangian thermoelastic constants up to fourth order in strain and first order in temperature change are given for aluminum in Table 3.2. Material constants for aluminum are given below the elastic constants in Table 3.1. Parameters used to simulate the high rate viscoplastic response of aluminum up to approximately 15 GPa are given in Table 4.1. Parameters with an (a) in the conversion column were adjusted either to fit experiments or known scaling relations. Other parameters were either converted from macroscopic to crystal level quantities by applying appropriate slip system or Taylor factor normalization ($M_{fcc} \approx 3$) or unaltered due to lack of information. All other parameters were taken directly from values given in literature. Recall that for simplicity, internal energy per unit length of dislocations is neglected, which is equivalent to assuming that all plastic work is dissipated as heat.

The cutting strength prefactor α_{cut} was increased threefold from a value based on quasistatic simulations given in [37] to reflect the increased resistance offered by obstacles when bypassing mechanisms that are present under quasistatic conditions may not exist at high

Table 4.1: Single Crystal HSRVP constants for aluminum

Parameter(s)	Value(s) in Ref	New Value	Units	Conversion	Equation(s)	Reference
			Strength parameters			
α_{pass}	0.1	0.1	none	none	(3.26)	[11]
α_{cut}	0.3	0.9	none	(a) M_{fcc}	(3.27)	[37]
g_0	0.65	1.0	none	(a)	(3.28)	[114]
p, q	0.5, 2	0.5, 2	none	none	(3.28)	[83]
			Hugoniot Elastic Limit Values			
$N^{\alpha}_{\mathrm{HEL}}$	6.7	0.56	$1/\mu m^2$	1/12		[36]
f_{HEL}	0.01	0.01	none	none		[36]
			Dislocation velocity parameters			
v_G		$1.0 \cdot 10^5$	$1/\mu s$	(a)	(3.29)	[35]
B_0 (300 K)	$1.8 \cdot 10^{-8}$	$1.8 \cdot 10^{-8}$	GPa $\cdot$ μs	none	(3.31)	[115]
			Dislocation density evolution parameters			
α_{het}	640	320	$1/\mu m^2$	(a) 1/2	(3.35)	[36]
m	0.8	0.8	none	none	(3.36)	[36]
τ_{min}	τ_{HEL}	τ_{HEL}	GPa	none	(3.36)	[36]
τ_{max}	$\mu_0/30$	$\mu_0/25$	GPa	(a) 6/5	(3.36)	[36]
p_{mult}		0.088	none	(a)	(3.37)	
α_{ann}	0.25	0.25	none	none	(3.38)	[36]
α_{dis}	0.017	0.051	none	(a) M_{fcc}	(3.39)	[36]

rates. Dislocation density evolution parameters were converted from macroscale viscoplastic quantities fit to polycrystalline aluminum data from [35] into crystal-level quantities by ensuring that the Swegle-Grady relation ($\Delta\sigma \propto \dot{\epsilon}^4$) was approximately maintained.

Typical shock loading profiles of [100] and [111] oriented single crystals shocked to approximately 5.5 GPa are compared with experimental profiles in Figure 4.3. Not only are the simulated rise times consistent with the measured quantities, but the simulated shock along the [100] orientation has a faster rise time and steeper shock front than the material shocked along the [111] direction, as is observed experimentally [12]. The rise time and peak strain rate for all three orientations are plotted as a function of peak shock pressure ($P^- = -\frac{1}{3}\sigma^-_{kk}$) in Figure 4.4 from 2 to 15 GPa. Figure 4.4a shows that at less than approximately 5 GPa rise times in [110] and [111] oriented crystals are similar, both of which are longer than the [100] oriented crystal. When the material is shocked between 5 and 15 GPa, the rise times for [110] and [111] orientations begin to diverge, which can be attributed to the [110] orientation having 4 additional slip systems that become activated at

elevated stress levels. The ordering of rise times from slowest to fastest for the [111], [110], then the [100] orientations is consistent with rise times observed in experiments performed on Cu single crystals shocked to 5 GPa performed by Jones and Mote [92]. Peak strain rate versus peak shock pressure for the single crystal orientations is given in Figure 4.4b and compared to the relation given by Swegle and Grady for aluminum polycrystals. The [111] and [110] orientations exhibit strain rates similar to what is experimentally measured in polycrystals, whereas the [100] orientation achieves higher strain rates than polycrystals and other orientations. Figure 4.4b also shows that the constitutive model obeys the Swegle-Grady 1/4 power scaling law.

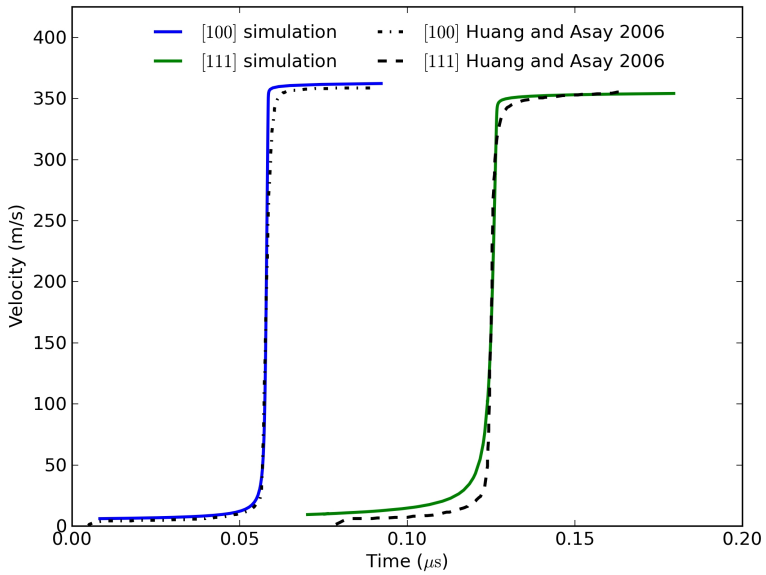

Figure 4.3: Simulated versus experimental [12] velocity-time profiles for single-crystal aluminum. Experimental profiles have been translated so that they are centered on the simulation results.

Material strength in the shocked state is an important quantity that can be inferred from experiments. Reshock and release experiments (RS/RL) infer the shocked strength of the material by assuming that unloading and reloading from the shocked state can be used to quantify the actual strength in the shocked state. However, many idealizations for both the constitutive response and loading behavior must be made, which may draw into question the applicability of this method [132]. A recent, more direct method to determine strength is

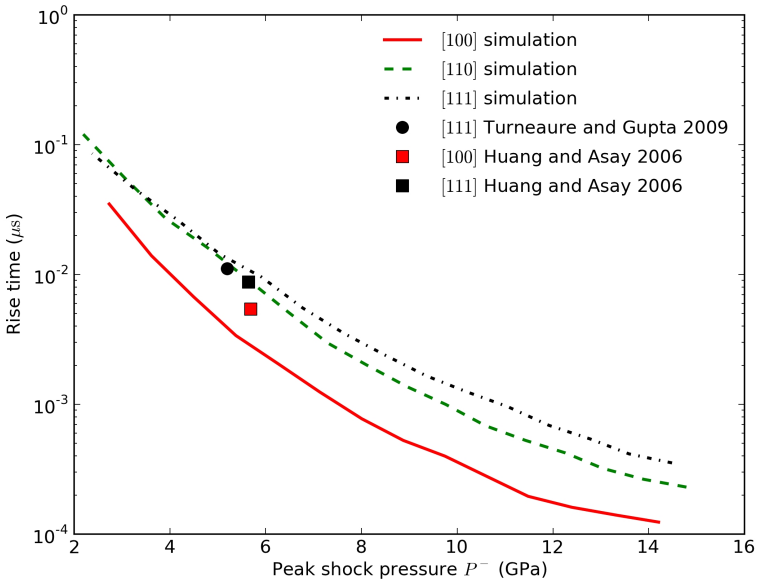

(a) 5% - 95% rise time for aluminum compared to experimentally measured values [15, 12].

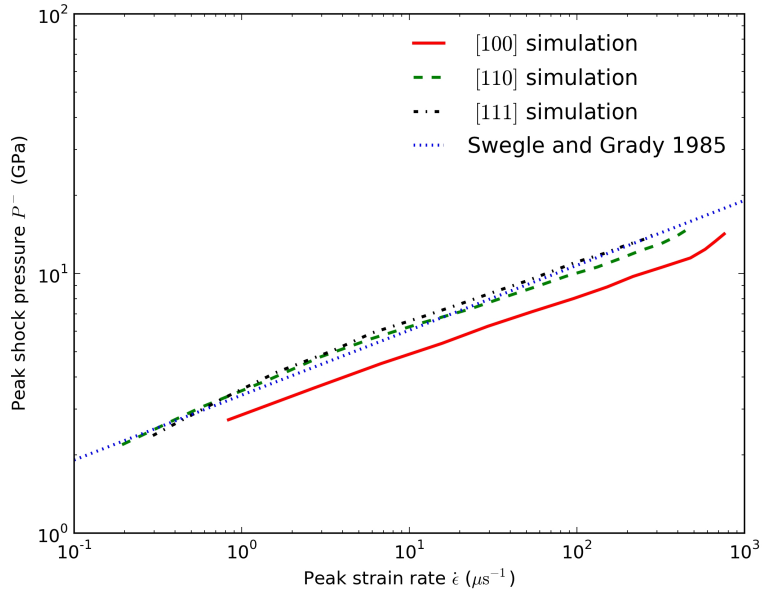

(b) Swegle-Grady plots from simulations compared to a fit to experimental data from polycrystal aluminum given in [131].

Figure 4.4: Orientation dependence of the wave profiles in the weak shock regime.

real time x-ray diffraction (XRD). Here, strength is determined by inferring shear strength from measured lattice strains near the free surface after the shock and subsequent release has occurred, but before lateral or reverberated longitudinal waves have influenced the lattice deformation [15]. The predicted shear stress in the shocked state ($\tau^- = \frac{1}{2}\left|\sigma_1^- - \sigma_3^-\right|$) is compared with values inferred from experiments in Figure 4.5. Figure 4.5 shows that simulation results agree not only with relative values given by XRD and RS/RL experiments, but also that the orientations [110], [111], and [100] are ordered from highest to lowest residual shear strength at similar peak shock pressures. These results suggest that the proposed strength model based on forest and parallel dislocations is reasonable, especially because adjustable parameters in Table 4.1 were only tuned to wave profile data and were not fit to experimental shock strength measurements.

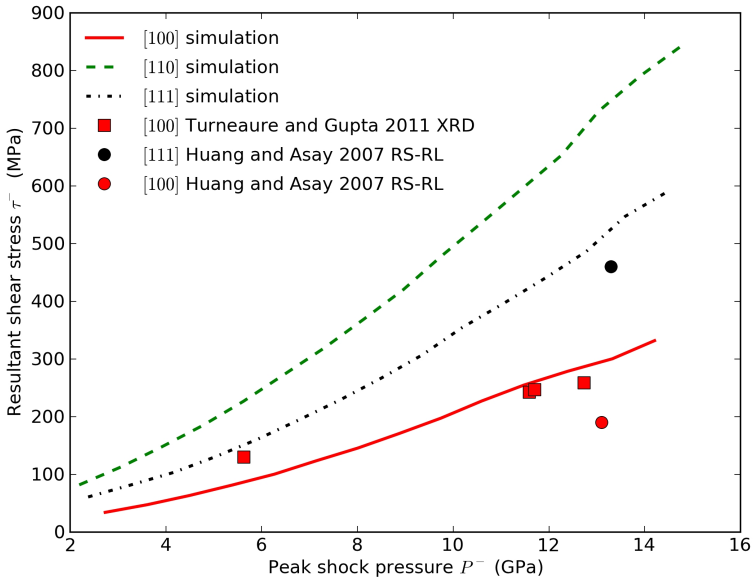

Figure 4.5: Simulated shear stress ($\tau^- = \frac{1}{2}\left|\sigma_1^- - \sigma_3^-\right|$) as a function of peak pressure P^- compared to experimental measurements [13, 14].

Up to this point, homogeneous dislocation nucleation has been omitted because the shear stresses that are generated are far below the ideal strength of the crystal. However, at high stresses where the plastic wave overtakes the elastic wave and the shock becomes overdriven (above approximately $13 - 17$ GPa in aluminum, depending on orientation), homogeneous

nucleation accounts for a significant portion of plastic deformation. Therefore, homogeneous nucleation is now included at the slip system level, and parameters given in [36] are shown in Table 4.2. Although converting $\tau_{0,hom}$ from its macroscale plasticity value to its single crystal plasticity value is straightforward, $\dot{N}_{0,hom}$ and $g_{0,hom}$ were adjusted to ensure relative continuity between heterogeneous and homogeneous dislocation nucleation regimes.

Table 4.2: Homogeneous dislocation nucleation rate parameters for aluminum

Parameter(s)	Value(s) in Ref	New Value	Units	Conversion	Equation(s)	Reference
$\dot{N}_{0,hom}$	$1.73 \cdot 10^9$	$2.88 \cdot 10^8$	$1/(\mu m^2 \cdot \mu s)$	(a) 2/12	(3.34)	[36]
$g_{0,hom}$	0.33	0.067	none	(a) 1/5	(3.34)	[36]
$\tau_{0,hom}$	$\mu_0/15$	$\mu_0/20$	GPa	(a) 3/4	(3.34)	[36]
χ_{hom}	0.008	0.008	none	none	(3.22),(3.23)	[36]
$\bar{x}_{hom}$	$40b$	$40b$	none	none	(3.20)	[36]

To understand how model parameters behave across different regimes, simulations were performed for longitudinal impact of a [100] oriented single crystal to peak shock stresses of 5, 10, 15, 20, 25, and 30 GPa. Longitudinal impact of [100] oriented single crystals is used because 8 slip systems experience the same resolved shear stress and respond identically, thus making it so slip-system level parameters can be plotted as scalars. The following plots are made to help understand the model response at these different peak pressures: dislocation evolution rates and mean dislocation velocity for a single slip system are plotted as a function of effective plastic strain in Figure 4.6; resolved shear stress and associated strengths are plotted as a function of effective plastic strain in Figure 4.7; total, elastic, and plastic temperature rise contributions are plotted as a function of positive compression in Figure 4.8; the instantaneous shear modulus is plotted as a function of positive compression in Figure 4.9; and the shear wave speed is plotted as a function of positive compression in Figure 4.10. These figures will be used to discuss trends that occur at each peak pressure level.

At 5 GPa dislocation multiplication and trapping are the dominant mechanisms that govern dislocation evolution, which occur when dislocation motion is in the thermally activated and drag dominated regimes. At this pressure level, most of the temperature change is due to elastic deformation, and the shear stresses and strength are relatively low, although

the shear stress still exceeds the cutting strength. At 10 GPa, heterogeneous nucleation has a larger influence on the dislocation rate at the beginning of deformation; however, multiplication and trapping are still the dominant mechanisms. Except at the beginning of deformation, dislocation motion is confined to the drag-dominated regime. At this pressure level, temperature rise due to plastic deformation is approximately one third of the total temperature rise. At 15 GPa, dislocation evolution and motion appear to evolve similar to the 10 GPa case, except at elevated rates. Note that at this pressure level, plastic deformation now accounts for approximately 45% of the total temperature rise, and the shear modulus and shear wave speed rise accordingly due to this temperature increase. At 20 GPa, the shock has become overdriven and finite elastic compression must occur to the point that the elastically compressed longitudinal wave speed matches the steady wave speed. At this elastically compressed state, the shear stress that each slip system experiences is approximately 1.4 GPa. Dislocation evolution is no longer controlled by heterogeneous nucleation, multiplication, and trapping, but rather by homogeneous nucleation. The mean dislocation velocity approaches the shear wave speed, which increases significantly with increasing compression. At this stress level, plastic deformation is responsible for approximately 70% of the total temperature rise. A similar situation for the 20 GPa shock is encountered for the case of the 25 and 30 GPa shock. Dislocation evolution is again dominated by homogeneous dislocation nucleation. The large homogeneous dislocation nucleation rates are due to the extremely large shear stresses encountered at the finite elastic compression that occurs before the main portion of the plastic wave. In the plane wave model it is assumed that instantaneous thermoelastic compression occurs up to the elastic limit, which in the case of a strong shock occurs when the elastic longitudinal wave speed reaches the steady plastic wave speed. This approximation may become unrealistic shock strength greatly exceeds the strong shock limit. In real shocks, conduction or other dispersive mechanisms not included in the plane wave formulation may spread out the wave and decrease the rate of compression before significant plastic deformation occurs.

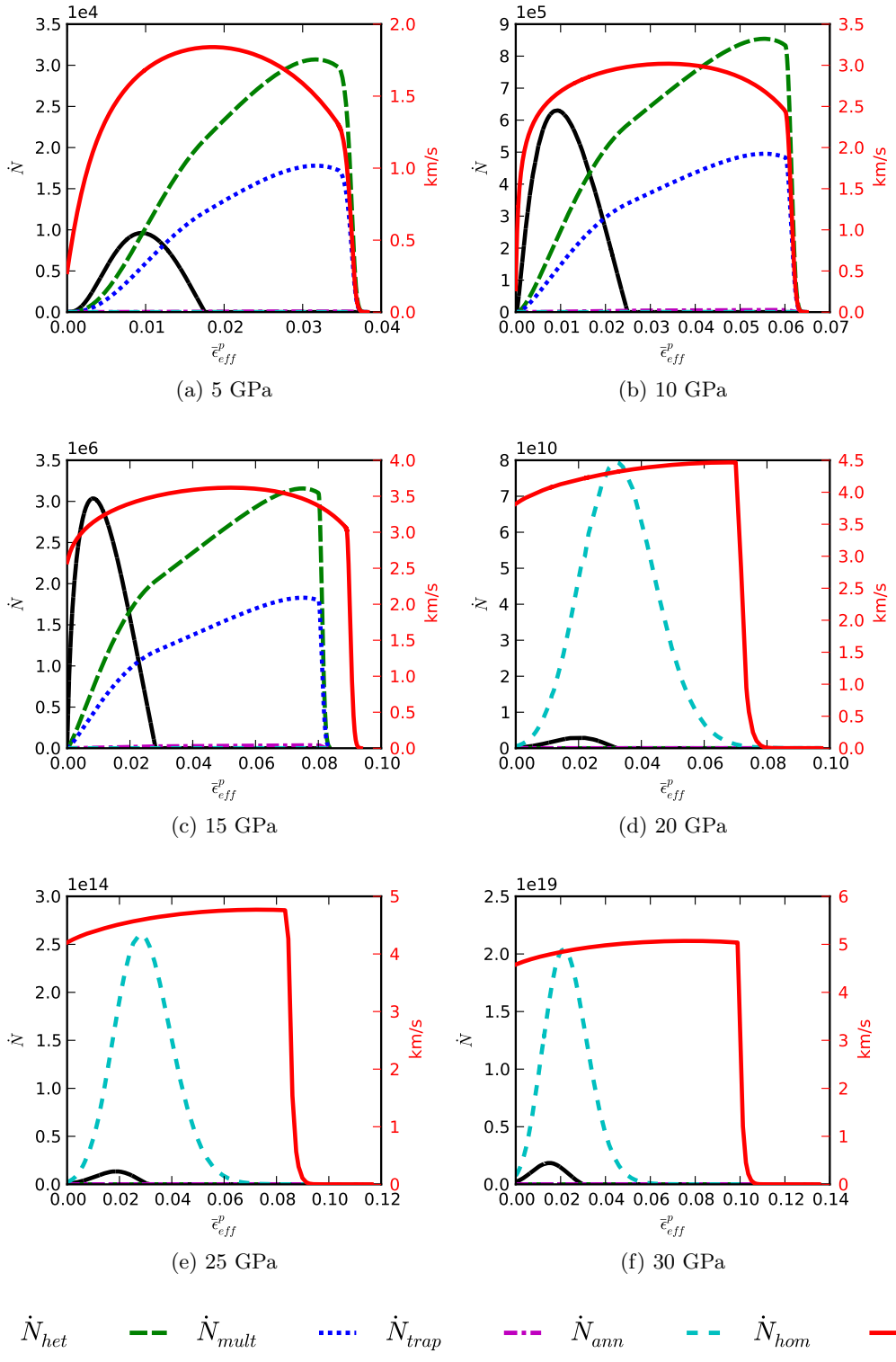

(a) 5 GPa (b) 10 GPa

(c) 15 GPa (d) 20 GPa

(e) 25 GPa (f) 30 GPa

Figure 4.6: Single slip system dislocation density evolution rates ($\dot{N}$ is in dislocations per square micron, per microsecond) for different mechanisms and dislocation velocity for [100] single crystal aluminum shocked to different peak pressures. Left axis corresponds to $\dot{N}$ and right axis corresponds to $\bar{v}$. Values correspond to quantities on one of the eight identical slip systems for longitudinal impact of a [100] crystal.

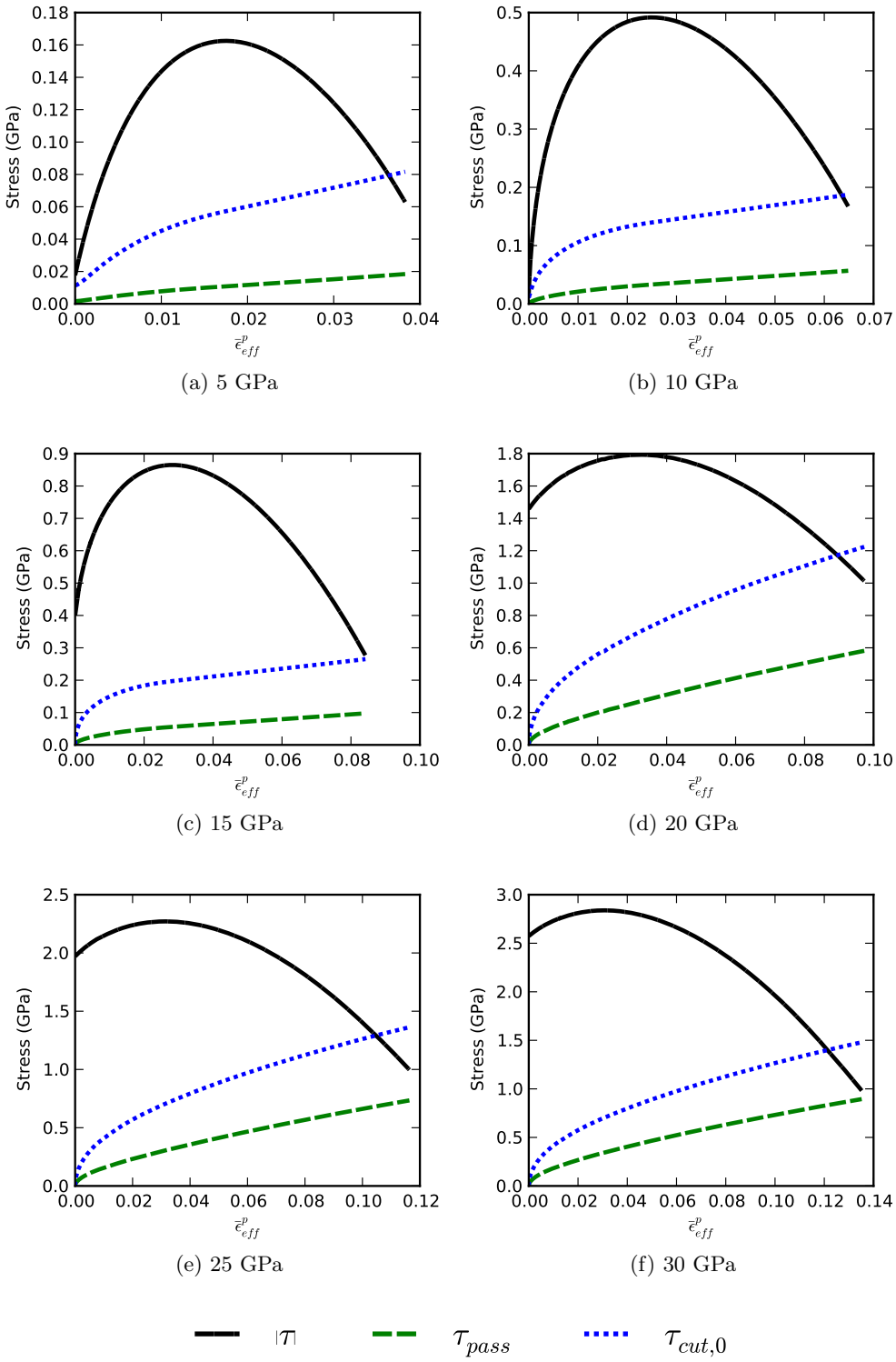

(a) 5 GPa (b) 10 GPa

(c) 15 GPa (d) 20 GPa

(e) 25 GPa (f) 30 GPa

Figure 4.7: Resolved shear stress and strength measures plotted as a function of effective plastic strain for [100] single crystal aluminum shocked to different peak pressures. Values correspond to quantities on one of the eight identical slip systems for longitudinal impact of a [100] crystal.

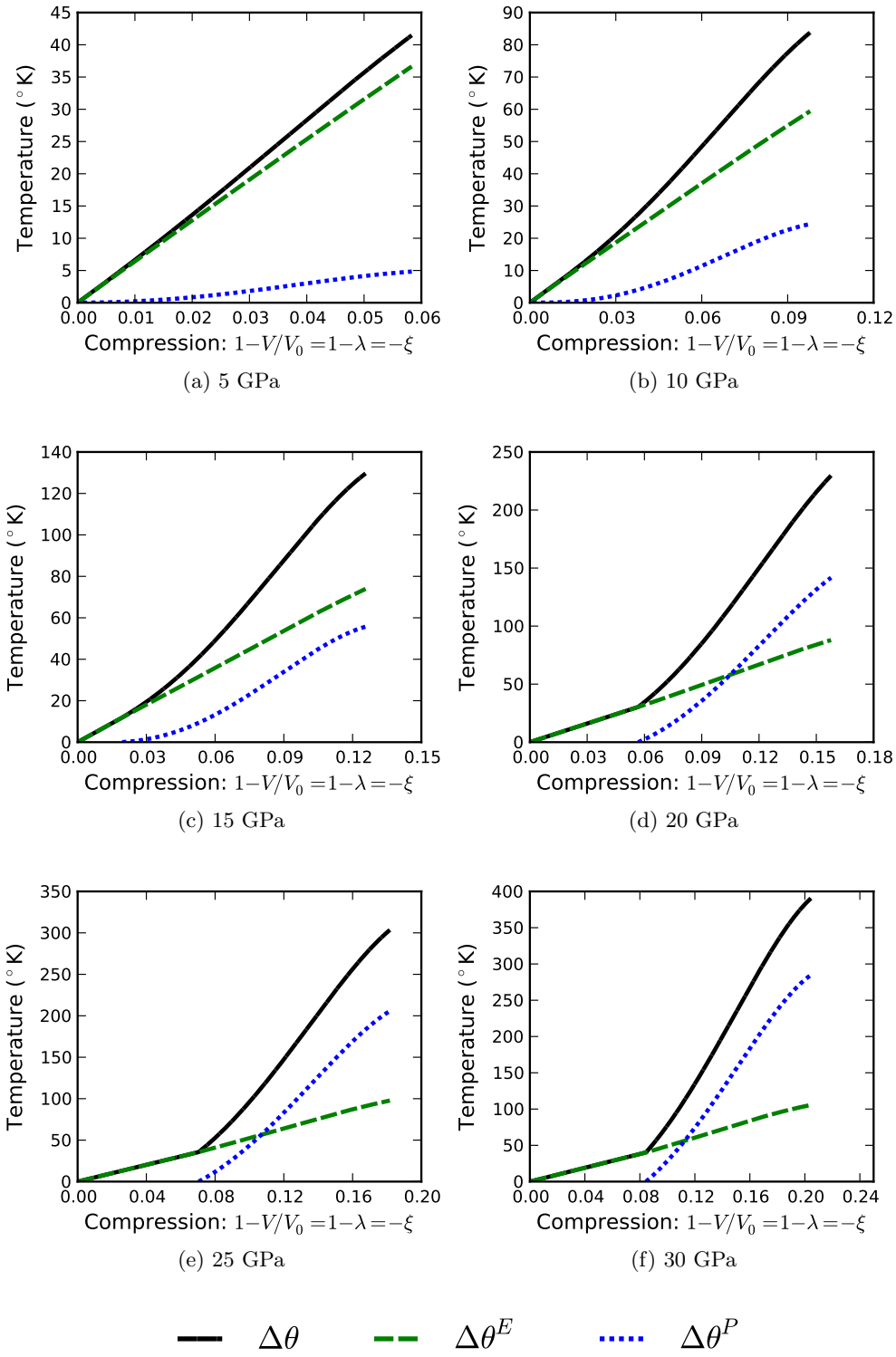

Figure 4.8: Total, elastic, and plastic temperature rise plotted as a function of positive compression for [100] single crystal aluminum shocked to different peak pressures. Note that no plastic deformation occurs until some level of finite compression for overdriven shocks (20, 25, and 30 GPa peak pressure).

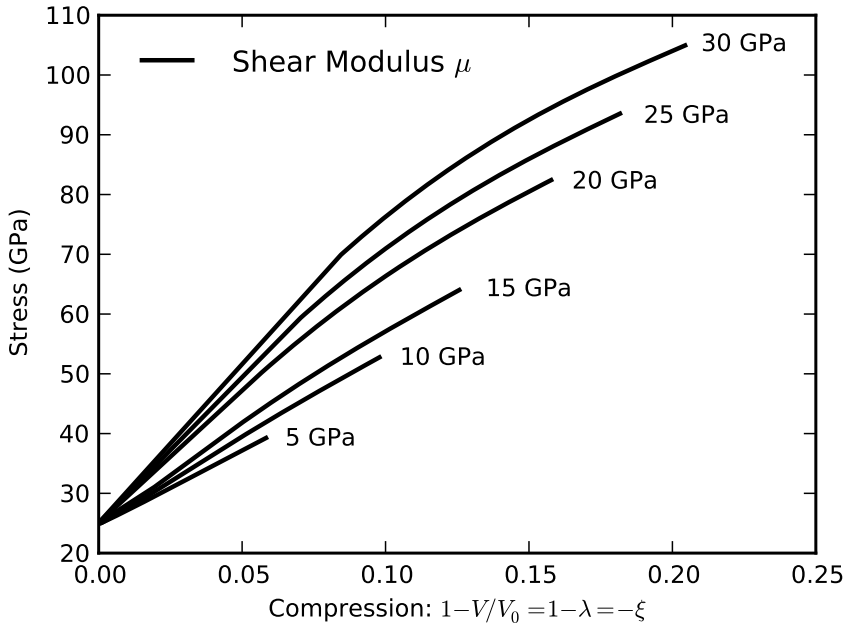

Figure 4.9: Shear modulus plotted as a function of compression for [100] single crystal aluminum shocked to different peak pressures.

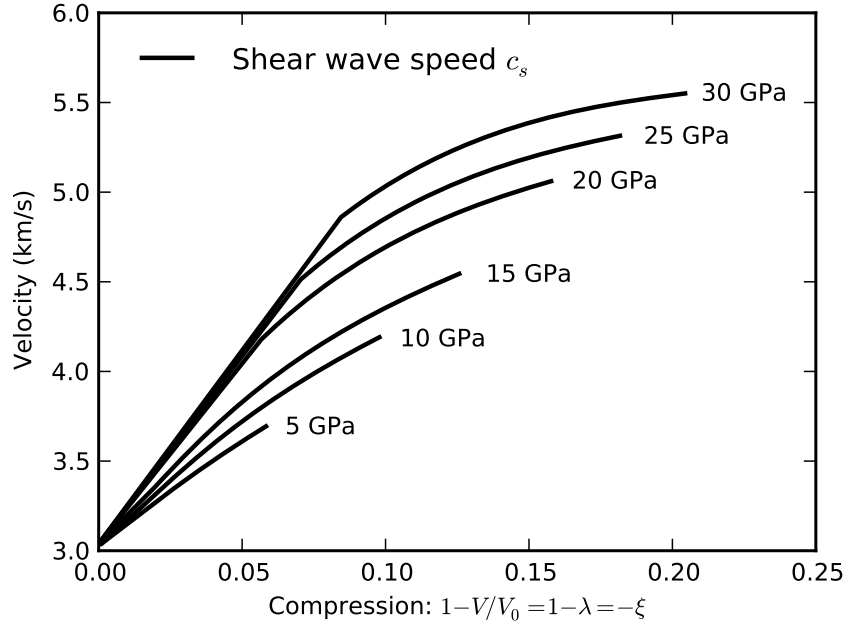

Figure 4.10: Shear wave speed plotted as a function of compression for [100] single crystal aluminum shocked to different peak pressures.

4.3.2 Simulation of random crystal orientations

In single crystal simulations and experiments, it is desirable to characterize the orientation of the material in terms of some scalar measure. Two historical measures used to quantify single crystal orientation effects are the Schmid and Taylor factor. The Schmid factor relates an imposed stress to the highest resolved shear stress that occurs in the material. Although the Schmid factor is useful for understanding the onset of plasticity in single crystals, it is less useful for understanding plastic deformation once more than a single slip system is activated. The Taylor factor has traditionally been used as a scalar measure to connect micromechanical plastic deformation processes with macroscopic imposed constraints for single crystals as well as polycrystals [133]. The multiaxial Taylor factor is a three-dimensional generalization of the classical Taylor factor [114], i.e.,

$$M = \frac{\sum_\alpha |\delta\gamma^\alpha|}{\delta E_{vm}}, \tag{4.23}$$

where $\delta\gamma^\alpha$ denotes the incremental shear on slip system α and δE_{vm} is the incremental effective von Mises strain defined as $\delta E_{vm} = \sqrt{2/3\delta\mathbf{E} : \delta\mathbf{E}}$. Generally, M is a function of both orientation and deformation history, which can be used to quantify the effect of evolving texture during simulations [134] and experiments [135]; however, for Full Constraints (FC) proportional loading of a perfectly plastic material, M can be expressed uniquely as a function of initial orientation for a variety of loading conditions given a set of potentially active slip systems [136]. Because M evolves during deformation, it cannot be used as a single scalar to connect micromechanical plastic deformation to the imposed deformation. Therefore, it is proposed that a modified Taylor factor $\langle M \rangle$ be used, which is defined as the integral of the Taylor factor over the entire deformation history, i.e.,

$$\langle M \rangle = \frac{\int \sum_\alpha |\delta\gamma^\alpha|}{\int \delta E_{vm}}. \tag{4.24}$$

In the case of the plane wave formulation, this integral is evaluated with respect to the initial (+) and shocked (−) states, i.e.,

$$\langle M \rangle = \frac{\int_+^- \sum_\alpha |\delta\gamma^\alpha|}{\int_+^- \delta E_{vm}}. \tag{4.25}$$

An inverse pole figure based on the initial orientations of 500 randomly oriented single crystals shocked between 0 and 30 GPa is shown in Figure 4.11, where points on the pole figure are colored according to their modified Taylor factor $\langle M \rangle$. Figure 4.11 shows that although there is some patterning consistent with Taylor factors observed in FCC single crystals undergoing finite uniaxial strain [136], most behavior is randomly distributed. To understand the main dissipation mechanisms and their effect on the wave profile and microstructure evolution, shock results are examined separately in different pressure regimes.

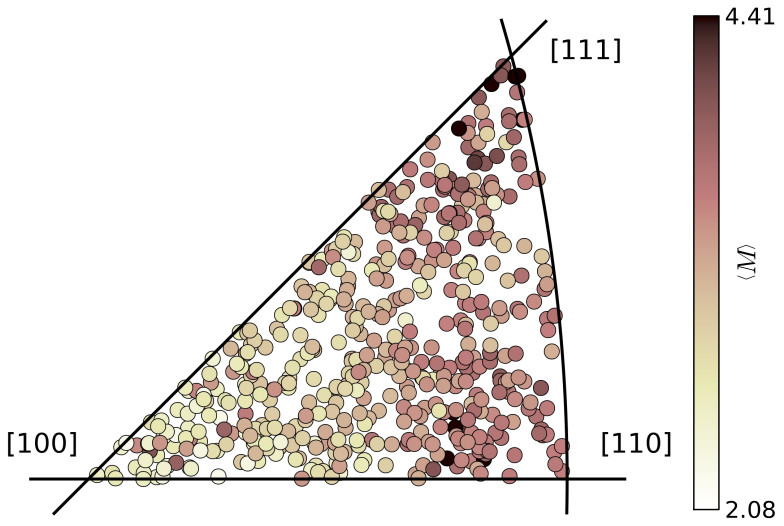

Figure 4.11: Inverse pole figure with [100] sample direction based on initial orientation for 500 randomly oriented single crystals shocked from $0 - 30$ GPa. Pole figure is colored according to the modified Taylor Factor $\langle M \rangle$.

In Figure 4.12, inverse pole figures were created for 200 randomly oriented crystals shocked to random peak shock pressures spanning 5 GPa intervals of peak shock pressure ranging from 0 to 30 GPa. For example, Figure 4.12a shows 200 randomly oriented crystals shocked to random peak pressures ranging from $0 - 5$ GPa. All of the pole figures use the same colorbar shown in Figure 4.11. These inverse pole figures are especially useful when combined with plots of deformation mechanisms and variables that affect them, which are shown in Figures 4.6-4.10 for [100] oriented crystals shocked in 5 GPa intervals. From $0 - 5$ GPa $\langle M \rangle$ is only slightly orientation-dependent because dislocation multiplication can occur on multiple systems and dislocations glide with relative easy in the thermally

activated and viscous drag regimes. As peak shock pressure increases from $5-15$ GPa, the deformation becomes more orientation-dependent. This orientation-dependence arises because more dislocations need to be generated to provide the increased peak plastic strain rate compared to lower pressures due to dislocation velocities on some slip systems being limited by the shear wave speed ($\bar{v}^{\alpha} < c_S$). Also, the primary dislocation generation mechanism transitions from dislocation multiplication to heterogeneous nucleation. As the shock transitions from $15-25$ GPa, the orientation-dependence of the single crystal begins to fade as homogeneous dislocation nucleation becomes the dominant plastic deformation mechanism. In the case where homogeneous nucleation dominates, nucleation occurs regardless of orientation, and a few slip systems oriented along the shock direction can provide a majority of the deformation, accounting for the "hot spots" on the inverse pole figures.

Not only do orientation and peak shock pressure play a role in governing the dominant plastic deformation mechanisms, but they also affect aspects of the wave profile. Figure 4.13a shows a plot of shock width versus peak pressure for 500 randomly oriented single crystals colored according to values of $\langle M \rangle$. It is observed that in the weak shock regime, crystal orientations that experience a lower ratio of slip to total plastic deformation have a smaller shock width and a higher peak strain rate. It is also observed that as peak pressure increases, fluctuations in shock width increase and the ratio of slip to macroscopic strain increases. The correlation between increasing strain rate with decreasing $\langle M \rangle$ in the weak shock regime is observed directly by examining the peak strain rate versus peak pressure, shown in Figure 4.13b. Again, higher strain rates are observed at similar peak pressures in orientations with a low value of $\langle M \rangle$.

As the material approaches the strong shock regime and homogeneous nucleation becomes the dominant deformation mechanism ($17-25$ GPa), no clear pattern emerges between values of $\langle M \rangle$ and shock width or peak strain rate. In this regime, a few well oriented slip systems that experience the abrupt transition to homogeneous dislocation nucleation dominate the plastic deformation response. Above 25 GPa, results indicate that values of $\langle M \rangle$ begin to correspond to a decreased shock width and increased peak strain rate again, however, not as distinctly as in the weak shock regime. Because $\langle M \rangle$ seems to correlate with

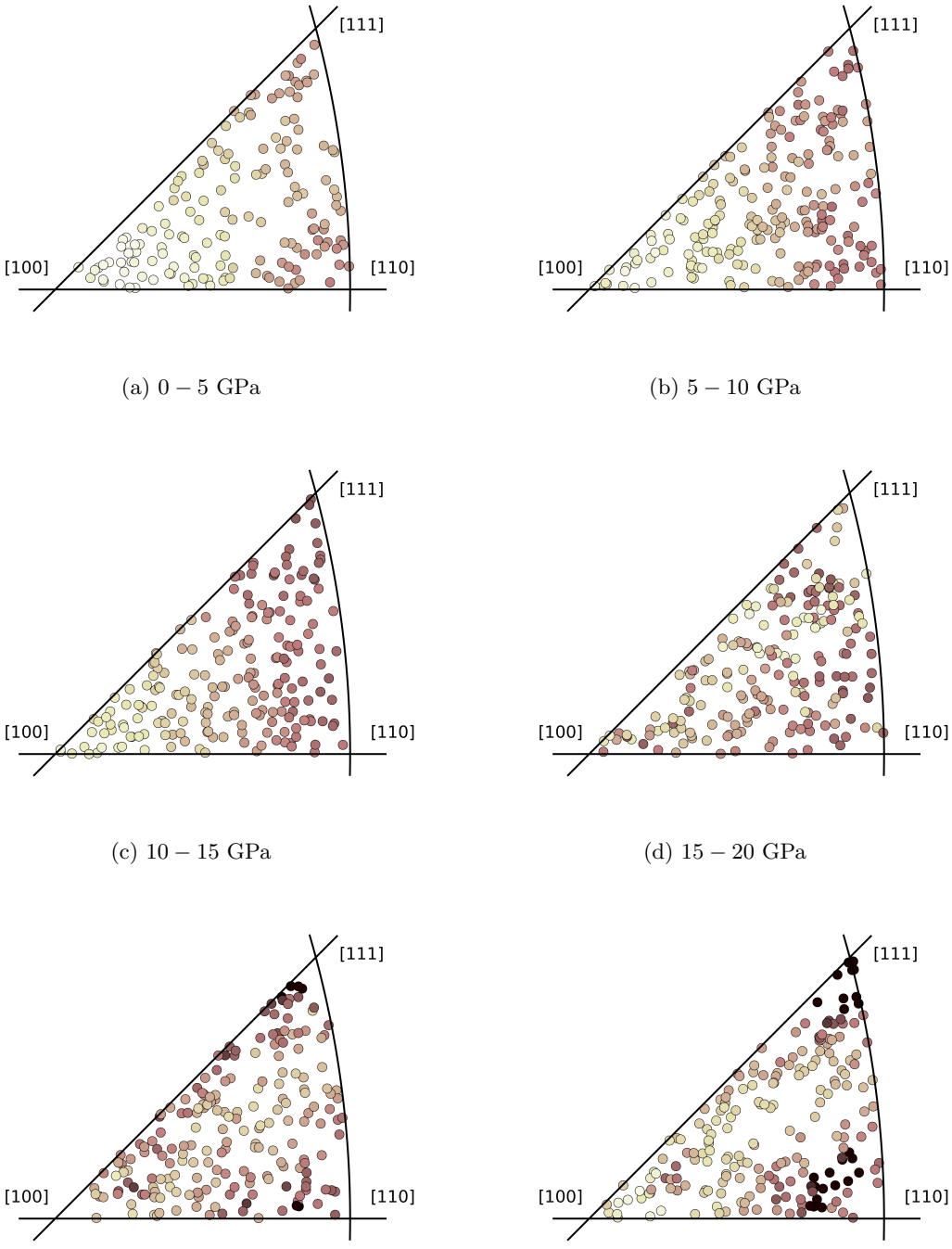

(a) $0 - 5$ GPa

(b) $5 - 10$ GPa

(c) $10 - 15$ GPa

(d) $15 - 20$ GPa

(e) $20 - 25$ GPa

(f) $25 - 30$ GPa

Figure 4.12: Initial orientations plotted on a [100] inverse pole figure for 200 simulations with random orientation shocked to different peak pressures. Coloring corresponds to values of $\langle M \rangle$ and uses the same colorbar as Figure 4.11.

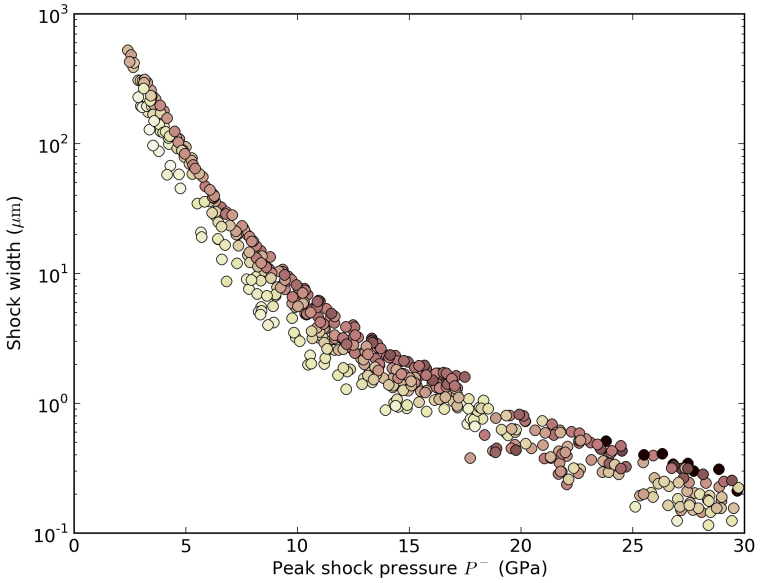

(a) Simulated peak pressure versus shock width.

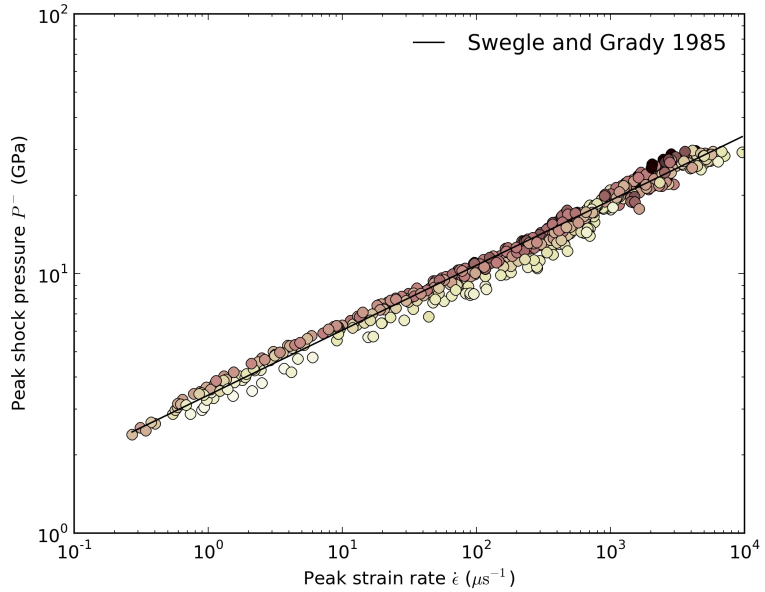

(b) Swegle Grady plot compared to trend fit to polycrystal aluminum data given in [131].

Figure 4.13: Simulated wave profile results for 500 randomly oriented aluminum single crystals shocked between 0 and 30 GPa. Coloring corresponds to values of $\langle M \rangle$ and uses the same colorbar as Figure 4.11.

shock characteristics in the weak shock regime, additional simulations were performed for peak pressures ranging from $2-15$ GPa to characterize how orientation influences the resultant shock behavior. It is also helpful to understand what other material and characteristics $\langle M \rangle$ correlates with.

In Figure 4.14, the initial orientation and subsequent rotation is plotted for 750 single crystals that were shocked at peak pressures ranging from $2-15$ GPa. Note that because this limited range of pressures is used, a new colorbar is introduced in Figure 4.14 that differs from the one that has been used up to this point to describe $\langle M \rangle$ from $0-30$ GPa. Figure 4.14 shows that predicted grain rotations during shock loading are similar to what is observed during quasistatic, axisymmetric compression, where crystals rotate to the [110] orientation along a dividing line passing approximately through the [311] orientation. This plot also shows that the magnitude of the subsequent crystal rotation cannot generally be described by $\langle M \rangle$. The subsequent rotation is described uniquely in this regime by the initial position on the inverse pole figure and the magnitude of the applied peak shock stress.

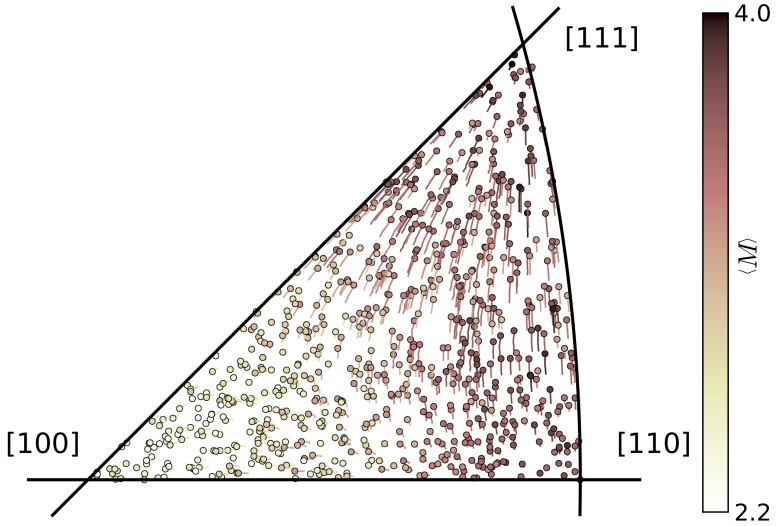

Figure 4.14: Inverse pole figure showing initial position (dot) and subsequent rotation (tail) due to shock loading for 750 randomly oriented single crystals shocked from 2-15 GPa. Pole figure is colored according to the modified Taylor Factor $\langle M \rangle$.

In Figure 4.15, the total temperature rise and residual dislocation density are plotted

as a function of peak shock pressure and are colored according to $\langle M \rangle$. Figure 4.15a shows several interesting trends. First, the total temperature rise increases with increasing $\langle M \rangle$, which occurs because grains that experience more plastic deformation at similar pressures will have an increased plastic temperature rise. This figure also shows that the variation in temperature rise increases with increasing peak shock pressure. At a peak pressure of 2 GPa there is negligible variation in temperature rise due to orientation because at this peak pressure elastic temperature change dominates the total temperature rise, whereas at 15 GPa temperature rise varies by approximately 15°K due to orientation changes. This increased variation can be understood by examining Figure 4.8c, which shows that at peak pressures of 15 GPa plastic deformation may account for up to 45% of the total temperature rise. Figure 4.15b shows how the residual dislocation density (dislocation density in the shocked state) varies with respect to orientation and peak shock stress. Unlike the temperature rise, residual dislocation density varies for different orientations even at small peak shock pressures and this variation increases with increased peak shock pressure. At lower peak shock pressures (approximately $2 - 6$ GPa) the residual dislocation correlates with $\langle M \rangle$ whereas at higher peak shock pressures (approximately $6 - 15$ GPa) variation in residual dislocation density does not correlate with $\langle M \rangle$. In the weak shock regime, it appears that residual dislocation density increases quadratically with respect to applied peak shock pressure, and that different orientations may have approximately 25% variation in residual dislocation density.

4.3.3 Discussion

In the previous section wave profile and material characteristics in the shocked state were examined. In many cases, especially in the weak shock regime, wave profile and material state characteristics were shown to correlate with $\langle M \rangle$; however, some material characteristics did not correlate with $\langle M \rangle$. Most characteristics did not correlate with $\langle M \rangle$ in the strong shock regime. Recall that the multiaxial Taylor factor M is ratio of incremental slip to the incremental in total deformation. For a perfectly plastic single crystal, M is based on the minimum slip that can satisfy the imposed deformation (least shear hypothesis), which

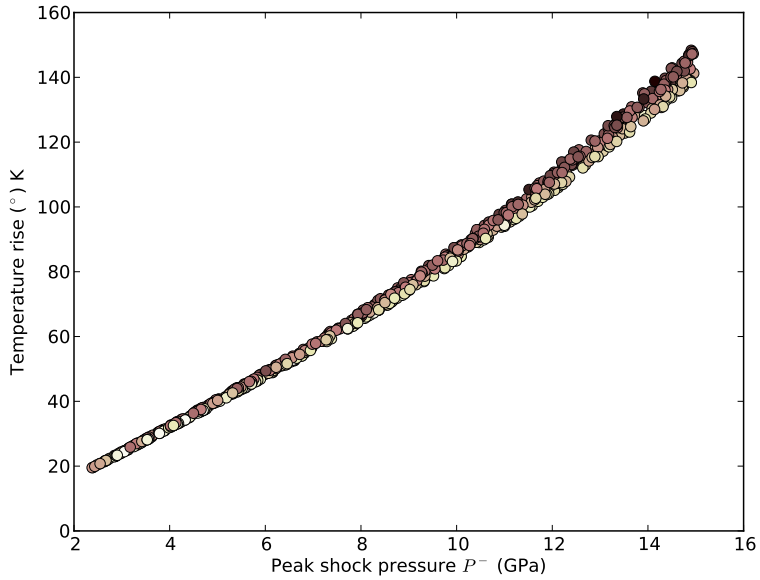

(a) Total temperature rise.

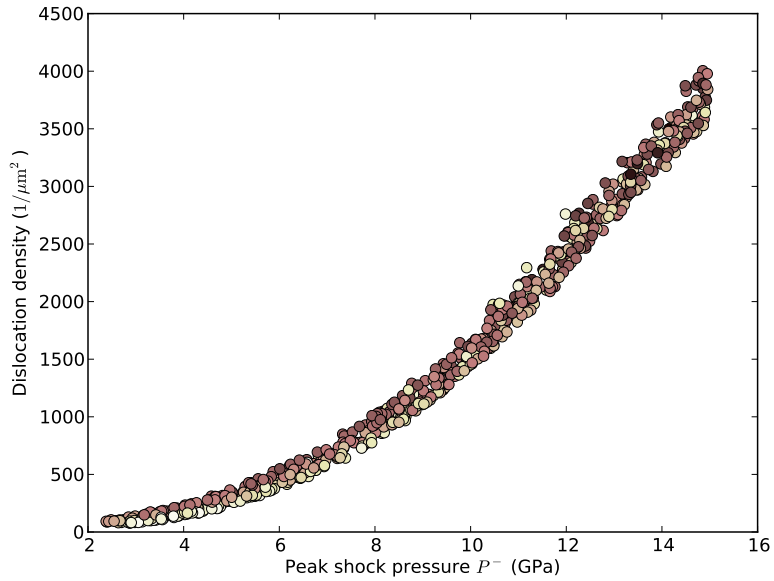

(b) Residual dislocation density.

Figure 4.15: Simulated wave profile results for 750 randomly oriented aluminum single crystals shocked between 2 and 15 GPa. Coloring corresponds to values of $\langle M \rangle$ and uses the same colorbar as Figure 4.14.

was shown to be equivalent to the maximum work principle [137, 138, 136]. For a material that obeys generalized normality, M will also correlate closely with plastic deformation characteristics as associative flow is ensured. Now consider the weak shock regime where $\dot{N}_{mult}$ and $\dot{N}_{trap}$ are the dominant plastic deformation mechanisms. The theory where plastic deformation is only due to the glide of these two mechanisms is very close to ensuring generalized normality (there is a slight dependence of μ on $\mathbf{E}^E$, which violates the form required by Equations (2.114) and (2.115), but this has a small influence during proportional loading), and $\langle M \rangle$ is seen to correlate closely with wave profile as well as shock deformation characteristics.

As heterogeneous and homogeneous nucleation begin to dominate plastic deformation, however, deformation may occur far from generalized normality due to these critical (instead of associative) type of processes occurring. Recall that $\dot{N}_m^\alpha$ depends on $|\dot{\tau}^\alpha|$ due to heterogeneous nucleation and $\dot{\gamma}^\alpha$ depends on $\dot{N}_{gen}^\alpha$ from homogeneous nucleation. These forms cause the constitutive relation to violate generalized normality. Indeed, it seems reasonable that at elevated stress levels wherein heterogeneous and homogeneous dislocation nucleation dominate, dislocations are generated and glide on most systems because of the large shear stresses, and not because they are optimally oriented in the direction of the imposed deformation. In this case, $\langle M \rangle$ is observed to poorly characterize the shock wave profile and material state characteristics in the shocked state.

4.4 Summary and conclusions

A thermodynamically consistent plane wave formulation that utilizes higher order thermoelastic constants has been developed for the simulation of viscoplastic single crystals. The total Lagrangian thermoelastic model presented in Section 3.2.1 was combined with the dislocation-based viscoplasticity model presented in Section 3.3 and these were implemented into the plane wave formulation to study the high strain rate behavior of single-crystal aluminum. Predictions of the shock wave response of symmetrically oriented aluminum single crystals are in agreement with available experimental data concerning the wave profile, peak

strain rate, shock width, and strength. Specifically, it was shown that at similar peak pressures, the peak resolved shear stress was ordered highest-to-lowest for [110], [111], and [100] orientations, whereas shock width was ordered from highest-to-lowest for [111], [110], then [100] orientations. The model was then used to study orientation-dependence of randomly oriented aluminum single crystals with peak shock pressures ranging from $0 - 30$ GPa. It was observed that the material's wave profile and microstructure evolution is sensitive to both orientation and peak pressure. Although desirable, this response cannot be predicted *apriori* using a classical Taylor or Schmid factor. Rather, it was seen that the calculated modified Taylor factor $\langle M \rangle$ was useful in understanding the response of the material. Specifically, in the $0 - 15$ GPa range, the peak strain rate increased with decreasing $\langle M \rangle$, and the peak strain rate sensitivity to $\langle M \rangle$ increased as peak pressure increased. A similar trend was shown where total temperature rise increased with increasing $\langle M \rangle$, and variation due to orientation increased with increasing peak pressure.

Although the plane wave formulation can be used to evaluate the steady wave response of a wide class micromechanics-based, thermoelastic-viscoplastic constitutive models, it also has limitations. The plane wave formulation developed in this Chapter has assumed that deformation is due to a steady longitudinal wave that imparts a state of uniaxial strain, whereas in plate impact experiments along materials with less than three-fold axis of symmetry both quasi-longitudinal and quasi-transverse waves form. Although for high stacking fault energy FCC metals this approximation may introduce a negligible error, it is not clear whether this assumption would introduce large errors when applied to lower symmetry single crystals, materials that twin, or heavily textured polycrystals. Direct comparison with finite element or finite difference simulations of plate impact experiments that allow formation of quasi-longitudinal and quasi-transverse waves must be made to quantify this error before applying the plane wave method to these materials. Also, the plane wave method must assume that the propagating wave has achieved a steady state. In simulations of plate impact experiments, not only does the thermoelastic-viscoplastic constitutive model dictate the shape of the steady plastic wave, but it also governs the attenuation rate of

the unsteady wave as it settles to its steady state as well as the response during unloading. Because of this limitation, the plane wave method is insensitive to aspects of the constitutive model that may be important for modeling unsteady wave propagation such as the fraction of dislocations that are initially mobile [36]. Despite its limitations, the plane wave method is able to characterize the wave profile and evolving material state in a computationally efficient framework without introducing spurious artificial viscous dissipation commonly employed in finite-difference and finite-element methods, and whose coupling with viscoplastic constitutive models is often neglected.

Many improvements can be made concerning both the plane wave formulation and the high strain rate single crystal constitutive law. For the thermoelastic formulation it is generally undesirable from a computational viewpoint to include fourth-order elastic constants. Second and third-order elastic constants are based on physical measurements that probe the crystal's entire symmetry [49], whereas fourth-order constants are generally fit to macroscopic equation of state data [103]. Therefore, it may be more appropriate to recast the Lagrangian thermoelastic formulation used in this Chapter to the Eulerian material strain theory presented in Section 3.2.2 [34]. Also, in this analysis the evolution of dislocation substructure energy (cold work) as a function of peak shock stress and orientation was neglected. Internal energy of substructure may play a role in dictating dislocation substructure refinement, which in turn affects localization behavior. Although relatively few models have been developed to capture substructure energy evolution (some of which were presented in Section 3.4), many experimental investigations have highlighted key differences between quasistatic and high rate substructure evolution [139].

To address limitations of the plane wave method presented in this Chapter, in the following Chapter an extended, one-dimensional finite difference method is developed to model spatio-temporal evolution of materials that exhibit anisotropic response subjected to shock loading. Eulerian material thermoelasticity is utilized in conjunction with the viscoplastic theory so that the model can be extended to model higher peak shock pressures. Then in Chapter 6, direct comparisons are made between simulations using the finite-difference formulation and the plane wave formulation.

CHAPTER V

FINITE-DIFFERENCE SIMULATIONS

5.1 Introduction

In this Chapter, the material Eulerian thermoelastic model developed in Section 3.2.2 is combined with the dislocation-based viscoplastic model from Section 3.3 and are implemented into a one-dimensional, extended finite-difference method for anisotropic materials to model the spatiotemporal evolution of single crystals subjected to longitudinal shock loading by plate impact as well as laser shock. This finite-difference method allows all three velocity components to vary with respect to the wave propagation direction, which is necessary to model the quasi-longitudinal and quasi-transverse waves that can form in shock wave experiments on anisotropic materials. Shock deformation of annealed, preferentially oriented, and cold rolled polycrystals will be examined and compared with existing experimental results. In all three of these cases, experimental microstructures are modeled by employing realistic dislocation densities, orientation distributions, and grain sizes. For cold rolled simulations, results from quasistatic crystal plasticity simulations are used to generate dislocation densities on individual slip systems.

5.2 Numerical Formulation

5.2.1 One-dimensional, extended finite-difference framework for anisotropic materials

Consider a thermoelastic-viscoplastic solid undergoing an adiabatic deformation process. Recall from Section 2.2.1 that the conservation equations for momentum and energy, as well as assumption of continuity are expressed as

$$\rho_0 \frac{\partial v_i}{\partial t} = \frac{\partial P_{iA}}{\partial X_A} - \frac{\partial q}{\partial X_A}\delta_{iA} \tag{5.1}$$

$$\rho_0 \frac{\partial \mathcal{E}}{\partial t} = \left(P_{iA} - q\delta_{iA}\right)\dot{F}_{iA} \tag{5.2}$$

$$\frac{\partial F_{iA}}{\partial t} = \frac{\partial v_i}{\partial X_A}, \tag{5.3}$$

where v_i is the velocity and q is the artificial viscosity typically included in shock simulations to introduce shock entropy generation not otherwise captured by the model. Note that the assumption of continuity is equivalent to specifying the mass conservation equation for a homogeneous solid [38]. The three-dimensional forms of the governing equations are readily solved using the finite-difference method; however, many experiments used to characterize the high rate constitutive and shock response of materials are one-dimensional in nature and direct imposition of the associated deformation constraints will reduce the computational cost. The one-dimensional approximation that assumes material isotropy has been used to model the response of materials subjected to uniaxial loading conditions using equations of state, elastic-plastic deformation, damage, and fracture [76]. This one-dimensional approximation cannot model impact loading of arbitrarily oriented crystals or directionally reinforced materials as well as non-axisymmetric impact geometries.

To model planar, quasi-longitudinal and quasi-transverse wave propagation that occurs for these lower symmetry materials and more general loading cases, it is convenient to use a formulation which enforces zero gradients in directions orthogonal to the direction of wave propagation [28, 140, 141]. Deformation is assumed to occur in all three directions; however, it is only allowed to vary with respect to the wave propagation direction, denoted X_1. Therefore, the deformation gradient takes the form

$$[\mathbf{F}] = \begin{bmatrix} F_{11} & 0 & 0 \\ F_{21} & 1 & 0 \\ F_{31} & 0 & 1 \end{bmatrix}. \tag{5.4}$$

The corresponding equations from Equations (5.1)-(5.3) reduce to

$$\rho_0 \frac{\partial v_i}{\partial t} = \frac{\partial P_{i1}}{\partial X_1} - \frac{\partial q}{\partial X_1}\delta_{i1} \tag{5.5}$$

$$\rho_0 \frac{\partial \mathcal{E}}{\partial t} = \left(P_{i1} - q\delta_{i1}\right)\dot{F}_{i1} \tag{5.6}$$

$$\frac{\partial F_{i1}}{\partial t} = \frac{\partial v_i}{\partial X_1}. \tag{5.7}$$

Numerical implementation of the finite-difference discretization that corresponds to Equations (5.5)-(5.7) is presented below. The spatiotemporal discretization of the grid

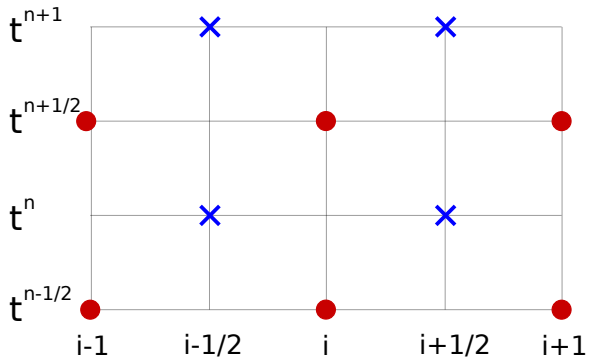

Figure 5.1: Finite difference discretization in space and time, where $\mathbf{v}$ is stored at (•) centered in space and at a half step in time, whereas $\mathcal{E}$, η, $\mathbf{P}$, ρ, and $\mathbf{F}$ are stored at (×) centered in time and at a half step in space. Artificial viscosity q is stored at the half step in both space and time.

closely follows the derivation presented in [76], and is shown schematically in Figure 5.1. To simplify the finite-difference analysis, the following restrictions are made: time steps are held constant throughout simulation, i.e., $t^{n+1} - t^n = \text{const} = \Delta t$; the simulation takes place on a uniformly spaced grid, i.e., $X_{1,i+1/2} - X_{1,i+1/2} = \text{const} = \Delta X_1$; and interfaces between materials with differing densities occur only at points centered in space, i.e., if two materials A and B have an interface at i with A on the left and B on the right, then $\rho_{0,i-1/2} = \rho_A$ and $\rho_{0,i+1/2} = \rho_B$. Temporal indices are subscripts and spatial indices are superscripts. Using these restrictions, the discretized one-dimensional form of Equations (5.5)−(5.7) for the conservation of momentum and energy, as well as continuity, are

$$\rho_0 \frac{v_i^{n+1/2} - v_i^{n-1/2}}{\Delta t} = \frac{\left(P^n_{i1,i+1/2} - q^n_{i+1/2}\delta_{i1}\right) - \left(P^n_{i1,i-1/2} - q^n_{i-1/2}\delta_{i1}\right)}{\Delta X_1} \tag{5.8}$$

$$\rho_0 \frac{\mathcal{E}^{n+1}_{i+1/2} - \mathcal{E}^n_{i+1/2}}{\Delta t} = \left[\frac{P^{n+1}_{i1,i+1/2} + P^n_{i1,i+1/2}}{2} - q^{n+1/2}_{i+1/2}\delta_{i1}\right] \frac{F^{n+1}_{i1,i+1/2} - F^n_{i1,i+1/2}}{\Delta t} \tag{5.9}$$

$$\frac{F^{n+1}_{i1,i+1/2} - F^n_{i1,i+1/2}}{\Delta t} = \frac{v^{n+1/2}_{i+1} - v^{n+1/2}_i}{\Delta X_1}. \tag{5.10}$$

In cases where two pairs of subscripts are separated by a comma, subscripts that occur before a comma denote the tensor's indices, whereas subscripts that occur after the comma denote the position on the grid. The artificial viscosity contains both linear [142] and quadratic terms [128], which are evaluated as

$$q^{n+1/2}_{i+1/2} = \frac{\rho^{n+1}_{i+1/2} + \rho^n_{i+1/2}}{2}\left(c_L a_1 \left|\Delta v^{n+1/2}_{1,i+1/2}\right| + a_2\left(\Delta v^{n+1/2}_{1,i+1/2}\right)^2\right) \tag{5.11}$$

where $\Delta v_{1,i+1/2}^{n+1/2} = v_{1,i+1}^{n+1/2} - v_{1,i}^{n+1/2}$, c_L is longitudinal wave speed, and $a_1 \approx 0.06$ and $a_2 \approx 2.0$ are values of fitting constants used to control the linear and quadratic viscosities taken from literature [143, 144]. The artificial viscosity is suppressed during expansion. For simplicity, the artificial viscosity in Equation (5.8) at step n is approximated as the viscosity calculated at step $n - 1/2$.

For thermoelastic materials and thermoelastic-viscoplastic materials, care must be exercised to ensure consistency between the energy calculated from the energy balance in Equation (5.9) and from the constitutive equation given by Equation (3.15). A general form of iterative equations that can be used to model crystals that employ a material Eulerian strain measure with terms up to third order in strain and second order in entropy, use mobile and immobile dislocation densities as internal state variables, and contain an uncoupled internal energy contribution of defects of the form $\Psi_2\left(N_m^\alpha, N_{im}^\alpha\right)$ is given by Equations (5.12)-(5.22), where a tilde indicates an intermediate value that is not stored

until convergence is satisfied:

$$\dot{\tilde{\gamma}}^{\alpha} = \sum_{\alpha=1}^{N} \tilde{N}_m^{\alpha} b \bar{v}^{\alpha} \left(\tilde{\tau}^{\alpha}, \mu^{\alpha}, \tilde{N}_m^{\alpha}, \tilde{N}_{im}^{\alpha}, \tilde{\theta} \right) + \dot{N}_{gen}^{\alpha} \left(\tilde{\tau}^{\alpha}, \tilde{\theta} \right) \bar{x}_{gen}^{\alpha} b, \tag{5.12}$$

$$\tilde{\mathbf{L}}_0^P = \sum_{\alpha} \dot{\tilde{\gamma}}^{\alpha} \left(\mathbf{s}_0^{\alpha} \otimes \mathbf{m}_0^{\alpha} \right), \quad \tilde{\mathbf{F}}^P = \exp\left(\tilde{\mathbf{L}}_0^P \Delta t \right) \mathbf{F}^P, \tag{5.13}$$

$$\tilde{\mathbf{F}}^E = \mathbf{F}^{n+1} \left(\tilde{\mathbf{F}}^P \right)^{-1}, \quad \tilde{\mathbf{D}}^E = \frac{1}{2} \left(\mathbf{I} - \left(\tilde{\mathbf{F}}^E \right)^{-1} \left(\tilde{\mathbf{F}}^E \right)^{-T} \right), \tag{5.14}$$

$$\tilde{\theta} = \theta_0 \left(1 + \frac{\Delta \tilde{\eta}}{\rho_0 c_{\epsilon}} - \left(\widehat{\mathbf{\Gamma}} + \frac{1}{2!} \tilde{\mathbf{D}}^E : \widehat{\mathbf{\Gamma}}_2 \right) : \tilde{\mathbf{D}}^E \right), \tag{5.15}$$

$$\tilde{\mathbf{\Pi}} = \left(\widehat{\mathbf{C}}_2 + \frac{\tilde{\mathbf{D}}^E}{2} : \widehat{\mathbf{C}}_3 \right) : \tilde{\mathbf{D}}^E - \Delta \tilde{\eta} \left(\widehat{\mathbf{\Gamma}} + \frac{\widehat{\mathbf{\Gamma}}_2}{2!} : \tilde{\mathbf{D}}^E \right), \tag{5.16}$$

$$\tilde{\boldsymbol{\sigma}} = \frac{1}{\det \tilde{\mathbf{F}}^E} \left(\tilde{\mathbf{F}}^E \right)^{-T} \tilde{\mathbf{\Pi}} \left(\tilde{\mathbf{F}}^E \right)^{-1}, \quad \tilde{\mathbf{P}} = \det \mathbf{F}^{n+1} \tilde{\boldsymbol{\sigma}} \left(\mathbf{F}^{n+1} \right)^{-T}, \tag{5.17}$$

$$\tilde{\tau}^{\alpha} = \tilde{\boldsymbol{\sigma}} : \left(\tilde{\mathbf{F}}^E \mathbf{s}_0^{\alpha} \otimes \mathbf{m}_0^{\alpha} \left(\tilde{\mathbf{F}}^E \right)^{-1} \right), \tag{5.18}$$

$$\tilde{N}_m^{\alpha} = N_m^{\alpha} + \dot{N}_m^{\alpha} \left(\tilde{\tau}^{\alpha}, \mu^{\alpha}, \tilde{N}_m^{\alpha}, \tilde{N}_{im}^{\alpha}, \tilde{\theta} \right) \Delta t, \tag{5.19}$$

$$\tilde{N}_{im}^{\alpha} = N_{im}^{\alpha} + \dot{N}_{im}^{\alpha} \left(\tilde{\tau}^{\alpha}, \mu^{\alpha}, \tilde{N}_m^{\alpha}, \tilde{N}_{im}^{\alpha}, \tilde{\theta} \right) \Delta t, \tag{5.20}$$

$$\tilde{\mathcal{E}} = \mathcal{E}^n + \left(\frac{\tilde{\mathbf{P}} + \mathbf{P}^n}{2} - q^{n+1/2} \mathbf{I} \right) : \frac{\mathbf{F}^{n+1} - \mathbf{F}^n}{\rho_0}, \tag{5.21}$$

$$\begin{aligned} &\frac{1}{2!} \frac{\Delta \tilde{\eta}^2}{\rho_0 \bar{c}} + \Delta \tilde{\eta} \left[1 - \left(\widehat{\mathbf{\Gamma}} + \frac{1}{2!} \tilde{\mathbf{D}}^E : \widehat{\mathbf{\Gamma}}_2 \right) : \tilde{\mathbf{D}}^E \right] \\ &+ \frac{1}{\theta_0} \left[\tilde{\mathbf{D}}^E : \left(\frac{\widehat{\mathbf{C}}_2}{2!} + \frac{\widehat{\mathbf{C}}_3}{3!} : \tilde{\mathbf{D}}^E \right) : \tilde{\mathbf{D}}^E + \Psi_2 \left(\tilde{N}_m^{\alpha}, \tilde{N}_{im}^{\alpha} \right) - \tilde{\mathcal{E}} \right] = 0. \end{aligned} \tag{5.22}$$

In Equation (5.22) $\widehat{\mathbf{\Gamma}}$, $\widehat{\mathbf{\Gamma}}_2$, $\widehat{\mathbf{C}}_2$, and $\widehat{\mathbf{C}}_3$ indicate the thermoelastic constants from Equation (3.15) and $\Delta \tilde{\eta}$ is obtained using the quadratic formula. These constants were given for single crystal aluminum in Table 3.3. A similar iterative scheme was developed to model the thermoelastic-viscoplastic response of crystals using an updated Lagrangian integration scheme in [145, 29].

5.2.2 Verification

To test whether or not the finite difference solution works properly for modeling plate in which quasi-longitudinal as well as quasi-transverse waves may form, the numerical method needs to be compared to a known analytical solution. Johnson developed an analytical method that can be used to model slip (boundary between impactor and target cannot

support shear stresses) and stick (boundary between impactor and target supports infinite shear stress) for longitudinal plate impact between linear elastic anisotropic materials that use infinitesimal strain [146]. A sample problem that exhibits large quasi-longitudinal as well as quasi-transverse waves is when X-cut quartz impacts Y-cut quartz. Due to its quartz's large elastic anisotropy, pronounced transverse waves form. Johnson expressed his solution in [146] in terms of non-dimensionalized sample length and impactor velocity, so that it could be applied to any problem of X-cut quartz impacting Y-cut quartz below the elastic limit.

Longitudinal plate impact was performed using a total Lagrangian elastic formulation in the finite-difference method presented in Section 5.2.1 and is compared to the analytical solution in Figure 5.2. Both the numerical and analytical result agree closely, except that the numerical solution predicts a wave that possesses a finite rise time. At first glance, this would appear to be due to mesh resolution or artificial viscosity; however, this is actually caused by the geometric softening inherent in compression when using the Green strain. Regardless of this slight difference, the numerical simulation shows that the finite difference method is capable of capturing the quasi-longitudinal as well as quasi-transverse wave formation, and that it occurs at the correct time as well.

5.3 Model parameterization

5.3.1 Determination of constants

Constants for the high strain rate viscoplastic material model were calculated in Chapter 4, and are either taken from literature [35, 36] or fit to single crystal shock experiments using plane wave simulations. Although plane wave simulations are able to capture the steady wave response, they are not sensitive to transient effects such as elastic precursor decay. Therefore, two constants have been adjusted that have little effect on the steady wave response, but significantly influence the precursor decay. The initial fraction of mobile dislocations is increased from $f = 0.01$ to $f = 0.30$. Also, the resolved shear stress at which heterogeneous nucleation occurs was adjusted from the resolved shear stress at the Hugoniot Elastic Limit (HEL) to $\tau_{min,het} = 0.1$ GPa.

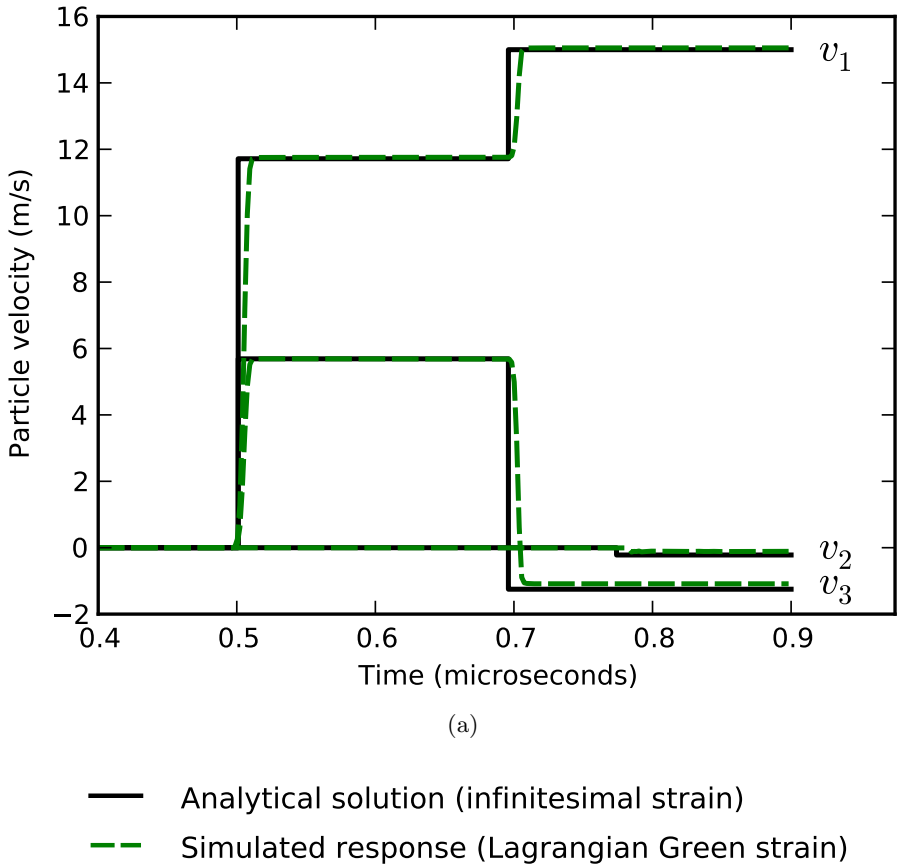

(a)

Figure 5.2: Analytical solution compared to numerical simulation for X-cut quartz traveling at 30 m/s impacting Y-cut quartz using second order elastic constants. The analytical solution uses an elastic infinitesimal strain $\boldsymbol{\epsilon}^e$ whereas the simulations use an elastic Lagrangian Green strain $\mathbf{E}^E$.

Parameters used to describe the homogeneous nucleation of dislocations in [147] were fit to obey the Swegle-Grady scaling relation and ensure a smooth transition between heterogeneous and homogeneous nucleation. Previously, Lagrangian thermoelasticity was used, which is applicable up to approximately 40 GPa using up to fourth order elastic constants; however, the formulation in this paper uses Eulerian material thermoelasticity to describe experiments that experience peak longitudinal pressures up to 110 GPa. Therefore, some of the material parameters have been adjusted to reflect experimentally observed transient elastic and plastic wave profiles. All of the parameters necessary to describe the constitutive model presented in Section 3.3 are given in Table 5.1, which indicates when parameters presented in this chapter differ from values given in Tables 4.1 and 4.2.

Table 5.1: Constants for single crystal high strain rate viscoplastic model of aluminum.

Parameter(s)	Value	Units	Equation(s)	Differs from Table 4.1 or 4.2?
Initial material state				
N_0^α	0.56	$1/\mu m^2$		no
f	0.3	none		yes
Homogeneous dislocation nucleation rate parameters				
$\dot{N}_{0,hom}$	$7.2 \cdot 10^7$	$1/(\mu m^2 \cdot \mu s)$	(3.34)	no
$g_{0,hom}$	0.04125	none	(3.34)	yes
$\tau_{0,hom}$	$\mu_0/20$	GPa	(3.34)	no
χ_{hom}	0.08	none	(3.34)	yes
$\bar{x}_{hom}$	$13.3b$	none	(3.34)	yes
Other dislocation density evolution parameters				
α_{het}	320	$1/\mu m^2$	(3.36)	no
m	0.8	none	(3.36)	no
τ_{min}	0.1	GPa	(3.36)	yes
τ_{max}	$\mu_0/25$	GPa	(3.36)	no
p_{mult}	0.088	none	(3.37)	no
α_{ann}	0.25	none	(3.38)	no
α_{dis}	0.051	none	(3.39)	no
Strength parameters				
α_{pass}	0.1	none	(3.26)	no
α_{cut}	0.9	none	(3.27)	no
Dislocation velocity parameters				
v_G	$1.0 \cdot 10^5$	$1/\mu s$	(3.33)	no
B_0 (300 K)	$1.8 \cdot 10^{-8}$	GPa $\cdot$ μs	(3.33)	no
g_0	1.0	none	(3.33)	no
p, q	0.5, 2	none	(3.33)	no

5.3.2 Model behavior in different regimes and effect of artificial viscosity

To understand how the thermoelastic-viscoplastic constitutive is affected by the artificial viscosity employed in the finite-difference numerical method, weak and strong shock loading simulations are performed on aluminum single crystals where the [100] direction is aligned with the loading direction. Recall that modeling normal impact on a [100] oriented single crystal is advantageous because 8 slip systems experience an equal resolved shear stress whereas the other 4 slip systems experience no shear stress. Also, because the [100] loading is stable under longitudinal compression, the crystal does not rotate. Therefore, quantities such as resolved shear stress, strength, dislocation rate, and mean dislocation velocity can be quantified in terms of single scalar quantities that are equal among all 8 slip systems.

Longitudinal plate impact of a Z-cut quartz flyer with a velocity of 435 m/s impacting a [100] oriented aluminum single crystal ($\sigma_{max} \approx 5$ GPa) were simulated both with and without an artificial viscosity. For both cases, the velocity profile, dislocation rates, shear stress, strength, and mean dislocation velocity were recorded a distance of 1.5 mm from the impact surface and are shown in Figure 5.3. The mesh resolution used in these simulations was $\Delta X_1 = 0.75$ μm, which implies approximately 100 material points were used to resolve the steady plastic wave. As shown in Figure 5.3, dislocation evolution is dominated by dislocation multiplication and trapping with some heterogeneous dislocation nucleation occurring during the initial stages. During the majority of plastic deformation dislocation velocity is proportional to the shear stress, which implies dislocations are in the drag-dominated regime. Plastic deformation slows down when dislocation velocity returns to the thermally activated regime and then ceases when $|\tau| \to \tau_{pass}$. There is little effect of artificial viscosity on the velocity profile except for slight oscillations about the HEL; however, the peak dislocation multiplication rate achieved is approximately 12% higher in the case of no artificial viscosity. This discrepancy demonstrates that even for this extremely refined mesh (which would most often be too computationally intensive for even 2d engineering problems) viscosity still plays a role, albeit subtle, in coupling with and damping the viscoplastic response. These simulations also show that given a fine enough mesh resolution, an artificial viscosity is not necessary to establish the shape of the plastic wave. Other weak shock loading

simulations are similar to the ones shown in Figure 5.3, with a notable difference that as the peak longitudinal stress experience by the material increases, the ratio of heterogeneous nucleation to other dislocation nucleation rates increases up to approximately 15 GPa. At higher stresses and depending on crystal orientation, homogeneous dislocation nucleation begins to play a more prominent role.

In the strong shock loading regime, a ramped stress boundary with $\sigma_{max} = 25$ GPa and $t_{rise} = 10$ ns was simulated for a [100] oriented aluminum single crystal with and without an artificial viscosity. The velocity profile and other viscoplastic characteristics were recorded at a position of 1.0 μm from the impactor surface for both cases and are shown in Figure 5.4. The mesh resolution used in these simulations was $\Delta X_1 = 0.5$ nm, which implies approximately 200 material points were used to resolve the plastic rise. Unlike the weak shock simulations performed at approximately 5 GPa, these strong shock simulations at 25 GPa show that the dislocation rate is dominated by the homogeneous nucleation rate. This homogeneous nucleation rate is also shown to be strongly dependent on the artificial viscosity. The peak homogeneous rate for the simulation without artificial viscosity is approximately one order of magnitude larger and oscillatory when compared to simulations that use an artificial viscosity. This numerical oscillation occurs because there are no dissipation mechanisms for the elastic wave and the finite-difference method cannot sufficiently resolve the shear stress jump and its effect on the increased homogeneous nucleation rate. The plot of dislocation velocity and shear stress shows a similar trend, where an artificial viscosity is needed to damp out numerical oscillations. For the simulation that uses an artificial viscosity, it is clear that the dislocation velocity has approached the relativistic regime as changes in the shear stress have minimal effect on the mean dislocation velocity until the shear stress decreases significantly. In this strong shock loading regime, the majority of plastic deformation is due to plastic deformation that occurs during homogeneous dislocation nucleation.

It is clear from these simulations that in the weak shock regime, given sufficient mesh resolution, the model does not need an artificial viscosity to resolve the plastic wave behavior; however, in the strong shock regime an artificial viscosity is necessary to damp out

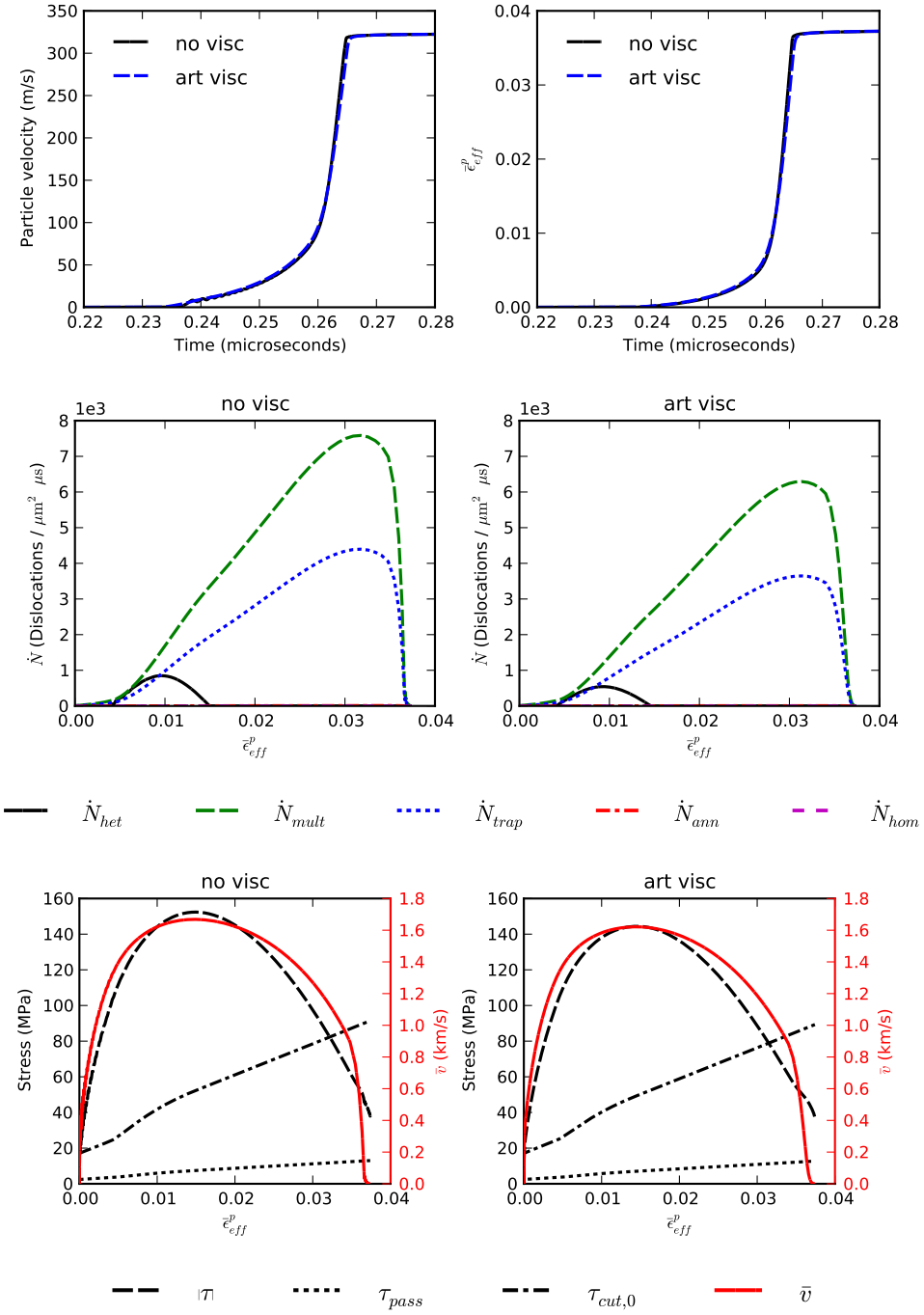

Figure 5.3: Velocity profile and viscoplastic deformation characteristics recorded at 1.5 mm for simulations (with and without an artificial viscosity) of a [100] oriented aluminum single crystal impacted by Z-cut quartz with a velocity of 435 m/s, which resulted in a peak longitudinal stress of 5 GPa. The dislocation density rate, resolved shear stress, strength, and velocity is plotted for one of the eight equally active slip systems. Effective plastic strain is defined as $\bar{\epsilon}^P_{eff} = \int_0^t \sqrt{2/3\mathbf{D}^P : \mathbf{D}^P}\, dt$.

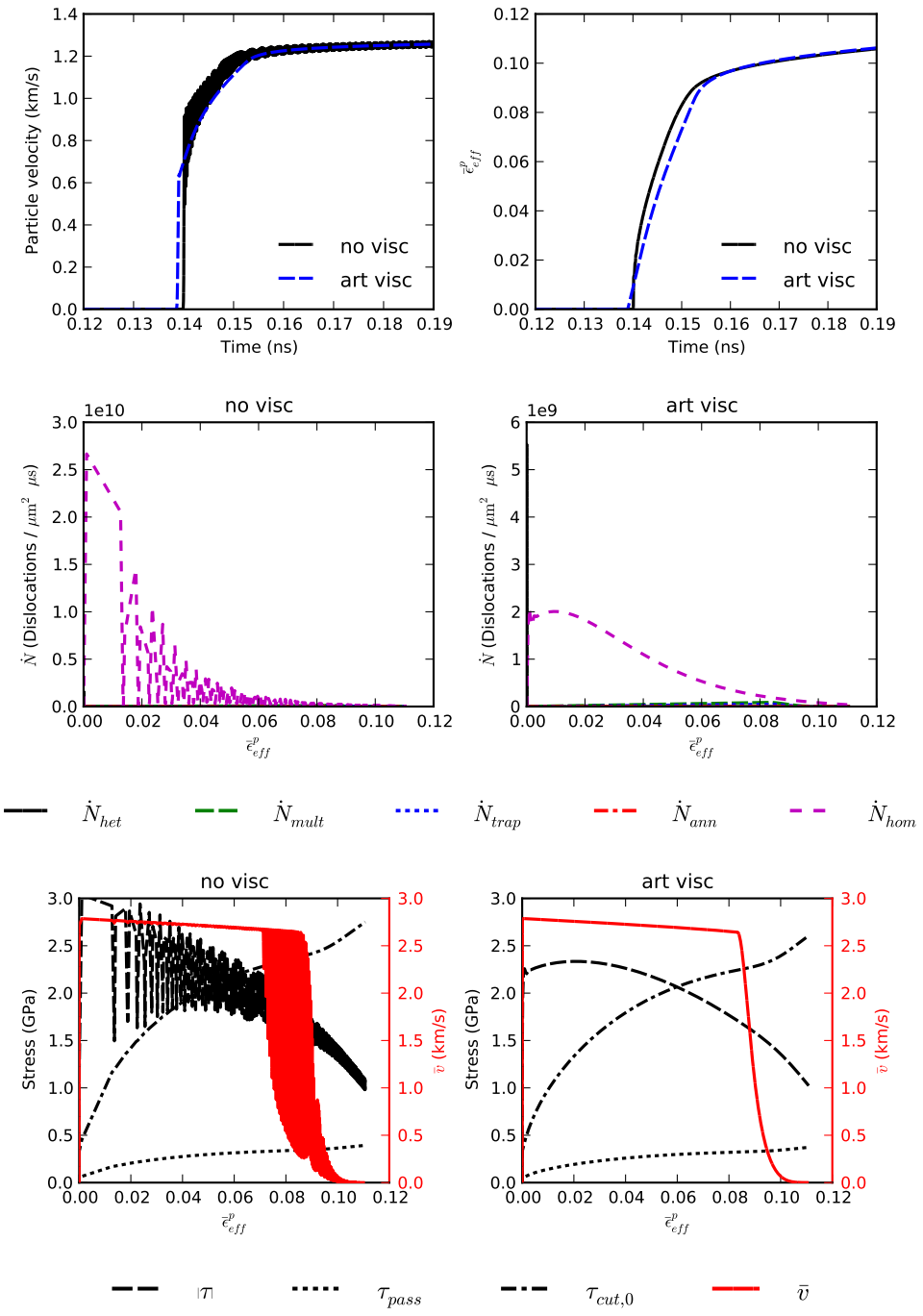

Figure 5.4: Velocity profile and viscoplastic deformation characteristics recorded at 1.0 µm for simulations (with and without an artificial viscosity) of a [100] oriented aluminum single crystal loaded with a stress boundary of $\sigma_{max} = 25$ GPa with $t_{rise} = 10$ µs. The dislocation density rate, resolved shear stress, strength, and velocity is plotted for one of the eight equally active slip systems. Effective plastic strain is defined as $\bar{\epsilon}^P_{eff} = \int_0^t \sqrt{2/3\mathbf{D}^P : \mathbf{D}^P} dt$. Note that the scale used for the dislocation rates differs for the case of no artificial viscosity and the case with an artificial viscosity.

the large stress change that occurs as the wave propagates. Although it is undesirable to use an artificial viscosity with a nonlinear viscoplastic model, it is shown to have a small effect on the plastic behavior and resultant velocity profile when a sufficiently fine mesh is used. If, however, the mesh is not sufficiently fine to resolve the shock width that would be predicted without an artificial viscosity, the solution will become highly dependent on the mesh and magnitude of the artificial viscosity.

5.4 Single crystal results

Plate impact and laser shock experiments are both used to probe the high strain rate shock response of materials. Plate impact imposes a discontinuous velocity jump at the boundary whereas laser shock imposes a ramped boundary loading, which is often idealized as a linearly ramped stress boundary condition, i.e,

$$\sigma(t) = \begin{cases} \sigma_{max}\,(t/t_{rise}) & \text{if } 0 < t < t_{rise} \\ \sigma_{max} & \text{if } t \geq t_{rise} \end{cases} \tag{5.23}$$

where σ_{max} is the peak loading stress and t_{rise} is the rise time.

Two main aspects of these experiments are examined by the high rate constitutive model: the attenuating transient elastic precursor and evolution of the wave to steady wave behavior. In a simplified sense, the attenuating precursor depends on the strain rate evolution at the onset of plastic flow. As the wave profile evolves towards a steady state, the strain rate at the elastic-plastic transition generally decreased, and the stress decreases commensurately. The plastic wave evolves to a state where a given stress increment produces the same momentum change along the wave front. Hence, the velocity profile at the wave front is governed by the constitutive model.

Normal plate impact experiments on Z-cut quartz striking [100] and [111] oriented single crystal aluminum specimens with various thicknesses [15, 12] are compared with plate impact simulations in Figure 5.5. The simulations explicitly modeled both the Z-cut quartz impactor and the target. Simulations did not include the Z-cut quartz window that was used by Huang and Asay (HA) (Turneaure and Gupta (TG) did not use a window); however, because the impedance of quartz is nearly that of aluminum, it is assumed to have a

negligible effect on the observed particle velocities for peak stresses $\sigma_{max} < 6$ GPa. For TG-[111] a peak stress of approximately 5.2 GPa was achieved using an impactor velocity of 623 m/s. For HA-[100] and HA-[111] a 5.6 GPa peak stress was achieved using an impactor velocity of 680 m/s. The experimental velocity profiles for TG-[111] and HA-[111] were shifted in time to match the simulated elastic wave because these experiments reported a time that was shifted, whereas HA-[100] used the time after impact, which can be directly simulated. All simulations employed a mesh spacing of $\Delta X_1 = 1.0$ μm.

Both the simulations and experiments show that for the [111] oriented single crystal with a specimen thickness of 0.82 mm the elastic precursor is higher than that of the [111] oriented single crystal with a specimen thickness of 2.985 mm. This suggests an attenuating elastic precursor, which is captured by the simulations. Note that some caution must be used when associating experiments of TG-[111] and HA-[111] as these experiments were performed years apart and the samples may have different purity and initial dislocation density; however, the simulations must assume that they have the same initial state. For the cases where a steady shock is assumed to have formed (HA) the simulations predict a greater rise time (5%-95% steady wave rise [131]) for the [111] orientation (36 ns) compared to the [100] orientation (22 ns), which is consistent with what is experimentally observed. The simulation correctly predicts the arrival time of the elastic wave and the slope of the steady wave for HA-[100] at later stages of the rise, but overestimates the amount of time over which the wave initially rises. The model also overestimates the elastic precursor for TG-[111]. Differences between the elastic precursor predictions and duration of plastic rise may occur because the model does not predict significant heterogeneous nucleation at these low stress levels; however, heterogeneous nucleation has even been observed in high purity single crystals [94]. Despite these differences, the model is able to reasonably capture orientation-dependence of single crystal aluminum in the weak shock regime, as indicated by a larger HEL and rise time in the [111] oriented single crystal as compared to the [100] oriented single crystals. A more stringent test of the constitutive model would be to measure both longitudinal as well as transverse velocity of low-symmetry orientations of single crystals; however, these measurements are more difficult to obtain than traditional

longitudinal measurements and are not known to these authors to exist in the literature.

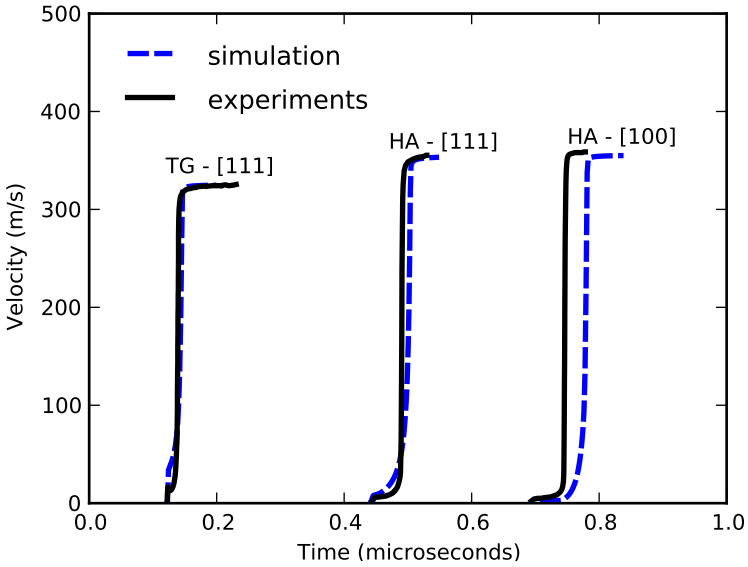

Figure 5.5: Particle velocity at the back face of the sample ($u_p \approx u_{fs}/2$) predicted by simulations of Z-cut quartz impacting single crystal aluminum compared with experiments. TG-[111] corresponds to an experiment performed by Turneaure and Gupta [15] on a [111] oriented single crystal with sample thickness 0.82 mm. HA-[111] and HA-[100] correspond to experiments performed by Huang and Asay [12] on [111] and [100] oriented single crystals with sample thicknesses of 2.985 mm and 4.501 mm, respectively.

One method to rapidly generate large stresses on the surface of a material is to use laser pulses to directly ablate the surface of the material. This ablated surface imparts a ramped loading on the target material due to momentum transfer at the ablated surface. Direct ablation experiments performed at peak stresses ranging from 20-40 GPa on vapor deposited aluminum [16] are compared with simulations in Figure 5.6 with various rise times. Vapor deposited aluminum has a strong [111] texture, which for these simulations is idealized as a [111] oriented single crystal. The direct ablation shock experiments were reported to have a laser pulse rise time of 10 ps; however, the rise time of the resulting pressure profile was not characterized, but is likely nonlinear. The experimental velocities were also averaged over a 10 ps window. The simulations explore the influence of a varying stress rise time t_{rise} on the observed particle velocity profile for specimen thicknesses of 0.72 and 1.44 μm. For the 20 GPa shock, both experimental and simulation results show a clear two-wave shock structure and an attenuating elastic precursor. For the 10 ps rise time

simulations, the elastic precursor rises sharply and abruptly transitions to the plastic wave. For 50 and 100 ps times, however, the elastic precursor and transition region before plastic deformation both have a finite width, which is consistent with experimental observations. For the 30 GPa, shock the model and simulation both predict an elastic precursor followed by the plastic wave. For the 30 GPa shock the 50 ps rise time fits the observed behavior most accurately, as was the case for the 20 GPa shock. For the 40 GPa shock, experimental results differ from simulations. For the 40 GPa shock, all of the simulated rise times predict that the plastic wave has not yet overrun the elastic precursor, where experimentally only a single shock structure is observed. This result will be discussed in depth in Section 5.5. Comparison of direct laser shock experiments and simulations show that for the 20 and 30 GPa cases, the observed experimental results can be captured by the model if the rise time is approximately 50 ps. These simulations highlight the sensitivity of the observed wave profile in direct ablation laser shock experiments on the stress boundary used to idealize the boundary conditions. Although the loading conditions present one factor that may greatly influence the observed response, other physical mechanisms may influence the wave profile such as the texture of the material, the purity of the sample, or residual porosity due to the vapor-deposition process. Without complete material characterization it is difficult to capture the influence of each of these mechanisms; however, texture influence will be explored in the next section.

Another method used to generate large stresses on the surface of a material, termed indirect ablation, is achieved by using lasers to rapidly heat a material or set of materials. As shock breakout occurs from the heated material, the ejected plasma piles up against and transfers its momentum to the target. Indirect ablation experiments at a peak stress of 110 GPa performed on vapor deposited aluminum [17] are compared with simulations in Figure 5.7. For the simulations, vapor deposited aluminum was approximated as a [111] single crystal and discretized with a mesh resolution of $\Delta X_1 = 75$ nm. There are distinct spatio-temporal differences between direct and indirect ablation experiments, which drastically alter their observed behavior. The indirect ablation experiments have a reported stress rise of $t_{rise} \approx 10$ ns, which was used in the simulations. This rise time is three orders of

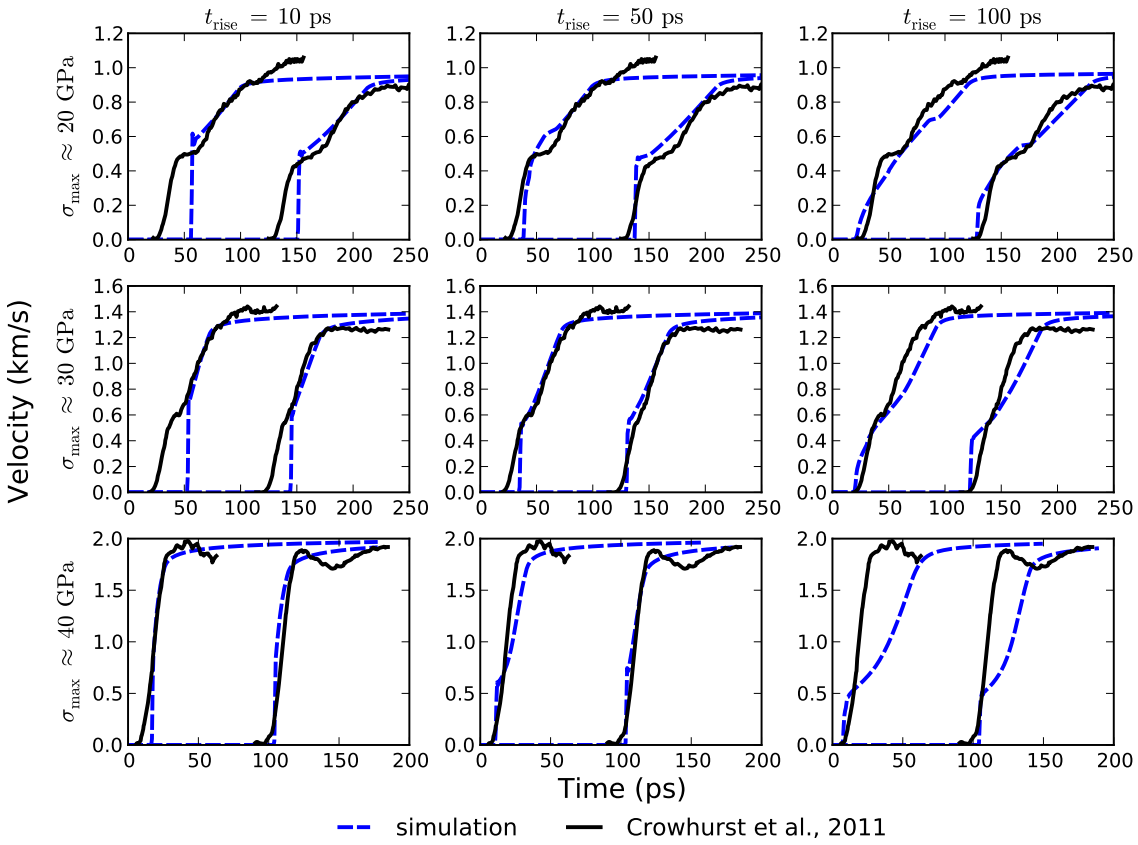

Figure 5.6: Comparison of simulated particle velocities of [111] oriented single crystals loaded with varying linearly ramped stress boundary conditions given by Equation (5.23) and experimental particle velocities ($u_p \approx u_{fs}/2$) given by direct ablation laser experiments in [16]. The wave profile on the left of each figure corresponds to the response at 0.72 μm whereas the wave profile on the right corresponds to the response at 1.44 μm. Experimental results were averaged using a 10 ps moving window.

magnitude longer than the reported laser rise in direct ablation experiments. Also, sample sizes in the indirect ablation are 30 μm, which is 15 times larger than used in the direct ablation experiments. The simulation results capture the steepening particle velocity of the plastic wave as it progresses from the 10, 20, and 30 μm steps. The simulations also capture the plateau that occurs before the main wave. Experimentally, no explanation was offered to explain this plateau as it was significantly higher than elastic precursors normally observed in shock experiments; however, simulation results suggest the plateau proceeding the plastic wave is an artifact of ramped boundary. This portion of the wave has not yet been overrun by the main steady wave because the relative time of the ramped loading conditions is large compared to the total simulation time. The simulation does not capture the finite width of the initial rise that is observed experimentally, however, this rise is due to loading in indirect ablation experiments. In these experiments, material with very low density first impacts the target prior to material with a substantial density, thus giving the leading foot behavior [148]. Because the loading is approximated by a simple linear stress boundary condition, the leading foot is not captured.

5.5 Polycrystal results

5.5.1 Preferentially oriented polycrystals

In most engineering applications, materials are both polycrystalline and have some initial texture. Effects of polycrystallinity due to the sensitivity of the ratio of shock width to characteristic dimension of grains has been quantified in previous work by Becker [129]. This work showed that as the process zone becomes much smaller than the grain size, as occurs in strong shock loading, the heterogeneity of residual plastic deformation is reduced. In this section, cases for which preferentially oriented polycrystalline samples significantly influence the observed behavior will be explored.

Gupta et al. [18] studied elastic precursor decay in small aluminum samples (50-200 μm). The samples were created by vapor deposition, which causes a columnar or needle-like structure to form in the direction of growth. The samples were shocked in the direction of growth, with an approximate length ranging from $3 - 6$ μm. Vapor deposited FCC

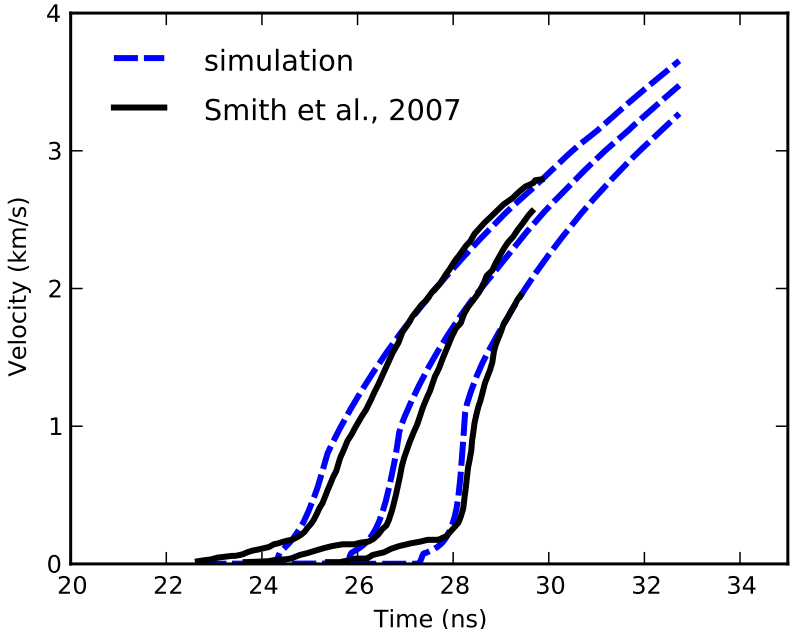

Figure 5.7: Comparison of simulated particle velocities of [111] oriented single crystals loaded with a linearly ramped stress boundary given by Equation (5.23) and experiments conducted by indirect ablation of vapor deposited aluminum samples performed by Smith et al. [17]. Both the experiments and simulations are have approximate loading conditions of $\sigma_{max} \approx 110$ GPa and $t_{rise} \approx 10$ ns. The curves from left to right correspond to 10, 20, and 30 μm steps. Experimental data were truncated when the release fan began to interfere with the measured signal. The peak temperature rise associated with the plotted data at the 10, 20, and 30 μm steps is 605, 615, and 665 K. At these temperatures it is appropriate to neglect shock melting effects.

samples often exhibit a strong [111] texture because the associated low index planes have the lowest surface energy of any orientation [149]. Therefore, if model parameters are used to fit precursor decay behavior, it is essential to understand how the decay is affected by the initial texture. A schematic of the idealized polycrystal is shown in Figure 5.8.

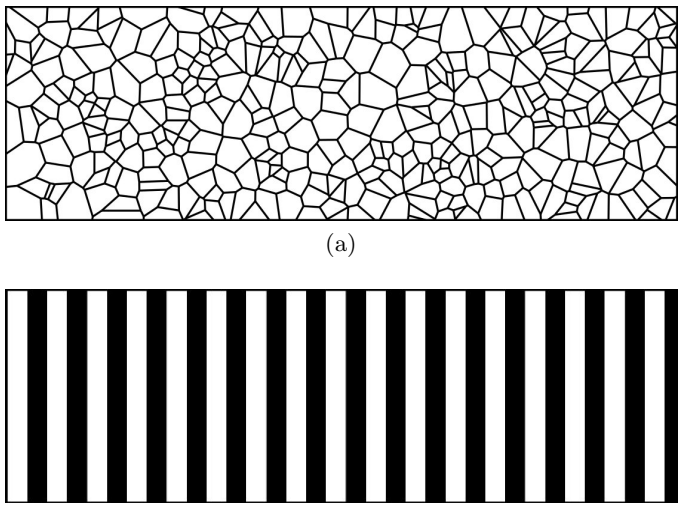

(a)

(b)

Figure 5.8: Schematic of (a) a realistic annealed polycrystal with many grains through the sample thickness and (b) its idealized representation using the extended, one-dimensional finite-difference method for anisotropic materials.

In Figure 5.9, simulated particle velocity profiles are shown at increasing times for single crystal and polycrystalline aluminum and are compared to observed elastic precursor data by Gupta et al. [18]. The polycrystal sample is idealized as a column of rectangular grains having an average grain size in the X_1 direction of 4.5 μm with a standard deviation of 1.0 μm. The mesh resolution is $\Delta X_1 = 0.055$ μm such that each grain is discretized by approximately 80 points, which is sufficient to allow intragranular stress gradients to develop. The polycrystalline samples have a preferential [111] texture, which is approximated by varying each of the three Euler angles randomly between 0 and $\pm n/2$ degrees, where n is the number indicated in the inverse pole figure inset for each graph. Figure 5.9 shows that as the texture increases from an ideal single crystal to a more random texture, model predictions more closely coincide with observed behavior. The simulated elastic precursor decreases by a factor of two as the texture transitions from a single crystal to a polycrystal with $n = 25$. These results show that increasing variability between grains increases

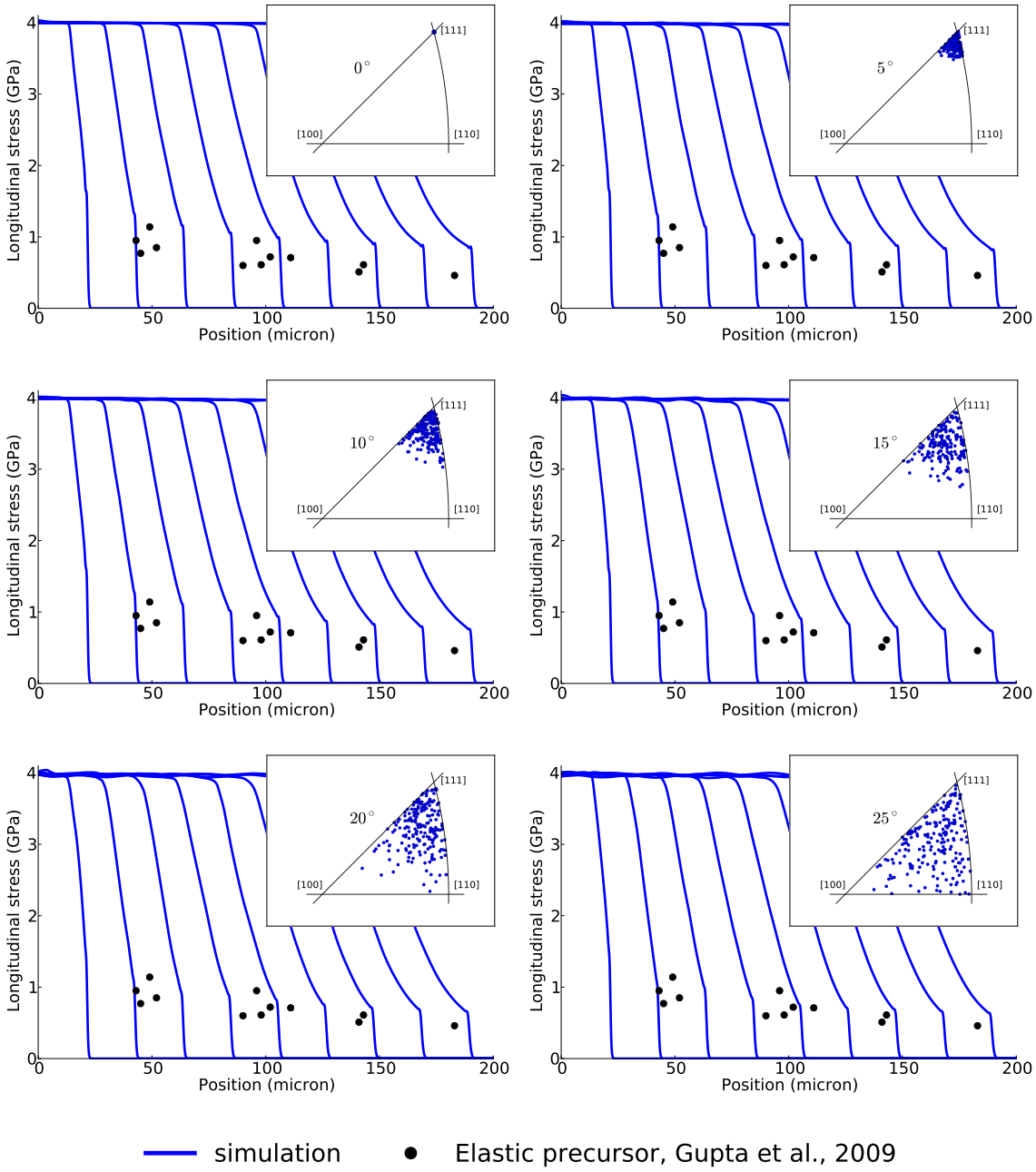

Figure 5.9: Simulation of attenuating wave profile at increasing times as a function of initial texture for plate impact experiments with Z-cut quartz impacting polycrystalline aluminum samples compared with experimentally measured elastic limits given in [18]. The simulations used a one-dimensional grain size of 4.5 μm with a standard deviation of 1 μm, which is used to represent the $3-6$ μm grain size reported in [18].

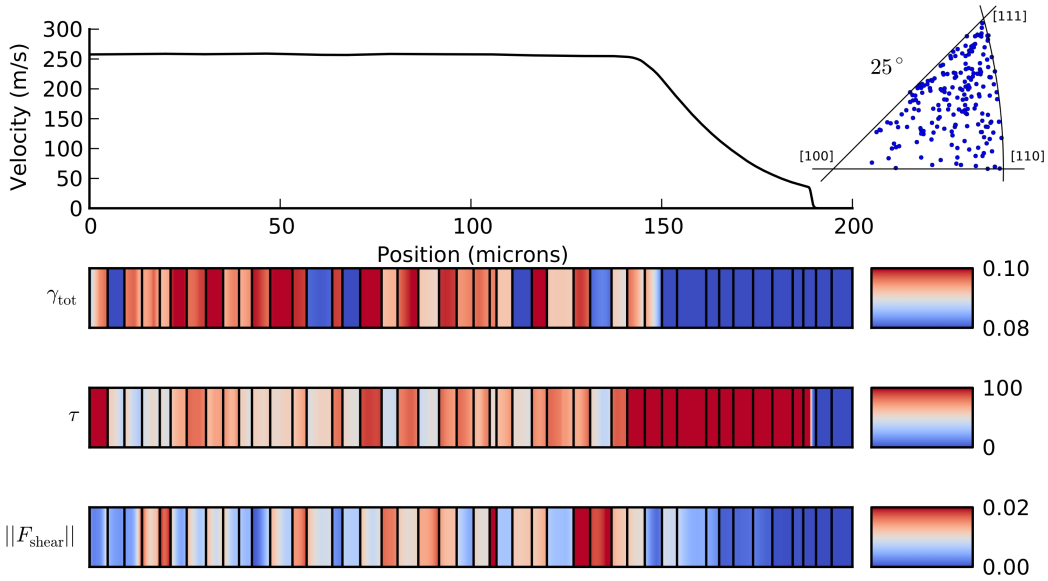

(a)

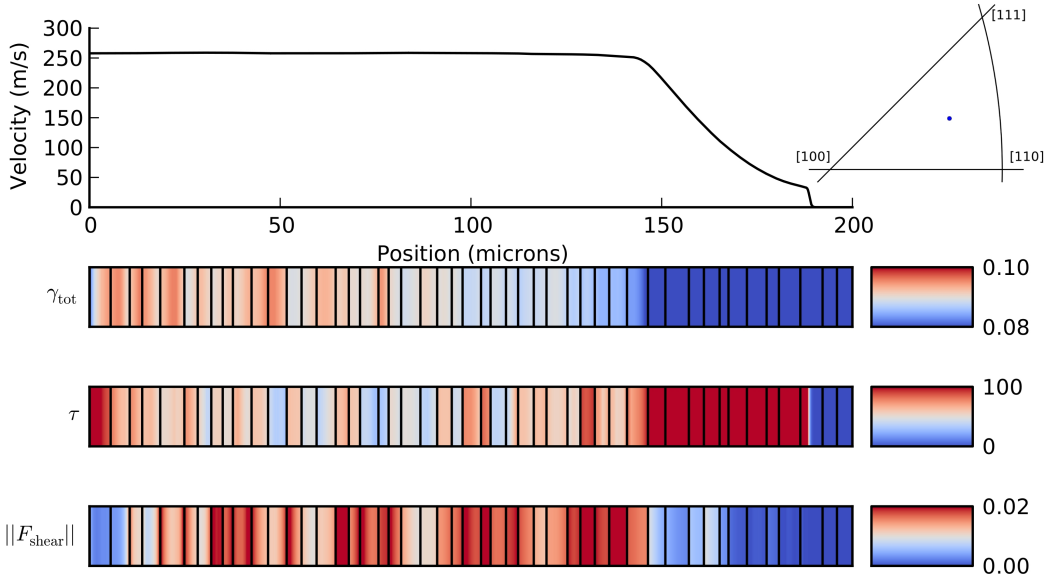

(b)

Figure 5.10: Velocity profile, total accumulated slip (γ_{tot}), shear stress ($\tau = \frac{1}{2}|\sigma_1 - \sigma_3|$ in MPa), and out of plane shear magnitude $||F_{\text{shear}}|| = \sqrt{F_{21}^2 + F_{31}^2}$ plotted for polycrystals with textures generated by (a) randomly varying Euler angles between 0° to ±12.5° about the [111] orientation and (b) first specifying a single orientation with 25° misorientation from [111] then varying the orientation randomly about the loading axis. Vertical lines indicate grain boundaries and all of the plots share the same position axis. Note that although (b) is a polycrystal that contains many different orientations, all orientations are represented by a single point on the inverse pole figure.

the attenuation rate of the elastic precursor; however, these simulations do not give the specific mechanism response for this attenuation. Many possible mechanisms may increase the attenuation rate such as differing longitudinal impedances between grains causing wave reverberation, varying dissipation rates between grains, shear mismatch induced at grain boundaries, and intragranular stress gradients between grains.

To isolate the specific mechanism responsible for the increased dissipation rate, polycrystals containing two different textures are simulated. First, a polycrystal is generated with grains randomly oriented randomly oriented about the [111] orientation with $n = 25$. Second, orientations are calculated by first generating an orientation that is misoriented 25° from the [111] orientation, and then randomly spinning this orientation about the loading axis. The result is a polycrystal in which every grain has the same Taylor factor and the same location on the inverse pole figure. The response of these two polycrystals is shown in Figure 5.10. Although the attenuated velocity profiles are nearly identical for the two polycrystals, their viscoplastic response differs significantly. The accumulated slip and shear stress varies drastically between grains for the polycrystal randomly oriented about [111] shown in Figure 5.10a, whereas the accumulated slip and shear stress is more uniform between grains for the polycrystal that has identical Taylor factors and longitudinal impedances between grains shown in Figure 5.10b. Although the polycrystal shown in Figure 5.10b has little accumulated plastic strain and shear stress heterogeneity, it has the same precursor attenuation rate as the polycrystal with grains randomly oriented about [111] due to large shear deformation components at grain boundaries induced by shear mismatch, which in turn create intragranular shear gradients. Because both polycrystals have nearly identical precursor attenuation rates but the polycrystal in Figure 5.10b has neither longitudinal impedance mismatch nor large plastic dissipation variation between grains, these simulations suggest that the shear mismatch between grains is responsible for increased elastic precursor decay. The shear mismatch induces shear stress and shear strain concentrations at grain boundaries, which induces large transgranular shear stress and shear strain gradients. Without taking into account the influence of crystallinity and

texture variation on precursor decay, constitutive model parameters derived from these simulations would have to include unrealistically large dislocation densities to achieve realistic precursor attenuation rates, which has been focus of previous studies [22, 150].

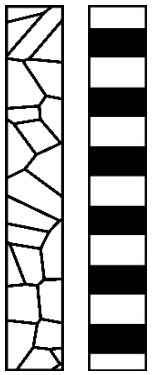

Figure 5.11: Schematic of (a) a realistic annealed polycrystal with few grains through the thickness and (b) its representation using the extended, one-dimensional finite-difference method for anisotropic materials. Note that if the region that is sampled to determine the back surface velocity is large compared to the grain size, this may be approximated as the average response of many individual crystals.

Although the above case highlights an example where orientation effects are manifested by the shock wave sequentially sampling the material, this is not the only case for which orientation effects are important. Consider the previous simulations in Figure 5.6 of direct ablation experiments [16], where the vapor deposited material is idealized as a [111] oriented single crystal. In reality, the vapor deposited material is again columnar in the direction of loading; however, these grains approximately span the 0.72 and 1.44 μm sample dimension. The grains were reported to have an in-plane diameter of approximately 100 nm whereas the spot size used to measure the velocity profile had a diameter of 20 μm. This implies that the measured velocity profile is the average response of thousands of individual grains. Schematically, this case is shown in Figure 5.11. In Figure 5.12, the response of a [111] single crystal is compared with the individual and aggregate response of 50 individually shocked single crystals with textures randomly varied about [111] by 15° and 25°. The simulations were loaded with a stress boundary condition of $\sigma_{max} \approx 40$ GPa with a rise time of $t_{rise} = 10$ ps, and employed a mesh resolution of $\Delta X_1 = 1$ nm. Figure 5.12 shows that at both depths and for both the 15° and 25° texture variations, the single crystals

individually exhibit an elastic precursor characterized by a two-wave structure; however, because the averaging process occurs over many orientations with slightly different elastic wave speeds and viscoplastic responses, the aggregate response is smooth. Experimentally, this response would be interpreted as a velocity profile with single wave structure, which is characteristic of an overdriven wave. Comparison of single crystal and polycrystal simulations suggest that discrepancies between single crystal simulations and experimentally measured wave profiles may be a manifestation of polycrystalline averaging effects instead of a characteristic of the single crystal viscoplastic dissipation response. This result may have significant implications for interpretation of Molecular Dynamics (MD) simulations of shock loading of single crystals, where inexplicably large elastic limits ($10 - 20$ GPa) are frequently observed [151, 152] even when large vacancy and defect concentrations are included [153]. In particular, if MD simulations of single crystals are compared with polycrystalline samples idealized as single crystals, the MD simulations may lack additional dissipation mechanisms and elastic smearing effects that occur in the real samples. This effect of polycrystal smearing on the elastic precursor has also been analyzed for certain idealized cases in a probabilistic framework, which predicted increased elastic rise times for increasing sample depth [154].

5.5.2 Rolled polycrystals

5.5.2.1 Generation of cold rolled microstructures

To quantify the effect of cold rolling on the shock response of polycrystals, realistic microstructures must be generated and input as initial conditions for shock loading simulations. For the constitutive model described in Section 3.3, the microstructure must have consistent values for both the grain orientation distribution and the dislocation density *on each slip system* that corresponds to each orientation. Taylor-type, rate-dependent crystal plasticity simulations have been shown to approximate texture evolution effects of single-phase FCC metals under a variety of loading conditions reasonably well [155].

To calculate the dislocation density on each slip system and texture due to rolling, the following procedure is used:

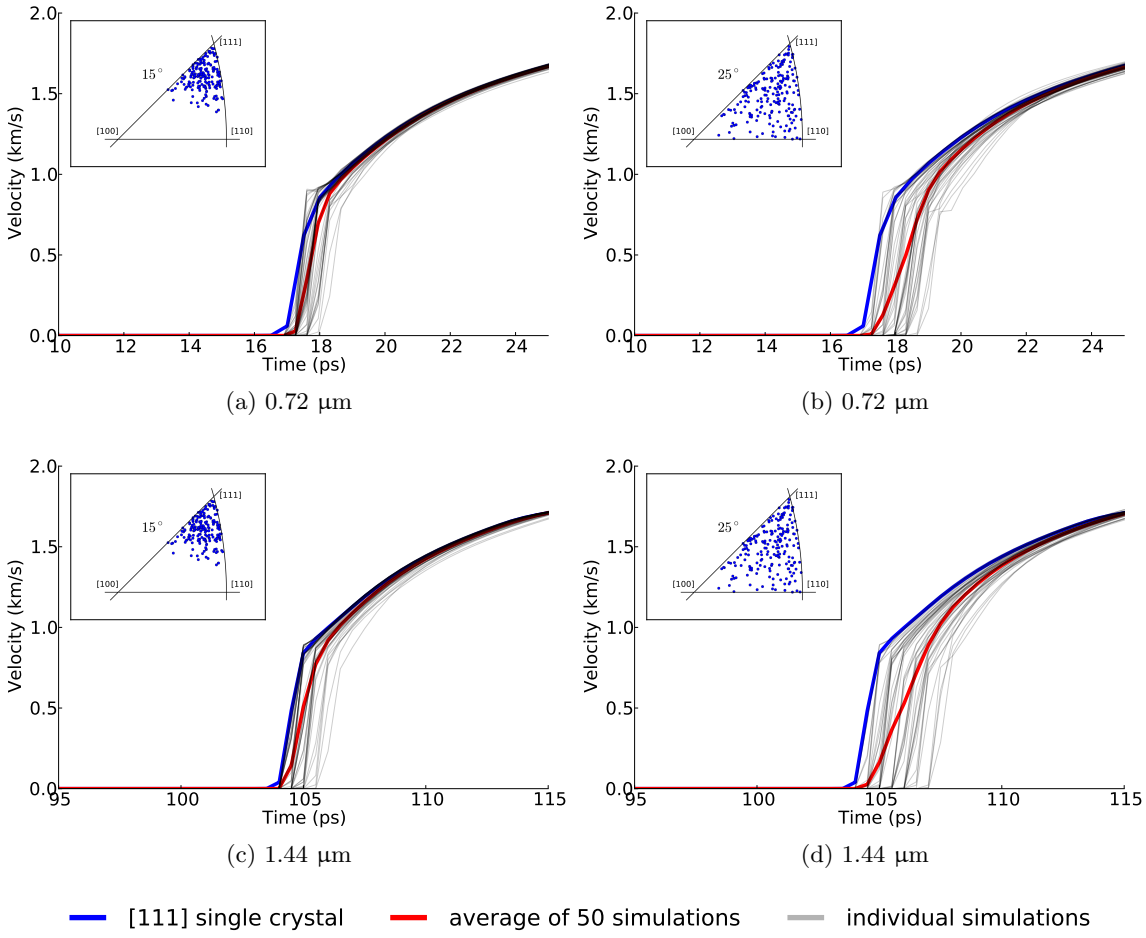

(a) 0.72 µm (b) 0.72 µm

(c) 1.44 µm (d) 1.44 µm

Figure 5.12: Comparison of [111] oriented single crystal simulation with the average response of 50 individual single crystal simulations with the initial texture given in the inset. All simulations used $\sigma_{max} = 40$ GPa and $t_{rise} = 10$ ps, the same as was used in the bottom left plot of Figure 5.6. Note that although each individual simulation has a two-wave structure with an elastic precursor, the aggregate averaged response exhibits a single wave shock structure characteristic of overdriven shock waves at both 0.72 and 1.44 µm, which is observed experimentally.

1. A hardening-recovery crystal plasticity model is fit to experimental quasistatic stress-strain compression data for aluminum from [156]

2. Plane-strain compression simulations are performed to rolling reductions of ($r = 0.05, 0.10, 0.30, 0.50$)

3. Final orientation and accumulated plastic strain ($\gamma^{\alpha}_{tot} = \int |\dot{\gamma}^{\alpha}| \, dt$) on each slip system ($\alpha$) are recorded for each grain in the simulations

4. The fraction of accumulated slip on each slip system for each grain ($f^{\alpha}_{sim} = \gamma^{\alpha}_{tot} / \sum_{\beta} \gamma^{\beta}_{tot}$) is recorded for each simulation

5. The simulated dislocation density on each slip system for each grain is calculated by the fraction of accumulated slip on each system times the experimental dislocation density given for various rolling reductions from [157] by Max $[N^{\alpha}_{tot} = f^{\alpha}_{sim} N_{tot,exp}, N_{ref}]$, where N_{ref} is the dislocation density in an annealed specimen

The crystal plasticity constitutive model used to simulate uniaxial and plane strain quasistatic compression closely follows that in [158], which is well documented [159, 160, 161] and is noted to be different than the viscoplastic model used for high rate deformation. Although the viscoplastic constitutive model presented in Section 3.3 could be used to simulate dislocation densities and associated textures at large strains, it possesses many features that are unnecessary to model quasistatic deformation. Therefore, the simpler model is used. The shearing rate on each slip system is driven by the resolved shear stress τ^{α}, i.e.,

$$\dot{\gamma}^{\alpha} = \dot{\gamma}_0 \left| \frac{\tau^{\alpha}}{g^{\alpha}} \right|^{1/m} \operatorname{sgn}(\tau^{\alpha}), \tag{5.24}$$

where $\dot{\gamma}_0$ is the reference shearing rate, g^{α} is the drag stress, and m is the strain rate sensitivity exponent. The drag stress evolves according to a hardening and recovery law [162]

$$\dot{g}^{\alpha} = H \sum_{\beta=1}^{N} q^{\alpha\beta} \left| \dot{\gamma}^{\beta} \right| - R g^{\alpha} \sum_{\beta=1}^{N} \left| \dot{\gamma}^{\beta} \right|, \tag{5.25}$$

where H is the direct hardening coefficient, R is the dynamic recovery coefficient, and $q^{\alpha\beta}$ is the latent hardening matrix. When the material is deformed at quasistatic rates, the

stress-strain response is insensitive to small changes to parameters $\dot{\gamma}_0$ and m. Values of the parameters $\dot{\gamma}$, m, and $q^{\alpha\beta}$ are taken as typical values from the literature, whereas values of $g_0^\alpha = g_0$, H, and R are found by performing a best fit of finite uniaxial strain simulations of 300 randomly oriented grains to experimental stress-strain data for aluminum [156] up to a true strain of -0.7, and are given in Table 5.2.

Table 5.2: Quasistatic crystal plasticity model parameters.

Parameter	Value	Units
$\dot{\gamma}_0$	0.0001	s^{-1}
m	50	
$q^{\alpha\beta}$	1	
g_0	20	MPa
H	68.17	MPa
R	1.573	

With the model parameters fit to finite uniaxial strain stress-strain data, cold rolling was simulated by performing plane strain calculations to rolling reductions of $r = 0.05$, 0.10, 0.30, and 0.50. The approximate dislocation density for the corresponding reductions levels are $N_{tot,exp} = 40$, 72, 227, and 465 $1/\mu m^2$, respectively. The total experimental dislocation density is found by averaging values given in [157] for different substructure types, noting that dislocation density was not observed to vary significantly among substructure types. The dislocation density on each slip system of each deformed grain is found by calculating $\mathrm{Max}\left[N_{tot}^\alpha = f_{sim}^\alpha N_{tot,exp}, N_{ref}\right]$ for each grain at each reduction level. The orientation of each of these deformed grains is also stored and used as initial conditions for the shock wave propagation problem.

5.5.2.2 Simulation results

Cold rolling has been studied extensively from the standpoint of its influence on the velocity profile and residual shocked microstructure; however, it is difficult to quantify how this pre-processing influences viscous plastic deformation processes in the shock wave. Direct simulation of the influence of cold rolling on the shock process circumvents experimental difficulties because plastic deformation characteristics can be tracked and evaluated in the shock wave. To understand whether simulation results agree with experimentally observed

behavior, experimental velocity histories from cold rolled aluminum are directly compared with simulations results. Williams et al. [19] recorded velocity histories for annealed and cold rolled aluminum shocked to different peak shock pressures in the weak shock regime. They used specimens 6 mm thick that were shocked along the normal direction (ND) to rolling. The pre-textured specimens were rolled to reductions of ($r = 0.30, 0.70, 0.80$). Because the experimental dislocation density [157] and wave profile is known for $r = 0.30$, both this reduction and annealed aluminum are simulated at different peak shock pressures, as shown in Figure 5.13. The simulations used a mesh resolution of $\Delta X_1 = 2.5$ μm. The simulations correctly predict that the HEL increases with increased rolling reduction, as shown in the inset for the 4 GPa case. The simulations also predict that rolling causes the shock to steepen significantly for the 4 GPa shock and that the 8 and 10 GPa shock profiles are not significantly influenced by rolling. Experimentally, however, the 4 GPa shock widths decrease more after rolling than simulations predict. This difference could be due to differing initial and resultant dislocation densities caused by rolling between [157] and [19], as dislocation density was not quantified in the shocked specimens. Although the experimental and simulated velocity profiles agree relatively well in most cases, they provide little insight on how both shock strength and rolling reduction influence dislocation-mediated plasticity.

Two metrics that have been employed in analysis of quasistatic crystal plasticity simulations are the total accumulated plastic slip on all of the slip systems (γ_{tot}) and the relative number of active slip systems (n_{active}) [114, 163]. In this chapter, n_{active} is defined as the number of slip systems that account for more than 5% of the total accumulated plastic slip. To illustrate the influence of cold rolling on these metrics, they are plotted for the material shocked at 10 GPa with different amounts of cold rolling in Figure 5.14. Qualitatively, two trends emerge from Figure 5.14; the heterogeneity of total accumulated slip decreases with increased cold rolling, and the number of active slip systems decreases with increased cold rolling. To help understand why this occurs, the individual mechanisms responsible for plastic deformation must be examined.

In the weak shock regime, viscoplastic deformation is controlled primarily by the glide

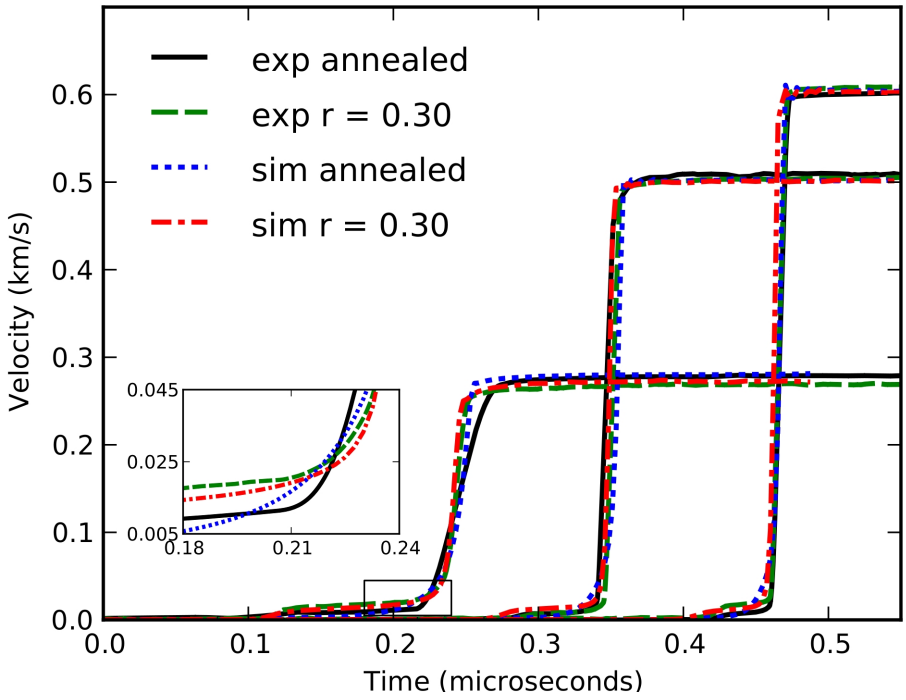

Figure 5.13: Comparison of particle velocity profiles for simulations and experiments [19] of plate impact experiments on both annealed ($r = 0$) and cold rolled ($r = 0.30$) aluminum shocked to peak stresses of approximately 4, 8, and 10 GPa. The sample thickness used in simulations and experiments is 6.0 mm. Time has been shifted so that all of the profiles are visible on a single chart. The inset is used to show the rise behavior for the 4 GPa shock in the region indicated by the small black rectangle.

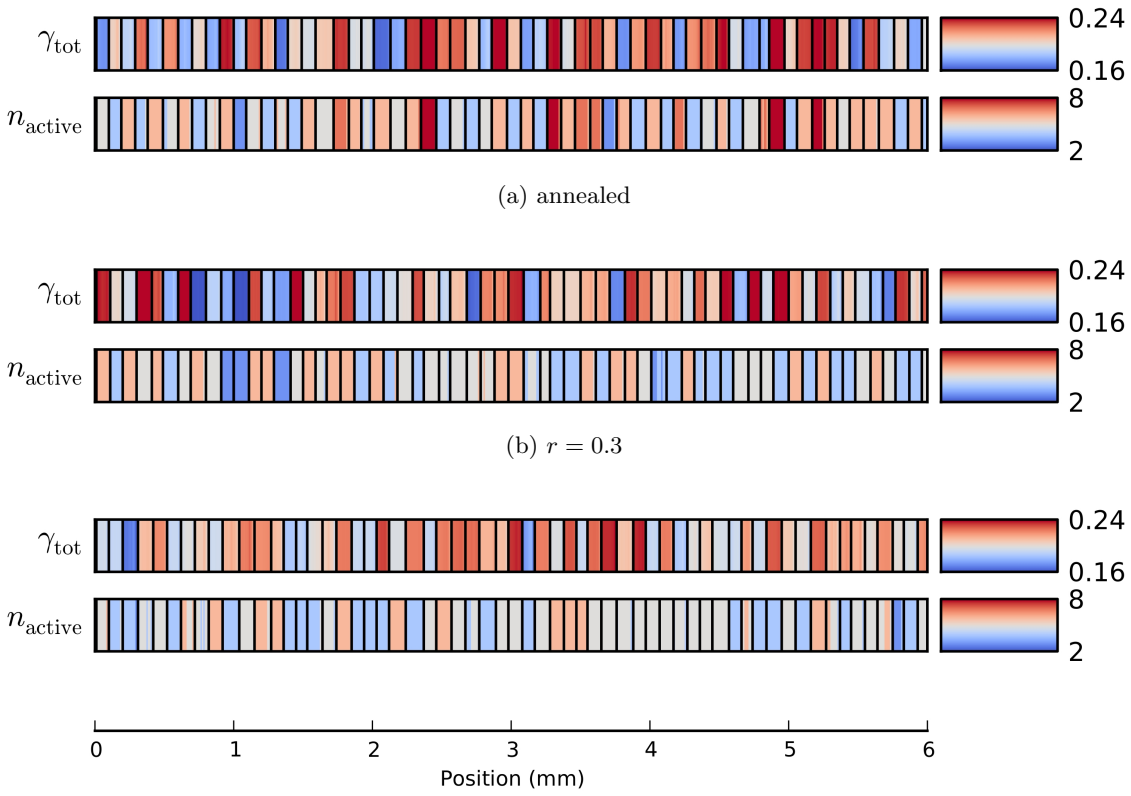

(a) annealed

(b) $r = 0.3$

(c) $r = 0.5$

Figure 5.14: Total accumulated slip (γ_{tot}) and number of active slip systems (n_{active}) for aluminum shocked to 10 GPa with different cold rolling reduction. Vertical lines indicate grain boundaries. Each grain is discretized by approximately 40 material points. All three sets of plots share a common longitudinal axis.

of mobile dislocations. For the viscoplastic model presented in Section 3.3, the mobile dislocation density in this regime is governed by the heterogeneous nucleation, multiplication, annihilation, and trapping mechanisms. The rates for which these mechanisms are operative are influenced by both the crystal orientation as well as the initial dislocation density. To quantify this influence, the mean and standard deviation for different plastic deformation metrics and dislocation mechanisms are plotted in Tables 5.3 and 5.4, respectively, where for example, $N_{\text{het,tot}}$ in Table 5.3 indicates the total density of dislocations created due to heterogeneous nucleation at each material point, averaged over all of the points in the domain. The values of the standard deviation of γ_{tot} and the mean of n_{active} for all three peak longitudinal stresses agree with the qualitative observation made from Figure 5.14 that accumulated slip heterogeneity decreases with increased rolling and that slip activity decreases for increased rolling. The mean value of n_{active} at the three different peak shock pressures shows that relative slip activity is most influenced in the 4 GPa case, and this influence decreases as the peak applied stress increases. Values for the mean total multiplication, trapping, and annihilation increase with increased rolling reduction; however, their relative ratios do not vary substantially. On the other hand, the number of dislocations produced by heterogeneous nucleation increases between a factor of 3-6, depending on the peak shock pressure. This increase can be attributed to both a decrease in the number of active systems and increased threshold stress on systems that were heavily deformed during the rolling process, necessitating heterogeneous nucleation to account for a larger portion of the total plastic deformation.

5.6 Discussion

The thermoelastic-viscoplastic model developed in Sections 3.2.2 and 3.3 has been shown to replicate experimentally observed aspects of single and polycrystal deformation of aluminum for peak shock pressures ranging from approximately $2 - 110$ GPa. Although the model may be applicable to even higher peak shock pressures, without experimental wave profiles resolved at these length and time scales, extrapolation of simulation results would be purely speculative. To the authors' knowledge, this is the first time the Eulerian material

Table 5.3: Mean values of viscoplastic deformation metrics and dislocation mechanisms averaged over all of the grains in 6 mm thick aluminum specimens with different cold rolling reduction, shocked to different peak shock pressures. Dislocation densities have units $1/\mu m^2$.

	$\sigma_{max} = 4$ GPa			$\sigma_{max} = 8$ GPa			$\sigma_{max} = 10$ GPa		
	$r = 0$	$r = 0.3$	$r = 0.5$	$r = 0$	$r = 0.3$	$r = 0.5$	$r = 0$	$r = 0.3$	$r = 0.5$
γ_{tot}	0.101	0.95	0.092	0.177	0.173	0.170	0.208	0.206	0.209
n_{active}	5.33	4.71	4.54	5.28	4.96	4.86	5.30	4.86	4.80
$N_{het,tot}$	1.2	0.8	3.85	11	35	66	19	56	124
$N_{mult,tot}$	164	373	481	452	838	1052	618	1074	1397
$N_{trap,tot}$	95	216	278	261	486	610	358	623	810
$N_{ann,tot}$	0.3	1.3	2.4	1.4	4.0	5.9	2.4	5.8	9.1

Table 5.4: Standard deviation of viscoplastic deformation metrics and dislocation mechanisms averaged over all of the grains in 6 mm thick aluminum specimens with different cold rolling reduction, shocked to different peak shock pressures. Dislocation densities have units $1/\mu m^2$.

	$\sigma_{max} = 4$ GPa			$\sigma_{max} = 8$ GPa			$\sigma_{max} = 10$ GPa		
	$r = 0$	$r = 0.3$	$r = 0.5$	$r = 0$	$r = 0.3$	$r = 0.5$	$r = 0$	$r = 0.3$	$r = 0.5$
γ_{tot}	0.012	0.010	0.008	0.020	0.020	0.018	0.024	0.023	0.016
n_{active}	0.95	1.02	0.87	1.23	1.01	0.79	1.21	0.95	0.77
$N_{het,tot}$	4.5	1.9	4.1	8.0	35	51	6.9	48	58
$N_{mult,tot}$	35	47	48	103	142	137	138	178	143
$N_{trap,tot}$	20	27	27	60	83	79	80	103	83
$N_{ann,tot}$	0.09	0.30	0.57	0.43	0.87	1.37	0.68	1.4	1.86

strain measure has been implemented into a numerical shock wave propagation framework to study spatio-temporal effects of shock wave propagation in single crystals. As shown when compared to the Green strain in Section 3.2.4, this strain measure is particularly useful because it can model these large shock pressures using terms only up to third order in strain in the internal energy. The dislocation-based viscoplastic model has been shown to reproduce shock wave attenuation and shock widths in both the weak and strong shock regimes, as well as the respective dislocation mechanisms that dominate these responses. In particular, this model can suggest regimes where different dislocation mechanisms are most active as well as the relative contribution of each slip system to the total deformation. Understanding the operative dislocation mechanisms as well as relative slip activity is useful for interpreting the microstructure of the material in the shocked state. Although experimental data is sparse that can confirm or refute the relative contributions of single-crystal deformation mechanisms predicted by the model, recent in situ x-ray diffraction measurement techniques may elucidate particular dislocation mechanisms and their respective rates [164].

Single crystal simulations of aluminum with different orientations showed relatively good agreement with the HEL and shock width measured in plate impact experiments [15, 12]. In particular, the results showed that the [100] orientation had a shorter rise time than the [111] orientation in the weak shock regime. Comparison of single crystal simulations with laser shock simulations showed a large dependence of the observed behavior on the loading conditions. For the 20 and 30 GPa shock cases, experimental wave profiles were only able to be reproduced if the stress rise time was approximately 50 ps, which differs than the laser rise time of 10 ps reported experimentally [16]. Simulations for the 40 GPa case exhibited an elastic precursor, whereas experiments showed the shock wave possessed a single-wave, overdriven structure. For the 110 GPa laser shock experiments, simulated and experimental velocity profiles profiles agreed closely [17]. Simulation results showed that for these experiments, the shock wave is steepening and not yet overdriven due to the slowly ramped boundary conditions. Furthermore, these simulations show that the observed velocity plateau is due to the loading conditions, whereas in the experiments the authors

were unable to resolve the cause of the large elastic precursor [17]. Both the direct and indirect ablation simulations highlight the difficulty in interpreting results of single-crystal shock experiments, especially for problems where time-dependent loading conditions may significantly influence the measured results such as occurs in laser shock experiments.

Polycrystal orientation effects were simulated for the case of elastic precursor attenuation in plate impact experiments and in laser shock experiments. Simulations of plate impact loading on vapor-deposited polycrystals with varying degrees of orientation spread to a peak shock stress of 4 GPa showed that as the orientation spread increases from a pure [111] oriented single crystal to a polycrystal with a 25° random spread about the [111] orientation, the magnitude of the observed elastic precursor decreased by a factor of 2. The decrease in amplitude for simulation results agreed with experimentally measured precursor decay [18] without using an unrealistically large initial dislocation density. In the 40 GPa peak pressure laser shock simulations on 1.44 μmthick vapor deposited samples, it was shown in Figure 5.12 that the average response over many crystals (as measured experimentally) many mask the apparent elastic precursor for both a 15 and 25° random spread about the ideal [111] orientation. Experimentally, the measured 40 GPa shock case shows a single overdriven shock; however, simulations suggest that for this sample size and loading rate an elastic wave separation is still developing. The difference between the response of an ideal oriented single crystal and the aggregate response of a polycrystal with multiple grains may resolve differences observed anomalously high elastic limits observed in MD simulations that make a direct comparison to polycrystalline laser shock experiments by idealizing them as single crystals.

Simulations of pre-textured polycrystals were performed by first simulating the rolling process using quasistatic crystal plasticity simulations to give the orientation and dislocation density on each grain, then using these quantities as initial conditions for the shock-wave simulation. Simulation and experimental wave profiles both predicted increased HEL and a decreased shock width for the 4 GPa peak shock stress at higher rolling reductions. For the 8 and 10 GPa peak shock pressures, neither simulations nor experiments showed a measurable change in shock width with rolling. Simulations and experiments agreed

concerning the effect of rolling on the HEL and shock profile. Simulation results showed the following trends emerged as the cold rolling reduction increased from $r = 0$ to 0.5: a decrease in the heterogeneity of plastic strain, a decrease in the number of active slip systems, with the lowest peak shock stress showing the largest decrease; and an increase in the total amount of heterogeneous deformation that occurs. Although increased rolling causes a strength increase, a decrease in the number of active slip systems may result in an increase in the number of high angle boundaries that form during shock deformation or the formation of strain localization regions. High angle boundaries have been shown to be possible nucleation sites during unloading [19], which may influence the spall strength of the material. Strain localization has been shown to occur in instances where less slip systems are active in both quasistatic [165, 166] and shock experiments [23]. Although this model does not explicitly address subgrain dislocation substructure formation, these simulations give insight into deformation behavior that influences subsequent substructure development and refinement during the shock loading process.

5.7 Conclusion

The work in this chapter establishes a framework for direct numerical simulation of the individual single crystal response due to shock loading for peak pressures up to 110 GPa. Model parameters have been developed for aluminum single crystals and give plausible results when compared with existing single crystal and polycrystal experimental results. In the case of both single crystal and polycrystal loading, simulations gave appreciably different results for the case when the initial microstructure was idealized as homogeneous as compared to the case when material heterogeneity due to randomly or preferentially oriented single crystals was included. It was shown that material heterogeneity significantly affected observed precursor decay and in some cases changed the observed shock structure from a single to a dual shock structure. Because these simulations show the large dependence of resultant wave profile on the initial material characterization for weak and strong shock loading experiments, without detailed information about the grain structure these studies must be considered incomplete. Studies lacking microstructure characterization should also

discuss approximations that arise by neglecting initial and evolving material heterogeneity.

These simulation results suggest that as more intricate single crystal high strain rate models are developed [129, 29, 30, 167, 33, 32], they must be considered only partially validated unless they are directly compared against realistic microstructures, such as laser-shock experiments performed by Whitley et al. [168] or studies that give detailed measurements of evolving dislocation densities. For some simulations in this chapter, either an assumed or simulated microstructure was used, and it was shown how this microstructure and its possible variations may influence the shock response. Although the high strain rate thermoelastic-viscoplastic model and its associated parameters gave plausible results for shock experiments simulated in this chapter, model parameters may be further refined as more experimental work that employs careful microstructural characterization becomes available.

CHAPTER VI

MODEL COMPARISONS AND EXTENSIONS

Up to this point, the thermoelastic-viscoplastic model has been considered in the context of two separate numerical integration schemes, i.e., the plane wave formulation presented in Chapter 4 and the finite-difference method presented in Chapter 5. One advantage of the plane wave method is that it does not employ an artificial viscosity, whereas the finite-difference method does. On the other hand, the plane wave method as formulated in this work must assume uniaxial strain, despite that impact problems may be encountered wherein impact is not symmetric and quasi-longitudinal as well as quasi-transverse waves form. In this Chapter, direct comparisons are made between predictions of the plane wave and finite-difference methods. Then, a formulation is presented to examine whether or not results from the plane wave method can replicate direct finite-difference simulations of polycrystals.

Because the plane wave method employs Lagrangian thermoelasticity and the material constants presented in Tables 4.1 and 4.2 whereas the finite-difference method uses Eulerian material thermoelasticity with the constants presented in Table 5.1, adjustments need to be made so that these two methods can be compared directly. Although Eulerian material thermoelasticity is considered superior for modeling shock loading, altering the plane wave method to use this strain measure would be extremely burdensome. Therefore, the finite-difference method was altered to use Lagrangian thermoelasticity. In both methods, only elastic constants up to third order were used and only constants up to first order in temperature (or entropy) were used. Both models used material constants given in Tables 4.1 and 4.2. With these changes, the material models used in the plane wave and finite difference simulations that follow are identical.

6.1 Comparison of plane wave and finite-difference methods

To evaluate approximations introduced by the plane wave and finite-difference methods, an array of test problems is created in which additional approximations are sequentially added and their effect is evaluated. Because the plane wave method must approximate strain as uniaxial, it should give an exact solution for impact problems where the target is shocked along a three-fold symmetry axis or greater (which results in uniaxial strain) and approximate for problems with lower symmetry (quasi-longitudinal and quasi-transverse waves form should form). In Section 5.3.2, it was shown that the finite-difference method can be used reasonably well to model weak shock loading problems without an artificial viscosity, but in the strong shock regime artificial viscosity is necessary to damp the large jump in velocity that precedes plastic deformation. To make a comparison between the methods, four types of simulations are run and are given in Table 6.1.

Table 6.1: Approximations introduced by numerical methods for four simulations.

Simulation Description	Plane wave approximation	Finite-difference approximation
5 GPa [100]	None	None
5 GPa low symmetry	Assumes deformation as uniaxial	None
25 GPa [100]	None	Uses artificial viscosity
25 GPa low symmetry	Assumes deformation as uniaxial	Uses artificial viscosity

6.1.1 Wave profile and viscoplastic response comparison

For finite-difference simulations, a 5 GPa shock was generated by longitudinal plate impact using an a-Sapphire impactor. The sample thickness used in this case is 1.5 mm and employed a mesh resolution of $\Delta X_1 = 0.75$ μm. Velocity profiles from the plane wave and finite-difference simulations are compared in Figure 6.1. Because plane wave simulations only have a notion of relative time, the wave profile was adjusted so that it was centered on the finite-difference solution, which uses total time after impact. As expected, the plane wave and finite-difference wave profiles give nearly identical results. There is a slight deviation at the elastic limit, which may be caused by numerical oscillations because an artificial viscosity was not used in these simulations. In Figure 6.2, viscoplastic deformation

characteristics (described using dislocation density rates, strength, and dislocation velocity) are compared. Figure 6.2 shows that the viscoplastic response is nearly identical for both sets of simulations.

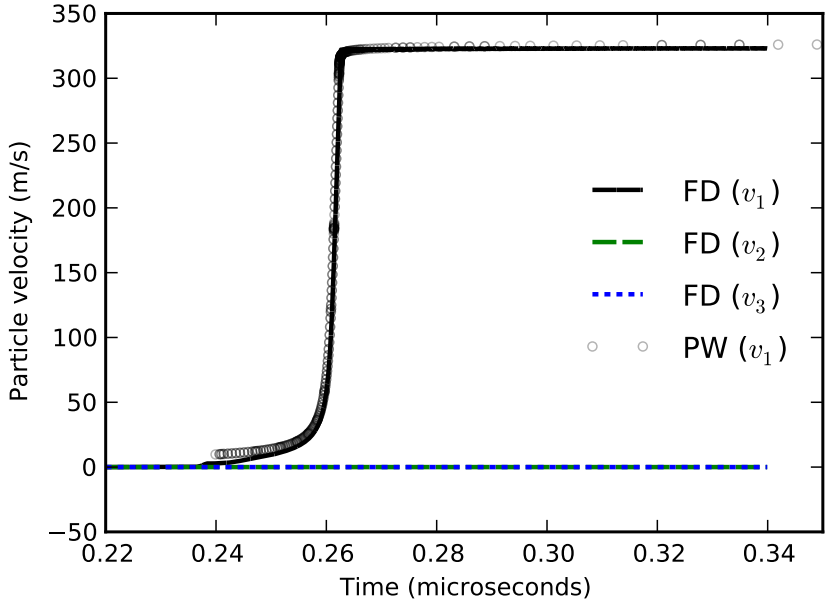

Figure 6.1: Particle velocity profile recorded at 1.5 mm for a [100] oriented aluminum single crystal shocked to approximately 5 GPa using the plane wave formulation (PW) and the finite-difference method (FD) without an artificial viscosity.

To simulate impact in the low-symmetry crystal, the same finite-difference simulations that were performed on the [100] oriented crystal are performed on the low-symmetry crystal, although the velocity of the a-Sapphire flyer was adjusted so that a 5 GPa longitudinal stress was achieved. The low symmetry orientation uses Bunge angles $\phi_1 = 43.7°$, $\Phi = 49.26°$, and $\phi_2 = 132.8°$, which corresponds to the orientation shown on the inverse pole figure shown in Figure 5.10b. The velocity profile from the finite-difference and plane wave simulations for this case is shown in Figure 6.3. Figure 6.3 illustrates that the plane wave method does a reasonable job approximating the longitudinal component of the quasi-longitudinal wave, although it cannot model the out of plane velocity components. At 0.45 μs after impact, a the quasi-transverse wave arrives at the back surface, which cannot be captured using the plane wave method. Unlike the case for impact on the [100] oriented crystal where dislocation density rates were nearly identical between the two

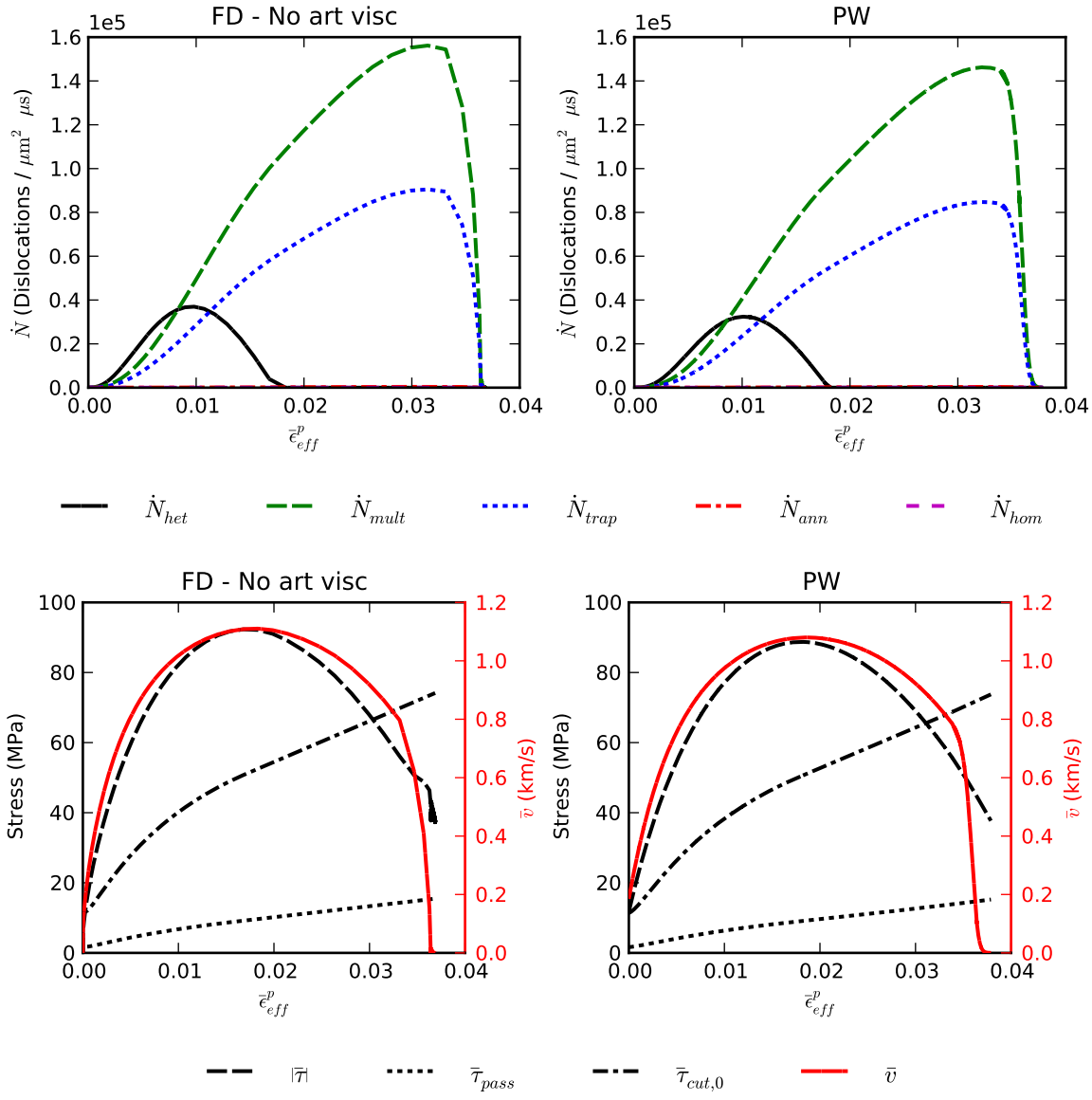

Figure 6.2: Viscoplastic deformation characteristics recorded at 1.5 mm for a [100] oriented aluminum single crystal shocked to 5 GPa using the plane wave formulation and the finite-difference method without an artificial viscosity. The dislocation density rate is summed over all systems, whereas the shear stress, strengths, and mean velocity are averaged over all slip systems.

methods, the dislocation density rates shown in Figure 6.4 indicate that the finite-difference method predicts slightly larger dislocation density rates than the plane wave method. This is understood by noting that the plane wave method neglects transverse wave components that increase the applied shear strain. Although predictions from the two methods deviate slightly, viscoplastic predictions from the plane wave method deviate less than 10% from predictions given by the finite-difference method, which are assumed to be correct in this case.

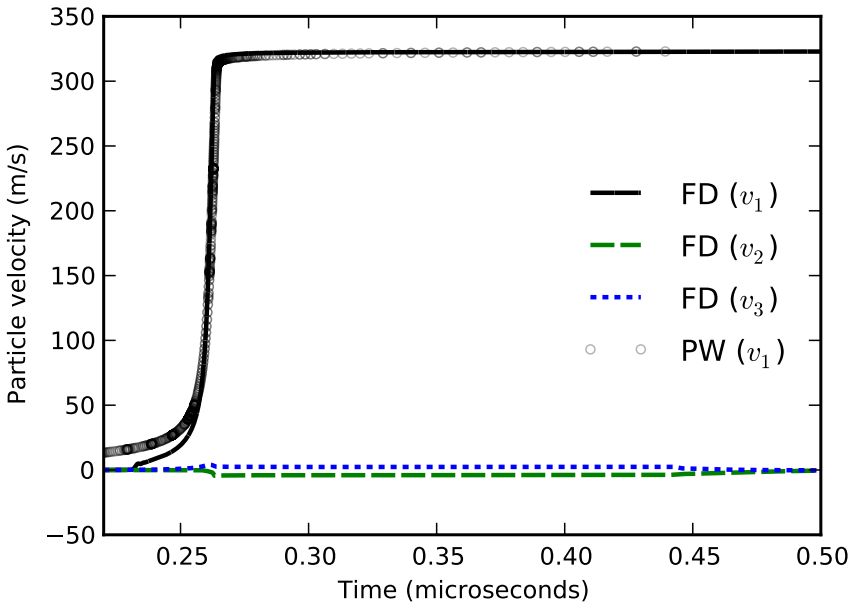

Figure 6.3: Particle velocity profile recorded at 1.5 mm for a low symmetry aluminum single crystal shocked to approximately 5 GPa using the plane wave formulation and the finite-difference method without an artificial viscosity. The plane wave solution uses relative time so the solution was translated so that it is centered on the FD profile.

For finite-difference simulations, a 25 GPa shock was again generated by longitudinal plate impact using an a-Sapphire impactor that is assumed to possess infinite strength. The sample thickness used in this case is at 0.75 μm and these simulations employed a mesh resolution of $\Delta X_1 = 0.375$ nm. Velocity profiles from the plane wave and finite-difference simulations are compared in Figure 6.1. Because the plane wave method begins to track the solution at an adiabatic elastic compression wherein the longitudinal elastic wave speed

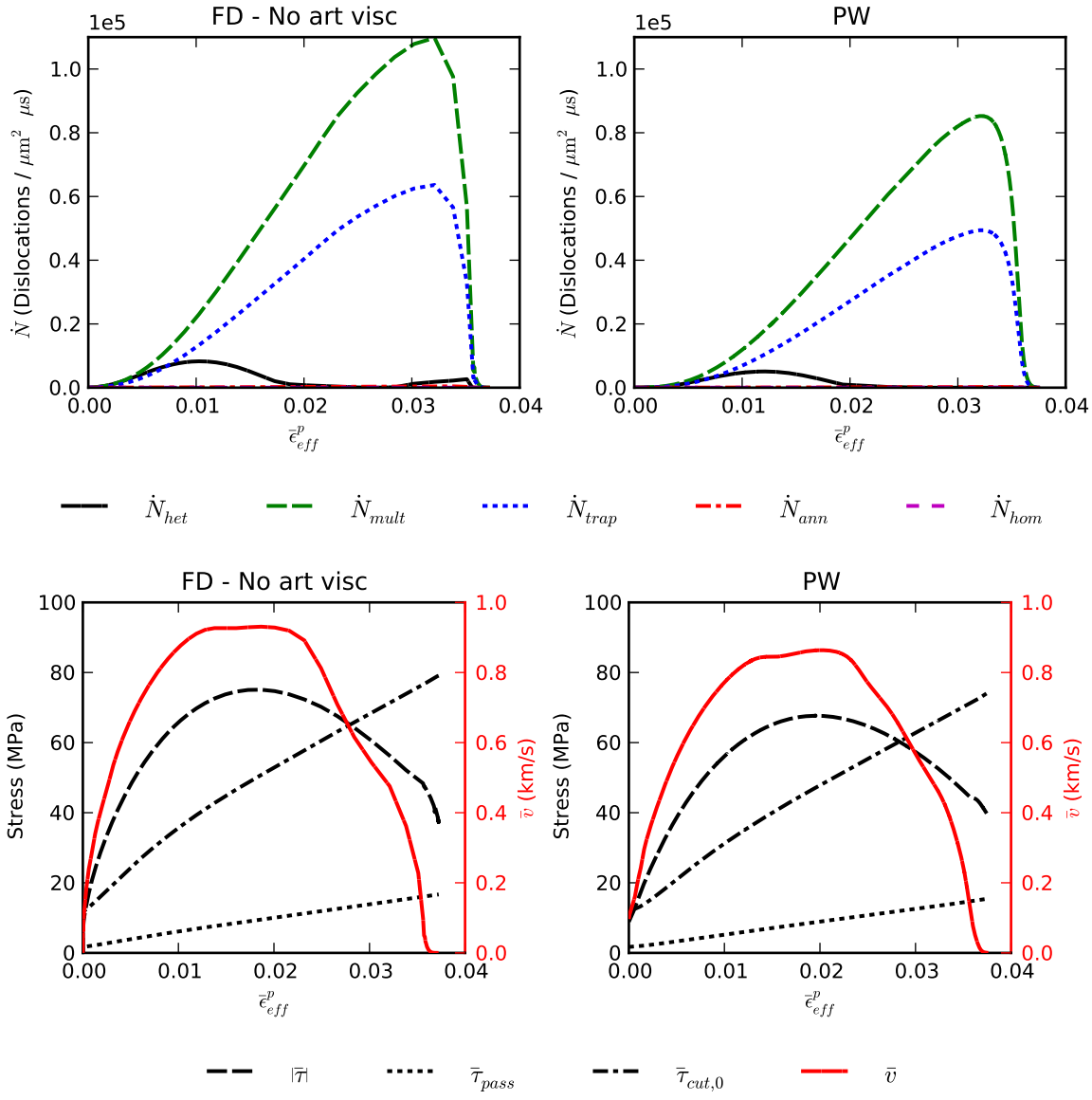

Figure 6.4: Viscoplastic deformation characteristics recorded at 1.5 mm for a [100] oriented aluminum single crystal shocked to 5 GPa using the plane wave formulation and the finite-difference method without an artificial viscosity. The dislocation density rate is summed over all systems, whereas the shear stress, strengths, and mean velocity are averaged over all slip systems.

equals the steady wave speed (in this case at approximately 0.5 km/s), it gives no information about the wave profile up to this velocity; however, the wave thickness predicted by the finite-difference method up to this velocity is solely due to the artificial viscosity, so no physical information is gained in finite-difference simulations up to this point either. At the peak velocity, the plane wave method predicts a more gradual evolution up to peak velocity whereas the finite-difference method predicts a more abrupt change. The differences in these predictions can be understood by examining Figure 6.6, where viscoplastic deformation characteristics between the two methods are compared. The plane wave simulations predict a homogeneous nucleation rate that is approximately three times greater than what is predicted using the finite-difference method. Additionally, the finite-difference method predicts negligible heterogeneous nucleation whereas the plane wave method predicts some finite heterogeneous nucleation. These discrepancies are caused by the additional damping from the artificial viscosity, wherein the actual stress is damped out causing decreasing dislocation density evolution rates. The coupling between the viscosity and viscoplastic deformation rates in the finite-difference method is undesirable, although it has a seemingly negligible influence on the resultant effective plastic strain and strength evolution.

To simulate impact in the low-symmetry crystal, the same finite-difference simulations were performed, although the velocity of the a-Sapphire flyer was adjusted so that a 25 GPa longitudinal stress was achieved. The predicted velocity response of the two methods is compared in Figure 6.7. Figure 6.7 shows that there are many aspects of the two predictions that differ. The finite-difference method again captures the formation of a quasi-longitudinal wave follows by a quasi-transverse wave, which cannot be captured using the plane wave method. Additionally, the finite-difference method predicts a single wave structure, whereas the plane wave methods indicates there is a some deformation that precedes the main rise. The plots of viscoplastic deformation characteristics shown in Figure 6.8 indicate that the finite-difference method predicts higher dislocation density rates than the plane wave method, but again predicts negligible heterogeneous nucleation. Both of the methods pick up the fluctuating dislocation velocity, which is due to the large rotation and shear stresses that rapidly activate and deactivate additional slip systems.

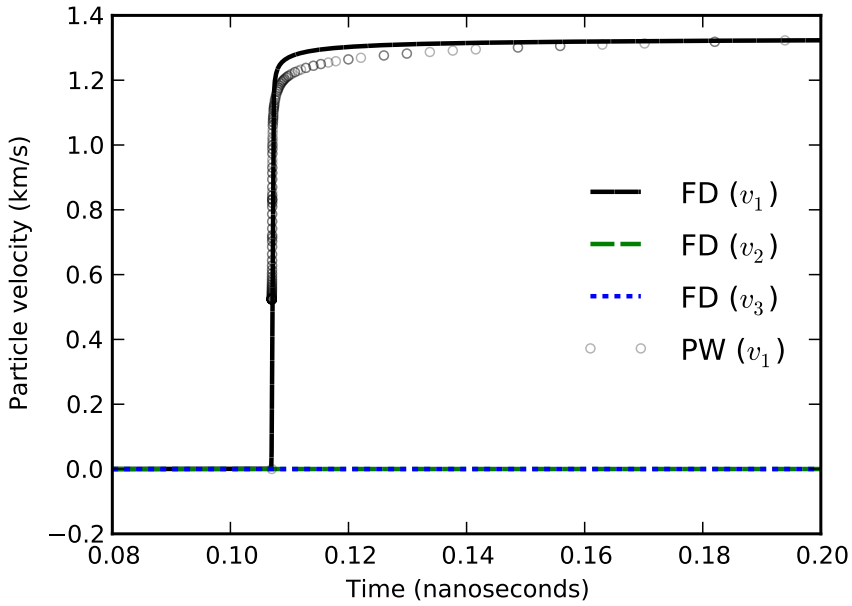

Figure 6.5: Particle velocity profile recorded at at 0.75 μm for a [100] oriented aluminum single crystal shocked to approximately 25 GPa using the plane wave formulation and the finite-difference method without an artificial viscosity. The plane wave solution uses relative time so the solution was translated so that it is centered on the FD profile.

6.1.2 Computational efficiency comparison

In Chapter 4, it was stated qualitatively that the plane wave method is a computationally efficient method; however, this was not justified by direct simulation. To make a direct comparison, the computational times for simulations performed in the previous section are compared in Table 6.2. Table 6.2 shows that in all cases, the plane wave method is significantly more computationally efficient than the finite-difference method. For all of the simulations, the plane wave method used an implicit Adams method to solve the equations, which resulted in significantly increased solution resolution around rapidly varying areas (the sharp plastic rise) and decreased resolution around slower varying areas. This is reflected by the detailed dislocation density evolution rates shown in Section 6.1.1 compared to the coarser resolution offered by the finite-difference method. If the relative tolerance used by the plane wave method was decreased to the tolerance used by the finite-difference method, the speedup factor would be approximately 10,000 times that of the finite-difference method.

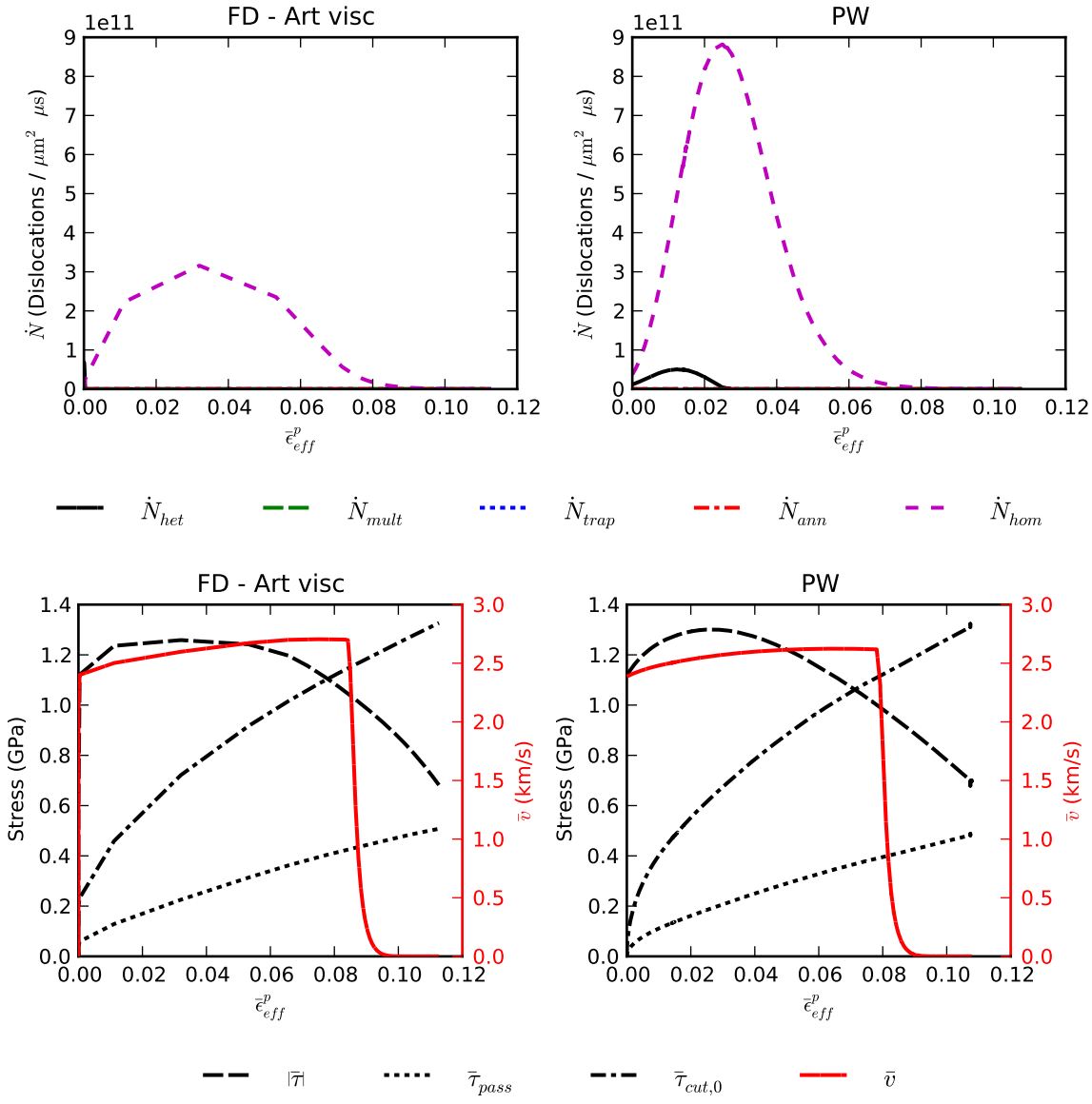

Figure 6.6: Viscoplastic deformation characteristics recorded at 1.5 mm for a [100] oriented aluminum single crystal shocked to 25 GPa using the plane wave formulation and the finite-difference method without an artificial viscosity. The dislocation density rate is summed over all systems, whereas the shear stress, strengths, and mean velocity are averaged over all slip systems.

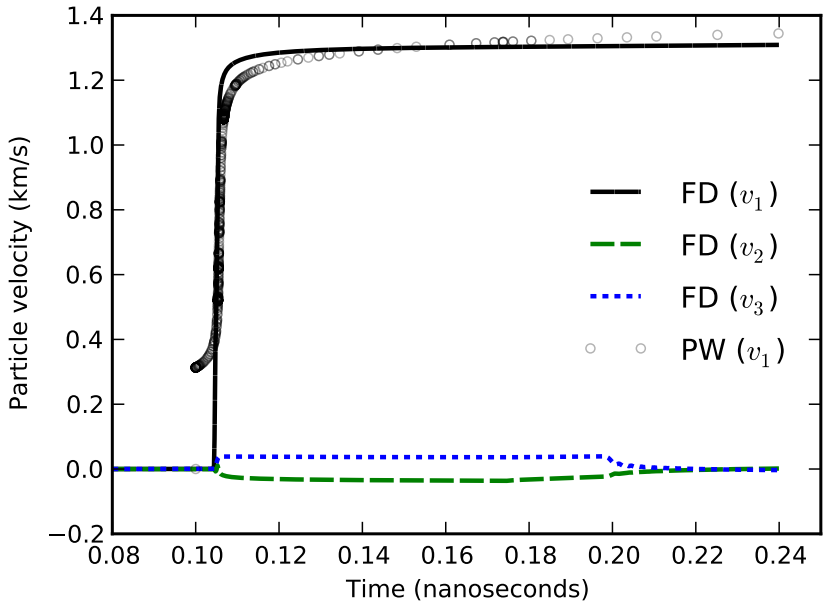

Figure 6.7: Particle velocity profile recorded at 0.75 μm for a low symmetry crystal shocked to 25 GPa using the plane wave formulation and the finite-difference method with an artificial viscosity. The plane wave solution uses relative time so the solution was translated so that it is centered on the FD profile.

Table 6.2: Comparison of total computational time to perform simulations shown in Section 6.1. Computation times are for a single 2.67 GHz Intel Xeon X5650 processor.

	Total machine time (s)		
Simulation Description	Plane wave	Finite-difference	Speedup factor
5 GPa [100]	32.38	7090	219.0
5 GPa low symmetry	58.24	21466	368.6
25 GPa [100]	15.99	31368	1961.7
25 GPa low symmetry	70.43	28555	405.4

Once caveat for using the plane wave method is that it is not readily parallelized. Because the finite-difference method is a local problem and most of the computational time is spent solving the thermoelastic-viscoplastic model, it is an "embarrassingly parallel" problem that scales nearly linearly with number of processors.

6.1.3 Discussion

In this section, approximations introduced by the finite-difference and plane wave methods were examined by directly comparing equivalent problems in the weak (5 GPa) and strong

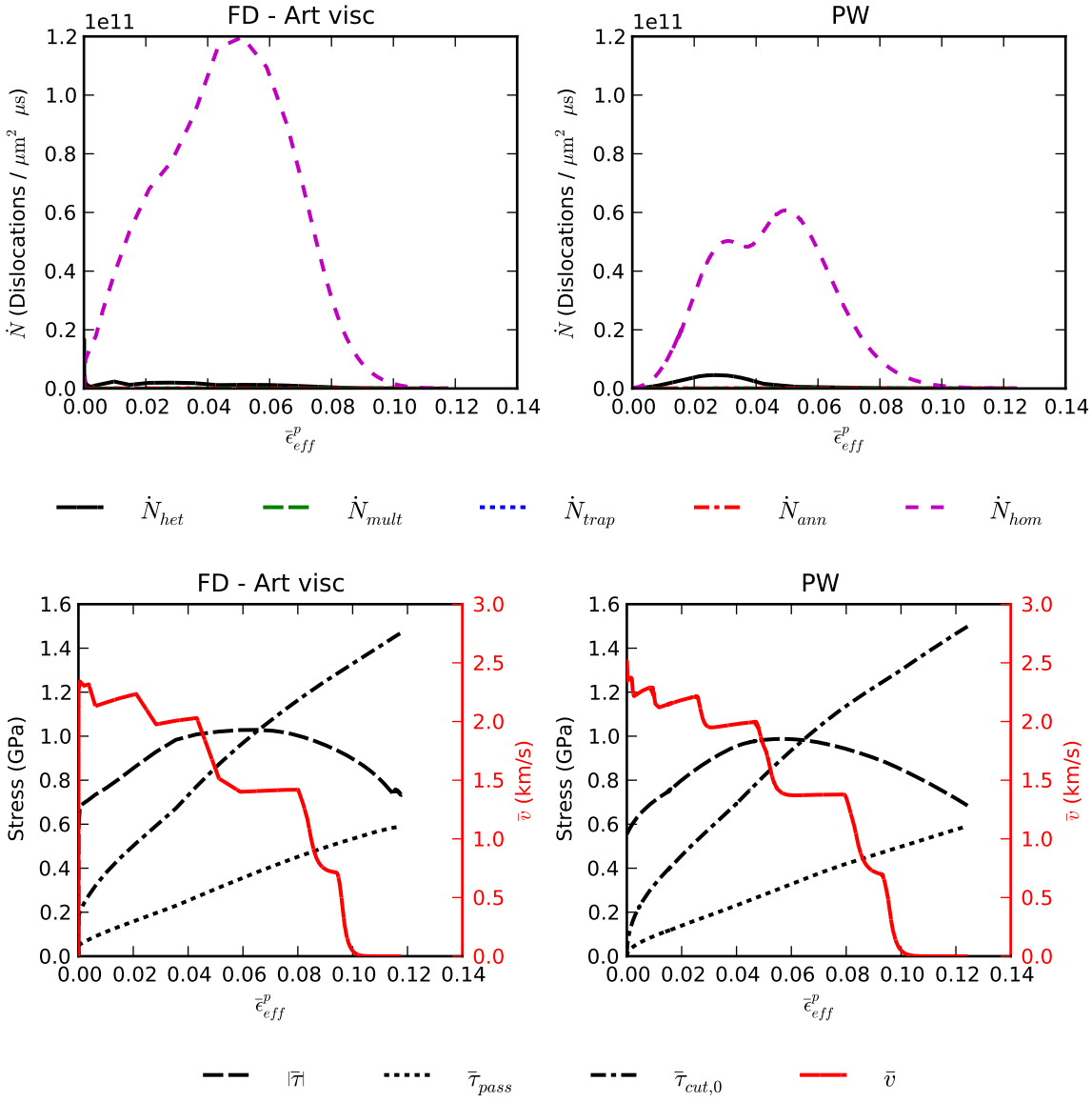

Figure 6.8: Viscoplastic deformation characteristics recorded at 0.75 µm for a low symmetry crystal shocked to 25 GPa using the plane wave formulation and the finite-difference method with an artificial viscosity. The dislocation density rate is summed over all systems, whereas the shear stress, strengths, and mean velocity are averaged over all slip systems.

(25 GPa) shock regime. The following conclusions can be made based on the simulations:

- Finite-difference and plane wave methods agree when modeling problems that result in only formation of longitudinal waves and can be modeled without artificial viscosity
- By neglecting the transverse velocity components during low symmetry impact, the plane wave method may under-predict dislocation density evolution rates by up to approximately 10%
- Using an artificial viscosity with a viscoplastic model decreases the rate of viscoplastic deformation
- Using an artificial viscosity with a viscoplastic model can suppress viscoplastic deformation mechanisms, such as dislocation nucleation

Computationally, it was shown that the plane wave method is two to three orders of magnitude faster than the finite-difference method for the case where the plane wave method has significantly higher resolution at the plastic shock front.

6.2 Coarse-grained model based on plane wave results

Although direct finite-difference simulation of single crystal and polycrystalline effects in Chapter 5 highlighted many instances in which deformation heterogeneity was greatly influenced by initial crystal texture, these simulations are computationally costly to implement and run. It is desirable to quantify deformation heterogeneity that is induced by crystal orientation effects by parameterizing the essential thermoelastic-viscoplastic single crystal behavior in a simplified framework and then use these results to inform an analytical treatment. With an analytical treatment in place, a connection can be made between macroscopic loading conditions and micromechanics-based results.

6.2.1 Formulation

In Section 4.3.2, it was shown that $\langle M \rangle$ was related to many orientation-dependent shock characteristics in the weak shock regime. Specifically, $\langle M \rangle$ was shown to correlate with the shock width, peak strain rate, and rise time, as well as viscoplastic behavior indicated by total temperature rise. Therefore, it is desirable to understand whether results of these

plane wave simulations can be used to replicate the response predicted by finite-difference simulations of polycrystal shock behavior, where $\langle M \rangle$ is used as an indicator of orientation-dependent, viscoplastic heterogeneity.

One disadvantage in using a modified Taylor factor $\langle M \rangle$ is that it is a *result* of a simulation and therefore cannot be calculated apriori. For a rate-independent crystal plasticity simulation of annealed polycrystalline FCC metals, it may be appropriate to express the value of M averaged over many grains as a function of accumulated plastic strain for a given deformation mode [134]. However, the high strain rate crystal plasticity simulations in Section 5.5 suggest that during shock loading, each grain experiences approximately the same peak longitudinal stress (σ^-, assumed positive) regardless of variation in texture rather than strain. Therefore, if $\langle M \rangle$ can be expressed as a function of initial orientation and peak longitudinal stress, i.e., $M_{approx} = f(\mathbf{g_0}, \sigma^-)$ where $\mathbf{g_0}$ is a vector in the reference frame that quantifies the crystal orientation, then approximate values of $\langle M \rangle$ can be found for each grain analytically instead of computationally. In Figure 6.9, the resultant $\langle M \rangle$ derived from approximately 800 individual plane wave simulations of single crystal aluminum is compared with the perfectly-plastic uniaxial strain Taylor factor, denoted M_0, which can be calculated based on initial orientation alone [136]. The results of Figure 6.9 indicate that $\langle M \rangle$ can be approximated as a linear combination of the classical uniaxial Taylor factor M_0 and the peak applied longitudinal stress σ^-, which is expressed as

$$\langle M \rangle_{approx} = f\left(\mathbf{g_0}, \sigma^-\right) \approx M_0\left(\mathbf{g}_0\right) + c_1 \sigma^-, \tag{6.1}$$

where $c_1 = 0.0256$ GPa^{-1} was found using a linear best fit. This linear increase in modified Taylor factor occurs more drastically in these high rate simulations than occurs in quasistatic simulations of axisymmetric compression, where the Taylor factor only increases by approximately 5% at an effective plastic strain of one [134]. Note that the functional form of the above relation assumes that the modified Taylor factor depends on initial orientation solely through M_0. This implies that orientation does not affect subsequent evolution of $\langle M \rangle$ due to increased peak longitudinal stress, which is clearly a first order approximation of the coupling between texture evolution and viscoplastic response at high rates.

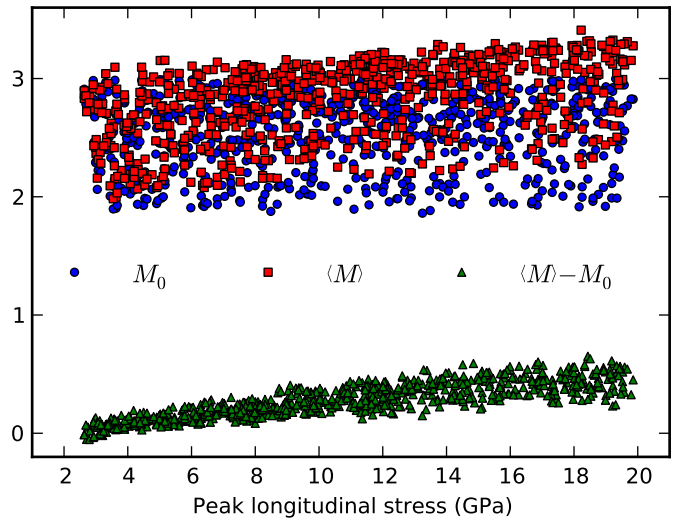

Figure 6.9: Comparison of resultant modified Taylor factor $\langle M \rangle$ with classical Taylor factor M_0 (assumes $\{111\}\langle 110 \rangle$ slip, perfectly plastic deformation, and uniaxial strain) for 800 randomly oriented aluminum single crystals shocked at peak longitudinal stresses ranging from approximately $2 - 20$ GPa using the plane wave method. Homogeneous dislocation nucleation was suppressed.

6.2.2 Comparison with finite-difference simulations

In this section, it is examined whether or not $\langle M \rangle_{approx}$ can be used to approximate values of $\langle M \rangle$ calculated directly using finite difference simulations. Finite difference simulations were performed on annealed polycrystals with peak shock pressures σ^- of 5, 10, and 15 GPa. The modified Taylor factor $\langle M \rangle$ derived from finite-difference simulation results is directly compared with values calculated using the linear fit for $\langle M \rangle_{approx}$ in Figure 6.10. For all three peak pressures $\langle M \rangle_{approx}$ captures the variation in the calculated values of $\langle M \rangle$ due to the randomly oriented grains; however, large values for $\langle M \rangle_{approx}$ slightly overestimate values found for $\langle M \rangle$ based on simulations. The relative mean error (RME) given by

$$\text{RME} = \text{avg}(|\langle M \rangle - \langle M \rangle_{approx}| / \langle M \rangle) \tag{6.2}$$

was 4.9%, 3.4%, and 4.2% for simulations with peak longitudinal stresses of 5, 10, and 15 GPa, respectively. Slight differences may arise because the plane wave simulations assume uniaxial strain whereas the finite-difference simulations allow shear components, which induce shear dissipation and variation at grain boundaries. Another difference is that as

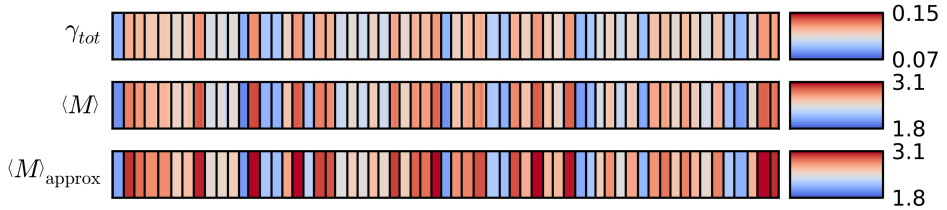

(a) $\sigma^- = 5$ GPa

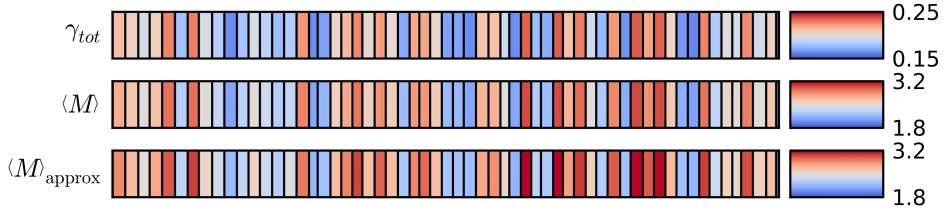

(b) $\sigma^- = 10$ GPa

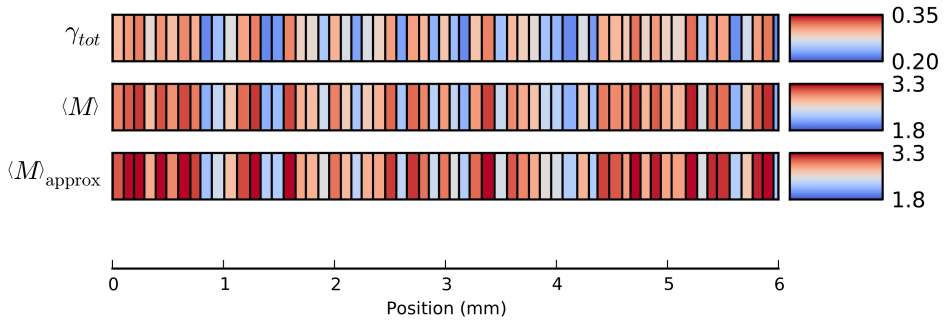

(c) $\sigma^- = 15$ GPa

Figure 6.10: Values of $\langle M \rangle$ calculated from finite-difference simulations plate impact experiments on 6 mm specimen shocked to different peak longitudinal stresses compared with predictions using Equation (6.1). All three sets of plots share a common longitudinal axis. In all cases, the plastic wave has completely passed through the specimen thickness.

the peak shock pressure increases, the approximation that the dependence of $\langle M \rangle$ on peak pressure and initial orientation can be treated independently may deteriorate.

6.2.3 Discussion

Because shock wave propagation simulations are computationally intensive, even for one-dimensional simulations, it is desirable to parameterize the essential behavior and implement it into a coarse-grained analytical framework. It was shown that computationally efficient plane wave simulation results could be used to approximate the orientation-dependent response of the elastic-viscoplastic model. It appears $\langle M \rangle_{\text{approx}}$ gives a reasonable approximation of plastic strain heterogeneity due to differences in crystal orientations for weak shock loading. Furthermore, because $\langle M \rangle_{\text{approx}}$ is calculated using the plane wave numerical method, it can be used to rapidly quantify the response of many different constitutive frameworks. This analysis has only been applied to weak shock loading of high stacking fault FCC metals that do not twin. Therefore, this method should not be used to approximate the response of lower symmetry crystals, materials that twin, or materials that exhibit a limited number of active slip systems unless direct comparisons are made between finite-difference and plane wave methods.

It may be useful to use input from this method to make an orientation-dependent equation of state type of model, such as the Steinberg-Guinan model presented in Section 2.6.1. By uniquely characterizing the accumulated plastic strain in terms of longitudinal stress (or in the hydrodynamic approximation of SG, pressure) and initial orientation, variation in material response due to crystallinity could be quantified without performing computationally intensive direct finite-difference simulations of single crystals and polycrystals.

CHAPTER VII

SUMMARY AND CONCLUSIONS

The goal of this work was to develop a framework that can directly model the influence of initial microstructure on the subsequent material response at high rates. Because instantaneous material characterization at extremely high rates is complicated by the violent nature of shock loading, physics-based computational models were developed and employed to directly model the influence of the initial material state of single crystal and polycrystalline aluminum on the resultant shock behavior. The primary effort of this work is concerned with the development of constitutive models that can capture aluminum single crystal behavior as well as numerical methods that can be used to capture behavior of aluminum single crystals, polycrystals, and pre-textured polycrystals in a computationally efficient framework without introducing spurious numerical artifacts.

7.1 Summary

Due to their low shear strengths, the treatment of shock loading of many metals has primarily been approached from a fluid mechanics perspective, wherein the deviatoric response is neglected. In this formulation, the shock itself causes finite entropy production as it travels through the material. All that remains for this theory is specifying an "equation of state", which captures the material state dependence on the instantaneous volume. On the other hand, solid mechanics deals with specifying the thermodynamic state of a solid that contains hidden internal state variables used to represent the evolving state of the material in conjunction with the thermoelastic response of the material. In Chapter 2, it is shown that the fluid treatment of solids is not only compatible with existing general theories of solids with internal state variables, but can be expressed explicitly in terms of this theory under a set of simplifying assumptions. Existing thermoelastic and viscoplastic theories are framed within this thermodynamic formulation and their capabilities as well as their limitations of are examined. It is shown that apart from the MTS model, "dynamic strength" models

give little information regarding the shocked material state, although due to their simplicity they are widely used to fit most high rate data. Dislocation-based viscoplastic models, on the other hand, are shown to be more closely tied to the physics and specific mechanisms responsible for high rate deformation.

To model single crystal thermoelastic-viscoplastic deformation at high rates, two thermoelastic theories that can be used to model single crystals are developed in Chapter 3. It is shown that the Eulerian material strain may capture more physically realistic behavior than the conventional Lagrangian Green strain often used in conjunction with viscoplasticity. Then, a single crystal viscoplastic model is developed by extending a dislocation-based, macroscopic high strain rate viscoplastic model [35, 36]. Because this macroscopic viscoplastic model uses many material constants that can be determined based on physics-based relations or direct observations, it is extended to the single crystal level with the goal of introducing a minimal number of additional parameters. This is done by combining this model with an existing crystal plasticity theory that quantifies dislocation interaction based on the geometric interaction of forest and parallel dislocation densities [37]. An uncoupled framework was also developed to include the internal energy contribution of lattice defects and potential forms of these contributions were given; however, in the remainder of this work, this contribution was neglected because there are too few experimental data that can confirm or refute specific values for the residual lattice defect energy due to the complication with in-situ temperature measurements in high rate tests.

Although the viscoplastic model presented in Chapter 3 uses mobile and immobile dislocation densities as internal state variables, it should be considered in the context of other high rate single crystal plasticity models. Schoenfeld and coworkers [169, 170, 171] developed crystal plasticity models for Ta and Ti-6Al-4V based on existing high rate strength models [77, 82] and explored the effect of pre-texturing on experiments such as Taylor impact cylinders, penetration of rolled plates, and explosive deep drawing. Becker used a similar viscoplastic power law model with a novel volumetric thermo-elastic relation to directly model the influence the coupling between loading rate and grain size on polycrystalline Ta [129]. Both of these viscoplastic models are able to capture first-order texture influences

but suffer from the same limitations that conventional macroscale dynamic strength models possess compared to dislocation-based models: they are unable to distinguish particular deformation mechanisms, give little information about the material in the shocked state, and capture the initial material state phenomenologically. Some recently developed models have used this power law or conventional dynamic strength approach to capture single crystal effects as well [172, 32], although one notable model by Hansen et al. [33] includes a detailed formulation concerning the geometry of slip-system level interactions between dislocations. Although this model captures geometric interactions in a more complex manner than the viscoplastic model presented in this thesis, there is a lack of experimental data concerning dislocation interactions at these high rates to inform specific material parameters concerning these interactions. If time-resolved high strain rate single crystal data becomes available, a more detailed treatment such as this may be warranted or may serve as a framework to incorporate more complex observed slip system interaction relations.

To model the orientation-dependent response of single crystals, a plane wave numerical method was developed in Chapter 4. Although the plane wave method had been used for over 60 years, it was incrementally improved upon up to the point that it could be used to model thermoelastic-viscoplastic deformation of isotropic materials with finite strength. In this work, under the assumption of uniaxial strain, a formulation was developed to model thermoelastic-viscoplastic deformation of anisotropic materials. Using this method, the predicted response of single crystal aluminum was compared with experimental strength and wave profile data. In the weak shock regime (less than approximately $15-20$ GPa, depending on orientation), the residual resolved shear stress in the shocked state was ordered from highest-to-lowest for [110], [111], and [100] orientations at similar peak shock pressures, whereas shock width was ordered from highest-to-lowest for [111], [110], then [100] orientations. Information concerning thermoelastic-viscoplastic deformation characteristics such as dislocation velocity, dislocation evolution rates, temperature rise, and other measures were distinguished as a function of peak shock pressure for ideal orientations. A parametric study was then performed to determine if shock characteristics could be quantified as a general function of orientation and peak pressure. It was then proposed that a modified

Taylor factor $\langle M \rangle$ be used to capture this orientation-dependence, and $\langle M \rangle$ was shown to correlate with plastic deformation and wave profile characteristics in the weak shock regime, but did not correlate well with plastic deformation and wave profile characteristics in the strong shock regime.

Because the plane wave method can only model steady shocks in single crystals, an extended one-dimensional finite-difference method was developed in Chapter 5 and was used to model spatio-temporal shock wave evolution in anisotropic materials. This numerical method is advantageous because it can represent the variation of all three spatial positions with respect to a single material coordinate system, in this case the shock direction. Accuracy of the finite-difference method was verified by comparing the numerical solution of impact conditions that generated quasi-longitudinal and quasi-transverse waves with analytical predictions. The Eulerian material thermoelastic model and the dislocation-based viscoplastic model were implemented in the finite-difference method and were used to model impact as well as laser shock loading problems for single crystals up to 110 GPa. The model was able to reproduce most aspects of observed wave profiles, although for laser shock loading it is difficult to separate the influence of loading conditions with the observed wave profile, as both direct and indirect ablation are highly complex, nonlinear loading processes.

For many of the cases in which the material was idealized as a single crystal, the real material used in experiments was a vapor-deposited polycrystal with some characteristic grain size. Realistic vapor-deposited polycrystals were generated, tested, and the following observations were made: (i) for polycrystals with many grains through the sample thickness, the predicted elastic precursor attenuation rate increases by nearly a factor of two as texture is spread from ideal to more random because of the shear mismatch induced at grain boundaries; (ii) for polycrystals that contain only a few grains through the sample thickness but whose area that velocity is sampled over contains many grains, the observed response can be spread out to the point that a response comprised of many dual wave shocks (implies unrelaxed response / not yet overdriven response) can be interpreted as a single wave shock. Microstructures representative of cold-rolled polycrystals were generated

using quasistatic crystal plasticity simulations. Then, these microstructures were used as initial conditions for shock-loading simulations of pre-textured polycrystals. The predicted polycrystal response was shown to agree favorably with experimental wave profiles from cold-rolled 1100-O aluminum samples. The influence of cold rolling on the subsequent deformation character was also analyzed, where it was shown that pre-texturing the material caused an decrease in the number of active slip systems and decrease in overall deformation heterogeneity.

As discussed in Chapter 4 the plane wave method must approximate strain as uniaxial, which is only exact for cases where deformation occurs along a three-fold or higher symmetry axis. The finite-difference method generally (but not always) uses an artificial viscosity to damp out numerical oscillations, which is often neglected but is shown in Chapter 5 to alter the material response. Both of these approximations have an undesirable influence on the calculated wave profile as well as viscoplastic material response and are viewed as one of the many impediments that has stalled development of advanced physics-based single crystal models for high rate deformation. The effect of these approximations and the computational efficiency of plane wave and finite-difference methods are evaluated in Chapter 6 by comparing predictions of these two methods by directly for [100] and low symmetry oriented single crystal aluminum in the weak and strong shock regime. It is shown that by approximating strain as uniaxial, the plane wave method may underestimate viscoplastic deformation rates by up to 10% in the weak shock regime because it does not capture the transverse deformation components. Using an artificial viscosity with a viscoplastic deformation model, however, is shown to greatly alter the observed deformation rates even for meshes that are generally unrealistically fine to model two and three-dimensional problems. The plane wave method is shown to do a superior job at resolving the plastic rise and is two to three orders of magnitude faster than the finite-difference method.

In Section 6.2, it is shown how results from the plane wave method can be used to replicate finite-difference predictions of the polycrystalline response of aluminum. Specifically, the pressure and orientation dependence of $\langle M \rangle$ is captured based on a linear fit to plane wave simulation results in the weak shock regime. Although this method is relatively crude,

it can be used as an analytical coarse-grained model to capture orientation-induced deformation heterogeneity without introducing the computational demands of finite-difference simulations.

7.2 Novel contributions

The novel contributions contained in this work include the following:

Constitutive model

- Two thermoelastic models that can be used to model materials with general anisotropy were implemented, and the Eulerian material strain measure was shown to converge towards more realistic behavior using less higher order constants than the Lagrangian Green strain. This appears to be the first time the Eulerian material strain has been used in conjunction with a viscoplastic model.
- A viscoplastic model for the high strain rate deviatoric response of aluminum single crystals has been developed and gives results that agree with experiments ranging from approximately $2 - 110$ GPa. The model distinguishes mobile and immobile dislocation densities on individual slip systems as its internal state variables, and relies on geometric interpretations of dislocation interactions so as to not introduce too many additional material constants.

Computational models

- A steady plane wave method was developed to model thermoelastic-viscoplastic deformation of anisotropic materials. This method was shown to be vastly more computationally efficient than conventional finite-difference methods, did not need to use an artificial viscosity to damp out numerical oscillations, and was shown to introduce a small error by approximating deformation of high stacking fault FCC metals as uniaxial strain. Comparison between plane wave and finite-difference simulations showed that for strong shocks deformation mechanisms differed between the two formulations because of the additional damping provided by the artificial viscosity.
- A program was developed to model plate impact problems in an extended, one-dimensional finite-difference framework for use with general thermoelastic-viscoplastic

materials. This program was used to model plate impact as well as laser shock (direct and indirect ablation) of single crystals as well as polycrystals. Grains are resolved explicitly using this method, and can be based on arbitrary texture, grain size distributions, as well as initial dislocation densities.

- A method was developed to model cold-rolled polycrystals, wherein results of quasistatic crystal plasticity simulations are used as initial conditions for discrete polycrystal shock loading simulations.
- A coarse-grained model was developed to capture essential orientation-dependent behavior from plane wave simulations and use this information in an analytical model for polycrystal deformation. The model was shown to replicate discrete polycrystal results based on computationally intensive finite-difference simulations within reason.

7.3 Conclusions

The following conclusions are drawn from this work:

- Both thermoelastic constitutive models give reasonable behavior using up to third order elastic constants, but the Eulerian material can be used to model much higher shock pressures.
- The geometric strength model based on forest and parallel dislocation interactions is able to predict available strength data for aluminum single crystals and suggests that the strengths are ordered from highest to lowest shear stress in the shocked state for [110], [111], and [100] orientations at similar peak pressures.
- A modified Taylor factor $\langle M \rangle$ was introduced and was shown to capture orientation-dependent shock and viscoplastic deformation characteristics in the weak shock regime for randomly oriented aluminum single crystals.
- The extended one-dimensional, finite-difference method for modeling anisotropic materials was shown to correctly capture quasi-longitudinal and quasi-transverse wave formation based on analytical solutions of plate impact problems with an X-cut quartz flyer impacting a Y-cut quartz target.

- It was shown that the thermoelastic-viscoplastic model can reproduce most aspects of wave profiles from plate impact and laser shock experiments performed on aluminum single crystals and preferentially-oriented polycrystals ranging from $2 - 110$ GPa. Although the model can be used at higher peak pressures, there is no available data to compare these results with, so the model results are not extended beyond 110 GPa.
- In cases where many grains are contained through the sample thickness it was shown that by varying the texture from an ideally oriented [111] texture to approximately $0^\circ - 25^\circ$ about the [111] orientation, observed precursor attenuation for a 4 GPa shock increased by a factor of two due to shear mismatch at grain boundaries, which increased plastic dissipation.
- In cases where the velocity profile is sampled from a region that contains many grains, the aggregate response of multiple single crystals with differing orientations that exhibit a dual shock structure could be misinterpreted as a single shock structure. This difference may explain why in molecular dynamics simulations that idealize vapor-deposited samples as single crystals, anomalously large elastic limits are observed.
- By directly simulating dislocation density as well as orientation distributions due to cold-rolling, realistic wave profiles were observed. Also, these cold-rolling predictions indicate that cold-rolling reduces slip heterogeneity and the number of active slip systems compared to annealed specimens in the weak shock loading regime.
- Approximations introduced by assuming uniaxial strain in the anisotropic plane wave formulation were quantified, and were shown to underestimate dislocation evolution rates by at most 10% for low symmetry single crystal orientations.
- The effect of using an artificial viscosity in the finite-difference formulation was quantified. It was shown to have a small ($< 10\%$ effect on dislocation evolution rates) influence on the shock behavior if a sufficient number of points were used (over 50 points to resolve the plastic rise), but was shown to have a significant effect in the strong shock regime or if a sufficient number of points were not used to discretize the plastic wave.

- A coarse-grained analytical model that quantified orientation-dependence of single crystals based on results of plane wave simulations was shown to do a reasonable job reproducing direct finite-difference simulations of annealed polycrystals.

7.4 Recommendations for future work

Preliminary calculations (not shown in this thesis) that included the internal energy contribution of lattice defects showed that it did not have a significant influence on the resultant wave profile and viscoplastic deformation characteristics; however, including this term may be important for modeling strain localization behavior. It would be interesting to quantify an orientation-dependent localization parameter at different strain rates, then understand how this parameter is influenced by adding the lattice defect contribution. Because detailed, reliable temperature measurements for single crystal aluminum are difficult to obtain in the shocked state, it is hard to justify adding this additional layer of complexity to an already complicated viscoplastic model. Regardless, if future studies are concerned with the influence of initial orientation on localization, the finite-difference and plane wave formulations developed in this work have been developed so that they can include this contribution.

One development that would enhance the viscoplastic model used in this work would be if detailed subgrain formation during shock loading could be captured. A problem that also ails classical crystal plasticity formulations is that because slip is treated in an aggregate sense, subgrain formation and its effect on subsequent hardening response must be captured phenomenologically by use of slip system interaction relations. At high rates, a large number of dislocations are generated. At some point (based on TEM of recovered specimens) they form coordinated structures. It is difficult to estimate the length and time scales these rearrangements occur during, although there is significant evidence that shock pulse duration is closely tied to substructure formation [173]. It is thought that high angle boundaries may serve as void nucleation sites during the spall response, which could imply that substructure formation predictions from the viscoplastic model could be fed directly into a damage model to capture the entire shock and release behavior of single crystals and polycrystals during spall [19].

Because the single crystal viscoplastic deformation model is based on the physics of dislocation motion, careful comparisons can be made between predictions of this model and resultant TEM and SEM images of shocked microstructures. Although the computational framework developed in this thesis has highlighted the influence of initial orientation and dislocation densities on the observed wave profile and viscoplastic deformation characteristics, nearly all of the specimens used in the experimental work on polycrystals that was referenced in in this thesis lacked *detailed microstructural characterization of the samples.* A goal of this work is that by quantifying the influence of initial microstructure on the observed response, it serves as an impetus for detailed characterization of specimens deformed at high strain rates. Therefore, additional experiments should be performed at high rates in which detailed observations of the microstructure before and after shock loading are compared.

Finally, it was shown that even though an artificial viscosity is often used in conjunction with complex viscoplastic models to capture high strain rate viscoplastic behavior, the viscosity couples nonlinearly with the viscoplastic response and provides additional dissipation not associated with the physics of the model. The elasto-dynamic fields associated with gliding dislocations have been studied extensively by Markenscoff and coworkers in a series of papers [174, 150, 175, 176] using analytical methods originally developed to solve the partial differential equations governing dynamic crack propagation in elastic solids [177]. Molecular dynamics simulations of steady waves at high strain rates also show that a complex elastic waves precede the main plastic wave in the strong shock regime [152]. Therefore it would be desirable to associate transient elastic waves created during dislocation motion and generation with an additional dissipation mechanism, or even viscosity, thereby circumventing the use of an artificial viscosity and replacing it with a more physical dislocation-based viscosity.

APPENDIX A

CONTINUUM IDENTITIES AND DEFINITIONS

If θ is a scalar field then the material and spatial derivatives of θ are related by

$$\nabla_0 \theta = \mathbf{F}^T \nabla \theta, \qquad \frac{\partial \theta}{\partial X_A} = \frac{\partial \theta}{\partial x_i}\frac{\partial x_i}{\partial X_A} = F_{iA}\frac{\partial \theta}{\partial x_i}. \tag{A.1}$$

Material time derivative:

$$\dot{f} \equiv \left.\frac{\partial f}{\partial t}\right|_{\mathbf{X}} \equiv \frac{Df}{Dt} \equiv \frac{df}{dt} = \frac{\partial f}{\partial t} + \frac{\partial f}{\partial x_k}\frac{dx_k}{dt}. \tag{A.2}$$

Piola's Identity:

$$\frac{\partial}{\partial X_A}\left(JF^{-1}_{Ai}\right) = 0. \tag{A.3}$$

Other identities:

$$\frac{\partial J}{\partial \mathbf{F}} = J\mathbf{F}^{-T}, \tag{A.4}$$

$$\frac{d}{dt}\left(\det\mathbf{F}\right) = \left(\det\mathbf{F}\right)\mathbf{F}^{-T} : \dot{\mathbf{F}} = \mathrm{tr}\left(\mathbf{F}^{-1}\cdot\dot{\mathbf{F}}\right), \qquad \therefore \qquad \dot{J} = \frac{\partial J}{\partial \mathbf{F}} : \dot{\mathbf{F}} = J\mathbf{F}^{-T} : \dot{\mathbf{F}}. \tag{A.5}$$

APPENDIX B

UNIT CONVERSION REFERENCE

From (kg-m-s) to (ng-μs-μm)

$$\rho_0 = 2700\frac{\cancel{\text{kg}}}{\cancel{\text{m}^3}}\frac{10^{12}\text{ng}}{\cancel{\text{kg}}}\frac{\cancel{\text{m}^3}}{(10^6\mu\text{m})^3} = 2.7\cdot 10^{-3}\frac{\text{ng}}{\mu\text{m}^3}$$

$$b_0 = 3\cdot 10^{-10}\cancel{\text{m}}\cdot\frac{10^6\mu\text{m}}{\cancel{\text{m}}} = 3\cdot 10^{-4}\mu\text{m}$$

$$c_p = 902\frac{\text{J}}{\text{kg}\cdot\text{K}} = 902\frac{\cancel{\text{kg}}\cdot\cancel{m^2}}{\cancel{s^2}}\frac{1}{\cancel{\text{kg}}\cdot K}\frac{\cancel{s^2}}{(10^6\mu\text{s})^2}\frac{(10^6\mu\text{m})^2}{\cancel{\text{m}^2}} = 902\frac{\mu\text{m}^2}{\mu\text{s}^2\cdot\text{K}}$$

$$\beta_{11} = 35\cdot 10^6\frac{\text{Pa}}{\text{K}} = 35\cdot 10^6\frac{\cancel{\text{kg}}}{\cancel{\text{m}}\cdot\cancel{s^2}\cdot\text{K}}\frac{\cancel{\text{m}}}{10^6\mu\text{m}}\frac{\cancel{s^2}}{(10^6\mu\text{s})^2}\frac{10^{12}\text{ng}}{\cancel{\text{kg}}} = 35\frac{\text{ng}}{\mu\text{m}\cdot\mu\text{s}^2\cdot\text{K}} = 35\frac{\text{MPa}}{\text{K}}$$

$$C_{11} = 106\cdot 10^9\text{Pa} = 106\cdot 10^3\frac{\mu\text{m}\cdot\text{ng}}{\mu\text{s}^2} = 106\cdot 10^3\ \text{MPa}$$

$$C_0 = 5\cdot 10^3\frac{\cancel{\text{m}}}{\cancel{s}}\frac{10^6\mu\text{m}}{\cancel{\text{m}}}\frac{\cancel{s}}{10^6\mu\text{s}} = 5\cdot 10^3\frac{\mu\text{m}}{\mu\text{s}}$$

$$N_{im,0} = 2\cdot 10^{14}\frac{1}{\cancel{\text{m}^2}}\frac{\cancel{\text{m}^2}}{(10^6\mu\text{m})^2} = 200\frac{1}{\mu\text{m}^2}$$

$$\dot{N}_m = 2\cdot 10^{14}\frac{1}{\cancel{\text{m}^2}\cdot\cancel{s}}\frac{\cancel{\text{m}^2}}{(10^6\mu\text{m})^2}\frac{\cancel{s}}{10^6\mu\text{s}} = 2\cdot 10^{-4}\frac{1}{\mu\text{m}^2\cdot\mu\text{s}}$$

$$\delta_{mult} = 3\cdot 10^5\frac{1}{\cancel{\text{m}}}\frac{\text{m}}{10^6\mu\text{m}} = 0.3\frac{1}{\mu\text{m}}$$

APPENDIX C

INDEX NOTATION USING PYTHON

Compared to compiled computer languages such as C or Fortran, interpreted computer languages (e.g. Python, Matlab, Ruby) can accomplish similar tasks as these compiled languages using less lines of code due to their built in features that simplify many aspects of data input, manipulation, and presentation. It is desirable to construct entire computational codes in Python; however, like most interpreted languages, it suffers in computational efficiency compared to compiled languages. Specifically, operations that may not introduce extra computational burden in compiled codes (using for loops for matrix multiplication of matrices regularly encountered in continuum calculations instead of optimized functions such as `matmul`) can slow down scripting languages like Python by several orders of magnitude. To remedy this deficiency, Python offers optimized functions to perform matrix multiplication, which perform only $2-3$ times slower than equivalent code written in Fortran77.

The code below shows sample calculations on how to use the functions `tensordot`, `outer`, and `reshape` from the `numpy` package to perform linear algebra operations. The functions are presented in order of increasing complexity, where some of the functions were used extensively in the plane wave numerical formulation. Conventional for loop constructions are included first, and are then followed by the computationally efficient versions of these statements. In these computations, it was found that on average, each for loop made the computation a factor of 10 slower than the computation using the functions `tensordot`, `outer`, and `reshape`. In the following examples the solution calculated using `for` loops is given by the array `temp`, and is equivalent to the solution calculated using the built in linear algebra operators given by the array `ans`.

Include statements

```
from numpy import outer, linalg, zeros, identity, reshape
```

```
from numpy import tensordot as td
```

Illustrative equations

Define δ_{ij}

```
kdel = identity(3)
```

$$C_{ijkl} = A_{ij}B_{kl}$$

```
temp = zeros((3,3,3,3))
for i in range(3):
  for j in range(3):
    for k in range(3):
      for l in range(3):
        temp[i,j,k,l] = a2[i,j]*b2[k,l]
ans=outer(a2,b2).reshape((3,3,3,3))
```

$$C_{ij} = A_{ki}B_{kj}$$

```
temp=zeros((3,3))
for i in range(3):
  for j in range(3):
    for k in range(3):
      temp[i,j]+=a2[k,i]*b2[k,j]
ans=td(a2,b2,(0,0))
```

$$D_{ij} = A_{jl}B_{lm}\delta_{1i}C_{1m}$$

```
temp=zeros((3,3))
for i in range(3):
  for j in range(3):
    for l in range(3):
      for m in range(3):
        temp[i,j]+=a2[j,l]*b2[l,m]*kdel[0,i]*c2[0,m]
ans=td(td(outer(kdel[0,:],c2[0,:]),b2,(1,1)),a2,(1,1))
```

More complicated equations, such as those encountered in plane wave method

$$\Sigma_{\alpha\beta} = \overline{C}_{\alpha\beta\gamma\delta}E^E_{\gamma\delta} + \frac{1}{2}\overline{C}_{\alpha\beta\gamma\delta\kappa\lambda}E^E_{\gamma\delta}E^E_{\kappa\lambda} - \overline{\beta}_{\alpha\beta}\Delta\theta - \overline{\beta}_{\alpha\beta\gamma\delta}E^E_{\gamma\delta}\Delta\theta.$$

```
temp=zeros((3,3))
for i in range(3):
  for j in range(3):
    temp[i,j]+=(-1.0)*beta2[i,j]*dtheta
    for k in range(3):
      for l in range(3):
        temp[i,j]+=c4[i,j,k,l]*ee[k,l]-dtheta*beta4[i,j,k,l]*ee[k,l]
```

```
        for m in range(3):
          for n in range(3):
            temp[i,j]+=0.5*c6[i,j,k,l,m,n]*ee[k,l]*ee[m,n]
ans=td(c4,ee,((3,2),(1,0)))+0.5*td(c6,outer(ee,ee).reshape(linspace(3,3,4)),\
((5,4,3,2),(3,2,1,0)))- beta2*dtheta - dtheta*td(beta4,ee,((3,2),(1,0)))
```

$$T_{11} = J^P F_{1\alpha}^{P^{-1}} \Sigma_{\alpha\beta} F_{1\beta}^{P^{-1}} (1+\xi)$$

```
temp = 0.0
for i in range(3):
  for j in range(3):
    temp+=fpi[0,i]*pk2[i,j]*fpi[0,j]*(1.0+xi)
ans=(1.0+xi)*td(pk2,outer(fpi[0,:],fpi[0,:]),((1,0),(1,0)))
```

$$F_{i\beta}^{E} = \left(\delta_{iK} + \delta_{1i}\delta_{1K}\xi\right) F_{K\beta}^{P^{-1}}.$$

```
temp=zeros((3,3))
for i in range(3):
  for j in range(3):
    for k in range(3):
      temp[i,j]+=(kdel[i,k]+kdel[0,i]*kdel[0,k]*xi)*fpi[k,j]
ans=td((kdel+xi*outer(kdel[0,:],kdel[0,:])),fpi, (1,0))
```

$$\sigma_{ij} = \frac{1}{J^E} F_{i\alpha}^{E} \Sigma_{\alpha\beta} F_{j\beta}^{E}.$$

```
temp = zeros((3,3))
for i in range(3):
  for j in range(3):
    for k in range(3):
      for l in range(3):
        efor[i,j]+=eidet*fe[i,k]*pk2[k,l]*fe[j,l]

ans=1.0/linalg.det(fe)*td(td(fe,pk2,(1,0)),fe,(1,1))
```

$$\tau^{\alpha} = \sigma_{ij} F_{i\beta}^{E} s_{\beta}^{\alpha} m_{\delta}^{\alpha} F_{\delta j}^{E^{-1}}$$

```
temp = zeros(12)
for w in range(12):
  for i in range(3):
    for j in range(3):
      for k in range(3):
        for l in range(3):
          temp[w]+=sig[i,j]*fe[i,k]*s0[k,w]*m0[l,w]*fei[l,j]
ans=td(s0m0,td(td(sig,fe,(0,0)),fei,(0,1)),((1,0),(1,0)))
```

$$L_{\beta\delta}^{P} = \sum_{\alpha=1}^{N} N_{m}^{\alpha} b^{\alpha} \bar{v}^{\alpha} \left(s_{\beta}^{\alpha} m_{\delta}^{\alpha}\right)$$

```
temp = zeros((3,3))
for i in range(3):
  for j in range(3):
    for w in range(12):
      temp[i,j]+=nm[w]*burg[w]*vel[w]*s0m0[i,j,w]
ans=td(s0m0,nm*burg*vel,(2,0))
```

REFERENCES

[1] Meyers M A 1994 *Dynamic behavior of materials* (New York City, NY: John Wiley & Sons)

[2] Steinberg D J, Cochran S G and Guinan M W 1980 *Journal of Applied Physics* **51** 1498

[3] Hoge K G and Mukherjee A K 1977 *Journal of Materials Science* **12** 1666–1672

[4] Steinberg D J and Lund C M 1989 *Journal of Applied Physics* **65** 1528

[5] Gilman J J 1960 *Australian Journal of Physics* **13** 327–346

[6] Clifton R 1971 *Shock Waves and the Mechanical Properties of Solids* ed Burke J and Weiss V (Syracuse, NY: Syracuse University Press) pp 73–116

[7] Johnson J N and Barker L M 1969 *Journal of Applied Physics* **40** 4321–4334

[8] Johnston W G and Gilman J J 1960 *Journal of Applied Physics* **31** 632–643

[9] Hull D and Bacon D J 2001 *Introduction to dislocations* (Elmsford, NY: Pergamon Press)

[10] Marsh S P 1980 *LASL Shock Hugoniot Data* (University of California Press)

[11] Ma A, Roters F and Raabe D 2006 *Acta Materialia* **54** 2169–2179

[12] Huang H and Asay J R 2006 *Journal of Applied Physics* **100** 043514

[13] Turneaure S J and Gupta Y M 2011 *Journal of Applied Physics* **109** 123510

[14] Huang H and Asay J R 2007 *Journal of Applied Physics* **101** 063550

[15] Turneaure S J and Gupta Y M 2009 *Journal of Applied Physics* **106** 033513

[16] Crowhurst J C, Armstrong M R, Knight K B, Zaug J M and Behymer E M 2011 *Physical Review Letters* **107** 144302

[17] Smith R F, Eggert J H, Jankowski A, Celliers P M, Edwards M J, Gupta Y M, Asay J R and Collins G W 2007 *Physical Review Letters* **98** 065701

[18] Gupta Y M, Winey J M, Trivedi P B, LaLone B M, Smith R F, Eggert J H and Collins G W 2009 *Journal of Applied Physics* **105** 036107

[19] Williams C L, Chen C Q, Ramesh K T and Dandekar D P 2013 *Journal of Applied Physics* **114** 093502

[20] Gilman J J 1969 *Micromechanics of Flow in Solids* (McGraw-Hill)

[21] Murr L 1981 *Shock Waves and High-Strain-Rate Phenomena in Metals* ed Meyers M and Murr L (New York, N.Y.: Plenum Press) pp 607–673

[22] Johnson J N, Jones O E and Michaels T E 1970 *Journal of Applied Physics* **41** 2330–2339

[23] Follansbee P and Gray III G 1991 *International Journal of Plasticity* **7** 651–660

[24] Minich R W, Cazamias J U, Kumar M and Schwartz A J 2004 *Metallurgical and Materials Transactions A* **35**

[25] Chen X, Asay J R, Dwivedi S K and Field D P 2006 *Journal of Applied Physics* **99** 023528

[26] Kanel G I 2010 *International Journal of Fracture* **163** 173–191

[27] Razorenov S V, Kanel G I, Garkushin G V and Ignatova O N 2012 *Physics of the Solid State* **54** 790–797

[28] Johnson J N 1972 *Journal of Applied Physics* **43** 2074–2082

[29] Winey J M and Gupta Y M 2006 *Journal of Applied Physics* **99** 023510

[30] Barton N R, Winter N W and Reaugh J E 2009 *Modelling and Simulation in Materials Science and Engineering* **17** 035003

[31] Barton N R, Bernier J V, Becker R, Arsenlis A, Cavallo R, Marian J, Rhee M, Park H, Remington B A and Olson R T 2011 *Journal of Applied Physics* **109** 073501

[32] Lusher D J, Bronkhorst C A, Alleman C N and Addessio F L 2013 *Journal of the Mechanics and Physics of Solids* **61** 1877–1894

[33] Hansen B L, Beyerlein I J, Bronkhorst C A, Cerreta E K and Dennis-Koller D 2013 *International Journal of Plasticity* **44** 129–146

[34] Clayton J D 2013 *Journal of the Mechanics and Physics of Solids* **61** 1983–2014

[35] Austin R A and McDowell D L 2011 *International Journal of Plasticity* **27** 1–24

[36] Austin R A and McDowell D L 2012 *International Journal of Plasticity* **3233** 134–154

[37] Ma A and Roters F 2004 *Acta Materialia* **52** 3603–3612

[38] Coleman B D and Gurtin M E 1967 *Journal of Chemical Physics* **47**

[39] Germain P and Lee E 1973 *Journal of the Mechanics and Physics of Solids* **21** 359–382

[40] Nemat-Nasser S 2004 *Plasticity: A Treatise on the Finite Deformation of Heterogeneous Inelastic Materials* (Cambridge University Press)

[41] Clayton J D 2011 *Nonlinear Mechanics of Crystals* vol 177 (Springer)

[42] Bilby B A, Gardner L R and Stroh A N 1957 *Proceedings of the 9th International Congress on Applied Mechanics* vol 8 (University of Brussels, France) pp 35–44

[43] Kröner E 1959 *Archive for Rational Mechanics and Analysis* **4** 273–334

[44] Chaboche J L 1993 *Journal of Applied Mechanics* **60** 813–821

[45] Rosakis P, Rosakis A, Ravichandran G and Hodowany J 2000 *Journal of the Mechanics and Physics of Solids* **48** 581–607

[46] Wallace D C 1998 *Thermodynamics of Crystals* (Courier Dover Publications)

[47] Taylor G I and Quinney H 1934 *Proceedings of the Royal Society of London. Series A* **143** 307–326

[48] Lemaitre J and Chaboche J 1994

[49] Thurston R 1974 *Encyclopedia of Physics: Mechanics of Solids IV* (Springer-Verlag) pp 109–308

[50] Walsh J M and Christian R H 1955 *Physical Review* **97** 1544–1556

[51] Rice M, McQueen R and Walsh J 1958 *Solid state physics* **6** 1–63

[52] McQueen R G, Marsh S P, Taylor J W, Fritz J N and Carter W J 1970 *High Velocity Impact Phenomena* ed Kinslow R (New York: Academic Press) pp 293–417

[53] Walsh J M, Rice M H, McQueen R G and Yarger F L 1957 *Physical Review* **108** 196–216

[54] Grüneisen E 1926 *Handbuch der Physik* vol 10 (Berlin: Springer-Verlag) p 1

[55] Murnaghan F D 1937 *American Journal of Mathematics* **59** 235–260

[56] Murnaghan F D 1944 *Proceedings of the National Academy of Sciences* **30** 244–247

[57] Birch F 1938 *Journal of Applied Physics* **9** 279–288

[58] Truesdell C 1961 *Archive for Rational Mechanics and Analysis* **8** 263–296

[59] Barsch G R 1968 *Journal of Applied Physics* **39** 3780–3793

[60] Guinan M W and Steinberg D J 1974 *Journal of Physics and Chemistry of Solids* **35** 1501–1512

[61] Birch F 1947 *Physical Review* **71** 809

[62] Ghate P B 1964 *Journal of Applied Physics* **35** 337–339

[63] Krishnamurty T S G 1963 *Acta Crystallographica* **16** 839–840

[64] Lazarus D 1949 *Physical Review* **76** 545–553

[65] Bateman T, Mason W P and McSkimin H J 1961 *Journal of Applied Physics* **32** 928–936

[66] Thurston R N and Brugger K 1964 *Physical Review* **133** A1604

[67] Thurston R N 1965 *The Journal of the Acoustical Society of America* **37** 348–356

[68] Clayton J D 2011 *Journal of Applied Mechanics* **78** 011013

[69] Graham R A 1972 *Physical Review B* **6** 4779–4793

[70] Hill R 1998 *The Mathematical Theory of Plasticity* vol 11 (Oxford University Press)

[71] McDowell D L 2005 *Handbook of Materials Modeling* (Springer) pp 1151–1169

[72] Rice J R 1971 *Journal of the Mechanics and Physics of Solids* **19** 433–455

[73] Lubliner J 1972 *International Journal of Non-Linear Mechanics* **7** 237–254

[74] Lubliner J 1973 *Acta Mechanica* **17** 109–119

[75] Marin E B and McDowell D L 1996 *International Journal of Plasticity* **12** 629–669

[76] Kipp M E and Lawrence R J 1982 Wondy V - A one-dimensional finite-difference wave propagation code Tech. Rep. SAND-81-0930 Sandia National Laboratory

[77] Johnson G R and Cook W H 1983 *Proceedings of the 7th International Symposium on Ballistics* vol 21 (The Hague, The Netherlands: International Ballistics Committee) pp 541–547

[78] Andrade U, Meyers M A, Vecchio K S and Chokshi A H 1994 *Acta Metallurgica et Materialia* **42** 3183–3195

[79] Zerilli F J and Armstrong R W 1987 *Journal of Applied Physics* **61** 1816–1825

[80] Zerilli F J and Armstrong R W 1990 *Journal of Applied Physics* **68** 1580–1591

[81] Zerilli F J and Armstrong R W 1992 *Acta Metallurgica et Materialia* **40** 1803–1808

[82] Follansbee P and Kocks U 1988 *Acta Metallurgica* **36** 81–93

[83] Kocks U, Argon A and Ashby M 1975 *Progress in Materials Science* **19** 1–281

[84] Regazzoni G, Kocks U and Follansbee P 1987 *Acta Metallurgica* **35** 2865–2875

[85] Preston D L, Tonks D L and Wallace D C 2003 *Journal of Applied Physics* **93** 211–220

[86] Wallace D C 1981 *Physical Review B* **24** 5597–5606

[87] Wallace D C 1981 *Physical Review B* **24** 5607–5615

[88] Johnston W G and Gilman J J 1959 *Journal of Applied Physics* **30** 129–144

[89] Estrin Y, Toth L S, Molinari A and Brechet Y 1998 *Acta Materialia* **46** 5509–5522

[90] Gillis P P, Gilman J J and Taylor J W 1969 *Philosophical Magazine* **20** 279–289

[91] Gilman J J 1965 *Journal of Applied Physics* **36** 2772–2777

[92] Jones O E and Mote J D 1969 *Journal of Applied Physics* **40** 4920–4928

[93] Gupta Y M, Duvall G E and Fowles G R 1975 *Journal of Applied Physics* **46** 532 –546

[94] Meir G and Clifton R J 1986 *Journal of Applied Physics* **59** 124–148

[95] Zhu T, Li J, Samanta A, Leach A and Gall K 2008 *Physical Review Letters* **100** 025502

[96] Tschopp M A and McDowell D L 2008 *Journal of the Mechanics and Physics of Solids* **56** 1806–1830

[97] Zhu T and Li J 2010 *Progress in Materials Science* **55** 710–757

[98] Armstrong R W and Zerilli F J 2010 *Journal of Physics D: Applied Physics* **43** 492002

[99] Clayton J D 2009 *Composites Part B: Engineering* **40** 443–450

[100] Thomsen L 1972 *Journal of Physics and Chemistry of Solids* **33** 363 – 378

[101] Truesdell C 1966 *Continuum Mechanics: The mechanical foundations of elasticity and fluid dynamics* vol 1 (Gordon and Breach)

[102] Thomas J F 1968 *Physical Review* **175** 955–962

[103] Zimmerman J A, Winey J M and Gupta Y M 2011 *Physical Review B* **83** 184113

[104] Wright T W 2002 *The Physics and Mathematics of Adiabatic Shear Bands* (Cambridge University Press)

[105] Wang K and Reeber R R 2000 *Philosophical Magazine A* **80** 1629–1643

[106] Wyckoff R W G 1960 *Crystal structures* vol 1 (Interscience publishers New York)

[107] Graham R A and Brooks W P 1971 *Journal of Physics and Chemistry of Solids* **32** 2311–2330

[108] Jackson P and Basinski Z 1967 *Canadian Journal of Physics* **45** 707–735

[109] Franciosi P and Zaoui A 1982 *Acta Metallurgica* **30** 1627–1637

[110] Wu T, Bassani J L and Laird C 1991 *Proceedings of the Royal Society of London. Series A: Mathematical and Physical Sciences* **435** 1–19

[111] Bassani J L and Wu T 1991 *Proceedings of the Royal Society of London. Series A: Mathematical and Physical Sciences* **435** 21–41

[112] Hirth J P and Lothe J 1982 *Theory of Dislocations* (John Wiley and Sons, Inc.)

[113] Bathe K 1996 *Finite Element Procedures* (New Jersey: Prentice-Hall)

[114] Kocks U F and Mecking H 2003 *Progress in Materials Science* **48** 171–273

[115] Leibfried G 1950 *Zeitschrift für Physik* **127** 344–356

[116] Lomdahl P S and Srolovitz D J 1986 *Physical Review Letters* **57** 2702–2705

[117] Roters F, Raabe D and Gottstein G 2000 *Acta Materialia* **48** 4181–4189

[118] Hodowany J, Ravichandran G, Rosakis A J and Rosakis P 2000 *Experimental Mechanics* **40** 113–123

[119] Rittel D, Silva M L, Poon B and Ravichandran G 2009 *Mechanics of Materials* **41** 1323–1329

[120] Schreyer H L and Maudlin P J 2005 *Philosophical Transactions of the Royal Society A: Mathematical, Physical and Engineering Sciences* **363** 2517–2541

[121] Nabarro F 1952 *Advances in Physics* **1** 269–394

[122] Kuhlmann-Wilsdorf D 1999 *Philosophical Magazine A* **79** 955–1008

[123] Arsenlis A and Parks D M 2002 *Journal of the Mechanics and Physics of Solids* **50** 1979–2009

[124] Clayton J D and Bammann D J 2009 *Journal of Engineering Materials and Technology* **131** 041201

[125] Von Karman T and Duwez P 1950 *Journal of Applied Physics* **21** 987–994

[126] Taylor G I 1948 *Proceedings of the Royal Society of London. Series A, Mathematical and Physical Sciences* **194** 289–299

[127] Molinari A and Ravichandran G 2004 *Journal of Applied Physics* **95** 1718–1732

[128] VonNeumann J and Richtmyer R D 1950 *Journal of Applied Physics* **21** 232

[129] Becker R 2004 *International Journal of Plasticity* **20** 1983–2006

[130] Johnson J N 1974 *Journal of Physics and Chemistry of Solids* **35** 609–616

[131] Swegle J W and Grady D E 1985 *Journal of Applied Physics* **58** 692–701

[132] Asay J R and Chhabildas L C 1981 *Shock Waves and high-strain-rate phenomena in metals* (New York City, NY: Plenum Press) pp 417–431

[133] Taylor G I 1938 *Journal of the Institute of Metals* **62** 307–324

[134] Tome C, Canova G R, Kocks U F, Christodoulou N and Jonas J J 1984 *Acta Metallurgica* **32** 1637–1653

[135] Kopacz I, Tóth L S, Zehetbauer M and Stüwe H P 1999 *Modelling and Simulation in Materials Science and Engineering* **7** 875–891

[136] Chin G Y and Mammel W L 1967 *Transactions of the Metallurgical Society of AIME* vol 239 pp 1400–1405

[137] Bishop J and Hill R 1951 *Philosophical Magazine* **42** 1298–1307

[138] Bishop J and Hill R 1951 *Philosophical Magazine* **42** 414–427

[139] Meyers M A and Murr L E 1981 *Shock waves and high-strain-rate phenomena in metals* (New York City, NY: Plenum Press)

[140] Gupta Y M 1984 *Polymer Engineering & Science* **24** 851861

[141] Ramesh K T and Clifton R J 1992 *Journal of Applied Mechanics* **59** 754–761

[142] Landshoff R 1955 A numerical method for treating fluid flow in the presence of shocks Tech. Rep. LA-1930 Los Alamos Scientific Laboratory

[143] Wilkins M L 1980 *Journal of Computational Physics* **36** 281–303

[144] Benson D J 1992 *Computer Methods in Applied Mechanics and Engineering* **99** 235–394

[145] Winey J M and Gupta Y M 2004 *Journal of Applied Physics* **96** 1993–1999

[146] Johnson J N 1971 *Journal of Applied Physics* **42** 5522 –5530

[147] Lloyd J, Clayton J D, Austin R A and McDowell D L submitted *Journal of the Mechanics and Physics of Solids, submitted*

[148] Park H S, Remington B A, Becker R C, Bernier J V, Cavallo R M, Lorenz K T, Pollaine S M, Prisbrey S T, Rudd R E and Barton N R 2010 *Physics of Plasmas* **17** 056314

[149] Vitos L, Ruban A V, Skriver H L and Kollar J 1998 *Surface Science* **411** 186–202

[150] Clifton R J and Markenscoff X 1981 *Journal of the Mechanics and Physics of Solids* **29** 227–251

[151] Bringa E M, Cazamias J U, Erhart P, Stolken J, Tanushev N, Wirth B D, Rudd R E and Caturla M J 2004 *Journal of Applied Physics* **96** 3793–3799

[152] Zhakhovsky V V, Budzevich M M, Inogamov N A, Oleynik I I and White C T 2011 *Physical Review Letters* **107** 135502

[153] Dávila L P, Erhart P, Bringa E M, Meyers M A, Lubarda V A, Schneider M S, Becker R and Kumar M 2005 *Applied Physics Letters* **86** 161902

[154] Meyers M A 1977 *Materials Science and Engineering* **30** 99–111

[155] Bronkhorst C A, Kalidindi S R and Anand L 1992 *Philosophical Transactions of the Royal Society of London, Series A: Physical Sciences and Engineering* **341** 443–477

[156] Hockett J 1967 *Transactions of the Metallurgical Society of AIME.* **239** 969–976

[157] Liu Q, Juul Jensen D and Hansen N 1998 *Acta Materialia* **46** 5819–5838

[158] Peirce D, Asaro R and Needleman A 1983 *Philosophical Transactions of the Royal Society of London, Series A: Physical Sciences and Engineering* **31** 1951–1976

[159] Asaro R J and Needleman A 1985 *Acta Metallurgica* **33** 923–953

[160] McGinty R D 2001 *Multiscale representation of polycrystalline inelasticity* Ph.D. thesis Georgia Institute of Technology Atlanta, Ga.

[161] Ling X W, Horstemeyer M F and Potirniche G P 2005 *International Journal for Numerical Methods in Engineering* **63** 548–568

[162] Armstrong P J and Frederick C O 1966 *A mathematical representation of the multiaxial Bauschinger effect* (C.E.G.B. Report)

[163] Haldrup K, McGinty R D and McDowell D L 2009 *Computational Materials Science* **44** 1198–1207

[164] Milathianaki D, Boutet S, Williams G J, Higginbotham A, Ratner D, Gleason A E, Messerschmidt M, Seibert M M, Swift D C, Hering P, Robinson J, White W E and Wark J S 2013 *Science* **342** 220–223

[165] Huang X and Winther G 2007 *Philosophical Magazine* **87** 5189–5214

[166] Winther G and Huang X 2007 *Philosophical Magazine* **87** 5215–5235

[167] Ding J L and Asay J R 2011 *Journal of Applied Physics* **109** 083505

[168] Whitley V H, McGrane S D, Eakins D E, Bolme C A, Moore D S and Bingert J F 2011 *Journal of Applied Physics* **109** 013505

[169] Schoenfeld S E 1998 *International Journal of Plasticity* **14** 871–890

[170] Schoenfeld S E and Kad B 2002 *International Journal of Plasticity* **18** 461–486

[171] Kad B, Schoenfeld S E and Burkins M S 2002 *Materials Science and Engineering: A* **322** 241–251

[172] Bronkhorst C A, Hansen B L, Cerreta E K and Bingert J F 2007 *Journal of the Mechanics and Physics of Solids* **55** 2351–2383

[173] Murr L 1981 *Shock waves and high-strain-rate phenomena in metals* ed Meyers M and Murr L (New York, N.Y.: Plenum Press) pp 753–777

[174] Markenscoff X 1980 *Journal of Elasticity* **10** 193–201

[175] Markenscoff X and Ni L 1993 *Journal of Elasticity* **30** 211–217

[176] Markenscoff X and Ni L 2001 *Journal of the Mechanics and Physics of Solids* **49** 1603–1619

[177] Freund L B 1998 *Dynamic Fracture Mechanics* (Cambridge University Press)

VITA

Jeffrey Townsend Lloyd was born in Charlotte, North Carolina on August 27, 1985. He is the son of Leslee Townsend Lloyd and Robert Michael Lloyd and the stepson of Catherine Meder Lloyd. Jeff graduated from Charlotte Latin High School in Charlotte, North Carolina in 2004. He was awarded the degrees of Bachelor of Science in Mechanical Engineering, with Highest Honor distinction, in 2008, and Master of Science in Mechanical Engineering in 2010, both from the Georgia Institute of Technology. Jeff was the recipient of the National Science Foundation Graduate Research Fellowship from $2008 - 2011$, the Georgia Institute of Technology President's Fellowship from $2008 - 2012$, and the Department of Defense SMART Fellowship from $2011 - 2013$. He worked at at Sandia National Laboratories in Livermore, California as an EPSRI Intern in the summer of 2010 as well as a SMART Summer Intern at the Army Research Laboratory in Aberdeen, Maryland in the summers of 2012 and 2013 during his tenure at Georgia Institute of Technology. Jeff was married to Melanie Rosher in Columbus, Georgia on September 22, 2012.